UNIVERSITY OF CALIFORNIA,
IRVINE

Expanding the Electronic Structure Toolkit for f-Element Chemistry: Advances, Best Practices, and Examples

DISSERTATION

submitted in partial satisfaction of the requirements
for the degree of

DOCTOR OF PHILOSOPHY

in Chemistry

by

Jason M. Yu

Dissertation Committee:
Professor Filipp Furche, Chair
Professor Kieron Burke
Professor William J. Evans

2022

TABLE OF CONTENTS

LIST OF FIGURES

LIST OF TABLES

LIST OF ABBREVIATIONS

1c	One-component
2c	Two-component
4c	Four-component
AMFSO	Atomic mean-field spin orbit
An	Actinide
ASCII	American standard code for information exchange
Au	Atomic units
BLAS	Basic linear algebra subroutines
CAS	Complete active space
CCSD	Coupled cluster singles doubles
CGO	Common gauge origin
COSMO	Conductor-like screening model
CT	Clock transition
DFT	Density functional theory
DKH	Douglas Kroll Hess
DKS	Dirac Kohn Sham
DLU	Diagonal local approximation
ECP	Effective core potential
EFG	Electric field gradient
EPR	Electron paramagnetic resonance
ET	Even tempered
FC	Fermi contact
GGA	Generalized gradient approximation
GIAO	Gauge-including atomic orbital
HFC	Hyperfine coupling constant
HOMO	Highest occupied molecular orbital
KS	Kohn Sham
Ln	Lanthanide
LUMO	Lowest unoccupied molecular orbital
MAE	Mean absolute error
MAPD	Mean average percent-wise deviation
ME	Mean error
MKL	Math kernel library
MLCT	Metal ligand charge transfer
MO	Molecular orbital
MP2	Second-order Møller–Plesset perturbation theory
NESC	Normalized elimination of the small component
NMR	Nuclear magnetic resonance
NQI	Nuclear quadrupole interaction
NR	Non-relativistic
QIS	Quantum information science
RI	Resolution-of-the-identity

RKB	Restricted kinetic balance
RMB	Restricted magnetic balance
RMS	Root mean squared
RSH	Range separated hybrid
SCF	Self-consistent field
SD	Spin dipole
SMM	Single molecule magnet
SNSO	Screened nuclear spin orbit
SO	Spin orbit
SOC	Spin orbit coupling
SOMO	Singly occupied molecular orbital
SR	Scalar-relativistic
TDDFT	Time-dependent density functional theory
THF	Tetrahydrofuran
UV	Ultraviolet
X2C	Exact two-component
XC	Exchange correlation
ZORA	Zeroth-order regular approximation

ACKNOWLEDGMENTS

I would first like to thank my mother for her unwavering love, guidance, and encouragement throughout my scientific journey. Without her support, I would be a very different person than I am today. I extend this thanks to the rest of my family, including Yang Yu, Ronny Choe, Jack Mattia, and Katharina Miyoshi. I am incredibly grateful to all of you.

My scientific mentors also deserve special mention. Thanks so much Professor Jackson Champer for acting as my scientific mentor across multiple scientific domains. Thanks also, Yannick Franzke, for being a great friend and collaborator during my graduate work. Last but most certainly not least, thank you Professor Filipp Furche for your enduring support, patience, and mentorship, which has empowered me to pursue a career in the sciences.

I would also like to thank all of my colleagues in the Furche group, both past and present. Namely, thank you Brandon Krull, Sree Balasubramani, Saswata Roy, Jordan Vincent, Matthew Agee, Luke Nambi Mohanam, Mikko Muuronen, Vamsee Voora, Gabriel Phun, Samuel Bekoe, Dmitrij Rappoport, Shane Parker, Nate Crawford, and Guo Chen. Scientific collaborators across various institutions have also played a key role in the contents of this thesis: thanks so much to Colin Gould, Krishnendu Kundu, Professor Stephen Hill, Professor William Evans, Jessica White, Samuel Moehring, and again to Yannick Franzke.

In addition, I would like to thank Professor Garnet Chan and the members of his lab for their support and guidance during my time at Caltech. Thanks particularly to James McClain, Narbe Mardirossian, Qiming Sun, Mario Motta, Henry Schurkus, Alec White, Matthew O'Rourke, Zhihao Cui, Chong Sun, Elvira Sayfutyarova, Yang Gao, Erika Ye, Zhendong Li, Artem Pulkin, Shi-Ning Sun, and Tianyu Zhu.

Lastly, I would like to thank the members of the Computational Chemistry group at Biogen for their guidance during my time as a Co-op. Thanks particularly to Lakshmi Akella, Govinda Bhisetti, and Cheng Fang for taking me as a student in this new role.

I acknowledge financial support from the UCI Department of Chemistry through teaching assistantships and the National Science Foundation (NSF) through the Graduate Research Fellowship Program (DGE-1839285) and Grants CHE-1800431 and CHE-2102568. I also acknowledge the high performance computing (HPC) infrastructure available at the Research Cyberinfrastructure Center (RCIC) at UCI (supported by the NSF under CNS-1828779) and the GreenPlanet cluster at UCI for facilitating the calculations performed in this work. The Eddleman Quantum Institute (EQI) is acknowledged.

This dissertation contains verbatim excerpts as they appear in (1) Gould, C. A.; McClain, K. R.; Yu, J. M.; Groshens, T. J.; Furche, F.; Harvey, B. G.; Long, J. R. *J. Am. Chem. Soc*, **2019**, *141*, 12967-12973, (2) Yu, J. M.; Furche, F. *Inorg. Chem.* **2019**, *58*, 16004-16010, (3) Franzke, Y. J.; Yu, J. M. *J. Chem. Theory Comput.* **2022**, *18*, 323-343, (4) Franzke, Y. J.; Yu, J. M. *J. Chem. Theory Comput.* **2022**, *18*, 2246-2266, used with permission from the American Chemical Society. This dissertation also contains verbatim excerpts as

they appear in (5) Kundu, K.; White, J. R. K.; Moehring, S. A.; Yu, J. M.; Ziller, J. W.; Furche, F.; Evans, W. J.; Hill, S. *Nat. Chem.*, **2021**, *14*, 392-397, used with permission from Springer Nature. Lastly, this dissertation contains verbatim excerpts as they appear in (6) Balasubramani, S. G. et al. *J. Chem. Phys.*, **2020**, *152*, 184107, used with permission from AIP Publishing. The co-authors listed in these publications directed, supervised, or conducted part of the research which forms the basis for the dissertation.

VITA

Jason M. Yu

EDUCATION

Doctor of Philosophy in Chemistry **2022**
University of California, Irvine *Irvine, CA*

Master of Science in Chemistry **2019**
California Institute of Technology *Pasadena, CA*

Bachelor of Science in Chemistry **2017**
University of California, Irvine *Irvine, CA*

REFEREED JOURNAL PUBLICATIONS

Quasi-Relativistic Calculation of EPR g-Tensors with Derivatives of the Decoupling Transformation, Gauge-Including Atomic Orbitals, and Magnetic Balance
Y. J. Franzke and J. M. Yu. *J. Chem. Theory Comput.* **2022**, *18*, 2246-2266

A 9.2-GHz clock transition in a Lu(II) molecular spin qubit arising from a 3,467-MHz hyperfine interaction
K. Kundu, J. R. K. White, S. A. Moehring, J. M. Yu, J. W. Ziller, F. Furche, W. J. Evans, and S. Hill. *Nat. Chem.* **2022**, *14*, 392-397

Hyperfine Coupling Constants in Local Exact Two-Component Theory
Y. J. Franzke and J. M. Yu. *J. Chem. Theory Comput.* **2022**, *18*, 323-343

Selfconsistent random phase approximation methods
J. M. Yu, B. D. Nguyen, J. Tsai, D. J. Hernandez, and F. Furche. *J. Chem. Phys.* **2021**, *155*, 040902

Recent developments in the PySCF program package
Q. Sun, X. Zhang, S. Banerjee, P. Bao [and forty-five others including J. M. Yu]. *J. Chem. Phys.* **2020**, *153*, 024109

TURBOMOLE: Modular program suite for *ab initio* quantum-chemical and condensed-matter simulations
S. Balasubramani, G. Chen, S. Coriani, M. Diedenhofen [and thirty-one others including J. M. Yu]. *J. Chem. Phys.* **2020**, *152*, 184107

Electronic structure of bulk manganese oxide and nickel oxide from coupled cluster theory
Y. Gao, Q. Sun, J. M. Yu, M. Motta, J. McClain, A. F. White, A. J. Minnich, G. K. L. Chan. *Phys. Rev. B* **2020**, *101*, 165138

Theoretical Study of Divalent Bis(Pentaisopropylcyclopentadienyl) Actinocenes
J. M. Yu and F. Furche. *Inorg. Chem.* **2019**, *58*, 16004-16010

Synthesis and magnetism of neutral, linear metallocene complexes of terbium (II) and dysprosium (II)
C. A. Gould, K. R. McClain, J. M. Yu, T. J. Groshens, F. Furche, B. G. Harvey, and J. R. Long. *J. Am. Chem. Soc.* **2019**, *141*, 16004-16010

Brominated luciferins are versatile bioluminescent probes
R. C. Steinhardt, C. M. Rathbun, B. T. Krull, J. M. Yu, Y. Yang, B. D. Nguyen, J. Kwon, D. C. McCutcheon, K. A. Jones, F. Furche, and J. A. Prescher. *Chem. Bio. Chem.* **2017**, *18*, 96-100

CONFERENCE and POSTER PRESENTATIONS

A DEL data analysis platform for the identification of diverse chemical series in drug discovery
J. M. Yu, L. Akella, and G. Bhisetti. **ACS Fall 2021**, *Atlanta, GA*, Presentation.

Computational Characterization of Ln(II) Molecular Spin Qubits using Density Functional Theory
J. M. Yu, K. Kundu, J. R. K. White, S. A. Moehring, J. W. Ziller, W. J. Evans, F. Furche, and S. Hill. **International Conference on Molecule Based Magnets 2021**, *Remote*, Poster.

Achieving Functional Self-Consistency in Post Kohn-Sham Methods
J. M. Yu, S. Balasubramani, V. Voora, J. Tsai, and F. Furche. **Southern California Theoretical Chemistry Symposium 2019**, *Los Angeles, CA*, Poster.

Developing a Genetic Algorithm to Optimize Luciferin Analogs for Bioluminescence Imaging
J. M. Yu, B. T. Krull, B. D. Nguyen, A. Le, and F. Furche. **Undergraduate Research Opportunities Program Symposium 2016**, *Irvine, CA*, Poster.

TEACHING EXPERIENCE

Scientific Computing Skills (Chem 5) — **SS2, 2021**
University of California Irvine — *Irvine, CA*

General Chemistry Lab (Chem 1LC) — **SS1, 2021**
University of California Irvine — *Irvine, CA*

General Chemistry Lab (Chem 1LD) — **Fall 2020**
University of California Irvine — *Irvine, CA*

SELECTED HONORS AND AWARDS

National Science Foundation
Graduate Research Fellowship **2018**
University of California, Irvine *Irvine, CA*

Rose Hills Graduate Fellowship **2017**
California Institute of Technology *Pasadena, CA*

Chancellor's Award for Excellence in Research **2017**
University of California Irvine *Irvine, CA*

POLYED Undergraduate Award
for Achievement in Organic Chemistry **2017**
University of California Irvine *Irvine, CA*

Rose Hills Foundation Undergraduate
Science and Engineering Scholarship **2014**
University of California Irvine *Irvine, CA*

ABSTRACT OF THE DISSERTATION

Expanding the Electronic Structure Toolkit for f-Element Chemistry: Advances, Best Practices, and Examples

By

Jason M. Yu

Doctor of Philosophy in Chemistry

University of California, Irvine, 2022

Professor Filipp Furche, Chair

In recent years, collaborative studies that leverage experimental synthesis, spectroscopic characterization, and electronic structure analysis have enabled significant advances in f-element chemistry through the discovery of newly accessible metal oxidation states and novel electronic configurations for lanthanide (Ln) and actinide (An)-containing species. With the purpose of extending the utility of computational approaches to maintain this positive trajectory, the present thesis discusses recent developments and applications of computational chemistry methods, with a focus on density functional theory (DFT), towards the accurate prediction and characterization of new f-element complexes. A DFT methodology based on (meta)-generalized gradient approximation (mGGA) density functionals, triple-ζ quality basis sets for metal atoms, and effective core potentials (ECPs) is shown to provide the electronic structure insights necessary to understand the unexpected stability of fully linear Dy and Tb-based metallocene species, $Dy(Cp^{iPr_5})_2$ and $Tb(Cp^{iPr_5})_2$. Calculations reveal that such unorthodox molecular geometry, which is rarely observed for lanthanides, is facilitated by a $4f^n5d^1$ electronic configuration of the metal center, which gives rise to a $\sigma-$bonding interaction between the $5d/6s$ HOMO and cyclopentadienyl ligand system. Further calculations using this DFT methodology predict the existence of stable, linear An-based metallocenes, and the results of this study are used to guide synthetic efforts to-

wards the experimental isolation of $U(Cp^{iPr_5})_2$, the first An-based "ferrocene" analog. A similar computational methodology which replaces the ECP with an all-electron approach is applied towards the characterization of Ln-based spin molecular qubits, $[Lu(OAr^*)_3]^-$, $[La(OAr^*)_3]^-$, and $[Lu(NR_2)_3]^-$, revealing the importance of $6s$ orbital contributions to the spin density to facilitate large Fermi-contact and thus hyperfine interactions. This thesis concludes by describing the prediction of accurate EPR parameters, such as the hyperfine coupling constant, electronic g-tensor, and quadrupole coupling constant in relativistic DFT for the broader study of candidate molecular qubits. An implementation of these quantities is presented within the relativistic exact two-component theory (X2C) method, and benchmark calculations on transition metal and f-element complexes are provided to evaluate choice of the relativistic Hamiltonian, basis set, and density functional approximation (DFA). A recommended set of parameters based on the results of these benchmarks is presented, and subsequently used to calculate the EPR parameters for the previous series of Lu and La molecular qubit systems. These predictions are found to reduce errors by roughly one order of magnitude when compared with the unrefined methodology, and are highly accurate when compared to experimental data- representing an advance for *in-silico* characterization of EPR spectra. Present challenges and future directions for the development of electronic structure methods for the study of the f-elements are assessed.

Chapter 1

Background and Theory

 This material is based on work supported by the National Science Foundation under grant no. CHE-1800431.

1.1 Introduction

The electronic structure of the f-elements poses a unique set of challenges for existing computational chemistry methods. The core-like nature of the f shells render them resilient against perturbation by a coordinating ligand field, thus making ground states difficult to resolve in f-element organometallic compounds.[1,2] At the same time, the highly charged nuclei of lanthanide (Ln) and actinide (An) atoms introduce relativistic effects that significantly influence their valence structure.[3,4] Striking a balance of treating both the (A) complex electronic correlation effects and (B) relativistic effects highlighted above, while (C) maintaining computational efficiency, represents the three principal challenges for describing the f-elements with quantum chemistry methods.

Despite the considerable methodological difficulty, computational investigations are essential for the progression of f-element chemistry. Recent breakthroughs have revealed that the electronic structures for Ln and An species can be controlled by careful choice of ligand environment,[5] leveraging their oftentimes low-lying $5d/6d$ excited configurations to stabilize new ground states.[6] Possessing d valence electrons may enable unique chemical properties and new reactivity by coaxing the otherwise reclusive f-elements to form covalent bonds with organometallic ligands. Thus, accessible d valence configurations stand to significantly expand the landscape of f-element organometallic chemistry, which has historically been considered completely distinct from that of the transition metals. This observation further emphasizes the need for highly accurate computational methods which are capable of facilitating the discovery and understanding of such novel Ln and An systems.

An electronic structure method that fulfills all of the above criteria has yet to manifest, although several options exist for particular applications. Multiconfigurational wavefunction-based methods, such as the complete active space self-consistent field theory (CASSCF), can resolve nearly-degenerate electronic states[2,7] and thus provide predictions of low-lying

excited states, relaxation barriers and crystal field parameters.[8,9] However, such methods rely on a parameterization of the configurational "active space" that is not generally conducive to exploratory calculations (i.e. to determine the ground state configuration),[10] and the method itself can be prohibitively costly for larger systems due to the factorial scaling of the number of possible Slater determinants.[11] The latter is especially true when considering scenarios that require higher-level treatments of electron correlation beyond the Hartree-Fock level for qualitative accuracy, such as the description of f-element ions with $5d^1$ and $6d^1$ ground states.

On the other hand, density functional theory (DFT) based on the Kohn-Sham (KS) formalism offers a single determinant description of electronic structure, facilitating a molecular orbital-based "model chemistry"[12] which simplifies the interpretation of electronic, chemical, and structural properties for a molecular system. The reduced computational cost associated with a single-reference method also enables the study of f-element complexes that would otherwise be too costly to address with multireference methods. Unfortunately, DFT struggles with resolving nearly-degenerate spin states and is oftentimes incapable of describing multiconfigurational character due to the shortcomings of common semilocal approximations in describing strongly correlated systems. Without making specific considerations for these effects, such limitations impact DFT's capacity to generate new hypotheses and guide synthetic efforts in the discovery of new f-element chemistry.

The prediction of magnetic properties also remains a significant hurdle common to both CASSCF and DFT for f-element species. Calculations of the isotropic hyperfine coupling (HFC) constant, for example, are typically limited to main-group radicals and transition metal species,[13] as the onset of spin-orbit coupling effects for the f-elements introduces errors in excess of one order of magnitude due to the divergence of the Fermi contact interaction.[14–16] Approaches to magnetic properties which include relativistic effects have been outlined, but their high computational cost precludes broad application to moderately sized

f-element compounds.[17–19] Due to the great recent interest in the magnetism of Ln and An species for applications as single molecule magnets and molecular qubits,[20–22] computational methods which accurately characterize the magnetic properties of such systems are inherently desirable.

Given the above context, the goal of this thesis is thus: (1) to demonstrate the utility of carefully-tailored electronic structure methods, with a particular emphasis on DFT, for the characterization and discovery of novel f-element species, and (2) to extend the electronic structure toolkit for magnetic properties not readily accessible with current methods, particularly through formulation of the hyperfine coupling constant, electronic g-tensor, and electric field gradients in a relativistic theory. In doing so, this work details progress in accurately modeling the electronic structure of the f-elements and provides a glimpse into remaining tasks and challenges.

This thesis is organized as follows. The remainder of Chapter 1 provides an introduction to the electronic structure of the f-elements and gives historical context into the discovery of unconventional oxidation states, unlocking their chemical flexibility. The chapter goes on to highlight current opportunities for computational chemistry methods as a means to lead synthesis efforts towards the discovery of new compounds, as well as to supplement their physical description and understanding. It concludes with a broad overview of DFT, the various parameters and methods which comprise the DFT description, and a set of general practices for the study of the f-elements.

Chapter 2 highlights two applications of density functional theory which proved essential for the characterization and understanding of f-element-based metallocene species. Section 2.2 details how DFT calculations uncovered an explanation for the unexpected stability of linear bis(pentaisopropylcyclopentadienyl) metallocenes of terbium and dysprosium by revealing covalent bonding interactions between the ligand system and $5d/6s$ HOMO. Building upon these observations, Section 2.3 presents an argument on the basis of DFT predictions for

the existence of the corresponding linear actinide metallocene analogs, insights which served to guide experimental efforts towards the discovery of the uranium analog shortly after publication.

Lastly, Chapter 3 illustrates developments in the prediction of electron paramagnetic resonance (EPR) parameters of f-element species using DFT. Section 3.2 presents initial predictions for the hyperfine coupling constant and quadrupole coupling tensors obtained from an all-electron relativistic theory for a series of Ln-based molecular spin qubit candidates. These initial approaches are subsequently refined in Section 3.3 for the hyperfine coupling constants, Section 3.4 for the electronic g-tensors, and Section 3.5 for the nuclear quadrupole coupling tensors through the use of two-component relativistic operators. Such new developments enable quantitative accuracy for the aforementioned EPR parameters, bridging the gap between experiment and computation for magnetic characterization of the f-elements.

1.2 The f-Elements

1.2.1 Electronic Structure

Carving out a block that (usually) begins under yttrium in group 3 of the periodic table,[23–26] the lanthanide and actinide elements possess unique electronic structures characterized by the gradual population of their $4f$ and $5f$ valence orbitals, respectively. For the lanthanides, which are composed of the 15 elements between lanthanum and lutetium with atomic numbers $57-71$, the high nodality and limited radial distributions of the $4f$ orbitals restrict both energetic and spatial capacity for covalent bonding, leading to large electropositive metals with reactivity dictated by steric interactions with coordinating ligands.[27] For the actinides, which refer to the 15 elements between actinium and lawrencium with atomic numbers $89-103$, the $5f$ valence orbitals are less contracted than the $4f$ orbitals, and are

oftentimes nearly degenerate with or higher in energy than the $6d$ shell for the earlier elements. However, later actinides tend to resemble the lanthanides in electronic structure due to the lowering of $5f$ orbital energies from inadequate shielding of the f shells.[28] To illustrate, atomic radial distribution functions of the lanthanide ion Lu^{2+} and the actinide ion Th^{2+} are plotted in Figure 1.1. Table 1.1 further provides the observed atomic electronic configurations and associated term symbols for the lanthanide and actinide elements as documented in the NIST database.[29]

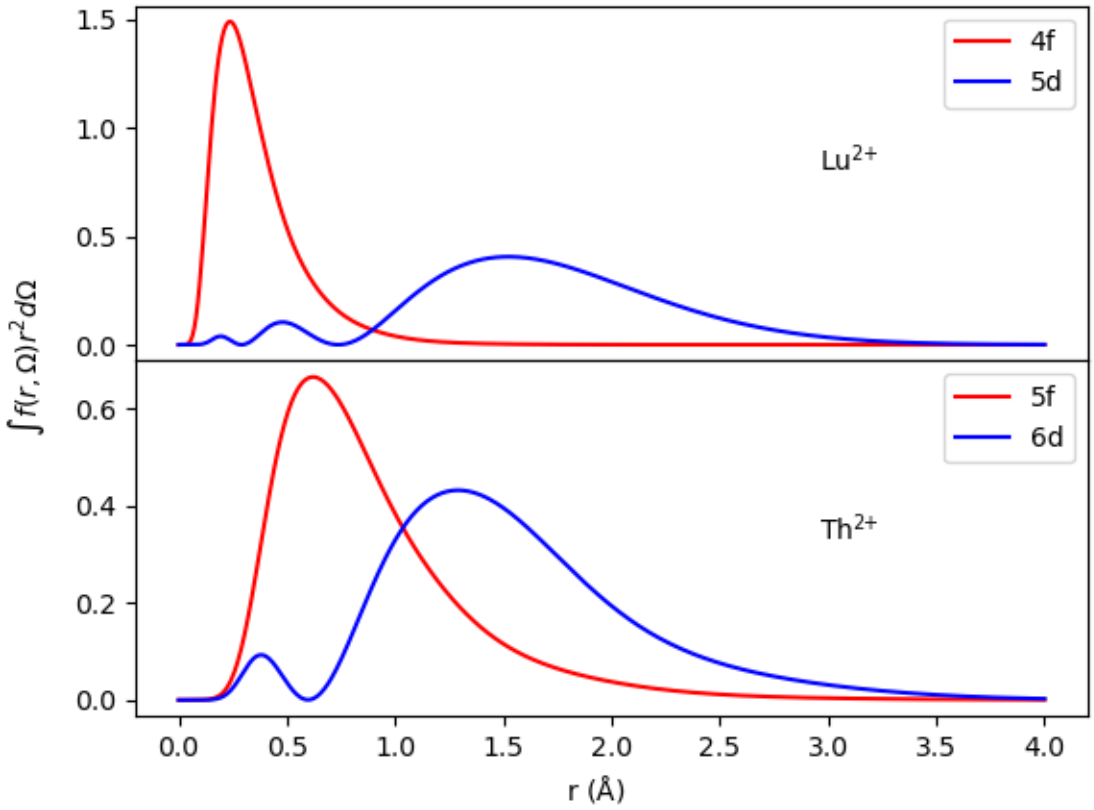

Figure 1.1: Atomic radial distribution functions of the electronic density for Lu^{2+} and Th^{2+} computed using scalar-relativistic DFT. The larger radial extent of the $5f$ shell relative to the $4f$ shell is depicted. Ground states were calculated using the PBE0 functional and small-core effective core potentials of the Stuttgart-Cologne group. Karlsruhe basis sets def2-TZVP (Lu) and def-TZVP (Th) were used. The radial distribution function was computed from the electron densities $f(r, \Omega)$ arising from the corresponding valence shells according to the integral contained in the y-axis label, where Ω denotes a spherical coordinate and r is the radial distance from the sphere center. Curves were normalized to 1.0 for ease of comparison.

As can be surmised, the large angular momentum of the f shell gives rise to a high density

Table 1.1: Electronic configurations and term symbols for Ln and An atoms as tabulated in the NIST spectral database[29] and the references contained therein. The degree symbol indicates odd parity.

Ln	Configuration	Term	An	Configuration	Term
La	[Xe] $5d^1\ 6s^2$	^{2}D	Ac	[Rn] $6d^1\ 7s^2$	^{2}D
Ce	[Xe] $4f^1\ 5d^1\ 6s^2$	^{1}G°	Th	[Rn] $6d^2\ 7s^2$	^{3}F
Pr	[Xe] $4f^3\ 6s^2$	^{4}I°	Pa	[Rn] $5f^2\ 6d^1\ 7s^2$	^{4}I°
Nd	[Xe] $4f^4\ 6s^2$	^{5}I	U	[Rn] $5f^3\ 6d^1\ 7s^2$	^{5}L°
Pm	[Xe] $4f^5\ 6s^2$	^{6}H°	Np	[Rn] $5f^4\ 6d^1\ 7s^2$	^{6}L
Sm	[Xe] $4f^6\ 6s^2$	^{7}F	Pu	[Rn] $5f^6\ 7s^2$	^{7}F
Eu	[Xe] $4f^7\ 6s^2$	^{8}S°	Am	[Rn] $5f^7\ 7s^2$	^{8}S°
Gd	[Xe] $4f^7\ 5d^1\ 6s^2$	^{9}D°	Cm	[Rn] $5f^7\ 6d^1\ 7s^2$	^{9}D°
Tb	[Xe] $4f^9\ 6s^2$	^{6}H°	Bk	[Rn] $5f^9\ 7s^2$	^{6}H°
Dy	[Xe] $4f^{10}\ 6s^2$	^{5}I	Cf	[Rn] $5f^{10}\ 7s^2$	^{5}I
Ho	[Xe] $4f^{11}\ 6s^2$	^{4}I°	Es	[Rn] $5f^{11}\ 7s^2$	^{4}I°
Er	[Xe] $4f^{12}\ 6s^2$	^{3}H	Fm	[Rn] $5f^{12}\ 7s^2$	^{3}H
Tm	[Xe] $4f^{13}\ 6s^2$	^{2}F°	Md	[Rn] $5f^{13}\ 7s^2$	^{2}F°
Yb	[Xe] $4f^{14}\ 6s^2$	^{1}S	No	[Rn] $5f^{14}\ 7s^2$	^{1}S
Lu	[Xe] $4f^{14}\ 5d^1\ 6s^2$	^{2}D	Lr	[Rn] $5f^{14}\ 7s^2\ 7p^1$	^{2}P°

of low-lying total angular momentum (J) states owed to coupling with unpaired electronic spin. In fact, the number of accessible configuration state functions is an order of magnitude larger than those corresponding to an equivalent number of unpaired electrons in a d valence shell, and two orders of magnitude larger than those for a p valence shell (see Figure 1.2). The energy levels themselves are closely spaced due to the reclusiveness of the $4f$ and $5f$ shells, producing average energy differences of roughly 0.25 kcal/mol for Gd and Cm.[1] As seen in Figure 1.3, this spacing is generally much smaller than those typically observed for the transition metals. Low-lying excited state configurations further contribute to the complexity of the electronic structure observed for lanthanide and actinide species.

Coordination chemistry of the lanthanide and actinide elements is notably distinct from that of the d block metals, in large part due to the distinctive properties of the f orbitals and the larger atomic nuclei. The lanthanides tend to form ionic complexes with negatively charged donor ligands, yielding large coordination numbers determined by energetic saturation of the atomic radius.[31] Coordination of organic ligands often result in air- or heat-unstable species,

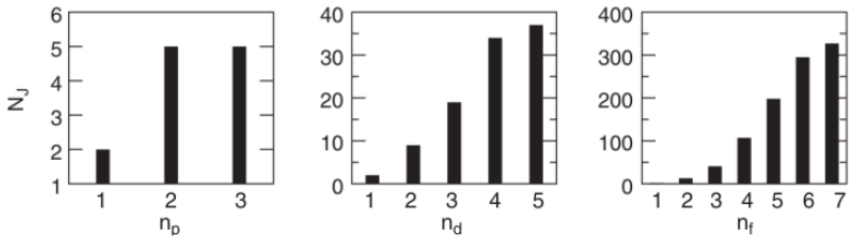

Figure 1.2: Number of determinants arising from n unpaired electrons for p (left), d (middle), and f (right) valence electronic configurations. Reprinted from *Computational Methods in Lanthanide and Actinide Chemistry*: Chapter 16: Shell Structure, Relativistic and Electronic Correlation Effects in f Elements and Their Importance for Cerium(III)-based Molecular Kondo Systems, 425-450, Copyright (2015), with permission from Wiley.

although certain ligands such as the cyclopentadienyl system yield well-characterized compounds and have been used to study periodic trends in lanthanide elements.[6] In comparison, the early actinides tend to better resemble transition metals due to their occupied $6d$ valence orbital, and some covalent interactions with ligands have been observed, although this remains a topic of considerable controversy.[32] Thus, the "conventional wisdom" is that lanthanide and actinide elements with f orbital valence configurations are known to behave predominantly as hard acids.

Despite the historical perspective towards these elements,[33] which initially regarded their "straightforward" tendency to form high coordinate, ionic complexes in predominantly trivalent oxidation states[31] as "boring", breakthroughs in organolanthanide and organoactinide chemistry have since reignited both scientific and industrial interest in these systems.[27] Recently, metal-ligand complexes of these elements have demonstrated novel catalytic and magnetic properties which have been subsequently explored for applications in small-molecule activation,[34–36] magnetism,[20,21] and separation of nuclear fission products.[37–39]

Some of these recent developments have arisen from a better understanding of the ways that one can take advantage of the chemistry of the f-elements to solve scientific problems. For example, saturated ligand systems with large unquenched angular momenta on the metal ion can enhance magnetic moments and simplify structural predictions, two inherently desirable

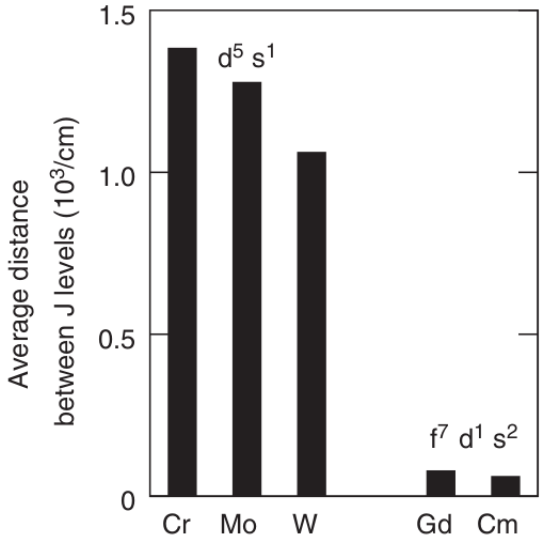

Figure 1.3: Average spread of energy levels for Cr, Mo, W atoms with d^5s^1 configurations, and Gd and Cm atoms with $f^7d^1s^2$ configurations. Data calculated by multi-configurational Hartree-Fock calculations as reported in [30]. Reprinted from *Computational Methods in Lanthanide and Actinide Chemistry*: Chapter 16: Shell Structure, Relativistic and Electronic Correlation Effects in f Elements and Their Importance for Cerium(III)-based Molecular Kondo Systems, 425-450, Copyright (2015), with permission from Wiley.

qualities for candidate single molecule magnet materials (SMMs).[20,21,40] Much of the recent interest in lanthanide and actinide elements has also arisen from a notable expansion in available chemistry via the discovery of newly accessible oxidation states and d electronic configurations for many elements. A description of this advancement is given in the following section.

1.2.2 Discovery of New Oxidation States Across the Ln and An Series

‘‘Lanthanum has only one important oxidation state in aqueous solution, the +3 state. With few exceptions, this tells the whole boring story about the other 14 Lanthanides.’’

G. C. Pimentel and R. D. Sprately on lanthanide chemistry,
‘‘Understanding Chemistry’’, Holden-Day, 1971, p.862

‘‘[Recent advances] provide an excellent lesson in how much new chemistry is awaiting discovery when the old traditional principles are overturned’’

W. J. Evans on the importance of questioning scientific assumptions, in Inorg. Chem. 2006, October 19th, 2006, p.3435

The most common oxidation state exhibited by the f-elements in a complex is M^{3+}, and until the mid 1990s only a few other oxidation states for the lanthanides were known to be stable in solution.[31,41] For this reason, a predominant view held at this time was that the chemistry of the f-elements was inherently limited, especially in contrast with the transition metals which exhibit a variety of oxidation states. However, within the last twenty years, a series of breakthroughs in reductive lanthanide and actinide chemistry has overturned these scientific assumptions, enabling new reactivity and applications that have stimulated the field anew.[6,27,42,43]

The most significant advancement came with the discovery of the divalent oxidation state for the majority of stable f-elements, whereas only those of Eu, Yb, and Sm were known prior to 1997.[6,44] Efforts in reductive lanthanide chemistry were active during this early period, and resulted in the discovery of molecular compounds containing Tm(II),[45] Dy(II),[46] and Nd(II)[47,48] between 1997 and 2001 by the research groups of Bochkarev and Evans. At the same time, Lappert and coworkers reported evidence of the first thermally stable La(II) complexes in 1997.[49] This initial burst of discoveries constitutes a “first wave” of newly accessible divalent states found for Ln complexes.

A second wave of innovation for reductive Ln and An chemistry has taken place over the past decade. Interestingly, these advances were fueled in part by insights derived from den-

sity functional theory calculations, which began with the discovery of significant $5d$ orbital occupations in a formal $(N_2)^{3-}$ complex of Dy, suggesting that such "transition metal-like" character (in the context of valence electronic structure) may facilitate the isolation of new electronic configurations[36,50] This observation inspired a collaborative experimental and computational effort to isolate and characterize divalent lanthanide complexes with valence d populations, leading to the discovery of the first molecular complexes containing formal 2+ oxidation states for the rare-earth metals Sc,[51] Y,[52] Ho,[53] Er,[53] Pr,[54] Gd,[54] Tb,[54] and Lu[54] and for the actinide metals Th,[55] U,[56] and Pu.[57] A visual summary of the sequence of these discoveries is given in Figure 1.4.

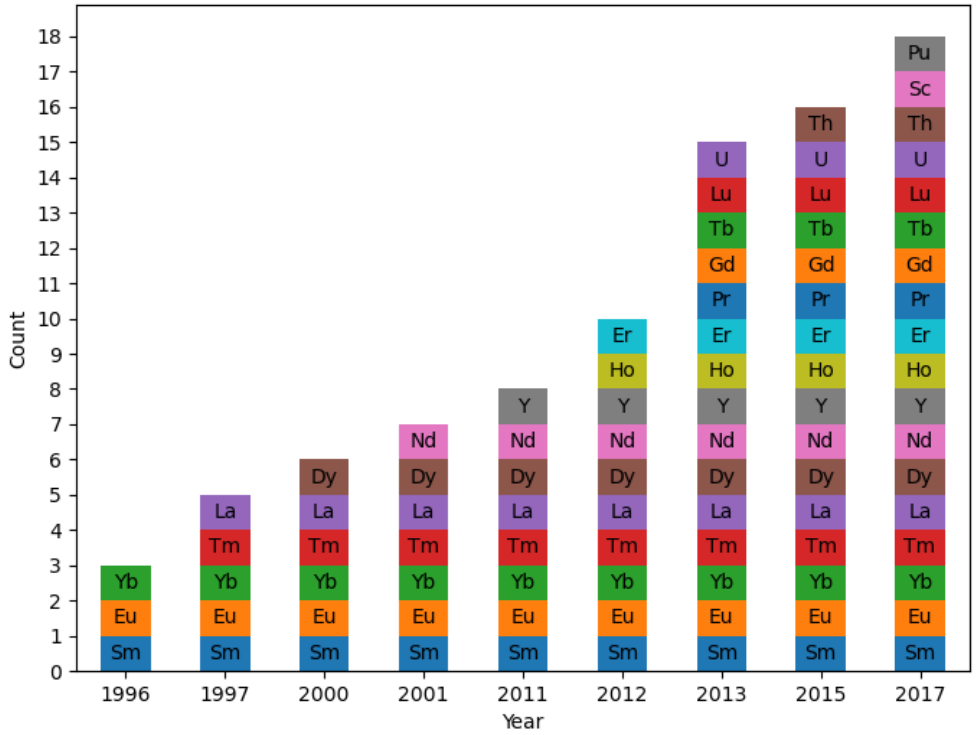

Figure 1.4: Timeline portraying the discovery of the first molecular examples of divalent lanthanide and actinide species. The year label includes all divalent oxidation states discovered up until the given time: For example, only divalent oxidation states of Sm, Eu, and Yb in molecular complexes were known prior to 1996.

A crucial product of these discoveries was that the ground state configurations for many new

divalent species did indeed exhibit occupied valence d orbitals, yielding greater chemical availability for bonding. These configurations were stabilized by what was oftentimes a trigonal field of substituted cyclopentadienyl ligands[6] or amide ligands.[51,58] The chemical properties of these systems deviated significantly from the hard Lewis acid characterization that one would may otherwise have expected, demonstrating greater tendency to interact with and be influenced by the ligand system and thus showing more diverse reactivity. As such, it is now known that the chemical properties of f-element complexes are notably versatile, with flexible electronic structure that can be modulated by the appropriate ligand field. Put more explicitly, it was shown that tris(Cp′) and tris(Cp″) (Cp′ = $C_5H_4(SiMe_3)$, Cp″ = $C_5H_3(SiMe_3)_2$) ligands preferentially stabilize $f^n d^1$ over f^{n+1} valence configurations for many Ln and An elements. In contrast, theoretical predictions of divalent uranium complexes have shown that the $5f^4$ ground state is more stable for the $(NHAr^{iPr_6})_2U$ (iPr = $-CH(CH_3)_2$) complex as opposed to the more traditional $5f^3 6d^1$ configuration.[59] As we will see in Chapters 2 and 3, even more ligand systems which stabilize the divalent oxidation state have since been discovered, leading to species that improve upon existing single molecule magnets[60] as well as represent new qubit technologies.[14] This adaptive electronic structure has also been used to facilitate metal-metal bond formation[61] and reduction of CO, CO_2, and N_2.[62]

Such dramatic advancements, which occurred within a brief period of time relative to the age of the discipline, demonstrate that the field of f-element chemistry is far from solved. Furthermore, this progress highlights the instrumental role of computational characterization and guidance in the discovery process. In this respect, there exists significant opportunity to make contributions towards both the physical understanding of Ln and An chemistry as well as the discovery of new species for technological applications.

1.2.3 Opportunities for Computational Methods

Due to the recent interest in f-element complexes for various industrial applications, the design and synthesis of new species that fit a desired chemical property profile is an important task.[63] In this respect, computational studies are essential to the discovery process, providing *in-silico* screening methods which can circumvent experimental challenges in their accessibility, handling, and characterization. Indeed, electronic structure calculations have a history of producing useful results for the f-elements, dating all the way back to Bursten's initial investigations of bonding in organometallic actinide complexes using the Xα method.[64–68]

Such computational efforts were crucial for the discovery of new oxidation states for a number of Ln and An elements, as mentioned in Section 1.2.2.[51,53–57] In addition to generating new hypotheses, a significant function of the computational studies conducted in these reports was to identify the electronic configurations of newly isolated species. This was generally accomplished in three separate ways: (1) prediction of ground state electronic structure, (2) geometry optimization for comparison with crystal structures, and (3) prediction of UV-vis spectra. While (1) provided straightforward corroboration of the metal oxidation state, conclusions from (2) also served to validate experimental findings that metal-ligand bond lengths were smaller for trivalent species than divalent species.[54] Furthermore, predicted UV-vis spectra from (3) reinforced the starkly contrasting features between spectra corresponding to trivalent and divalent species. Owed to potential occupation of a d valence orbital, metal-to-ligand charge transfer excitations with significant oscillator strengths in the 250 to 950 nm region are observed only for Ln(II) and An(II) compounds.[54] In contrast, purely f electron valence configurations yield spectra with peaks of much lower intensity arising predominantly from Laporte forbidden f-f transitions. Taking these results together, current computational methods are already capable of verifying predicted electronic configurations and oxidation states via comparison to experiment in the form of structural and spectroscopic data.

Despite this progress, several major challenges to their theoretical characterization endure. The near degeneracy of the f and possibly d valence orbitals (*vide infra*) necessitates the incorporation of static correlation effects, subverting the blanket application of single-reference methods and all of their conveniences. The presence of bulky and oftentimes tailor-designed ligands also requires methods with low computational cost, especially if one wishes to perform calculations on extended systems and materials. The situation is also complicated by solvation and relativistic effects, which must be considered for an accurate description. Lastly, the need for large basis sets due to the slow convergence of dynamic correlation with high angular momentum basis functions limits the scalability of electronic structure methods for systems with many metal atoms.

Knowing this, there is still an unmet need for the development of electronic structure methods that are capable of addressing such persistent challenges. The expansion of observables that can be predicted by existing methods must furthermore be pursued in parallel to bolster *in-silico* screening efforts and to enable more direct comparisons to experimental results.

Although high-level wavefunction methods have been used to study small compounds or simplified model systems,[69–71] DFT and post-KS methods remain the primary workhorse for routine computations of rare-earth and actinide complexes with large ligands.[72] The theoretical underpinnings of density functional theory are laid out in the following section, along with a discussion of the special considerations required to study f-element complexes and the areas that require further attention and development.

1.3 Density Functional Theory

1.3.1 Theoretical Background

In the following, a brief review of the main theoretical concepts underpinning density functional theory, with a particular focus on those significant for modeling f-element species, is provided. A more comprehensive introduction to the topic, which is outside of the scope of this work, can be found in many standard electronic structure textbooks.[73,74]

At the foundation of DFT lies the Hohenberg-Kohn (HK) Theorem, which establishes the fundamental connection between an external potential influencing a many-electron system and the corresponding ground state electronic density.[75] The theorem states that the external potential $\nu(\mathbf{r})$ is uniquely determined by the electronic density $n(\mathbf{r})$, and thus the total energy is also a unique functional of n. Hohenberg and Kohn further demonstrated that the energy functional,

$$E_\nu[n] \equiv \int \nu(\mathbf{r}) n(\mathbf{r}) d\mathbf{r} + F[n], \tag{1.1}$$

which is constructed from the external potential $\nu(\mathbf{r})$ and a "universal density functional" $F[n]$ valid for any external potential and particle number, is minimized at the correct value of $n(\mathbf{r})$. As a result, if $E_\nu[n]$ is known, the ground state energy could be found via the straightforward application of the variational principle as a functional of the density:

$$E_\nu[n] = \min_n \left\{ F[n] + \int d\mathbf{r} \nu(\mathbf{r}) n(\mathbf{r}) \right\}, \tag{1.2}$$

where

$$F[n] = \inf_{\Psi \to n} \langle \Psi | \, \hat{T} + \hat{V}_{ee} \, | \Psi \rangle \, . \tag{1.3}$$

In Eq. 1.3, Ψ is a general many-electron wavefunction with density constrained to n, $\hat{T}$ is the kinetic energy operator, and $\hat{V}_{ee}$ is the two-electron repulsion operator..

Whereas the validity of the HK theorem makes clear that such a universal functional of the density exists in principle, an explicit and computationally tractable representation has eluded researchers in the 60+ years since Hohenberg and Kohn shared their findings. This precludes the direct application of Equation 1.1 to calculate the total energy from knowledge of the density for a general many-electron system under the influence of an external potential. Approximations to the universal density functional have been developed, and some have even existed before the conception of DFT.[76] However, a fundamental difficulty to these approaches arises from the errors incurred from approximating the interacting kinetic energy as a functional of the density.

To circumvent this, Kohn and Sham introduced the idea of adopting a non-interacting reference system, which is constrained to reproduce the exact density of the interacting system.[77] The benefits of such a substitution can be illustrated by the alternative minimization problem:

$$E_s[n] = \min_n \left\{ T_s[n] + \int d\mathbf{r} \nu_s(\mathbf{r}) n(\mathbf{r}) \right\}, \tag{1.4}$$

where

$$T_s[n] = \inf_{\Phi \to n} \langle \Phi | \, \hat{T} \, | \Phi \rangle \, . \tag{1.5}$$

In the above, the non-interacting ground-state energy E_s is minimized with respect to the density, and the external potential (or Kohn-Sham potential, as it is usually called) ν_s serves to constrain the minimizing density to that of the physical system. A notable difference between Equations 1.2 and 1.4 is that the universal functional of the density is instead replaced with the exact non-interacting kinetic energy T_s. As the minimizing solution to 1.4 can be written as a single determinant wavefunction Φ, T_s can be evaluated exactly once it is obtained.

The Kohn-Sham formalism is, in principle, exact in the sense that this analogous minimization problem produces the physical electron density as the minimizing solution and the exact total energy can therefore be computed. However, the need to make approximations endures in practice. To illustrate this reality, one can find the Kohn-Sham potential to consist of three individual components:

$$\nu_s(\mathbf{r}) = \nu(\mathbf{r}) + \int d\mathbf{r} \frac{n(\mathbf{r})}{|\mathbf{r} - \mathbf{r}'|} + \nu_{XC}[n](\mathbf{r}), \tag{1.6}$$

where

$$\nu_{XC}(\mathbf{r}) = \frac{\delta E_{XC}}{\delta n(\mathbf{r})}. \tag{1.7}$$

The first two terms represent the electron-nucleus external potential and the Coulomb potential, respectively. The so-called exchange-correlation energy, E_{XC}, is defined as the difference between the exact and non-interacting energy functionals of the density, and is the infamous quantity that must be approximated in KS calculations. For the exact E_{XC}, the exact total energy can be recovered from the non-interacting energy simply via

$$E_0 = E_s - \int \left(\int d\mathbf{r}' \frac{n(\mathbf{r}')}{|\mathbf{r} - \mathbf{r}'|} + \nu_{XC}[n](\mathbf{r}) \right) n(\mathbf{r}) d\mathbf{r} + E^H[n] + E^{XC}[n], \tag{1.8}$$

where E^H is the Hartree energy.

While it may appear from the above summary that KS theory amounts to a simple reshuffling of the quantities that must be approximated to determine the total energy as a functional of the electronic density, there are several distinct advantages with this approach over the so-called "orbital-free" DFT laid out by Hohenberg and Kohn. The most significant implication of the KS approach is that the source of the error has been offloaded from the entire kinetic energy, which is a significant contribution to the total energy, and assigned instead to the exchange correlation energy, which is a significantly smaller component. In addition, the non-interacting reference system is, by definition, amenable to a single-particle, mean-field approach, which facilitates a qualitative description of the "model chemistries" interpreted with molecular orbitals and simple bonding pictures.[12] This single-determinant approach is also very useful for leveraging past developments in self-consistent field (SCF) routines designed for Hartree-Fock methods.

Owed in part to these benefits, the majority of DFT calculations today are performed using the Kohn–Sham scheme using finite basis sets and density functional approximations (DFAs) to the exchange-correlation energy. A set of single-particle Kohn–Sham equations are constructed and solved to obtain the Kohn-Sham orbitals and density, which can be subsequently used to evaluate functionals of the density, expectation values with the KS determinant, and other chemical properties.

This also holds true for density functional theory-based studies of f-element complexes. As such, the KS approach is adopted in all computational studies presented in later chapters. The rest of this section is dedicated to reviewing specific considerations of the DFT method when applied to describe coordination complexes containing f-elements.

1.3.2 Effective Core Potentials

For DFT calculations containing the f-elements, effective core potentials (ECPs) are often employed.[78] As their name implies, ECPs approximate the interactions of core electrons contained within specified atoms with the rest of the chemical system, relying on the so-called "frozen-core" assumption that such electrons remain unperturbed by new molecular environments.[79] The use of ECPs impart several notable advantages for electronic structure calculations, including: (1) reduced computational cost due to treating a fewer number of explicit electrons in the SCF routine and (2) inclusion of relativistic effects through fitting the ECPs to experimental data or more rigorous four-component relativistic calculations.[80–82]

To incorporate these potentials into the electronic structure description, the atomic Hamiltonian is reformulated into that which only explicitly considers so-called "valence electrons" that are not accounted for by the ECP:[83]

$$H_A = -\frac{1}{2}\sum_i \nabla_i^2 + \sum_i V_A(r_i) + \sum_{i<j} \frac{1}{r_{ij}}. \tag{1.9}$$

The corresponding molecular Hamiltonian can thus be written as

$$H = -\frac{1}{2}\sum_i \nabla_i^2 + \sum_i \sum_A V_A(r_i) + \sum_{i<j} \frac{1}{r_{ij}} + \sum_{A<B} \frac{Z_A Z_B}{r_{AB}} \tag{1.10}$$

In Equations 1.9 and 1.10, ∇_i is the standard electronic kinetic energy operator for valence electron index $i, j, k...$ and Z is the nuclear charge for atomic index $A, B, C....$ The one-electron pseudopotential operator, $V(r_i)$, can be chosen in the semi-local pseudopotential approximation to take the form

$$V_A(r_i) = -\frac{Z_A}{r_i} + \sum_l C_l e^{-c_l r_i^2} P_l, \tag{1.11}$$

where C_l and c_l are pseudopotential parameters and P_l is a projection operator onto a basis of spherical harmonics defined by angular momentum quantum number l and the magnetic quantum number m_l:

$$P_l = \sum_{m_l} |lm_l\rangle \langle lm_l| . \tag{1.12}$$

In the Phillips-Kleinman procedure,[84,85] Equation 1.11 is fit to reproduce the valence electron eigenspectrum for a given system at a chosen level of theory. For example, the Hartree-Fock equation for the valence molecular orbitals (ϕ_v) of a molecular system is represented as

$$F |\phi_v\rangle = \epsilon_v |\phi_v\rangle . \tag{1.13}$$

Pseudo-valence orbitals can be constructed from mixing core and valence orbitals in the Phillips-Kleinman ansatz ($\chi_v = \phi_v + \sum_c a_{cv}\phi_c$), which leads to a modified Fock equation,

$$(F_v + V_A(r_i)) |\chi_v\rangle = \epsilon_v |\chi_v\rangle , \tag{1.14}$$

that is constructed to reproduce the eigenspectrum of valence energies by fitting V_A.

From Equation 1.11, one can see that a linear combination of Gaussian functions is chosen for the form of the ECP, owed to the computational convenience of the Gaussian product theorem and their ease of use with existing integral quadrature routines. A consequence of this formalism is that the electronic spin density in the vicinity of the nucleus is quali-

tatively incorrect, which impacts the prediction of magnetic properties. Furthermore, the pseudopotential does not produce the oscillations in electronic density in the core region due to the radial part of the pseudo-orbitals being nodeless, which gives rise to differences between values produced by all-electron and ECP density functional calculations.[3]

An additional spin-orbit contribution, H_A^{so}, can also be added to Equation 1.9, which takes the form:

$$H_A^{so} = \sum_{l=1}^{3} [2\Delta V_l(r)(2l+1)] P_l \mathbf{l} \cdot \mathbf{s} P_l, \tag{1.15}$$

where $\Delta V_l(r)$ is the difference of relativistic potentials differing by angular momentum quantum number l. It is parameterized as

$$\Delta V_l(r) = \alpha^2 D_l e^{-d_l r^2}, \tag{1.16}$$

and can be fit to reproduce spin-orbit splittings measured for the atom. In the above, α denotes the fine structure constant. This ansatz was first described by Pitzer and Winter,[86] and used by Dolg et al. in their development of ECPs for the rare-earth elements.[87]

As can be expected, the use of an ECP within the Hamiltonian of the molecular system comes with additional formal considerations. For example, the assumption of additivity of atomic contributions may need correction when considering larger cores.[88] Furthermore, the remaining valence orbitals do not exhibit the same nodal structure as those derived from an all-electron approach. Working with these simplified pseudo-valence orbitals constitutes what is known as the "pseudopotential" approach and subsequently enables the use of smaller valence basis sets leading to reduced computational cost.[80,82]

Over the past thirty years, the Stuttgart/Cologne group has produced many ECPs with

Table 1.2: Available ECPs released by the Stuttgart/Cologne group for the f-elements. "N_{core}" denotes the number of core electrons and "Method" denotes the level of theory for the reference calculation from which the ECP was parameterized. More detailed information can be accessed from the corresponding website given in Ref. [99]

Ln	N_{core}/Method	An	N_{core}/Method
La	28HF/WB, 46HF/WB, 47WB	Ac	60HF/WB/DF, 78WB
Ce	28HF/WB, 47HF/WB, 48HF/WB	Th	60HF/WB/DF, 78WB, 79WB
Pr	28HF/WB, 47WB, 48HF/WB, 49 HF/WB	Pa	60HF/WB/DF, 78WB, 78WB, 80WB
Nd	28HF/WB, 48WB, 49HF/WB, 50HF/WB	U	60HF/WB/DF, 78WB, 79WB, 80WB, 81WB
Pm	28HF/WB, 50HF/WB, 51HF/WB	Np	60HF/WB, 80WB, 81WB, 82WB
Sm	28HF/WB, 51HF/WB, 52HF/WB	Pu	60HF/WB, 81WB, 82WB, 83WB, 84WB
Eu	28HF/WB, 52HF/WB, 54HF/WB	Am	60HF/WB, 82WB, 83WB, 84WB, 85WB
Gd	28HF/WB, 53HF/WB, 54HF/WB	Cm	60HF/WB, 84WB, 85WB, 86WB
Tb	28HF/WB, 53WB, 54 HF/WB, 55HF/WB	Bk	60HF/WB, 85WB, 86WB, 87WB
Dy	28HF/WB, 54WB, 55HF/WB, 56HF/WB	Cf	60HF/WB, 86WB, 87WB, 88WB
Ho	28HF/WB, 56HF/WB, 56HF/WB	Es	60HF/WB, 88WB, 89WB
Er	28HF/WB, 57HF/WB, 58HF/WB	Fm	60HF/WB, 89WB, 90WB
Tm	28HF/WB, 58HF/WB, 59HF/WB	Md	60HF/WB, 90WB, 91WB
Yb	28HF/WB, 59HF/WB, 60HF/WB/DF, 68DF	No	60HF/WB, 91WB, 92WB
Lu	28WB, 60HF/WB	Lr	60HF/WB, 92WB

corresponding valence basis sets for the f-elements.[87,89–98] A variety of ECPs are available for each element, and some have been fit to reproduce the results of relativistic calculations at different levels of theory (i.e. to Dirac-Fock (DF) or quasirelativistic Wood-Boring results (WB)), in addition to Hartree-Fock (HF) calculations. The ECPs can also contain different numbers of electrons within the core, and are generally divided into "small-core" and "large-core" forms. For the f-elements, small-core ECPs contain electrons up to principal quantum number $n = 3$ for Ln (28 electrons) and $n = 4$ for An (60 electrons). Large-core ECPs on the other hand contain valence f electrons in the core, and are tailored to individual oxidation states. A summary of available f-element ECPs is provided in Table 1.2.

While it is usually advisable to use an ECP which is fit to the highest level of theory that is available, the choice between large or small-core ECPs is more dependent on the system under study. For example, if the valence electrons play a reduced role in bonding for a given f-element complex, as is often the case for electrostatically interacting systems, a large-core ECP may be sufficient and also offers additional computational savings by minimizing the number of valence electrons that are explicitly treated. However, there exist cases where large-core ECPs are insufficient,[100] and examples will be provided in later chapters where the use of a small-core pseudopotential, or no pseudopotential at all, is required for accurate

description of an f-element containing system.

1.3.3 Relativistic Effects and Exact Two-Component Theory

Relativistic effects significantly influence the electronic and magnetic properties of f-element containing compounds,[3] with consequences for their applicability in high-interest areas such as single molecule magnetism[22,101] and next generation qubit development.[14] As a simple example, the impact of relativistic effects on valence orbital energies for single Ln or An atoms is often on the order of 5-10 kcal/mol. Energy differences between these levels can even change sign, as observed for the uranium atom depicted in Figure 1.5,[3] invariably impacting the metal-ligand interactions and subsequent chemistry of Ln/An compounds.

The origin of these effects is conceptually simple: the highly-charged nuclei of the f-elements give rise to fast-moving core electrons, which subsequently induces the relativistic mass increase, the relativistic contraction of the inner-s and -p orbitals, and other physical consequences which are independent of spin. These effects are collectively known as scalar-relativistic (SR) effects. At the same time, electronic spin couples with the magnetic field of charged nuclei to induce spin-orbit (SO) splitting of the electronic states.[4,102,103] As a rule of thumb the leading relativistic energy contributions for atomic systems increase with the nuclear charge Z as roughly $Z^4\alpha^2$, where α is again the fine structure constant.[82] In comparison, the nonrelativistic energy increases as Z^2. A robust computational treatment of these systems must take both effects into account.

Multiconfigurational self-consistent field (MCSCF) methods have often been employed for calculations of f-element compounds in an effort to address the significant static correlation that is observed for systems with nearly-degenerate electronic configurations.[2] While relativistic treatments are, in principle, applicable to CAS methods, they significantly increase the computational cost for an already expensive approach. For example, the relativistic

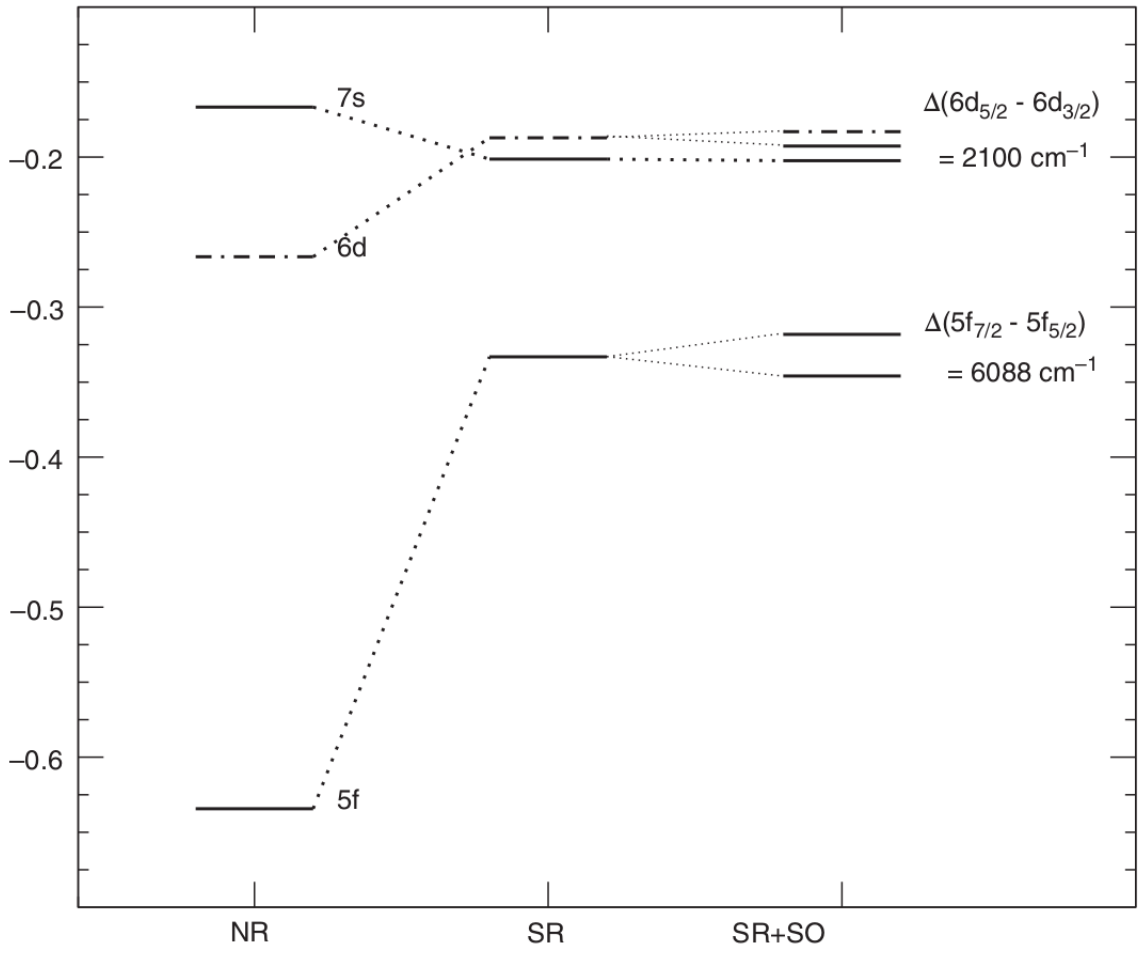

Figure 1.5: Valence orbital energy splittings between non-relativistic (NR), scalar-relativistic (SR), and fully-relativistic (SR+SO) descriptions calculated using Hartree-Fock theory for a neutral uranium atom. Reprinted from *Computational Methods in Lanthanide and Actinide Chemistry*: Chapter 3: Relativistic All-Electron Approaches to the Study of f Element Chemistry, 55-87, Copyright (2015), with permission from Wiley.

integral transformations are roughly 10 times the cost of those for an SR method, which neglects SO effects.[104] In order to achieve general applicability, especially for cases where the electronic ground state for a given species is uncertain (as is the case for all studies reported in Chapter 2 of this work), other methods that (1) do not rely on parameterization of the electronic structure and (2) are amenable to cost-effective relativistic treatments must be used.

A number of different strategies to incorporate relativistic effects are commonly applied in

the DFT framework. For example, ECPs which have been fit to reproduce the results of relativistic Dirac-Fock calculations, as described in Section 1.3.2 can be used. Employing ECPs has the benefit of computational savings from reducing the number of explicitly considered electrons in the SCF procedure and has the convenience of incorporating SR effects while remaining in a one-component (1c) electronic description. ECPs can also include the spin-dependence of one-electron operators, which allow additional incorporation of SO effects, but they are less commonly used.

Alternatively, one can attempt to solve the Dirac equation directly. For a molecular system with electron-nucleus external potential V_{ext}, the one-electron Dirac equation is given by

$$\begin{pmatrix} V_{ext} & c(\vec{\sigma}\cdot\vec{p}) \\ c(\vec{\sigma}\cdot\vec{p}) & V_{ext} - 2mc^2 \end{pmatrix} \begin{pmatrix} \psi^{\mathrm{L}} \\ \psi^{\mathrm{S}} \end{pmatrix} = \begin{pmatrix} \psi^{\mathrm{L}} \\ \psi^{\mathrm{S}} \end{pmatrix} E, \tag{1.17}$$

where $\vec{\sigma} = (\sigma_x, \sigma_y, \sigma_z)$ is the set of Pauli matrices, $\vec{p}$ is the (generalized) momentum operator, c is the speed of light in a vacuum, and m is the electron mass. To solve this equation, the Hamiltonian is expanded in a basis set, and the four-component (4c) spinors and resulting expansion coefficients are split into large and small components: $\psi = (\psi^L, \psi^S)$ and $\begin{pmatrix} \mathrm{C}^{\mathrm{L}} \\ \mathrm{C}^{\mathrm{S}} \end{pmatrix} = \begin{pmatrix} \mathrm{C}^{\mathrm{L}}_{-} & \mathrm{C}^{\mathrm{L}}_{+} \\ \mathrm{C}^{\mathrm{S}}_{-} & \mathrm{C}^{\mathrm{S}}_{+} \end{pmatrix}$, respectively. The relevant matrices are constructed after choice of an appropriate one-electron basis, which satisfies a "balance condition" that ensures the correct nonrelativistic limit with or without external fields.[105–107] For the rest of this section, 4c matrices are denoted as $\mathbb{M}$, two-component (2c) matrices as $\mathbf{M}$, and one-component matrices as $\boldsymbol{M}$.

The difficulty of solving the above equation within a finite basis set in quantum chemistry has given rise to many methods which employ varying levels of approximations. Direct solution using a one-electron theory such as Dirac-Fock or Dirac-Kohn-Sham has the advantage of

being conceptually straightforward and amenable to studies of magnetic properties, but suffers from significant computational expense due to the large basis sets necessary to describe four-component spinors.[108,109] Alternatively, methods which use approximate two-component relativistic Hamiltonians reduce this computational cost by isolating the positive-energy solutions via a unitary decoupling transformation of the one-electron Dirac Hamiltonian, thus reducing the basis set size.[110] A comprehensive presentation of relativistic all-electron approaches is beyond the scope of this work, and the interested reader is referred to existing reviews.[103,111] Instead, the fundamentals of one approach to evaluating the Dirac equation, namely the exact two-component theory (X2C) method, is briefly mentioned. This method is applied extensively throughout Chapter 3 to study transition metal and f-element complexes.

The four-component Dirac Hamiltonian can be reduced to a two-component form with a unitary transformation as suggested by Foldy and Wouthuysen.[112] Heully *et al.* later derived the explicit expression of the unitary matrix.[113] In X2C, this unitary transformation is carried out for the matrix representation of the Dirac Hamiltonian in one step and the X2C Hamiltonian[114–120] is written as

$$\mathbf{h}^{+} = \mathbf{R}^{\dagger}\mathbf{L}\mathbf{R} \tag{1.18}$$

where the matrix representation of the normalized elimination of the small component (NESC) operator is given by[121–124]

$$\mathbf{L} = \mathbf{V} + \mathbf{X}^{\dagger}\mathbf{\Pi} + \mathbf{\Pi}^{\dagger}\mathbf{X} + \mathbf{X}^{\dagger}\left(\frac{1}{4c^2}\mathbf{W} - \mathbf{T}\right)\mathbf{X}. \tag{1.19}$$

In the above equation, $\mathbf{\Pi}$ is the generalized momentum matrix, $\mathbf{V}$ is the scalar potential operator, and $\mathbf{W}$ is the relativistically modified potential. These matrices are obtained from representation of the Dirac Hamiltonian in the chosen relativistic basis set, and their forms are outlined more explicitly later in Chapter 3. In X2C, the decoupling matrix $\mathbf{X}$ is computed

based on a diagonalization of the Dirac matrix $\mathbb{D}$ according to

$$\mathbf{X} = \mathbf{C}_+^{\mathrm{S}}(\mathbf{C}_+^{\mathrm{L}})^{-1} \tag{1.20}$$

Additionally, the relativistic metric must be transformed to the non-relativistic metric $\mathbf{S}$. This introduces the renormalization matrix $\mathbf{R}$, which allows one to integrate the resulting X2C Hamiltonian into the existing non-relativistic 1c or 2c infrastructure. The renormalization matrix is calculated as[119]

$$\mathbf{R} = \mathbf{S}^{-1/2}\left(\mathbf{S}^{-1/2}\tilde{\mathbf{S}}\mathbf{S}^{-1/2}\right)^{-1/2}\mathbf{S}^{1/2} \tag{1.21}$$

$$\tilde{\mathbf{S}} = \mathbf{S} + \frac{1}{2c^2}\mathbf{X}^\dagger\mathbf{T}\mathbf{X} \tag{1.22}$$

This one-electron Hamiltonian is then commonly combined with the non-relativistic two-electron interaction. To account for the missing two-electron picture-change correction, the modified screened nuclear spin–orbit (mSNSO) ansatz[125–128] is often used. It has been found to significantly improve observables, such as EPR parameters, predicted with X2C.[15,129]

All X2C steps are carried out in the uncontracted or primitive basis set. Thus, the $\mathcal{O}(N^3)$ scaling of the diagonalization may limit the applicability of X2C for very large molecular systems.[130] Here, N denotes the number of basis functions. Therefore, local approximations are commonly introduced.[131] For example, in the diagonal local approximation to the unitary decoupling transformation (DLU),[132], the unitary decoupling transformation matrix $\mathbb{U}$ is approximated as a direct sum of atomic blocks according to[133]

$$\mathbf{U}^{\mathrm{LL}} = \bigoplus_A \mathbf{U}_{AA}^{\mathrm{LL}} = \bigoplus_A \mathbf{R}_{AA} \tag{1.23}$$

$$\mathbf{U}^{\mathrm{SL}} = \bigoplus_A \mathbf{U}_{AA}^{\mathrm{SL}} = \bigoplus_A \mathbf{X}_{AA}\mathbf{R}_{AA} \tag{1.24}$$

where an atomic diagonal block is denoted as AA and a general block AB. The atomic blocks

are formed according to the atom centers of the basis functions of the respective matrix elements. Therefore, the decoupling and the renormalization matrix are also approximated as a direct sum of atomic blocks. Note that **V** and **W** still include the sum over all nuclei.

As will be shown in Chapter 3, both the DLU and (m)SNSO approaches significantly improve the accuracy of magnetic properties calculated using DFT and X2C when compared to experimentally obtained results.

1.4 The Bread and Butter: Established DFT Methodology for f-Elements and Example Application to $\{Th[C_5H_3(SiMe_3)_2]_3\}^-$

The state-of-the-art implementation of DFT in TURBOMOLE,[134] a quantum chemistry software package developed by an international research community and managed by Turbomole GmBH,[135] has been shown to be well suited for the f-element calculations. On the basis of previously reported work, a general DFT methodology has been developed by the Furche group at the University of California, Irvine, which consists of a representative set of general parameters and considerations that can be leveraged by any modern DFT program package. The broad approach, along with justifications for each choice, are described below. Note that what follows is meant to provide a summary of computational details typically recommended for the study of f-element complexes in DFT, and is not intended to be exhaustive or fully compatible with every system.

Basis sets: The choice of basis set for each atom that comprises an f-element complex is crucial for successfully describing its electronic structure.[136] Depending on whether an effective core potential (small- or large-core) is used, both all-electron basis sets[137] or the

corresponding valence basis sets may be considered.[138] Note that multiple valence basis sets corresponding to the same ECP may also be available, see for example the ECP28MWB-SEG basis set from Cao et al.[90] versus the x2c-TZVPall-2c basis sets of Pollak et al.[137]

As mentioned previously, the high angular momentum of the valence orbitals exhibited by an f-element atom requires larger basis sets to adequately describe their shape and nodality. Studies using triple-ζ quality basis sets have been shown to yield qualitatively accurate descriptions of the electronic structure when compared with experimental data or reference calculations.[137] For example, x2c-TZVPall all-electron basis sets by Pollak et al. produce errors ranging from 0.3 to 5.6 kJ/mol for atomization energies, dipole moments between 0.02 to 0.15, and HOMO energies between 0 to 0.22 eV for a large test set of molecules with elements spanning the $2s$ to $6p$ shells.[137] These numbers are comparable to the valence-only Karlsruhe "def2" counterparts.[139] Basis sets employed for ligand atoms are usually smaller due to having secondary impact on the valence electronic structure, and typically those of double-ζ quality are chosen. Many basis sets for the f-elements are freely available on the Basis Set Exchange library.[140]

Effective Core Potential: As described in Section 1.3.2, ECPs have been developed and applied towards the description of f-element species. Both large- and small-core ECPs are available from the Stuttgart/Cologne group, and have been fit to various levels of relativistic theory. Excitation energies and ionization energies calculated using quasirelativistic, large-core ECPs for individual atoms agree to within 0.1 eV when compared to relativistic all-electron calculations for the lanthanides[87] and 0.2 eV for the actinides.[93] Small-core ECPs typically exhibit larger errors, typically up to 0.6 eV for the first four ionization potentials of the lanthanides[89] and 0.3 eV for the first ionization potentials of the actinides (with lack of experimental data precluding further calibration).[94] Note that the error corresponding to the valence basis set is included in the given error values.

An ECP should be considered if available, although one should be cautious that the elec-

tronic configuration assumed by the ECP is correct for the system under consideration. For example, ECPs which assume a trivalent oxidation state will not be useful for divalent species, or those where the valency of the metal is yet to be confirmed. Furthermore, chemical properties which are determined by core electronic structure, such as EPR or nuclear magnetic resonance (NMR) parameters, cannot be predicted using ECPs, and must instead rely on an all-electron approach.

Density Functional: Generalized gradient approximation (GGA), meta-GGA, and hybrid functionals have been successfully used in DFT studies of f-element complexes, and such DFAs typically comprise the "lowest rung" of Jacob's ladder[141] that can be expected to produce useful results for such systems.[142] How far the functional "ceiling" extends to increased accuracy is, of course, under active investigation; the performance of range-separated and long-range corrected hybrids are evaluated later in Chapter 3. In the course of numerous computational studies,[5,54–58,143,144] ground state geometries are often reproduced to less than 0.1 Å in metal-ligand distance when using these functionals, and bond-length differences between divalent and trivalent species observed in experiment are also reproduced. For time-dependent density DFT (TDDFT) calculations, hybrid functionals produce more accurate excitation energies and oscillator strengths when compared to experimental spectra,[145] and should be used if computational cost does not become prohibitive. Note that functionals which contain empirical parameters should be avoided, for general application to metal-containing systems.

The remainder of this section is dedicated to presenting an example DFT study of an actinide-based cyclopentadienyl complex using the methodology outlined above, thus providing a "general scenario" for applying DFT to an f-element system. Table 1.3 showcases the speed and energy consumption of KS-DFT and post-KS calculations on $\{\mathrm{Th(II)[C_5H_3(SiMe_3)_2]_3}\}^-$ (Figure 1.6), a divalent thorium compound, performed in TURBOMOLE. Notably, these same calculations were crucial to identifying the first example of the 2+ oxidation state for

Table 1.3: Total computational time (min) and energy consumption (kWh) for DFT single point, analytic Hessian, and TDDFT calculations on $\{Th[C_5H_3(SiMe_3)_2]_3\}^-$ using TPSS and TPSSh functionals. The calculations were performed on an Intel Xeon Gold 6148 @ 2.40 GHz CPU with 16 cores and on an AMD Ryzen 9 3900X @ 3.8 GHz CPU with 12 cores. Adapted from Balasubramani et al. *J. Chem. Phys.* **2020**, *152*, 184107, with the permission of AIP Publishing.

		Intel		AMD	
Calc.	Func.	t (min)	Energy (kWh)	t (min)	Energy (kWh)
DFT	TPSS	3	0.01	2	0.01
	TPSSh	8	0.02	7	0.01
Hessian	TPSS	270	0.68	197	0.34
	TPSSh	640	1.60	502	0.88
TDDFT	TPSS	215	0.54	181	0.32
	TPSSh	1823	4.56	1880	3.29

thorium and an isolable ion in a $6d^2$ electron configuration.[55] In the table, "DFT" refers to a single-point DFT calculation using the `ridft` module with the def-TZVP basis set on the Th atom and the def2-SV(P) basis set on the C, H, Si atoms, totaling 795 basis functions. The Stuttgart/Cologne ECP was used for Th.[94] "Hessian" refers to a force constant calculation for vibrational normal modes using the `aoforce` module with the same basis as the `ridft` calculations. Lastly, "TDDFT" refers to a TDDFT calculation for the lowest 60 excitations using the `escf` module with the def-TZVP basis set on the Th atom and the def2-SVPD basis set on the C, H, Si atoms. As apparent from the data, ground-state energy calculations on such systems can be completed within ten minutes, highlighting the computational efficiency of the method. This subsequently enables calculations of the molecular hessian and excitation energies to take on the order of 3 to 5 hours for pure density functionals, and 10 to 30 hours for hybrid density functionals. The TDDFT results visualized in Figure 1.6, when compared with the solution-phase UV/Vis spectrum, played an important role for the characterization of the Th $6d^2$ configuration, where the strong absorption in the visible region is assigned to excitations from the valence d_{z^2} orbital, as also demonstrated for its Ln(II) and U(II) analogs.[56,143] The "Bread and Butter" model thus provides useful insights for the characterization of novel species while maintaining the computational efficiency embodied

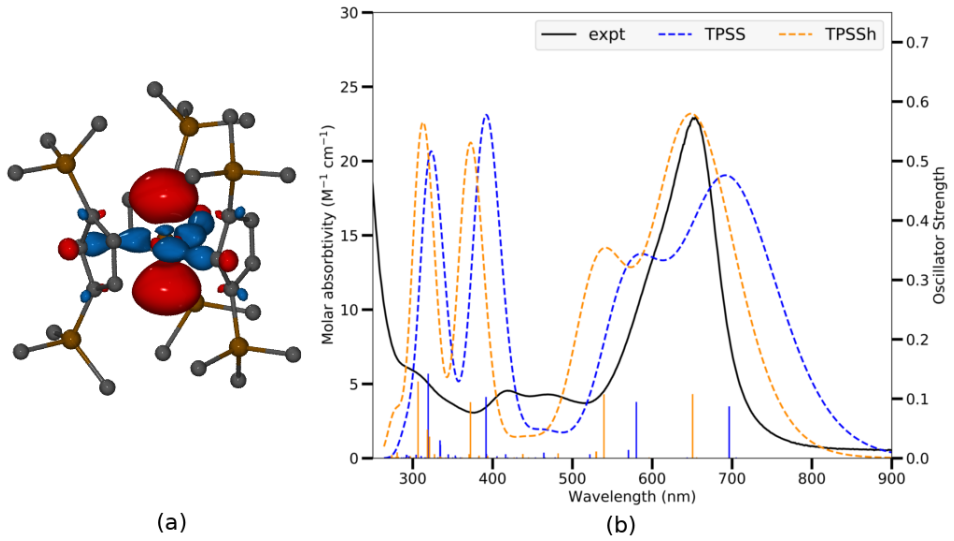

Figure 1.6: (a) Molecular orbital contour for $6d_{z^2}$ HOMO of $\{Th[C_5H_3(SiMe_3)_2]_3\}^-$ at 0.05 isovalue. Hydrogen atoms are omitted for clarity. (b) Experimental and TDDFT simulated UV/Vis spectra of $\{Th[C_5H_3(SiMe_3)_2]_3\}^-$ using the TPSS and TPSSh functional. A universal blue shift of 0.25 eV was applied. Reproduced from Balasubramani et al. *J. Chem. Phys.* **2020**, *152*, 184107, with the permission of AIP Publishing

by DFT methods. In the chapters that follow, this tried and true approach will be tested, providing useful results for the systems studied in Chapter 2 and subsequently revised and improved to describe those of Chapter 3.

Chapter 2

Computational Characterization of Linear Bis(cyclopentadienyl) Metallocenes

 This material is based on work supported by the National Science Foundation under grant nos. CHE-1800431 and DGE-1839285.

2.1 Background

Bis(cyclopentadienyl) metallocenes of the transition-metal elements are prototypical organometallic compounds.[146–149] The interaction of metal-centered valence d orbitals with ligand π orbitals in these species gives rise to rich coordination chemistry, enabling applications for numerous synthetic and catalytic purposes including stereoselective addition,[150] olefin polymerization,[151–153] and N_2 activation.[154] A central goal of lanthanide and actinide chemistry is the discovery, isolation, and characterization of new compounds which exhibit chemistry similar to the transition-metals. However, π-bonded coordination compounds in low valence states are rare for the f-elements, and no bis(cyclopentadienyl) actinocene analog existed until recently.[31] From an electronic structure perspective, this discrepancy may be rationalized by the properties of the f valence shell, which is less available for coordinative bonding due to its contracted nature and high nodality.[155] Rather than forming bis(cyclopentadienyl) metallocenes known from transition metal elements, it was predicted by early calculations[156] and experimentally verified[157] that the actinides instead preferred tetravalent bis(COT) (COT $= \eta^8 - C_8H_8$) structures with primarily electrostatic bonding.[95,158–160] Synthetic attempts towards bis(cyclopentadienyl) structures have produced linear or nearly linear species that include equatorial donor ligands bound to the metal.[161–163] Nevertheless, the higher metal oxidation states of these compounds preclude much of the organometallic activity exhibited by their transition-metal congeners.

Substituted cyclopentadienyl ligands[6,43,164–166] have led to the isolation of the first divalent lanthanide compounds with three equatorial Cp′ (Cp′ $= (C_5H_4SiMe_3)^-$) ligands.[5,56,143] Isolation of the actinide compounds $[Th^{II}(Cp'')_3]^-$, $[U^{II}(Cp')_3]^-$, and $[Pu^{II}(Cp'')_3]^-$ (Cp″$= (C_5H_3(SiMe_3)_2 - 1,3)^-$) followed soon after, with those for Th and U analogously exhibiting $5f^06d^2$ and $5f^36d^1$ configurations akin to transition-metal species.[55–57,71] The unexpected discovery of divalent actinide compounds with substituted cyclopentadienyl groups suggested that other organometallic f-element compounds with unconventional electronic structures

could be accessed with suitable ligands.

In this chapter, the first examples of low-valent, fully linear metallocenes of dysprosium and terbium ($Dy(Cp^{iPr_5})_2$ and $Tb(Cp^{iPr_5})_2$, iPr = $-CH(CH_3)_2$) are presented in Section 2.2. The electronic origin for this novel geometry is explained through application of density functional theory, which reveals σ-bonding interactions facilitated by the divalent metal center and the cyclopentadienyl ring system. Furthermore, in Section 2.3, a DFT study is performed to gauge the synthetic feasibility of a series of predicted actinide metallocene analogs, $An(Cp^{iPr_5})_2$ (An = Th, U, Pu, Am, Bk, No, and Lr). It is demonstrated that the computational methodology employed for the study of $Tb(Cp^{iPr_5})_2$ and $Dy(Cp^{iPr_5})_2$ also provides useful characterizations of these theoretical actinide species, guiding synthetic efforts towards the subsequent synthesis of $U(Cp^{iPr_5})_2$.

2.2 Linear Metallocenes of Tb(II) and Dy(II): $Tb(Cp^{iPr_5})_2$ and $Dy(Cp^{iPr_5})_2$

2.2.1 Introduction

Fine control over coordination geometry is essential to the design of single-molecule magnets. For instance, increasing the axiality of the ligand field can maximize the thermal barrier to magnetization reversal (U_{eff}) for oblate Dy^{III} and Tb^{III} ions and reduce transverse anisotropy, which can, in turn, decrease the rate of through-barrier relaxation.[101,167–172] Enforcing a high symmetry is also important, particularly for complexes containing lanthanide ions with integer spin (non-Kramers ions)–such as Tb^{III} for which $\pm M_J$ degeneracy is not guaranteed.[173–181]

Recent studies have demonstrated that molecular complexes containing Ln^{II} centers can

be isolated across the entire lanthanide series and that these ions can in some instances possess $4f^n5d^1$ electron configurations.[6,27,53,54,58,143,182–184] It was reasoned that such an electronic structure might enable the synthesis of complexes with predictable, high-symmetry geometries– arising from covalent interactions between ligands and the valence $5d$ electron– that also maintain the high anisotropy imparted by the $4f^n$ electrons. As complexes of the type $[Dy(Cp^R)_2]^+$ possess the highest operating temperatures reported to date for single-molecule magnets, the effect of metal reduction on bis(cyclopentadienyl) lanthanide complexes was studied.[22,185–187] Increasing the axial symmetry in such molecules could enhance magnetic properties and this approach could also provide a valuable opportunity to study the impact of reducing Ln^{III} to Ln^{II} on single-molecule magnet behavior.

Reduction of $Ln(Cp^{iPr_5})_2I$ (Ln = Tb, Dy) in benzene with KC_8 and subsequent crystallization from hexane afforded orange-amber crystals of $Ln(Cp^{iPr_5})_2$ (Ln = Tb (**1**), Dy (**2**)), the first neutral, linear metallocenes for any divalent lanthanide more reducing than samarium(II).[188] The solid-state structures of **1** and **2** were determined by single crystal X-ray diffraction analyses. The metal ions are located on an inversion center, resulting in a Cp-Ln-Cp angle of 180° and Cp-Ln-Cp core symmetry (excluding isopropyl groups) of D_{5d}. The high symmetry of the structures are significant, as most $4f^n$ lanthanide metallocenes are bent.[189–198] In a contrasting experiment, iodide extraction of $Tb(Cp^{iPr_5})_2I$ produced the terbium(III) complex salt $[Tb(Cp^{iPr_5})_2][B(C_6F_5)_4]$, echoing the synthesis of $[Dy(Cp^{iPr_5})_2][B(C_6F_5)_4]$ demonstrated in prior work.[187] Notably, the metallocenium salts show bent structures. Figure 2.1 depicts both synthesis schemes described here.

To investigate the electronic structure giving rise to the observed linear geometry of the neutral metallocene species, and to confirm if they exhibit $4f^n5d^1$ ground-state configurations which facilitate high symmetry, DFT calculations were performed on **1** and **2**. The computational details and results are given in the following sections.

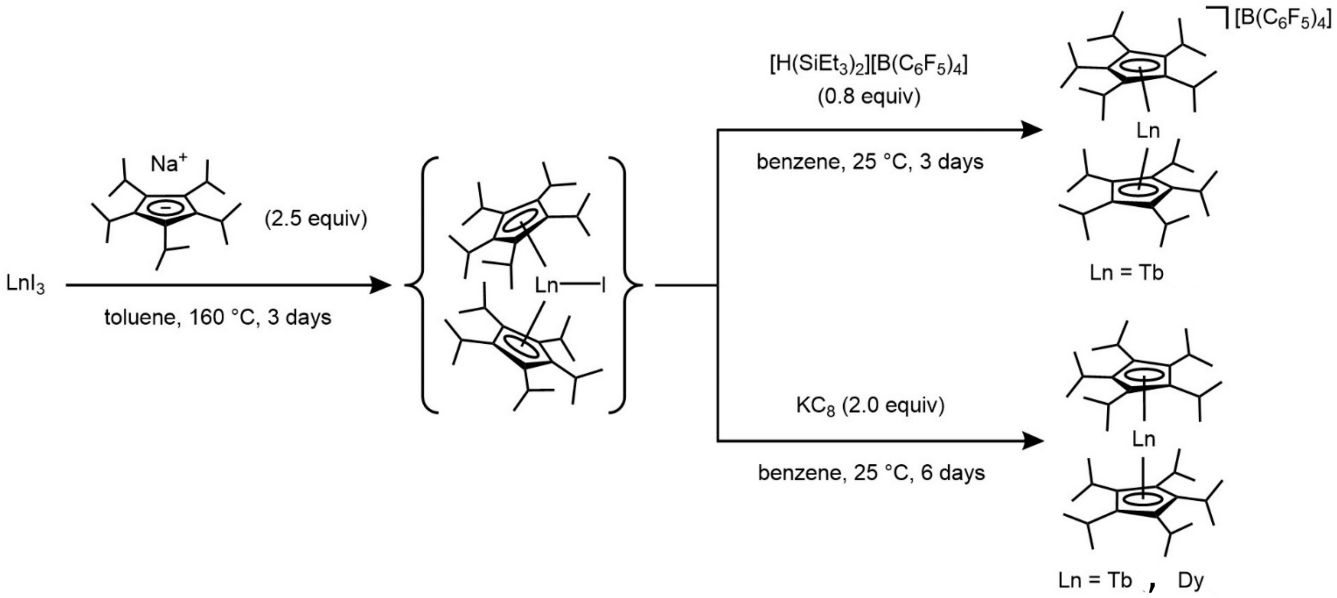

Figure 2.1: Synthetic routes to the Tb(III) metallocenium salt (top) and Ln(II) metallocene complex (bottom); Ln = Tb, Dy.

2.2.2 Computational Details

Structures were taken from X-ray crystallographic data of $Tb(Cp^{iPr_5})_2$ as a starting point for the computational studies of $Ln(Cp^{iPr_5})_2$ (Ln = Dy, Tb). These structures were optimized via DFT calculations to a geometry convergence tolerance of 10^{-4} a.u. and an electron density convergence tolerance of 10^{-7}. Quadrature grids of size 4 were used for integral evaluation. The TPSS meta-generalized gradient approximation (meta-GGA) density functional was used for structural optimizations.[199] Grimme's D3 dispersion correction and the resolution of the identity (RI-J) approximation were also used for computations.[200,201] In all cases, structural convergence was verified via vibrational analysis.[202]

To converge the electronic structure of $Ln(Cp^{iPr_5})_2$ (Ln = Dy, Tb) with $4f^n5d^1$ valence configurations, both the double-ζ quality split valence basis set with polarization functions (def2-SV(P)) and triple-ζ quality basis set (def2-TZVP) was used.[138,139] In conjunction, an out-of-core scalar relativistic def2 effective core potential (ECP) for the Ln atoms was also used.[91]

To obtain the relative energy differences between $4f^n5d^1$ valence configurations where the d electron is aligned or not aligned with unpaired f electrons (i.e, the "ferromagnetic" and "antiferromagnetic" cases, respectively), Fermi smearing was performed with a starting temperature between 2000-3000 K and ending temperature of 100-200 K with an annealing factor of 0.85 to obtain ground state occupations. The occupation numbers were constrained during Fermi smearing to ensure the desired spin multiplicity.

For study of the $4f^{n+1}$ valence configurations, an f-in-core quasi-relativistic ECP was used with the corresponding basis set (SCecp-mwb) on the metal to ensure that the Ln = Dy, Tb atom housed all valence electrons in the $4f$ orbital.[94,98] This ECP and basis was available from the Stuttgart–Cologne basis set and pseudopotential library. See Table 2.1 for the number of explicit electrons considered for each ECP used.

Time-dependent DFT (TDDFT) calculations were performed for each electronic configuration to obtain excitation energies for $Ln(Cp^{iPr_5})_2$ (Ln = Dy, Tb).[203–205] These were done using the TPSS hybrid meta-GGA functional and the same choice of basis mentioned above. A convergence tolerance of 10^{-5} was used for the self-consistent procedure. Generation of visible absorption spectra was conducted with the lowest 10 excitations for each IR-active vibrational mode, or the lowest 55 if C_1 symmetry was adopted. Visualizing UV-Vis spectra was performed with a root mean square (RMS) width of 0.15 eV, a blue shift of 0.15 eV, and a vertical scaling of 0.5 eV. The blue-shift value is based on empirical observation of the performance of the TPSS functional.

Orbital visualization was performed with the VMD program with a contour value of 0.03.[206] All calculations in this study were performed with the TURBOMOLE 7.3 quantum chemistry package.[134]

Table 2.1: Number of electrons treated by f-out-of-core and f-in-core ECPs used with corresponding basis set to describe Tb and Dy.

	def2-SV(P)/TZVP	SCecp-mwb
Ln	f-out-of-core	f-in-core
Tb	28	55
Dy	28	56

Table 2.2: Structural and electronic properties of $Dy(Cp^{iPr_5})_2$ calculated with def2-SV(P) basis set for $4f^n5d^1$ configurations. The SCecp-mwb basis set on Dy is used for $4f^{n+1}$ configurations. *Brackets around the electron configuration indicate that the electrons corresponding to the orbital are located inside the core of the ECP. **Relative energy is not compared for the $4f^{n+1}$ case as the number of explicitly included electrons, and thus the computed energy systematically differs.

Point Group	Term Symbol	Main Config.	Relative Energy (eV)	Dy-Cp distance (Å)
S_{10}	^7A_g	$4f^95d^1$	0	2.482
S_{10}	^5A_g	$4f^95d^1$	0.15	2.482
S_{10}	^7A_u	$[4f^{10}]^*$	-**	2.574
D_5	$^7A_1$	$4f^95d^1$	0.01	2.481
D_5	$^5A_1$	$4f^95d^1$	0.22	2.493
D_5	$^5A_2$	$[4f^{10}]$	-	2.547

2.2.3 Results and Discussion

$Dy(Cp^{iPr_5})_2$

Optimized structures for $Dy(Cp^{iPr_5})_2$ were obtained from DFT calculations in both D_5 and S_{10} point group symmetries. Comparison of electronic and structural properties between

Table 2.3: Structural and electronic properties of $Dy(Cp^{iPr_5})_2$ calculated with def2-TZVP basis set for $4f^n5d^1$ configurations. The SCecp-mwb basis set on Dy is used for $4f^{n+1}$ configurations.

Point Group	Term Symbol	Main Config.	Relative Energy (eV)	Dy-Cp distance (Å)
S_{10}	^7A_g	$4f^95d^1$	0	2.487
S_{10}	^5A_g	$4f^95d^1$	0.13	2.488
S_{10}	^7A_u	$[4f^{10}]^*$	-	2.561
D_5	$^7A_1$	$4f^95d^1$	0.01	2.489
D_5	$^5A_1$	$4f^95d^1$	0.15	2.484
D_5	$^5A_2$	$[4f^{10}]$	-	2.560

Table 2.4: Natural population analysis conducted for the $^7A_1$ term symbol for $Dy(Cp^{iPr_5})_2$. *Includes natural occupancies from all other d orbitals besides z^2. **Represents summed contribution from the 10 C atoms located on the two Cp rings.

Atom	n(s)	n(p)	n(d_{z^2})	n(d rest)*
Dy	0.6947	0	0.1816	0
C**	0.0068	0.0528	0	0

these structures are included for both def2-SV(P) and def2-TZVP basis sets in Tables 2.2 and 2.3, respectively. Between the electronic configurations studied, those corresponding to ^7A_g or $^7A_1$ were found to be lowest in energy for S_{10} or D_5 symmetry, respectively. These terms correspond to $4f^9 5d^1$ configurations. Further comparison was made between the septet and quintet spin multiplicities for this electronic configuration, which were obtained by flipping the spin of the $5d^1$ electron. Term symbols denoting the symmetry of the ground state configuration state function were determined by subduction of the direct product representation of the molecular point groups (S_{10} and C_1) spanned by all occupied molecular orbitals.

Energy differences between the septet and quintet spin multiplicities of the $4f^9 5d^1$ electron configurations were found to be roughly 0.15 eV, which may indicate a preference towards the high-spin state in the scalar-relativistic picture. Comparison of Dy-Cp distances from DFT optimized $Dy(Cp^{iPr_5})_2$ structures between the $4f^9 5d^1$ and $4f^{10}$ electronic configurations support the experimentally observed lengthening on the order of 5.0x10^{-2} Å. These results are in line with previous studies and reinforces the observed $4f^9 5d^1$ configuration.[143] Energy differences between $Dy(Cp^{iPr_5})_2$ in the D_5 and S_{10} point group fall within 0.01 eV, and thus are considered roughly isoenergetic.

Calculation of natural orbital populations for the HOMO revealed significant $6s$ mixing and small contributions originating from ligand p orbitals. Although the ratio of s to d character seems high, population analysis schemes often largely overestimate the relative s contribution. Mixing from ligand orbitals lend to stabilization of the $5d_{z^2}$ orbital as the

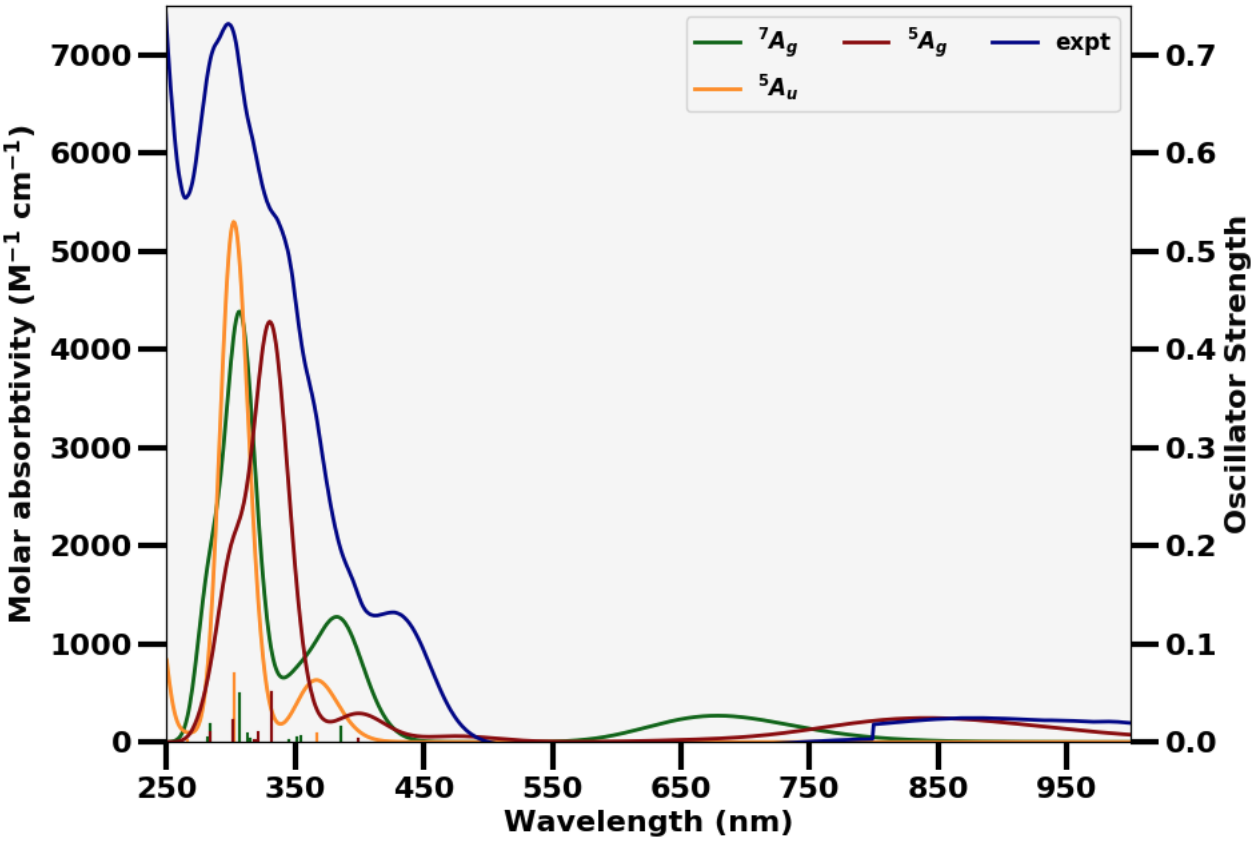

Figure 2.2: Computed UV-Vis spectra for $Dy(Cp^{iPr_5})_2$ with corresponding ground terms in the S_{10} point group. A RMS width of 0.15 eV, a blue shift of 0.15 eV, and a vertical scaling of 0.5 eV was used

HOMO, and the ordering of $5d$ energies thus differs from the traditional textbook picture. The present results are however supported both from photoionization profiles and more recent computational studies of ferrocene.[207,208]

Intense peaks found at around 430 nm and 296 nm in the experimental spectra were predicted as blue-shifted ligand-metal charge transfer excitations through DFT. Between predicted spectra for the ^7A_g, ^5A_g, and ^5A_u term symbols, the two aforementioned peaks occurred in roughly the same locations (although the ^5A_g spectra was blue-shifted away from the other two). Broad peaks near the red end of the visible spectrum were found around 680 nm and 840 nm for the ^7A_g and ^5A_g terms, which were predicted to be due to a $4f$ to $5d$ excitation.

Table 2.5: Structural and electronic properties of $Tb(Cp^{iPr_5})_2$ calculated with def2-SV(P) basis set for $4f^n5d^1$ configurations. The SCecp-mwb basis set on Dy is used for $4f^{n+1}$ configurations. *As before, brackets around the electron configuration indicate that the electrons corresponding to the orbital are located inside the core of the ECP.

Point Group	Term Symbol	Main Config.	Relative Energy (eV)	Tb-Cp distance (Å)
C_1	^{8}A	$4f^85d^1$	0	2.492
C_1	^{6}A	$4f^85d^1$	0.15	2.476
C_1	^{6}A	$[4f^9]^*$	-	2.600

Table 2.6: Structural and electronic properties of $Tb(Cp^{iPr_5})_2$ calculated with def2-TZVP basis set for $4f^n5d^1$ configurations. The SCecp-mwb basis set on Dy is used for $4f^{n+1}$ configurations. *As before, brackets around the electron configuration indicate that the electrons corresponding to the orbital are located inside the core of the ECP.

Point Group	Term Symbol	Main Config.	Relative Energy (eV)	Tb-Cp distance (Å)
C_1	^{8}A	$4f^85d^1$	0	2.520
C_1	^{6}A	$4f^85d^1$	0.11	2.493
C_1	^{6}A	$[4f^9]^*$	-	2.588

This peak is notably absent in the ^5A_u term, possibly due to the $5d_z^2$ orbital sitting further above the 4f orbitals in energy for the $4f^{n+1}$ configuration. These peaks may correspond to that located around 850 nm from the experimentally obtained spectra, and could thus lend further credibility to identifying the suspected $4f^95d^1$ configuration.

$\mathbf{Tb(Cp^{iPr_5})_2}$

Optimized geometries for $Tb(Cp^{iPr_5})_2$ were found to have C_1 symmetry from comparison of relative total energies, which differs from the $Dy(Cp^{iPr_5})_2$ complex above, see Tables 2.5 and 2.6. This is possibly due to the observance of Jahn-Teller effects from partial occupation of degenerate e orbitals in the S_{10} and D_5 symmetries.

Relative energy differences between ^{8}A and ^{6}A term symbols show similar preference for spin multiplicities in the $4f^85d^1$ configuration. However, the difference is again small (on the order of 2 kcal/mol), and within the accuracy range that DFT typically performs. Comparison of Tb-Cp distances between the $4f^85d^1$ and $4f^9$ electronic configurations again support

Table 2.7: Natural population analysis conducted for the $^8A_1$ term symbol for $Tb(Cp^{iPr_5})_2$. *Includes natural occupancies from all other d orbitals. **Represents summed contribution from the 10 C atoms located on the two Cp rings.

Atom	n(s)	n(p)	n(d_{z^2})	n(d rest)*
Tb	0.7261	0	0.1555	0
C**	0.0073	0.0394	0	0

experimentally observed lengthening, although the computed change is closer to 0.1 Å. These results suggest adoption of the $4f^8 5d^1$ configuration.

Similar results are observed as from the population analysis as that for $Dy(Cp^{iPr_5})_2$, with the HOMO s orbital stabilization of the $5d_{z^2}$ HOMO. p orbital contributions from the ligand serve to further stabilize the orbital relative to the other $5d$ orbitals. While the ratio of s to d character is again uncharacteristically high, this is attributed to overestimation of s contributions in the natural population analysis method.

Due to instabilities in the TDDFT routine, electronic excitations were unable to be computed with a triple-ζ quality basis set on the metal atom, so the def2-SV(P) basis was used. The obtained experimental UV-Vis spectrum is similar to that of $Dy(Cp^{iPr_5})_2$, with two primary peaks predicted to correspond to ligand-metal charge transfer excitations. The spectra predicted with DFT for the ^8A and ^6A terms also correspond well with the Dy case despite being limited to a smaller basis, see Figure 2.3. The ^6A $4f^8 5d^1$ spectrum is again red-shifted from the other two predicted spectra. The ligand-metal excitation is however much weaker than that of the others. There is also an absence of metal-metal excitations with longer wavelengths, as seen in the $Dy(Cp^{iPr_5})_2$ case. This is likely due to the smaller basis set used for the lanthanide atom. The ^8A $4f^8 5d^1$ spectrum again qualitatively matches the experimental spectrum better than that of the $4f^9$ configuration.

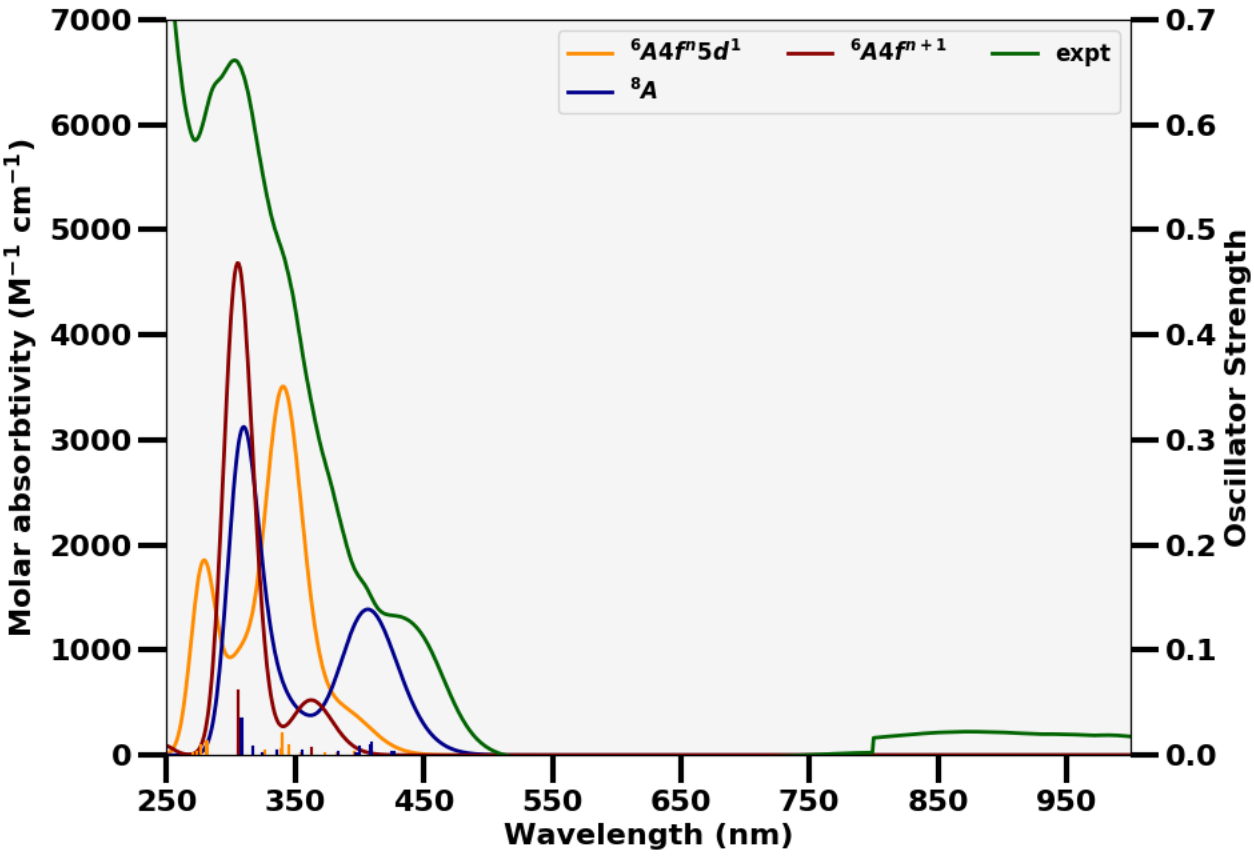

Figure 2.3: Computed UV-Vis spectra for $Tb(Cp^{iPr_5})_2$ with corresponding ground terms in the C_1 point group. A RMS width of 0.15 eV, a blue shift of 0.15 eV, and a vertical scaling of 0.5 eV was used

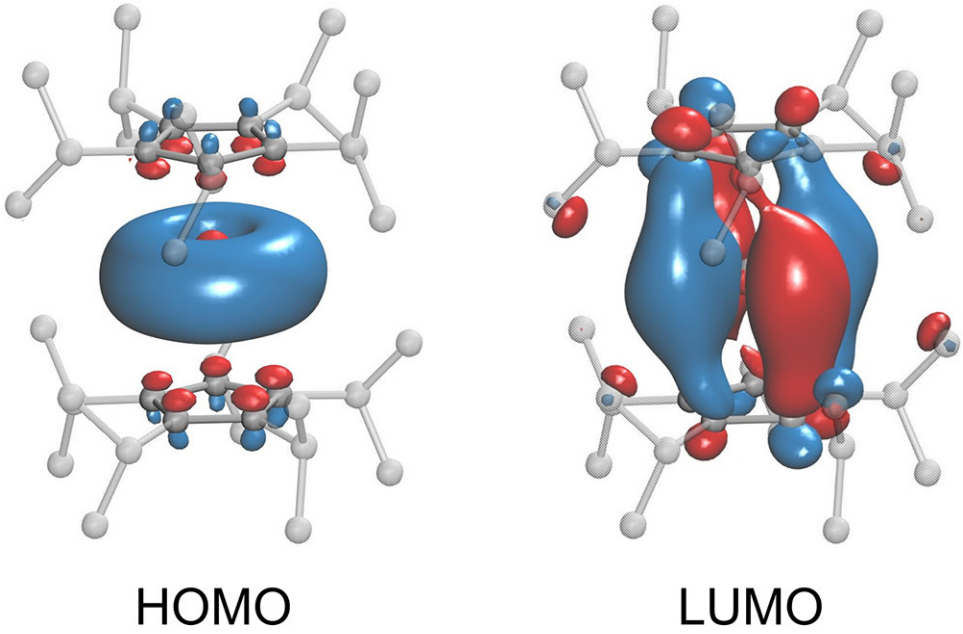

Figure 2.4: HOMO (left, 170aα, contour value 0.03) and LUMO (right, 172aα, contour value 0.03) for Dy(Cp^{iPr_5})$_2$ with hydrogen atoms excluded for clarity. The HOMO and LUMO for Tb(Cp^{iPr_5})$_2$ are isolobal with those of Dy(Cp^{iPr_5})$_2$.

2.2.4 Summary

Taken together, the DFT calculations performed on the optimized structures of Tb(Cp^{iPr_5})$_2$ and Dy(Cp^{iPr_5})$_2$ afforded ^{8}A (in C_1 symmetry) and $^7A_1$ (in D_5 symmetry) ground terms, respectively, corresponding to a $4f^n5d^1$ configuration. These calculations support a nondegenerate HOMO with significant $5d_{z^2}$ character (Figure 2.4). Natural population analysis revealed that the HOMO also has considerable $6s$ character due to the $5d_{z^2}-6s$ orbital mixing (see Figure 2.4).[209] Covalent σ-bonding interactions between these metal-based orbitals and the cyclopentadienyl ligands likely support the linear coordination geometry observed for these divalent metallocenes. The LUMO is doubly degenerate and has significant $d_{xy}/d_{x^2-y^2}$ character, consistent with the orbital ordering found in ferrocene.[210]

2.3 Theoretical Study of Divalent Bis(Pentaisopropyl-cyclopentadienyl) Actinocenes

2.3.1 Introduction

As reported above, divalent Dy and Tb complexes with bis(Cp^{iPr_5}) ligands were synthesized by reduction of trivalent $Ln(Cp^{iPr_5})_2I$ intermediates and characterized by X-ray crystallography, magnetic measurements, and DFT calculations, representing the first examples of bis(cyclopentadienyl) lanthanocene compounds more reducing than samarium.[60] These structures maintain a $4f^n5d^1$ ground state configuration and exhibit covalent σ-bonding between the cyclopentadienyl ligands and metal-based orbitals, resembling the bonding in transition-metal metallocenes.

Here the viability of bis(pentaisopropyl)cyclopentadienyl actinocene compounds (Figure 2.5) is assessed by characterizing the electronic structure of $An(Cp^{iPr_5})_2$ for An = (Th, U, Pu, Am, Bk, No, Lr). Our computational methodology has been extensively validated in prior work on crystallographically characterized lanthanide complexes such as $Dy/Tb(Cp^{iPr_5})_2$,[60] $[Ln\{N(SiMe_3)_2\}_3]^-$,[58] $[Ln(C_5Me_4H)_3]^-$,[5] $[Ln(Cp')_3]^-$, $[Ln(Cp'')_3]^-$,[54,143] as well as the organoactinide complexes $[Th(Cp'')_3]^-$,[55] $[U(Cp')_3]^-$,[56] $[Pu(Cp'')_3]^-$,[57] and $U(C_5Me_4H)_3NO$.[144] The current study focuses on key qualitative features of bis(Cp^{iPr_5}) actinide compounds including trends in dominant electronic configurations of the metal, symmetries, and properties relevant to guide synthetic efforts. More detailed calculations including spin-orbit interactions, a quantitative treatment of near-degeneracy effects, and a more complete description of low-lying excited states with different spin multiplicities are left to future work.

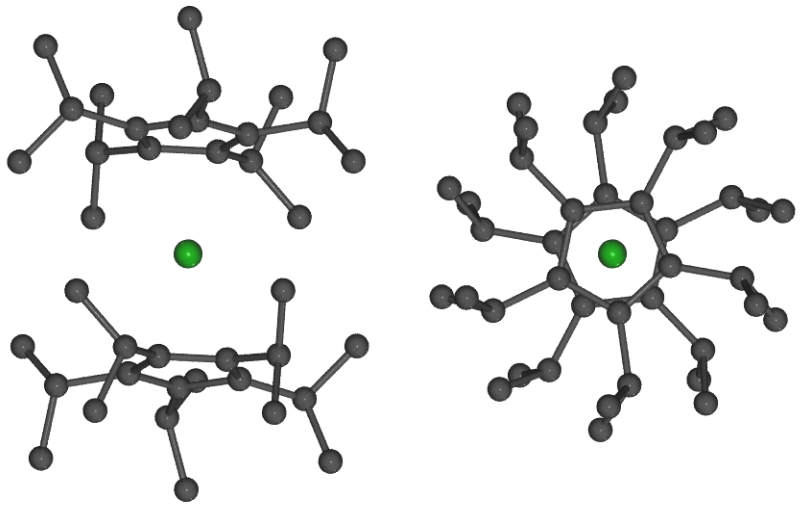

Figure 2.5: Side-on and end-on views of the $An(Cp^{iPr_5})_2$ molecular structure. Hydrogen atoms are omitted for clarity.

2.3.2 Computational Details

Structure optimizations using the TPSS meta-generalized gradient approximation (meta-GGA)[211] density functional were performed for $An(Cp^{iPr_5})_2$ starting from the X-ray structure of $Dy(Cp^{iPr_5})_2$.[60] Stuttgart-Cologne scalar-relativistic small core ECPs were used for An = (Th, U, Pu, Am, Bk, No, Lr).[96] The corresponding valence basis set[94,97] was used for the actinide atoms, and a double-ζ quality basis set (def2-SV(P))[139] was used for the ligands. The exchange-correlation terms were evaluated on a DFT quadrature grid of size m4 and total energies were converged in the SCF procedure to a tolerance of 10^{-7} hartrees. The RI-J approximation[212] and D3 dispersion corrections by Grimme and co-workers[201] were employed.

Optimized structures were obtained to a threshold of 10^{-4} a.u. Each converged structure was verified to be a minimum by harmonic vibrational analysis.[213] Electronic configurations were assigned based on inspection of molecular orbitals and their natural atomic orbital populations.[209] Molecular coordinate files, orbital occupations, and visualizations of frontier

orbital contours are available in the original publication.[214]

TDDFT calculations to study electronic excitations were performed at optimized geometries with the gauge-invariant TPSSh hybrid functional.[205,211] Absorption spectra were simulated from the results using normalized Gaussian functions scaled by predicted oscillator strength. A root mean square width of 0.15 and empirical blue shift of 0.15 eV were used, consistent with parameters chosen to fit experimental spectra for the divalent lanthanocenes Dy/Tb(Cp^{iPr_5})$_2$.[60] The lowest 10 excitations for each dipole allowed transition were computed for An = (Th, U, Bk, No, Lr) and the lowest 30 for An = (Pu, Am). To study the synthetic accessibility of the divalent and monovalent bis(Cp^{iPr_5}) actinide compounds, implicit solvent corrections were included in DFT through COSMO.[215] These calculations were performed using the dielectric constant for tetrahydrofuran (ϵ = 7.520).[216] The harmonic oscillator-rigid rotor approximation at 298.15 K was used for free-energy calculations.

Molecular orbital plots were generated using the VMD program with a contour value of 0.03.[206] All electronic structure calculations were performed with the TURBOMOLE 7.3 quantum chemistry software package.[134]

2.3.3 Electronic Structure

Dominant An electron configurations, ground state term symbols, frontier orbital energies, and metal-centroid distances are displayed in Table 2.8 and Figure 2.6. In all An(Cp^{iPr_5})$_2$ species, the An 6d orbitals split into orbitals transforming according to the a_g, e_{1g} and e_{2g} irreducible representations of the S_{10} point group, ordered by increasing energy in the ligand field. The 5f shell is split into two sets of degenerate orbitals transforming as e_{2u}, one set of degenerate orbitals as e_{1u}, and one orbital as a_u. The relative energies of the An 5f orbitals differ by actinide: Th, Am, No, and Lr possess an α spin orbital ordering of (e_{2u}, e_{2u}, a_u, e_{1u}) in increasing order, whereas U and Pu possess orderings that place the a_u orbital between

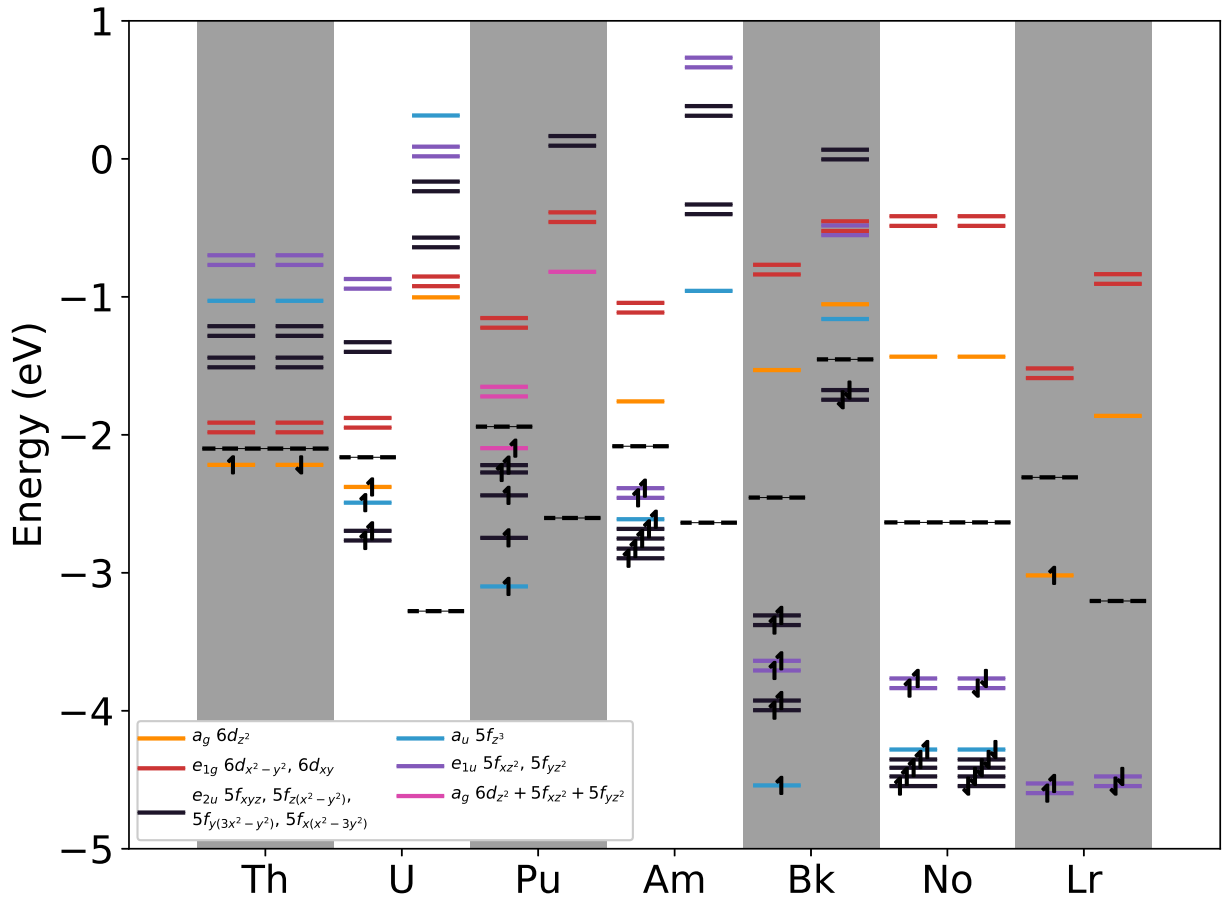

Figure 2.6: Frontier molecular orbitals of both α (left) and β (right) spins labeled by term symbol and function for $An(Cp^{iPr_5})_2$; An = (Th, U, Pu, Am, Bk, No, Lr). Orbital energies were computed with DFT using the TPSS functional and small core ECPs for each An atom. Fermi levels are denoted with a dashed line. The $6d$ orbitals transforming as e_{2g} occur above 1 eV and are not included for simplicity.

Table 2.8: Assigned electronic configurations, term symbols, HOMO and LUMO energies (eV), metal-centroid bond lengths (Å), and bond length differences with known tris(Cp′/Cp″) structures for $An(Cp^{iPr_5})_2$; An = (Th, U, Pu, Am, Bk, No, Lr).

	Config.	Term	E_{HOMO}(eV)	E_{LUMO}(eV)	M-Cp(Å)	$\Delta[(Cp)_3 - (Cp^{iPr_5})_2]$(Å)
Th	$6d^2$	^1A_g	-2.218	-1.982	2.534	0.004
U	$5f^3 6d^1$	^4A_g	-2.368	-1.948	2.483	0.038
Pu	$5f^{5\dagger}$	^6A	-2.097	-1.785	2.490*	0.032
Am	$5f^7$	^8A	-2.408	-1.758	2.542*	
Bk	$5f^9$	$^{10}A_g$	-1.746	-1.531	2.455	
No	$5f^{14}$	^1A_g	-3.836	-1.434	2.442	
Lr	$5f^{14} 6d^1$	^2A_g	-3.019	-1.589	2.417	

† Pu possesses a mixed configuration with $5f^{n+1}$ and $6d^1$ character

* Averaged between the two M-Cp^{iPr_5} distances

or before the two sets of e_{2u} orbitals, respectively. For Bk, the placement of orbitals with both a_u and e_{1u} symmetry results in an α spin orbital ordering of (a_u, e_{2u}, e_{1u} e_{2u}).

Ground state configurations of $5f^0 6d^2$ and $5f^3 6d^1$ were found for $Th(Cp^{iPr_5})_2$ and $U(Cp^{iPr_5})_2$, respectively, giving rise to a HOMO with both $6d_{z^2}$ and $7s$ character. Symmetry-allowed $6d_{z^2} - 7s$ mixing increases the stabilization of this orbital relative to the $5f$ shell. The orbital contour for $U(Cp^{iPr_5})_2$ is visualized in Figure 2.7. Qualitatively similar HOMOs are also found in the Ln(II) metallocenes $Dy(Cp^{iPr_5})_2$ and $Tb(Cp^{iPr_5})_2$, suggesting that the linear coordination environment facilitates such orbital mixing. Indeed, the corresponding tris(Cp′) and tris(Cp″) structures for both Ln(II) and An(II) species contain a HOMO lacking significant s character.

The HOMO of $Pu(Cp^{iPr_5})_2$ has mixed $5f$ and $6d_{z^2}/7s$ character. Natural atomic populations arising from the actinide atom for the HOMO are presented in Table 2.9, along with those for the U and Bk compounds to illustrate the configurational mixing. This mixing is also observed for Pu in the tris(Cp″) environment[57], demonstrating its tendency to exhibit nearly-degenerate $6d$ and $5f$ shells in structures with cyclopentadienyl ligands. The HOMO and LUMO contours for the Pu structure are visualized in Figure 2.8.

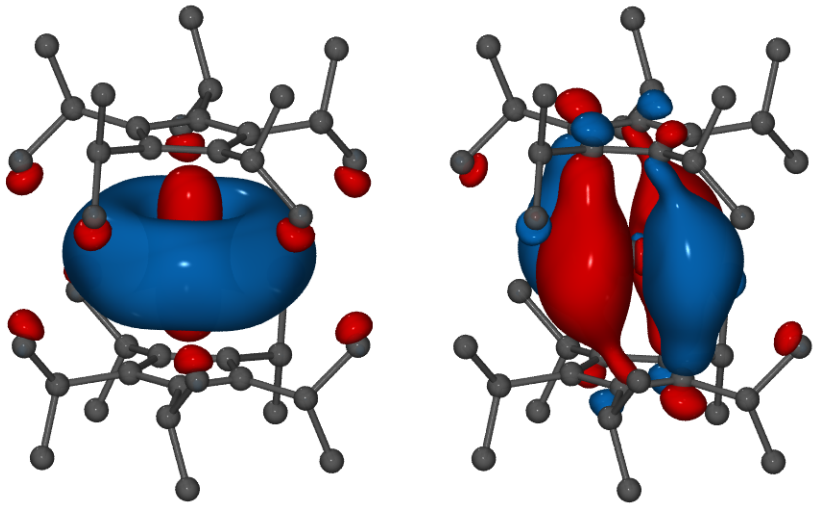

Figure 2.7: Contour plot of HOMO and LUMO for $U(Cp^{iPr_5})_2$ at 0.03 isovalue computed with DFT using the TPSS functional.

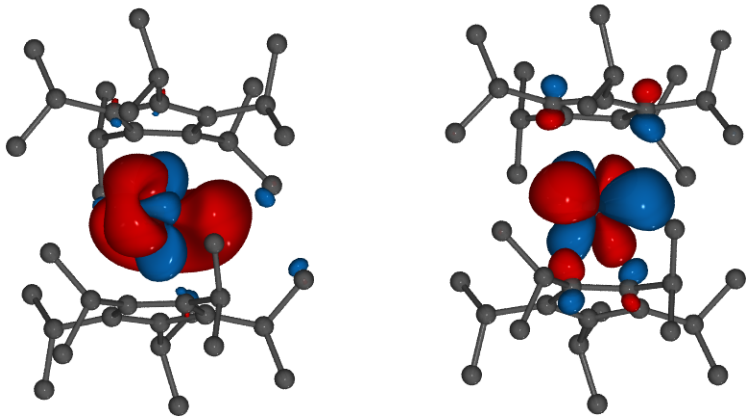

Figure 2.8: Contour plot of HOMO and LUMO for the divalent Pu metallocene at 0.03 isovalue computed with DFT. The predicted electron configuration is predominantly $5f^5$ with $6d_{z^2}$ and $7s$ admixture.

Table 2.9: Natural atomic populations of the HOMO arising from the An atom for $An(Cp^{iPr_5})_2$; An = (U, Pu, Bk).

An	s	p	d	f
U	0.388	0.000	0.408	0.000
Pu	0.162	0.017	0.168	0.538
Bk	0.000	0.000	0.000	0.959

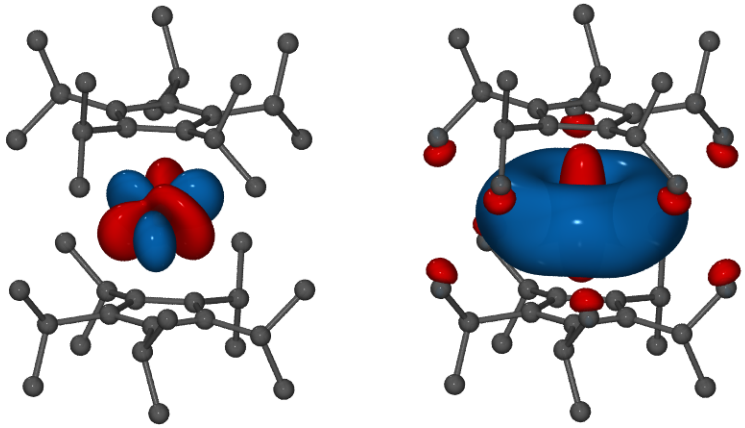

Figure 2.9: Contour plot of HOMO and LUMO for the Bk compound at 0.03 isovalue computed with DFT.

The Am, Bk, and No compounds adopt $5f^{n+1}$ ground states. This is due to the stabilization of the $5f$ orbitals with increasing nuclear charge, which is greater than ligand field stabilization of the $6d$ shell.[217] The HOMO and LUMO contours for Bk are visualized in Figure 2.9, illustrating the assigned $5f^{n+1}$ configuration.

2.3.4 Molecular Structure and Bond Length

Highly symmetric structures with S_{10} symmetry were obtained for An = (Th, U, Bk, No, Lr). In $Pu(Cp^{iPr_5})_2$ and $Am(Cp^{iPr_5})_2$, slightly bent structures resulted from geometry optimization, with dihedral angles of 11° and 12°, as illustrated in Figure 2.10. Similar distortions were also observed in the equilibrium structure of $[Pu(Cp'')_3]^-$,[57] and may be rationalized as Pseudo-Jahn-Teller effects reflecting the presence of two nearly degenerate ground state

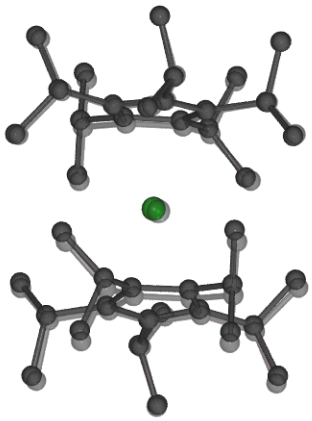

Figure 2.10: Converged structure of the Pu metallocene compound overlaid with the general S_{10} structure, computed with DFT. The structure deviates from linearity, leading to a dihedral angle of 11°.

configurations.

The predicted metal-centroid bond lengths for $An(Cp^{iPr_5})_2$ are reported in Table 2.8. A decreasing trend across the actinide series is observed for compounds with both $6d$ configurations (An = Th, U, Lr) and $5f^{n+1}$ configurations (An = Am, Bk, No), as expected due to f-block contraction. However, this trend is interrupted by the Pu and Am species showing an increase in metal-centroid distance compared to the earlier actinides. This may reflect the loss of bonding interactions with the ligand as the $6d$ orbital is depopulated and an increased electron repulsion in the $5f$ shell.

In general, bond lengths were shorter than that observed for the corresponding tris(Cp'/Cp'') compounds, $[An(Cp'/Cp'')_3]^-$ (An = Th, U, Pu). These results are consistent with the lower coordination number of bis-coordinate compounds, and analogous to the decrease in bond lengths from tris(Cp') to bis(Cp^{iPr_5}) structures observed for the Ln(II) species. Compared to $U(COT)_2$ and $Th(COT)_2$, the $U(Cp^{iPr_5})_2$ and $Th(Cp^{iPr_5})_2$ metal-centroid distances are larger by 0.559 Å and 0.530 Å, respectively, which may be rationalized by the higher formal charge of the COT ligands compared to the present cyclopentadienyl ligands.

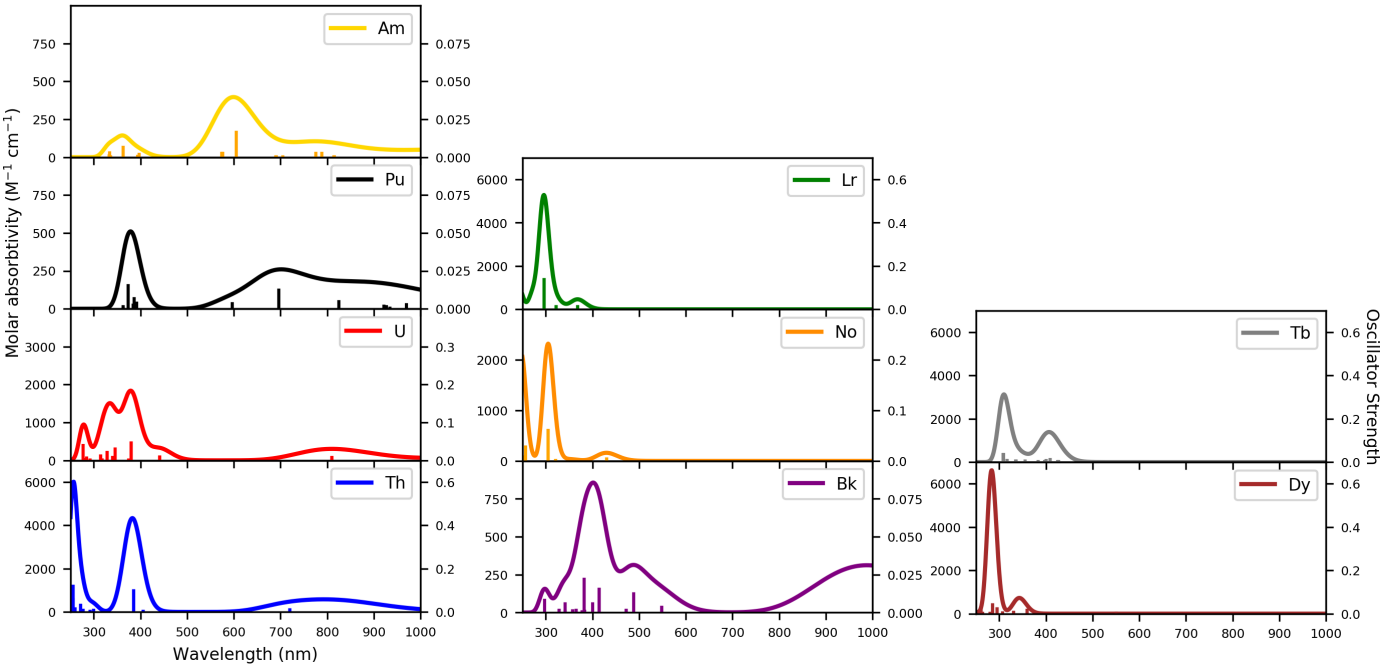

Figure 2.11: Comparison of absorption spectra for An(Cp^{iPr_5})$_2$; An = (Th, U, Pu, Am, Bk, No, Lr) computed with TDDFT using the TPSSh functional. Spectra were fit using normalized Gaussians with a root mean square width of 0.15 and an empirical blue shift of 0.15 eV. These parameters are consistent with those used in the previous study of Ln(II) metallocenes.[60] The broad peak in the infrared part of the spectrum for the Pu compound occurs off the plot at 1112 nm.

2.3.5 Absorption Spectra

Simulated electronic absorption spectra for An(Cp^{iPr_5})$_2$ (An = Th, U, Pu, Am, Bk, No, Lr) are reported in Figure 2.11. The spectra for Th(Cp^{iPr_5})$_2$ and U(Cp^{iPr_5})$_2$ show strong peaks in the UV-VIS region, which correspond to metal-ligand charge transfer (MLCT) excitations out of the $6d_{z^2}$ orbital transforming as a_g. Such excitations from a HOMO with $6d$ character are also observed for the tris(Cp′/Cp″) actinide and bis(Cp^{iPr_5}) lanthanide species.

Strong MLCT bands are not predicted for the spectra of Pu(Cp^{iPr_5})$_2$, Am(Cp^{iPr_5})$_2$, Bk(Cp^{iPr_5})$_2$, and No(Cp^{iPr_5})$_2$; instead, the main features are low intensity transitions from the occupied $5f$ shell to the $6d$-type orbital transforming as e_{1g}. The Pu species exhibits small MLCT excitations out of the HOMO near 390 nm that are absent with the Am species, likely a

consequence of its mixed orbital character. The f to d transition near 315 nm for No is more intense than that of other compounds with $5f^{n+1}$ configurations due to the closed shell ground state. Going across the series, $Lr(Cp^{iPr_5})_2$ again exhibits strong MLCT excitations in the predicted spectral range, as expected from a $6d^1$ configuration.

For $An(Cp^{iPr_5})_2$ (An = Th, U, Pu, Am, Bk), a broad peak of low intensity in the 600 to 1000 nm region was observed. This peak was found to originate from a $6d$ to $5f$ transition for An = (Th, U) and a $5f$ to $6d$ transition for An = (Pu, Am, Bk). Such excitations are also present in the spectra of the Dy(II) and Tb(II) metallocenes. Peak maxima of common MLCT transitions between $Th/U(Cp^{iPr_5})_2$ and $Dy/Tb(Cp^{iPr_5})_2$ are slightly red-shifted, but otherwise remain in the same energy range.

2.3.6 Thermodynamic Stability

Synthetic feasibility of the bis(Cp^{iPr_5}) actinocenes can be assessed by considering their energetic stability, which is controlled by both kinetic and thermodynamic factors. Predicting kinetic stability, on the other hand, is much more difficult and typically requires knowledge of specific experimental conditions. Our discussion thus focuses mainly on thermodynamic stability of the bis(Cp^{iPr_5}) structures, which is a necessary but not a sufficient condition for their synthetic feasibility.

To investigate the thermodynamic stability of the bis(Cp^{iPr_5}) actinocenes, reduction of $[An(Cp^{iPr_5})_2]^+$ to obtain $An(Cp^{iPr_5})_2$ was modeled with DFT including solvation effects with COSMO. The trivalent bis(Cp^{iPr_5}) compound for uranium was isolated recently,[163] indicating that these species may be stable synthetic precursors. Adiabatic reduction potentials including zero point energy and thermal corrections were computed from the free energy differences of the metallocenium cations and corresponding neutral species. Optimized structures for the cations did not deviate significantly from those of the neutral species.

Table 2.10: Adiabatic reduction potentials for $An(Cp^{iPr_5})_2$, An = (Th, U, Pu, Am, Bk, No, Lr), computed with DFT using the TPSS functional and COSMO implicit solvation model.

An	$E^{\circ}_{[An(Cp^{iPr_5})_2]^+ - An(Cp^{iPr_5})_2}$(V)
Th	2.78
U	3.99
Pu	4.20
Am	3.97
Bk	4.25
No	5.06
Lr	3.90

The absolute computed reduction potentials in Table 2.10 need to be interpreted with caution, since they refer to an artificial reference of a free electron in the gas phase, and may be affected strongly by errors inherent in the implicit solvation model used here. However, the results suggest that the reduction of cationic to neutral bis(Cp^{iPr_5}) actinide complexes is indeed thermodynamically favorable.

2.3.7 Monovalent Bis(Cyclopentadienyl) Actinides

To assess whether monovalent bis(cyclopentadienyl) actinide compounds might also be accessible, the adiabatic reduction potential of $Th(Cp^{iPr_5})_2$ was computed with the same methodology as the above. $Th(Cp^{iPr_5})_2$ was selected because it has an unoccupied $6d$ orbital with comparatively low orbital energy.

Optimized structures for the neutral and anionic species were obtained with DFT including COSMO solvent corrections. The additional electron of the anion was found to occupy the metal-like $6d$ orbital transforming as e_{1g}. A slightly lower metal-centroid bond length of 2.52 Å was observed. Results are given in Table 2.11, and show that the $6d$ HOMO of the monovalent species remains bound. Furthermore, the calculated reduction potential suggests that anion formation is favored for this species.

Table 2.11: Adiabatic reduction potentials and HOMO energy for $Th(Cp^{iPr_5})_2$ and $Th(C_5F_5)_2$ computed with DFT using the TPSS functional and COSMO implicit solvation model.

Compound	E°(eV)	E_{HOMO}(V)
$Th(Cp^{iPr_5})_2$	1.93	-0.38
$Th(C_5F_5)_2$	2.30	-1.70

To test if modification of the substituted cyclopentadienyl ligands with electron withdrawing groups could further stabilize this state, this energy calculation was repeated for optimized bis(pentafluorocyclopentadienyl) structures. A larger reduction potential is observed and the electron in the HOMO is further bound.

2.4 Commentary and Conclusions

The foregoing computational studies demonstrate that lanthanide reduction in bis(penta-isopropyl)cyclopentadienyl metallocenes has a substantial impact on both the coordination geometry and metal-ligand bonding. In particular, the $4f^n5d^1$ electronic configuration of $Ln(Cp^{iPr5})_2$ supports axial, high-symmetry structures, likely a result of enhanced covalency in metal-ligand interactions. Although not the primary focus for this chapter, magnetic properties are also enhanced for divalent species; the more axial symmetry of $Dy(Cp^{iPr5})_2$ results in higher hysteresis temperatures relative to $[Tb(Cp^{iPr5})_2]^+$, although both complexes feature non-Kramers ions. Furthermore, reduction of terbium(III) to terbium(II) results in a drastic enhancement of the magnetic relaxation time for $Tb(Cp^{iPr5})_2$ and gives rise to the highest thermal barrier to magnetic inversion and highest magnetic blocking temperature yet observed for a non-dysprosium single-molecule magnet. These results thus highlight the utility of lanthanide redox chemistry in modulating magnetic relaxation.

The computational studies presented in the latter half of this chapter suggest that the theoretical divalent actinocenes $An(Cp^{iPr5})_2$ (An = Th, U, Pu, Am, Bk, No, and Lr) are worthwhile targets for synthesis and experimental characterization. If experimentally confirmed,

these compounds would represent the first examples of low-valent cyclopentadienyl actinide complexes with linear or nearly linear coordination. From the data, the Th and U compounds appear particularly promising for initial synthetic attempts, whereas synthetic access to the latter actinides is limited by their short lifetimes. In fact, the very same U-based metallocene was experimentally isolated shortly after these results were first published.[218] The report also includes a DFT-based analysis which closely reproduces the results obtained above.

Both $5f$ and $6d$ ground-state configurations were observed for the predicted An-based metallocenes, with the Pu compound representing a borderline case. Further judicious ligand modifications could make it possible to extend the $6d$ configuration to the later actinides or even access the monovalent oxidation state for the early actinides. The chemistry of these compounds is expected to be closer to that of transition metal metallocenes than typical actinide complexes in higher oxidation states.

In summary, we have demonstrated in this chapter that scalar-relativistic density functional theory is capable of both characterizing the electronic origin of novel lanthanide and actinide molecular structures and predicting their synthetic feasibility *in-silico*. DFT thus offers a theoretically robust and computationally efficient means to support experimental studies and guide synthetic efforts to novel Ln- and An- chemical space.

Chapter 3

Prediction of Electron Paramagnetic Resonance Parameters with Density Functional Theory and Application to Molecular Spin Qubit Systems

 This material is based on work supported by the National Science Foundation under grant nos. CHE-1800431, CHE-2102568, and DGE-1839285.

3.1 Background

The field of quantum information science is witnessing remarkable progress, with prototype devices reaching the point of practical quantum advantage.[219] The fundamental building block of a quantum computer is the physical quantum bit, or qubit, which can be any two-state quantum system. Many candidates are currently under investigation, including superconducting circuits,[220] trapped ions,[221] photons,[222] topological states in condensed matter,[223] as well as electron and nuclear spins in solids[224,225] or on surfaces.[226,227] However, continued scale-up to the point where fault-tolerant quantum logic is possible with vast numbers of qubits remains challenging. For this reason, research focusing on next-generation quantum technologies is very active.[228]

In parallel, this great interest has given rise to a renewed need for the development of new computational methods which are capable of guiding the synthetic design of new qubit systems. The desired features and performance of such methods will inevitably differ with the physics underlying the qubit itself, but they should generally be accurate in their evaluations of a candidate, computationally inexpensive within the context of optimizing physical properties, and flexible enough to be applicable across the expected variety of chemical space associated with discovery efforts.

Towards this end, the present chapter will serve to highlight how DFT may provide a reliable and computationally efficient means to characterize the properties of candidate molecular qubit systems which operate through their electronic and nuclear spins. This is accomplished through an accurate description of various magnetic properties such as the hyperfine interaction and the electronic g-tensor, which dictate the capacity of a single molecule to act as the basis of a qubit system.[229]

The direct application of conventional DFT methodology is, however, generally not sufficient to study these systems. For example, the ECPs used to study the f-element metallocenes

as detailed in Chapter 2 cannot be used to describe the properties of core electrons and their subsequent interactions with nuclei, which are crucial for the evaluation of hyperfine energy splittings as binary qubit states. These systems also oftentimes contain one or several metal atoms which preclude the use of popular empirical density functionals and require a more comprehensive relativistic treatment.[102] As illustrated in the following studies, the combination of a relativistic, all-electron density functional theory description of the ground state electronic structure, along with the appropriate relativistic expressions for the EPR parameters, is necessary to study these systems.

Section 3.2 of this chapter will focus on an initial proof-of-concept for the use of electronic spins in Ln-based coordination complexes as molecule-based qubits, providing a preliminary DFT-based methodology to characterize the electronic and magnetic properties of these systems. Sections 3.3 and 3.4 expand this initial DFT approach by improving predictions of the hyperfine coupling constant, electronic g-tensor, and electric field gradients through their calculation within exact two-component theory (X2C). It is shown that using the proper relativistic expression to predict these spin hamiltonian parameters, rather than those derived in the nonrelativistic limit (and thus lacking crucial terms such as the paramagnetic spin orbit interactions),[13,16] reduce errors by one order of magnitude when compared to experimental results. These studies go on to provide extensive benchmarks of basis set, density functional approximation, timings, and relativistic ansätze for transition metal and f-element species, resulting in a set of best practices for studying the properties of future molecular spin qubit candidates.

3.2 Computational Characterization of a Lu(II) Molecular Spin Qubit with a 9.2-GHz Clock Transition

3.2.1 Introduction

The $S = 1/2$ spin associated with an unpaired electron represents one of the simplest examples of a two-state quantum system that is easily manipulated using decades-old and well-understood magnetic resonance techniques.[230] Nature provides a rich, albeit finite, variety of quantum states in atoms and ions that may be trapped and organized into arrays with controllable interactions.[221] By comparison, coordination chemistry affords almost limitless tunability of the quantum states associated with unpaired electron spins in molecules, while also offering routes to large-scale assembly via supramolecular approaches.[231] However, this flexibility comes at a cost in terms of coherence due to the inherent coupling to magnetic and vibrational modes associated with the environment.

In spite of this, excellent phase memory times (T_m) have been demonstrated for isolated molecular spin qubits.[232] Further protection from magnetic noise has been achieved via the engineering of so-called clock transitions,[228,229,233,234] -avoided level crossings associated with the Zeeman splitting of qubit states such that the transition frequency, f, becomes insensitive to the local magnetic induction, B_0, that is, $df/dB_0 \rightarrow 0$ at the splitting minimum, δCT. In the first molecular example, an avoided crossing was generated via off-diagonal crystal-field terms in the Hamiltonian matrix of a Ho(III) ion ([Xe]$4f^{10}$ electronic configuration) encapsulated within a polyoxometalate cage,[235] resulting in a substantial T_m enhancement for a crystal rich in fluctuating electron and nuclear spins.[233] Although providing important insights, the Ho(III) example also highlighted limitations of crystal-field engineered clock transitions. In particular, achieving clock transition frequencies in the gigahertz range relies on spin–orbit coupling (SOC), which also promotes spin-lattice (T_1) relaxation.[233] For these

reasons, attention has shifted to alternative mechanisms for generating clock transitions, including electron–nuclear hyperfine interactions[229] and microwave dressing.[236]

This section demonstrates the viability of coordination chemistry for engineering hyperfine clock transitions in magnetic molecules with tunable operating frequencies up to approximately 10 GHz. The discovery that $4f^n$ Ln(III) complexes of Ln = La, Ce, Pr, Gd, Tb, Ho, Er and Lu in the appropriate ligand environments can be reduced to $4f^n5d^1$ Ln(II) complexes[6,54,237–239] rather than the traditional $4f^{n+1}$ Ln(II) previously found for Eu, Yb, Sm and Tm[6,240] has provided an alternative type of rare-earth electron configuration for development in quantum information science (QIS). The La(II) and Lu(II) congeners feature closed shell core configurations ([Xe] and [Xe]$4f^{14}$, respectively) and a single $S = 1/2$ unpaired electron residing in an orbital with mixed $5d/6s$ character.

As will be demonstrated in the following computational study, variation of the ligands in these Ln(II) complexes[239] facilitates synthetic control over the degree of s-orbital character that dominates the Fermi contact interaction with the associated nucleus, providing a means of tuning the hyperfine interaction strength. Moreover, increased %s-orbital character minimizes SOC, resulting in reduced spin–lattice relaxation relative to most Ln species with spin–orbital moments $J > 1/2$ (Ref. [241]). For La and Lu in particular, the dominant isotopes have large $I = 7/2$ nuclear moments (99.9% and 97.4% natural abundance for ^{139}La and ^{175}Lu, respectively), which further enhances the corresponding clock transition frequency and reduces the second-order sensitivity to magnetic noise, $d^2f/dB_0^2 \ \alpha \ \delta\mathrm{CT}^{-1}$ (refs. [242, 243]). These factors give rise to a molecular qubit platform similar to the $^{171}\mathrm{Yb}^+$ ion (formally [Xe]$4f^{14}6s^1$, $I = 1/2$) that is ubiquitous in the ion trap QIS community,[221] but with the added benefit of chemical tunability.

Towards this end, a series of La(II) and Lu(II)-based compounds were selected for study of their electronic and magnetic properties using both experimental and computational methods: $\mathrm{LuCp'_3}$ (**1**; Cp′ = $\mathrm{C_5H_4SiMe_3}$), $[\mathrm{La(OAr^*)_3}]^-$ (**2**; OAr* = 2,6-$\mathrm{Ad_2}$-4-tBu-$\mathrm{C_6H_2O}$),

$[Lu(NR_2)_3]^-$ (**3**; R = $SiMe_3$), and $[Lu(OAr^*)_3]^-$ (**4**). Compounds **2**−**4** exhibited large hyperfine coupling constants in experimental measurements, and Complex **4** is found to have a particularly huge hyperfine interaction of $A_{\text{iso}} = 3,467 \pm 50$ MHz, giving rise to a giant clock transition and the enhanced coherence central to this investigation. Specific details regarding the synthesis and experimental characterization using EPR spectroscopy are given in Ref. [14]. In the following, we focus on computational investigations concerning compounds **2**−**4** using density functional theory, illuminating the electronic origin behind these large hyperfine interactions which enable desirable clock transitions in next-generation qubit materials.

3.2.2 Spin Hamiltonian

Characterization of the hyperfine spectra of **2**−**4** is carried out according to the effective spin Hamiltonian of Equation 3.1, which describes a lone $S = 1/2$ electron coupled to an $I = 7/2$ nuclear spin:[244]

$$\hat{H} = \mu_B B_0 \cdot \overleftrightarrow{g_e} \cdot \hat{S} - \mu_N g_N B_0 \cdot \hat{I} + \hat{S} \cdot \overleftrightarrow{A} \cdot \hat{I} + \hat{I} \cdot \overleftrightarrow{Q} \cdot \hat{I}, \tag{3.1}$$

where the first two terms respectively denote the electron and nuclear Zeeman interactions ($\overleftrightarrow{g_e}$ is the electron g-tensor) and the third term represents the electron–nuclear hyperfine interaction ($\overleftrightarrow{A}$ is the hyperfine coupling tensor). Meanwhile, for **3** and **4**, a significant nuclear quadrupole interaction (NQI) specified by the matrix $\overleftrightarrow{Q}$ is observed (Ref. [245]). Precise constraint of the anisotropic $\overleftrightarrow{g_e}$, $\overleftrightarrow{A}$ and $\overleftrightarrow{Q}$ tensors in EPR is aided by performing measurements in a high-field regime dominated by the electron Zeeman interaction. In this limit, the electron and nuclear spin projection quantum numbers, m_S and m_I, are exact. For compounds **2**−**4**, this leads to a linear Zeeman splitting of the $m_S = \pm 1/2$ states, each of

which is further split into eight sub-levels due to the hyperfine interaction with the $I = 7/2$ nuclear spin (we neglect minority isotopes), see Ref. [14].

3.2.3 Computational Details

All-electron DFT calculations were performed using the TPSS[199] functional for each compound and the self-consistent field (SCF) procedure was converged to 10^{-7} Hartree (E_h). x2c-TZVPPall-s basis sets were used for the Ln centers, and x2c-SVPall basis sets were used for each respective ligand atom.[246] Relativistic corrections were included using the all-electron variational X2C method, both with and without spin–orbital coupling effects.[133] The finite nucleus model[247] and local approximation[132] were also used in the relativistic treatment. All calculations were performed using the TURBOMOLE V7.5 quantum chemistry software.[134]

Each DFT calculation was performed using the RI-J approximation[200] and D3 dispersion corrections.[248] Solvation effects were modeled using COSMO.[215] The employed computational methodology was chosen after an extensive survey of basis sets, relativistic methods, and density functionals, representing a useful compromise between computational cost and accuracy. However, the observed trends in SOMO character (Table 3.3) and isotropic hyperfine coupling constants (Table 3.2) persist for other GGA/mGGA and hybrid functionals, larger basis sets, and a fully-relativistic X2C treatment. Starting structures were obtained from crystallographic data, and geometry optimizations in C_1 symmetry were performed using the above methodology to a Cartesian gradient norm of 10^{-4} au (au = atomic units). Vibrational analysis was used to confirm that the structures represented minima. All molecular visualizations were constructed using the VMD software.[206]

3.2.4 Hyperfine Coupling Constants in DFT

$$A_{\text{iso}} = \frac{4\pi}{3} g_e g_n \mu_B \mu_N \langle S_z \rangle^{-1} \int n_s(\mathbf{r}) \rho(\mathbf{r}) d^3\mathbf{r}. \tag{3.2}$$

The isotropic hyperfine coupling constants for the Ln nuclei can be calculated using Equation 3.2, where $\langle S_z \rangle$ is the expectation value of the spin operator in the z direction, and $\int n_s(\mathbf{r}) \rho(\mathbf{r}) d^3\mathbf{r}$ is a Fermi contact-like interaction involving the spin density, $n_s(\mathbf{r})$, over a nuclear charge distribution $\rho(\mathbf{r})$. For the present study, this charge distribution is modeled as both a point charge and as a finite spherical Gaussian charge distribution. The choice of a point charge simply takes $\rho(\mathbf{r})$ to be a delta function, and the integral thus simplifies to the spin density at the point of the nucleus. For the finite nucleus model, a Gaussian charge distribution was chosen according to the procedure detailed by Malkin et al.[18]

$$\rho(\mathbf{r}) = eZ \left(\frac{\xi}{\pi} \right)^{\frac{3}{2}} e^{-\xi |\mathbf{r} - \mathbf{R}|^2}, \tag{3.3}$$

and ξ is approximated in $1/\text{fm}^2$ by

$$\xi = 1.5(0.836 M^{1/3} + 0.570)^{-1}, \tag{3.4}$$

where M is the mass number, Z is the nuclear charge, ξ is the Gaussian coefficient, and $\mathbf{R}$ is the position of the Ln nucleus. Using this model nuclear charge density, the Fermi integral was evaluated with Gauss-Hermite quadrature. Nuclear g-factors were taken to be 0.6378 for ^{175}Lu and 0.7952 for ^{139}La from Ref. [249].

3.2.5 Nuclear Quadrupole Interaction in DFT

The NQI coupling tensors $\overleftrightarrow{Q}$ are approximated according to the equation

$$\overleftrightarrow{Q} = \begin{pmatrix} Q_{xx} & 0 & 0 \\ 0 & Q_{yy} & 0 \\ 0 & 0 & Q_{zz} \end{pmatrix} = \frac{eQV_{zz}/h}{4I(2I-1)} \begin{pmatrix} -(1-\eta) & 0 & 0 \\ 0 & -(1+\eta) & 0 \\ 0 & 0 & 2 \end{pmatrix}, \tag{3.5}$$

where e is the elementary charge, Q is the nuclear quadrupole moment, η is a dimensionless asymmetry parameter, and V_{zz} is the principal component of the diagonal EFG tensor calculated at the position of each Ln nucleus for compounds **2**−**4**. The calculated EFGs are given in Table 3.1, and the resulting NQI tensors are presented in the following section.

Table 3.1: Calculated electric field gradients in the molecular frame for compounds **2**−**4** using all-electron, scalar-relativistic DFT.

Compound	V_{xx} (au)	V_{yy} (au)	V_{zz} (au)	V_{xy} (au)	V_{xz} (au)	V_{yz} (au)
4	0.392	0.406	-0.797	-0.005	-0.139	0.048
3	0.286	-0.572	0.286	-0.001	0.000	-0.001
2	0.188	0.195	-0.382	-0.003	-0.007	-0.022

$\overleftrightarrow{Q}$ can also be obtained using $\overleftrightarrow{V}$ in au (= E_h/ea_0, where a_0 is the Bohr radius) and Q in barn (b) with the following equation, which includes the necessary conversion factors:

$$\overleftrightarrow{Q}(MHz) = -5.5944\ Q(\mathrm{b})\overleftrightarrow{V}(\mathrm{au}) \tag{3.6}$$

3.2.6 Results and Discussion

To analyze the electronic structure responsible for the observed hyperfine and nuclear quadrupole interactions, scalar-relativistic X2C DFT calculations[130] were performed. The converged spin-unrestricted Kohn–Sham ground states for each compound are consistent with the elec-

tronic configurations of [Xe]$5d^1$ for **2** and [Xe]$4f^{14}5d^1$ for **3** and **4**. The spin density for the three compounds was found to arise almost exclusively from the SOMO in every case, with predominant $5d_{z^2}$ character and varying degrees of $6s$-orbital mixing, see Figure 3.1. Isotropic hyperfine coupling constants for the Ln nuclei were obtained from the computed spin density using both point and finite nuclear charge models, and compared to experimentally determined results (Table 3.2).[247] Although the calculations systematically overestimate the coupling strength, presumably due to systematic errors in the DFT approximations and relativistic treatment,[250] the experimental ordering, $\mathbf{2} < \mathbf{3} < \mathbf{4}$, is reproduced from natural population analysis of the SOMO (See Table 3.3).[209] Two factors govern the magnitude of the hyperfine coupling in these compounds:[102] (1) the larger amplitude of the SOMO at the nucleus due to increasing nuclear charge and (2) an increased s character in the SOMO from La to Lu caused by greater energetic overlap between the $5d$ and $6s$ valence shell. The latter observation suggests that the s-orbital character, n(s), of the SOMO is a useful descriptor of electronic structure for designing similar compounds with large hyperfine coupling.

The quadrupole coupling tensors for the Ln nuclei were also calculated in the point nuclear charge model and reported in Table 3.2 for comparison with experiment. The results systematically underestimate the couplings compared to those obtained from EPR simulations, but the deviations are in line with previous benchmark DFT studies of electric field gradients,[251–254] showing significant variation depending on the relativistic treatment and functional used. In particular, the experimental ordering of NQI constants is reproduced ($\mathbf{2} << \mathbf{3} < \mathbf{4}$), supporting the observation of a pronounced NQI in the Lu compounds in comparison to those of La. In all three cases, the principal axes of the nuclear quadrupole moments are aligned with the pseudo-three-fold symmetry axis perpendicular to the $Ln(O)_3$ and $Ln(N)_3$ planes.

Experimental quadrupole moments of 3.49 b and 0.20 b were used for Lu and La nuclei, respectively from Ref [255]. The results are tabulated in Table 3.2. Ellipsoid plots of the

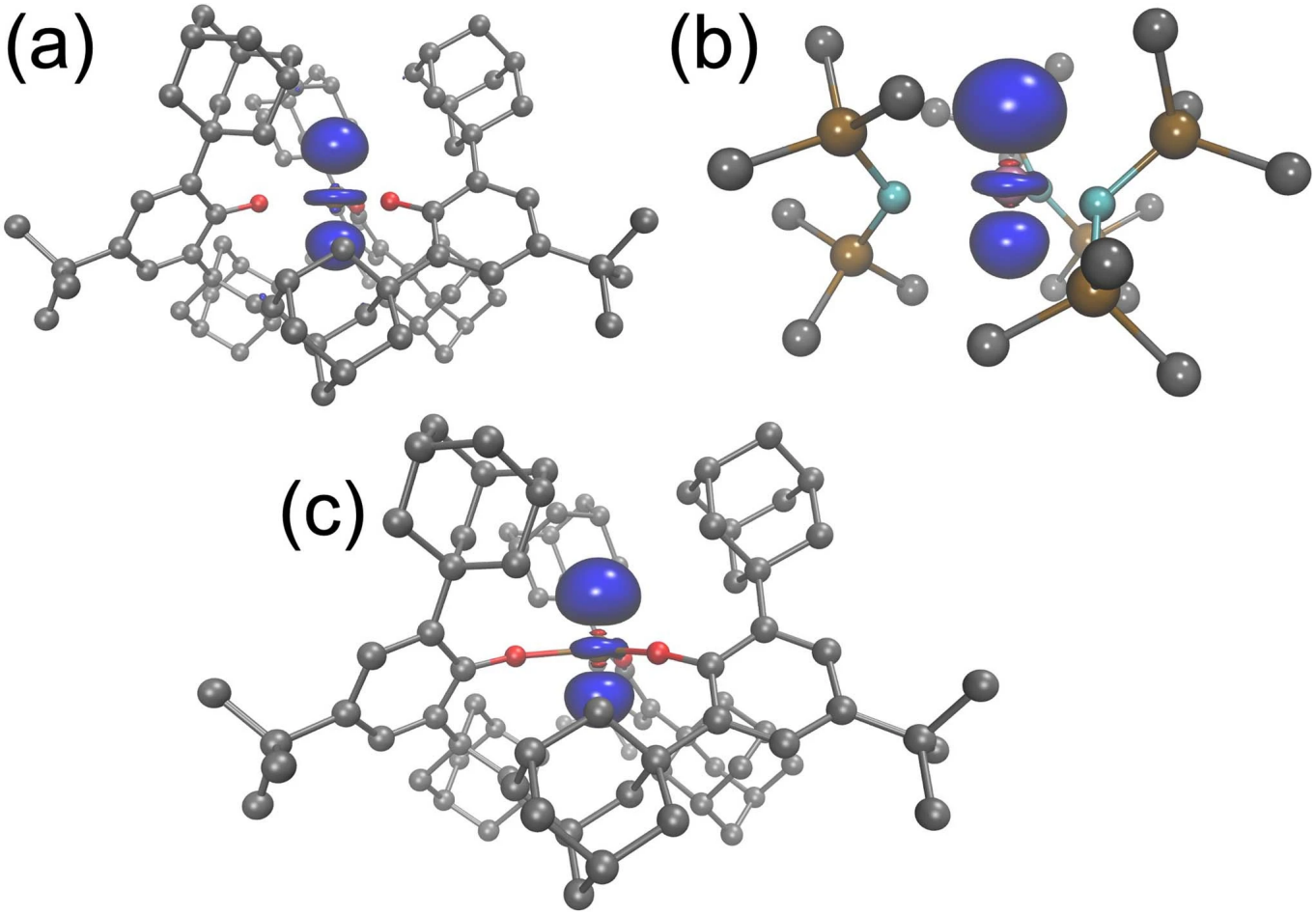

Figure 3.1: Contours of the spin density (blue) computed with DFT for compounds **2** (a), **3** (b), and **4** (c) plotted at a contour value of 0.005. Hydrogen atoms have been omitted. Color codes: Grey = C, Red = O, Brown = Si, Teal = N, Pink = Ln.

Table 3.2: Spin Hamiltonian parameters derived from electron paramagnetic resonance measurements (Ref. [14]) and DFT calculations. [a]Uncertainties refer to the mean values of the associated distributions. [b]A-strain (δ_A) and peak-to-peak linewidths (lw_{pp}) used for simulations with no associated uncertainties; values correspond to the full-width at half maximum (FWHM) of the distribution (=2.35σ, where σ is s.d.). Values are obtained from the best simulations of the experimental data (errors denote estimated uncertainties) and from theory (no associated uncertainties) for the three compounds (**2**−**4**) investigated in this work.

	2	3	4
Experiment			
A_{xx} (MHz)[a]	1,870 ± 25	2,480 ± 50	3,500 ± 50
A_{yy} (MHz)[a]	1,870 ± 25	2,550 ± 50	3,500 ± 50
A_{zz} (MHz)[a]	1,780 ± 25	2,300 ± 50	3,400 ± 50
A_{iso} (MHz)[a]	1,840 ± 25	2,443 ± 50	3,467 ± 50
Q_{zz} (MHz)	0	60 ± 20	100 ± 20
g_{xx}	1.876 ± 0.002	1.882 ± 0.002	1.915 ± 0.002
g_{yy}	1.886 ± 0.002	1.898 ± 0.002	1.915 ± 0.002
g_{zz}	2.000 ± 0.002	2.000 ± 0.002	2.000 ± 0.002
Δ_A (MHz)[b]	100	100	100
lw_{pp} (mT)[b]	8	5	5
Theory			
A_{iso}^{point} (MHz)	9,040	19,530	27,360
A_{iso}^{finite} (MHz)	8,274	17,040	23,950
Q_{xx} (MHz)	-0.194	-5.57	-7.76
Q_{yy} (MHz)	-0.243	-5.60	-8.17
Q_{zz} (MHz)	0.436	11.2	15.9

Table 3.3: Natural population analysis. Natural atomic populations of the SOMO arising from Ln = La or Lu for compounds. **2**−**4**

Compound	n(s)	n(p)	n(d)	n(f)
4	0.346	0.039	0.483	0.003
3	0.276	0.074	0.531	0.002
2	0.265	0.018	0.544	0.002

nuclear quadrupole moments are visualized in Fig. 3.2 using Jmol.[256] These surface plots are defined by the real space vector, $\mathbf{r}$, according to the parametric equation:

$$\mathbf{r}^{\mathrm{T}} \overleftrightarrow{T}^{-1} \mathbf{r} = s^2 \tag{3.7}$$

where the following equation gives the nuclear quadrupole moment tensor in the principal axes system,

$$\overleftrightarrow{T} = \frac{Q}{2} \begin{pmatrix} -(1-\eta) & 0 & 0 \\ 0 & -(1+\eta) & 0 \\ 0 & 0 & 2 \end{pmatrix} = \frac{2I(2I-1)h}{eV_{zz}} \overleftrightarrow{Q} \tag{3.8}$$

and s is a dimensionless scale factor.

3.2.7 Summary

The main findings of this study stem from the demonstration that it is possible to control the degree of s-mixing into spin-bearing orbitals of molecular Ln(II) complexes by varying the ligands, and that this enables chemical tuning of the electron–nuclear hyperfine and quadrupole interactions, leading to a giant hyperfine clock transition frequency (>9 GHz). Furthermore, density functional theory calculations are found to correctly predict the relative magnitudes of EPR parameters for these Ln species and provide physical explanations for these results based on the described electronic structure. When compared to experimental measurements, these predictions differ by roughly an order of magnitude, suggesting the need for more refined theoretical approaches if quantitative accuracy is desired. Such improvements are described in detail in Sections 3.3 and 3.4.

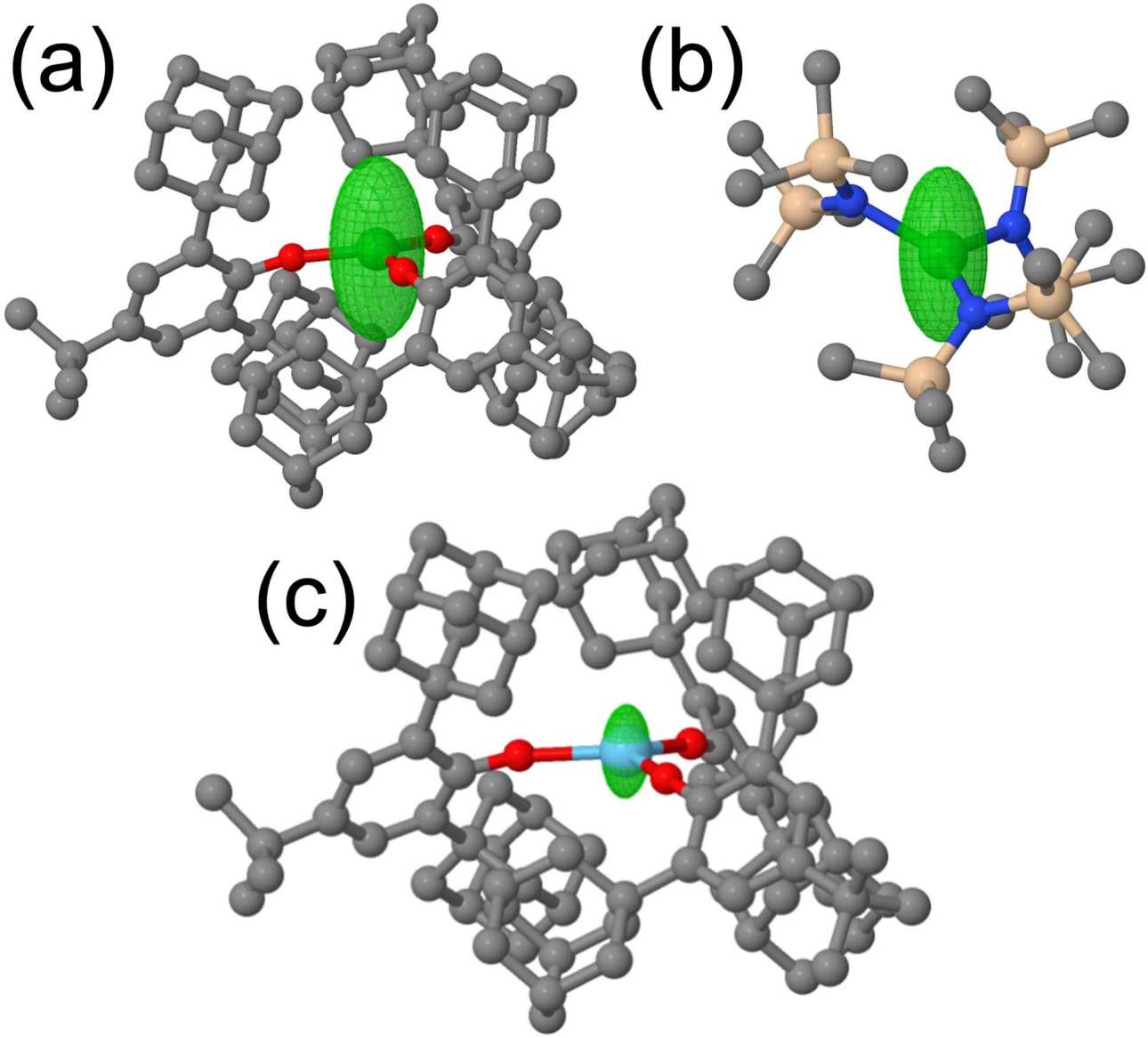

Figure 3.2: Visualization of the quadrupole tensors arising from the Ln nucleus computed with DFT for compounds **4** (a), **3** (b), and **2** (c). Because η is small, the ellipsoids are effectively spheroidal in all three cases. Scaling factors, s, of 5.5 x 10^3, 5.5 x 10^3, and 1.65 x 10^4 were applied in (a), (b), and (c), respectively. Hydrogen atoms were omitted for clarity. Color codes: Grey = C, Red = O, Brown = Si, Teal = N, Pink = Ln.

Although the details of the magnetic measurements were not discussed here, an enhancement in coherence is demonstrated at the hyperfine clock transition of compound **4**, with a maximum T_m value exceeding 10 μs at the relatively high temperature of 5 K, which is more than a factor of 10 longer than that of conventional EPR transitions. Taking the computational and experimental results together, such observations suggest routes to QIS technologies based on molecular design principles, with many parallels to approaches currently employed in more mature ion trap quantum computing architectures.[221]

3.3 Hyperfine Coupling Constants in Local Exact Two-Component Theory

3.3.1 Introduction

The accurate description of electron-nucleus hyperfine interactions in chemical systems is essential for the interpretation of EPR spectra and the *in silico* design of novel magnetic materials. As demonstrated in Section 3.2, First principles prediction of hyperfine spectra can be used to facilitate the discovery of molecular qubits which exhibit so-called "clock transitions," a type of hyperfine transition that is particularly resilient against quantum decoherence,[242,257] for quantum computing applications.[258] Realizing methods which efficiently and accurately calculate the hyperfine structure of high-interest systems and guide synthetic efforts is thus a prominent goal of the molecular magnetism community.

A variety of computational approaches are routinely employed to approximate the hyperfine structure of molecules such as the CASSCF or restricted active space self-consistent field (RASSCF),[259,260] DFT,[13] and correlated wavefunction methods.[261,262] Due to the known sensitivity of hyperfine interactions to relativistic effects,[4] scalar-relativistic corrections[124]

are also commonly included to different levels of approximate two-component theory, and used with a non-relativistic hyperfine operator.[263] These methods have been demonstrated to perform well for organic radicals and metal complexes with valence shells of high orbital angular momentum.

However, calculating the hyperfine interaction becomes significantly more complex for systems containing heavy elements or nearly degenerate electronic states, where spin–orbit coupling effects become large.[17,102,103,263–270] For example, it was observed in Section 3.2 that scalar-relativistic DFT was found to exhibit large errors in the hyperfine coupling tensor predicted for a series of La(II) and Lu(II)-based organometallic complexes, likely due to the divergence of the relativistic spin density near the nucleus and subsequent overestimation of the non-relativistic Fermi-contact term, resulting in errors reaching an order of magnitude. These large errors also presumably occur in CASSCF, which can be inferred from the unexpectedly large hyperfine couplings recently reported for a Tb(II)-based complex with similar electronic structure.[16] Thus, to study single molecule magnets, which include the prospective molecular qubit systems mentioned previously, the method must accurately treat both scalar-relativistic and spin–orbit coupling effects and also use the correct relativistic hyperfine expression.

Four-component (4c) and two-component (2c) relativistic methods for calculating EPR parameters at the DFT level have been previously explored, with the implementation by Malkin *et al.*[271] in a Douglas–Kroll–Hess (DKH) framework,[272–274] the application of the zeroth-order regular approximation[275–277] (ZORA) by Autschbach and co-workers[17,278] to the HFC coupling constant, and the four-component level implementation in the groups of Malkin and Kaupp[279,280] representing major milestones. More recently, EPR parameters calculated via the X2C Hamiltonian[114–120] were reported independently by the group of Autschbach[19,281] as well as Wodyński and Kaupp.[129] X2C represents a robust ansatz with general application to chemical systems.[103,110,282] However, the aforementioned X2C implementations neglect the

derivatives of the X2C renormalization and decoupling matrices when calculating the derivative of the X2C Hamiltonian,[283–287] introducing an additional approximation into describing the hyperfine tensor. Furthermore, the cost associated with these methods precludes their use for large chemical systems or materials. The relativistic decoupling is performed in the fully decontracted or uncontracted basis which consequently results in considerable memory demands and computation times for molecules with several thousand basis functions[130] due to the $\mathcal{O}(N^3)$ scaling of the diagonalization of the 4c Dirac matrix, where N measures the system size.

Here, a new implementation of the quasi-relativistic X2C approach is presented that includes the full derivative of the spin–orbit X2C Hamiltonian and additionally utilizes the diagonal local approximation to the unitary decoupling transformation[110] (DLU) to achieve highly efficient calculations of the hyperfine coupling matrix. To begin, the expression of the relativistic hyperfine coupling matrix is briefly reviewed before presenting the calculation of X2C and DLU-X2C Hamiltonian derivatives as implemented in this work. The method's accuracy and the speed-up achieved by using DLU is then demonstrated through comparison of the hyperfine matrix with that obtained from the 4c method of Gohr *et al.*[280] for a series of transition-metal complexes. Efficiency is further shown for a larger platinum complex $[Pt(C_6Cl_5)_4]^-$ described with 4700 primitive basis functions. The error introduced from neglecting the decoupling and renormalization matrix derivatives for these systems is additionally evaluated. It is shown that the error introduced by DLU is smaller than the latter. An evaluation of commonly used relativistic all-electron basis sets and density functional approximations to identify best practices for general application to molecules is also conducted. Finally, the method is applied to compute the isotropic hyperfine coupling constants for a series of rare-earth single molecule magnets, demonstrating its novel capacity to describe these systems of great interest.

3.3.2 Theory

Notation

As has been done previously for DLU-X2C,[130,133,288–290] we use a matrix notation similar to that of Reiher and Wolf.[269] Matrices in the space of spin-free or one-component (1c) basis functions $\{\lambda_\mu\}$ are indicated as $\boldsymbol{M}$, while matrices in the basis of two-component (2c) functions $\{\phi_\mu\}$ are written as $\mathbf{M}$. The 2c spinor basis functions are chosen as the direct product of the scalar basis functions with spin functions, $\{\lambda_\mu\} \otimes \{\alpha, \beta\}$. $\mathbb{M}$ refers to the corresponding matrices in the space of four-component (4c) functions. A split notation for large (L) and small (S) components is used. The subscripts $-$ and $+$ refer to the so-called positronic and the electronic states. Cartesian coordinates are denoted with u, v. Furthermore, atomic units are used throughout unless explicitly stated otherwise. Gaussian-based units are used for the magnetic interaction. The corresponding superscripts and subscripts refer to the derivative, i.e.

$$\mathbf{h}_u^N = \left(\frac{\mathrm{d}\mathbf{h}}{\mathrm{d}m_{N,u}}\right)_{m_{N,u}=0} \tag{3.9}$$

Note that the derivatives are formed in the limit of a vanishing perturbation.

Hyperfine Coupling Constant

The EPR spin Hamiltonian[264] for a given nucleus N reads

$$\hat{H}_N^{\mathrm{EPR}} = \vec{I}_N \overleftrightarrow{A}_N \vec{S} \tag{3.10}$$

The HFC matrix or so-called hyperfine coupling tensor $\overleftrightarrow{A}_N$ is defined as the second derivative of the energy with respect to the electron spin $\vec{S}$ and nuclear spin $\vec{I}$

$$A_{N,uv} = \frac{\mathrm{d}^2 E}{\mathrm{d}I_{N,u}\mathrm{d}S_v} = g_N \beta_N \frac{\mathrm{d}^2 E}{\mathrm{d}m_{N,u}\mathrm{d}S_v} \tag{3.11}$$

Here, g_N denotes the nuclear g-factor, β_N is the nuclear magneton, and $\vec{m}_N$ is the magnetic dipole moment of nucleus N. In non-relativistic approaches, the hyperfine coupling is commonly split into the Fermi-contact (FC) and the spin-dipole (SD) interaction, see for instance the discussion in Refs. [261]. and [278]. The Fermi-contact term only contributes to the isotropic HFC constant and is commonly computed with the excess spin density $\rho^{\alpha-\beta}$ at the origin of the nucleus, $\vec{N}$, according to

$$A_{N,\mathrm{iso}}^{\mathrm{FC}} = \frac{4\pi}{3} g_N \beta_N \langle \hat{S}_z \rangle^{-1} \ \rho^{\alpha-\beta}(\vec{N}) \tag{3.12}$$

Note that this expression exploits the point charge model. In contrast, the spin-dipole interaction contributes to the anisotropy

$$A_{N,uv}^{\mathrm{SD}} = \frac{1}{2} g_N \beta_N \langle \hat{S}_z \rangle^{-1} \sum_{\mu\nu} \boldsymbol{P}_{\mu\nu}^{\alpha-\beta} \ \langle \lambda_\mu | \hat{r}_N^{-5} \left[\hat{r}_N^2 \delta_{uv} - 3 \ \hat{r}_{N,u} \ \hat{r}_{N,v} \right] | \lambda_\nu \rangle \tag{3.13}$$

with $\vec{r}_N = \vec{r} - \vec{N}$ and the excess spin density matrix $\boldsymbol{P}_{\mu\nu}^{\alpha-\beta}$. Additionally, δ_{uv} is the Kronecker delta and r is the shorthand notation for $|\vec{r}|$.

In a quasi-relativistic 2c framework, the spin derivatives are evaluated using three generalized collinear calculations[17,19,291,292] or the generalized non-collinear approach[271,279,280,293] with the spin aligned along a coordinate axis. Herein, we adopt the latter ansatz as the non-collinear formalism incorporates spin polarization effects and is straightforwardly applicable beyond Kramers doublets. Also, this approach is commonly used in 4c calculations.[279,280,293] The energy depends on the orientation of the magnetization vector, $\vec{J} = \left(\vec{S} + \vec{L} \right)$, along the axis

v. $\vec{L}$ denotes the angular momentum. The hyperfine coupling matrix reads[271,279,280]

$$A_{N,uv} = \frac{g_N \beta_N}{\langle \tilde{S}_v \rangle} \frac{\mathrm{d}E(J_v, \vec{I}_N)}{\mathrm{d}I_{N,u}} = \frac{g_N \beta_N}{\langle \tilde{S}_v \rangle} \operatorname{tr}\left[\mathbf{h}_u^N \mathbf{P}(J_v)\right] \tag{3.14}$$

$\langle \tilde{S}_v \rangle$ is the effective spin along the direction v and $\mathbf{P}$ denotes the two-component density matrix. Thus, three SCF calculations with orthogonal magnetization J_v are required. The effective spin is formally given by the electronic ground state and its term symbol. In case of symmetry the three axes are already defined. For large or non-symmetric molecules, a proper orientation of the molecule is required to directly obtain the HFC tensor in its diagonal form.[271,279,280] To evaluate Eq. 3.14 the derivative of the X2C or the DLU-X2C Hamiltonian is required—similar to nuclear magnetic resonance (NMR) coupling constants.[290,294] We will first discuss the (full) X2C approach and then apply the DLU scheme. Here, we aim for a self-contained derivation for an implementation-ready formulation. Emphasis will be put on the derivatives of the unitary decoupling transformation.

Derivatives of the X2C Hamiltonian

The formulation of the complete derivatives in one-electron X2C requires the following four major steps. First, the Dirac equation is constructed in the presence of a magnetic perturbation. Second, a (finite) basis set is introduced to arrive at its matrix representation. Third, the unitary decoupling step in the spirit of Foldy and Wouthuysen[112] is carried out. Fourth, the actual derivatives of the X2C Hamiltonian with respect to the magnetic perturbation are formed using the product rule.

To account for magnetic perturbations, the generalized momentum operator $\hat{\vec{\pi}}$ is introduced according to the principle of minimal coupling[295]

$$\hat{\vec{\pi}} = \hat{\vec{p}} + \frac{1}{c}\hat{\vec{\mathcal{A}}} = \hat{\vec{p}} + \frac{1}{c}\sum_N \hat{\vec{\mathcal{A}}}_N \tag{3.15}$$

where $\hat{\vec{p}}$ is the linear momentum operator and $\vec{\mathcal{A}}$ is the vector potential associated with the nuclear magnetic moments. The vector potential in a finite nucleus model is given by[296,297]

$$\vec{\mathcal{A}}_N(\vec{r}) = \vec{m}_N \times \vec{\nabla}_N G_N(\vec{r}) \tag{3.16}$$

$$G_N(\vec{r}) = \int \frac{w_N(\vec{R}_N)}{|\vec{r} - \vec{R}|} d\vec{R} \tag{3.17}$$

where w_N describes the shape of the nuclear charge distribution. A derivation for this expression is also provided in Appendix A.1 for finite and point charge distributions. For a Gaussian charge distribution and a nucleus placed at the position $\vec{N}$, the shape function w_N reads

$$w_N(\vec{R}_N) = \left(\frac{\eta}{\pi}\right)^{3/2} \exp\left(-\eta R_N^2\right) \tag{3.18}$$

$$\vec{R}_N = \vec{R} - \vec{N} \tag{3.19}$$

Parameters for the exponent η in this model are available in Ref. [247]. Replacing the linear momentum $\hat{\vec{p}}$ by its generalization $\hat{\vec{\pi}}$ in the one-electron Dirac–Hamilton operator and subsequent expansion in a restricted kinetically balanced (RKB) basis set[105] according to

$$\left|\psi_i^{\mathrm{L}}\right\rangle = \sum_{\mu} c_{\mu i}^{\mathrm{L}} \left|\phi_\mu\right\rangle \tag{3.20}$$

$$\left|\psi_i^{\mathrm{S}}\right\rangle = \sum_{\mu} c_{\mu i}^{\mathrm{S}} \frac{\vec{\sigma} \cdot \hat{\vec{p}}}{2c} \left|\phi_\mu\right\rangle \tag{3.21}$$

leads to the one-electron Dirac equation in a matrix representation

$$\mathbb{DC} = \mathbb{MCE} \tag{3.22}$$

In the super-matrix form, this reads

$$\begin{pmatrix} \mathbf{V} & \mathbf{\Pi}^\dagger \\ \mathbf{\Pi} & (\frac{1}{4c^2}\mathbf{W} - \mathbf{T}) \end{pmatrix} \begin{pmatrix} \mathbf{C}_-^{\mathrm{L}} & \mathbf{C}_+^{\mathrm{L}} \\ \mathbf{C}_-^{\mathrm{S}} & \mathbf{C}_+^{\mathrm{S}} \end{pmatrix} = \begin{pmatrix} \mathbf{S} & \mathbf{0}_2 \\ \mathbf{0}_2 & \frac{1}{2c^2}\mathbf{T} \end{pmatrix} \begin{pmatrix} \mathbf{C}_-^{\mathrm{L}} & \mathbf{C}_+^{\mathrm{L}} \\ \mathbf{C}_-^{\mathrm{S}} & \mathbf{C}_+^{\mathrm{S}} \end{pmatrix} \begin{pmatrix} \boldsymbol{\epsilon}_- & \mathbf{0}_2 \\ \mathbf{0}_2 & \boldsymbol{\epsilon}_+ \end{pmatrix} \tag{3.23}$$

Here, $\mathbf{S}$, $\mathbf{T}$, and $\mathbf{V}$ are the overlap matrix, the kinetic energy matrix, and the scalar potential matrix, for which we use the finite nucleus model.[247,298,299]. These matrices are block-diagonal in the two-component space. The generalized momentum matrix $\mathbf{\Pi}$ is not block-diagonal and reads

$$\mathbf{\Pi}^\dagger_{\mu\nu} = \left\langle \phi_\mu \middle| c\ \vec{\sigma} \cdot \left(\hat{\vec{p}} + \frac{1}{c}\hat{\vec{\mathcal{A}}} \right) \middle| \left(\frac{\vec{\sigma} \cdot \hat{\vec{p}}}{2c} \right) \phi_\nu \right\rangle \tag{3.24}$$

We note in passing that quadratic terms in $\hat{\vec{\mathcal{A}}}$ are obtained by an expansion according to the restricted magnetic (RMB) balance condition.[294,300] However, the impact of RMB is of minor importance for the derivatives with respect to the magnetic moments[19,290,301–304] and the HFC constant is also evaluated with the RKB condition in 4c approaches.[279,280] Matters are different for NMR shifts[288,305–308] and magnetic circular dichroism.[309] The relativistically modified potential $\mathbf{W}$ can be evaluated from four real matrices $\boldsymbol{W}^0$, $\boldsymbol{W}^x$, $\boldsymbol{W}^y$, and $\boldsymbol{W}^z$ as

$$\mathbf{W}_{\mu\nu} = \begin{pmatrix} \boldsymbol{W}^0 + \mathrm{i}\boldsymbol{W}^z & \boldsymbol{W}^y + \mathrm{i}\boldsymbol{W}^x \\ -\boldsymbol{W}^y + \mathrm{i}\boldsymbol{W}^x & \boldsymbol{W}^0 - \mathrm{i}\boldsymbol{W}^z \end{pmatrix} \tag{3.25}$$

with

$$\boldsymbol{W}^0_{\mu\nu} = \langle \lambda_\mu | \hat{p}_x \hat{V} \hat{p}_x + \hat{p}_y \hat{V} \hat{p}_y + \hat{p}_z \hat{V} \hat{p}_z | \lambda_\nu \rangle \tag{3.26}$$

$$\boldsymbol{W}^x_{\mu\nu} = \langle \lambda_\mu | \hat{p}_y \hat{V} \hat{p}_z - \hat{p}_z \hat{V} \hat{p}_y | \lambda_\nu \rangle \tag{3.27}$$

$$\boldsymbol{W}^y_{\mu\nu} = \langle \lambda_\mu | \hat{p}_z \hat{V} \hat{p}_x - \hat{p}_x \hat{V} \hat{p}_z | \lambda_\nu \rangle \tag{3.28}$$

$$\boldsymbol{W}^z_{\mu\nu} = \langle \lambda_\mu | \hat{p}_x \hat{V} \hat{p}_y - \hat{p}_y \hat{V} \hat{p}_x | \lambda_\nu \rangle \tag{3.29}$$

$\boldsymbol{W}^0$ is a symmetric matrix whereas $\boldsymbol{W}^x$, $\boldsymbol{W}^y$, and $\boldsymbol{W}^z$ are antisymmetric matrices. Within

the (modified) screened nuclear spin–orbit (SNSO, mSNSO) approximation,[125–128] the integrals for the spin-dependent parts ($\boldsymbol{W}^x$, $\boldsymbol{W}^y$, $\boldsymbol{W}^z$) are re-scaled to (approximately) account for the missing two-electron picture-change effects.[127,310]

Application of the unitary decoupling transformation yields the X2C Hamiltonian[114–120] as introduced in Chapter 1.3.3, Equation 1.18. The matrix representation of the normalized elimination of the small component operator[121–124] is thus recovered from Equation 1.19. The decoupling matrix $\mathbf{X}$ is obtained in one shot by diagonalization of the Dirac matrix $\mathbb{D}$ with the metric $\mathbb{M}$ as Equation 1.20, and the renormalization matrix $\mathbf{R}$[119] follows as Equation 1.22. Note that the renormalization matrix is non-Hermitian yet positive definite.[311]

Differentiating the X2C Hamiltonian in Eq. 1.18 with respect to the magnetic moments yields

$$\mathbf{h}^{+,N} = \mathbf{R}^{\dagger,N}\mathbf{L}\mathbf{R} + \mathbf{R}^{\dagger}\mathbf{L}^{N}\mathbf{R} + \mathbf{R}^{\dagger}\mathbf{L}\mathbf{R}^{N} \tag{3.30}$$

where the derivative of the NESC matrix is obtained in a straightforward manner using the product rule

$$\begin{aligned}\mathbf{L}^{N} = \quad & \boldsymbol{\Pi}^{\dagger,N}\mathbf{X} + \boldsymbol{\Pi}^{\dagger}\mathbf{X}^{N} + \mathbf{X}^{\dagger,N}\boldsymbol{\Pi} + \mathbf{X}^{\dagger}\boldsymbol{\Pi}^{N} \\ & + \frac{1}{4c^2}\left(\mathbf{X}^{\dagger,N}\mathbf{W}\mathbf{X} + \mathbf{X}^{\dagger}\mathbf{W}\mathbf{X}^{N}\right) \\ & - \mathbf{X}^{\dagger,N}\mathbf{T}\mathbf{X} - \mathbf{X}^{\dagger}\mathbf{T}\mathbf{X}^{N}\end{aligned} \tag{3.31}$$

The derivative of the generalized momentum matrix is given by the respective one-electron integral derivatives[290]

$$\left(\boldsymbol{\Pi}^{\dagger}_{\mu\nu}\right)^{N}_{u} = \frac{1}{2c}\left\langle \phi_\mu \middle| \left(\vec{\nabla}_N \hat{G}_N \times \vec{\sigma}\right)_u \middle| \left(\vec{\sigma}\cdot\hat{\vec{p}}\right)\phi_\nu \right\rangle \tag{3.32}$$

In the non-relativistic limit and the point charge model ($\eta \to \infty$), this integral expression reduces to the well known form of the Fermi-contact, the spin-dipole, and the paramagnetic

spin–orbit interaction.[312] The derivative of the decoupling and the renormalization matrix arise for many-electron systems as the decoupling is performed in the presence of a perturbation.[283,285] As the decoupling matrix depends on the coefficients, response equations are used to form the derivatives. This formalism is similar to coupled-perturbed Hartree–Fock theory,[313,314] however, the response equations are solved in one step for X2C as only one-electron terms are involved. Consequently, the (one-electron) orbital rotation matrix $\mathbb{O}$ is introduced to calculate the so-called perturbed coefficients

$$\begin{pmatrix} \mathbf{C}_{\mathrm{L}-}^{N} & \mathbf{C}_{\mathrm{L}+}^{N} \\ \mathbf{C}_{\mathrm{S}-}^{N} & \mathbf{C}_{\mathrm{S}+}^{N} \end{pmatrix} = \begin{pmatrix} \mathbf{C}_{\mathrm{L}-} & \mathbf{C}_{\mathrm{L}+} \\ \mathbf{C}_{\mathrm{S}-} & \mathbf{C}_{\mathrm{S}+} \end{pmatrix} \begin{pmatrix} \mathbf{O}_{--}^{N} & \mathbf{O}_{-+}^{N} \\ \mathbf{O}_{+-}^{N} & \mathbf{O}_{++}^{N} \end{pmatrix} \tag{3.33}$$

The elements of the orbital rotation matrix $\mathbf{O}_{-+}$ can be calculated as

$$(\mathbf{O}_{-+}^{N})_{kl} = \frac{(\tilde{\mathbf{D}}_{-+}^{N})_{kl}}{(\mathbf{E}_{++})_{ll} - (\mathbf{E}_{--})_{kk}} \tag{3.34}$$

where the notation $\tilde{\mathbf{D}}_{-+}^{N}$ indicates that the perturbed Dirac matrix is formed in the basis of the unperturbed solutions according to

$$\tilde{\mathbf{D}}_{-+}^{N} = \mathbf{C}_{-}^{\mathrm{L},\dagger} \boldsymbol{\Pi}^{\dagger,N} \mathbf{C}_{+}^{\mathrm{S}} + \mathbf{C}_{-}^{\mathrm{S},\dagger} \boldsymbol{\Pi}^{N} \mathbf{C}_{+}^{\mathrm{L}} \tag{3.35}$$

The numerical stability of Eq. 3.34 is ensured by the large energetic gap between the so-called positronic and the electronic states. Using the normalization of the large component

$$\mathbf{C}_{\mathrm{L}+}^{\dagger}\ \tilde{\mathbf{S}}\ \mathbf{C}_{\mathrm{L}+} = \mathbf{I} \tag{3.36}$$

where $\mathbf{I}$ is the unit matrix, the derivative of the decoupling matrix follows as[285,311]

$$\mathbf{X}^{N} = (\mathbf{C}_{\mathrm{S}-} - \mathbf{X}\mathbf{C}_{\mathrm{L}-})\ \mathbf{O}_{-+}^{N}\ \mathbf{C}_{\mathrm{L}+}^{\dagger}\ \tilde{\mathbf{S}} \tag{3.37}$$

Therefore, the derivative of the decoupling matrix can be obtained by using simple basic linear algebra subroutines (BLAS).[315,316] We refer to the appendix of Ref. [288] for further details on the derivation and a comparison of the different approaches for the one-electron response equations. Finally, the derivative of the renormalization matrix is evaluated based on[124]

$$\mathbf{RR} = \tilde{\mathbf{S}}^{-1}\mathbf{S} \tag{3.38}$$

This yields the Sylvester matrix equation for the perturbed renormalization matrix

$$\mathbf{RR}^N + \mathbf{R}^N\mathbf{R} = \tilde{\mathbf{S}}^{-1}\tilde{\mathbf{S}}^N\mathbf{RR} \tag{3.39}$$

with the derivative $\tilde{\mathbf{S}}^N$ of the right-hand side given by

$$\tilde{\mathbf{S}}^N = \frac{1}{2c^2}\mathbf{X}^{\dagger,N}\mathbf{TX} + \frac{1}{2c^2}\mathbf{X}^{\dagger}\mathbf{TX}^N \tag{3.40}$$

The Sylvester matrix equation is solved with an eigenvalue decomposition method.[311]

Derivatives of the DLU-X2C Hamiltonian

The algebraic operations such as matrix multiplications and diagonalizations for the X2C Hamiltonian and its derivatives are typically carried out in a large uncontracted basis. Therefore, their computation leads to substantially increased demands when compared to the ground-state energy calculation,[133] which are in and of themselves computationally expensive in the X2C scheme for a few thousand basis functions.[130] Thus, we apply the DLU scheme to reduce the computational overhead for the inclusion of the derivatives of $\mathbf{X}$ and $\mathbf{R}$. In the non-orthogonal basis set of the last subsection, the unitary decoupling matrix is

approximated according to[133]

$$\mathbf{U}^{\mathrm{LL}} = \bigoplus_A \mathbf{U}^{\mathrm{LL}}_{AA} = \bigoplus_A \mathbf{R}_{AA} \tag{3.41}$$

$$\mathbf{U}^{\mathrm{SL}} = \bigoplus_A \mathbf{U}^{\mathrm{SL}}_{AA} = \bigoplus_A \mathbf{X}_{AA}\mathbf{R}_{AA} \tag{3.42}$$

Here, the atomic blocks are defined according to the atom center of the basis functions for the respective matrix element of the one-electron integrals. We denote an atomic diagonal block as AA and a general atomic block as AB. Therefore, the atomic blocks of the Hamiltonian are generally defined as

$$\mathbf{h}^{+}_{AB} = \mathbf{R}^{\dagger}_{AA}\mathbf{L}_{AB}\mathbf{R}^{\dagger}_{BB} \tag{3.43}$$

which yields the working equation for the ground-state energy

$$\begin{aligned}\mathbf{h}^{+}_{AB} = \; & \mathbf{R}^{\dagger}_{AA}\left(\mathbf{V}_{AB} + \mathbf{\Pi}^{\dagger}_{AB}\mathbf{X}_{BB} + \mathbf{X}^{\dagger}_{AA}\mathbf{\Pi}_{AB}\right)\mathbf{R}_{BB} \\ & + \mathbf{R}^{\dagger}_{AA}\left(\mathbf{X}^{\dagger}_{AA}\left[\frac{1}{4c^2}\mathbf{W}_{AB} - \mathbf{T}_{AB}\right]\mathbf{X}_{BB}\right)\mathbf{R}_{BB}\end{aligned} \tag{3.44}$$

Accordingly, only the atomic diagonal block of the Dirac matrix is diagonalized to obtain $\mathbf{X}_{AA}$ and $\mathbf{R}_{AA}$. Therefore, the formal scaling is reduced from $\mathcal{O}(N^3)$ for the full X2C Hamiltonian to $\mathcal{O}(N)$ for the atomic diagonal blocks and overall to $\mathcal{O}(N^2)$ due to the number of atom pairs for the atomic diagonal block. N measures the size of the system.

The derivatives of the DLU-X2C Hamiltonian for the HFC matrix follow as

$$\begin{aligned}\mathbf{h}^{+,N}_{AB} = \; & \mathbf{R}^{\dagger,N}_{AA}\mathbf{L}_{AB}\mathbf{R}^{\dagger}_{BB} + \mathbf{R}^{\dagger}_{AA}\mathbf{L}_{AB}\mathbf{R}^{\dagger,N}_{BB} \\ & + \mathbf{R}^{\dagger}_{AA}\left(\mathbf{\Pi}^{\dagger,N}_{AB}\mathbf{X}_{BB} + \mathbf{X}^{\dagger}_{AA}\mathbf{\Pi}^{N}_{AB}\right)\mathbf{R}_{BB} \\ & + \mathbf{R}^{\dagger}_{AA}\left(\mathbf{\Pi}^{\dagger}_{AB}\mathbf{X}^{N}_{BB} + \mathbf{X}^{\dagger,N}_{AA}\mathbf{\Pi}_{AB}\right)\mathbf{R}_{BB} \\ & + \mathbf{R}^{\dagger}_{AA}\left(\mathbf{X}^{\dagger,N}_{AA}\left[\frac{1}{4c^2}\mathbf{W}_{AB} - \mathbf{T}_{AB}\right]\mathbf{X}_{BB}\right)\mathbf{R}_{BB} \\ & + \mathbf{R}^{\dagger}_{AA}\left(\mathbf{X}^{\dagger}_{AA}\left[\frac{1}{4c^2}\mathbf{W}_{AB} - \mathbf{T}_{AB}\right]\mathbf{X}^{N}_{BB}\right)\mathbf{R}_{BB}\end{aligned} \tag{3.45}$$

To evaluate these derivatives, first the atomic diagonal blocks of the unperturbed decoupling matrix $\mathbf{X}_{AA}$ and the unperturbed renormalization matrix $\mathbf{R}_{AA}$ are computed. Second, the atomic diagonal blocks of the perturbed Hamiltonian are calculated by a straightforward application of the response and Sylvester matrix, Eqs. 3.33–3.40. The atomic diagonal blocks $\mathbf{X}^N_{AA}$ and $\mathbf{R}^N_{AA}$ are then used to perform the matrix multiplications in Eq. 3.45. Note that both the atomic diagonal and atomic off-diagonal blocks of the perturbed generalized momentum matrix $\mathbf{\Pi}^N$ need to be evaluated. However, the one-electron integrals and integral derivatives themselves are negligible in terms of computational demands.

3.3.3 Implementation

We have implemented the DLU-X2C and X2C approach for HFC constants into the TURBOMOLE[134,135,317,318] quantum chemistry program suite. The derivatives of the decoupling and the renormalization matrix are obtained based on the one-electron response routines of Refs. [133], [288], and [290]. The integral derivatives are taken from the latter references, whereas the parent (unperturbed) integrals were implemented in Ref. [133]. Consequently, all integrals are evaluated using Gauss–Rys[319,320] and Gauss–Hermite integration. Parameters for the Gaussian charge distribution are taken from Ref. [247] and the (modified) screened nuclear spin–orbit approximation is available to re-scale the spin-dependent contributions of $\mathbf{W}$.[125–128] Nuclear g factors are calculated based on the available gyromagnetic ratios.[255,321,322] A value of $c = 137.0359990840\,\text{a.u.}$[323] is used for the speed of light in atomic units.

Our implementation in the ridft module[130,133,137,324–327] is completely integral direct and makes use of the OpenMP parallelization[328] throughout all integrals and algebraic operations.[329] The Intel® Math Kernel Library (Intel MKL) is further used in this work. The resolution of the identity approximation to the Coulomb integrals, RI-J,[324,330,331] and its

multipole-accelerated variant MARI-J[332] as well as to the exchange integrals, RI-K,[324,333] and the seminumerical exchange approximation[326,327] are available. Furthermore, the integrals can be calculated without these approximations.[137,325] COSMO[215,334] is supported to simulate the counter ions in case of charged systems or to consider the environment in solution. We note that two-component generalized Kohn–Sham calculations require tailored grids for all-electron approaches and therefore we use the grids of Ref. [246]. Currently, functionals up to the fourth rung of Jacob's ladder,[335–337] including GGAs, *meta*-GGAs, and their respective (range-separated) hybrids, are supported. Interfaces to Libxc[338–340] and XCFun[341] are further provided. We validated the implementation by comparison to the scalar-relativistic approach[342] and the non-relativistic limit.[322,342]

Pre-processing and post-processing scripts are available so that only converged unrestricted Hartree–Fock or Kohn–Sham (UHF/UKS) orbitals are required and the complete two-component procedure can be carried out in a "black-box" fashion. The spin contributions to the HFC matrix are evaluated at the end of each SCF calculation. The post-processing script assembles the full HFC matrix and calculates the principal components. These may be obtained with the rank-2 tensor $\overset{\leftrightarrow}{A}_N \overset{\leftrightarrow T}{A}_N$. The eigenvectors of this quantity form the principal axis system of the HFC and the square root of the eigenvalues are the principal HFC values, i.e. $A^{\mathrm{PAS}}_{N,11}$, $A^{\mathrm{PAS}}_{N,22}$, and $A^{\mathrm{PAS}}_{N,33}$. Note that the sign information is lost in the rank-2 tensor, and so the signs are determined by comparison to the one-component ansatz and by algebraic considerations, i.e. the sign of the determinant of $\overset{\leftrightarrow}{A}_N$ and $\overset{\leftrightarrow \mathrm{PAS}}{A}_N$ is identical.[17] Another way to transform the HFC matrix to a diagonal form is to form the symmetric contribution, $\frac{1}{2}\left(\overset{\leftrightarrow}{A}_N + \overset{\leftrightarrow T}{A}_N\right)$, and diagonalize it. Similar to the 4c implementation in ReSpect,[343] our implementation supports both ansätze.[344] The isotropic HFC constant, $A_{N,\mathrm{iso}}$ or simply A_N, is a third of the trace, $A_N = \frac{1}{3}\sum_u A^{\mathrm{PAS}}_{N,uu}$.

3.3.4 Computational Details

To begin, we consider the general parameters of a relativistic calculation for a set of transition-metal compounds in Sec. 3.3.5, i.e. the Hamiltonian, the basis set, and the method to treat electron correlation. For the latter, we use DFT. Finally, applications to large molecular systems are presented in Secs. 3.3.6 and 3.3.7. Note that the finite nucleus model is used for the scalar potential[133] and the vector potential[288,290] throughout the main text. MO and spinor files use the ASCII format (American Standard Code for Information Interchange).

First, the quasi-relativistic two-component X2C and DLU-X2C Hamiltonian are compared to the "fully" relativistic four-component Hamiltonian. This is done for the test set of 17 transition-metal complexes compiled in Ref. [280], namely $[MoNCl_4]^{2-}$, $[MoOF_4]^-$, $[MoOCl_4]^-$, $[MoOF_5]^{2-}$, $[MoOBr_5]^{2-}$, $[WOCl_4]^-$, $[WOF_5]^{2-}$, $[WOBr_5]^{2-}$, $[TcNF_4]^-$, $[TcNCl_4]^-$, $[TcNBr_4]^-$, $[ReNF_4]^-$, $[ReNCl_4]^-$, $[ReNBr_4]^-$, $[ReOBr_4]$, $[ReOF_5]^-$, and $[OsOF_5]$. Structures are taken from this reference. The same basis sets as therein are employed. Therefore, the uncontracted IGLO-III bases are used for N, F, and Cl[345] while the Dyall-VTZ basis set is used for Br[346,347] and the Dyall-TZ bases are selected for Mo, Tc, W, Re, and Os.[347–349] Herein, the HFC is calculated with the mSNSO-DLU-X2C and the mSNSO-X2C Hamiltonian in a finite nucleus model. We note that all approaches employ the finite nucleus model for both the scalar and the vector potential. The PBE0[350,351] functional (grid 5a,[246,352,353] SCF convergence threshold $10^{-9}\,E_h$) is chosen. While it was shown that an increased amount of HF exchange improves the agreement with the experimental findings,[280] we first assess the error introduced by DLU and compare the X2C Hamiltonian to its 4c parent. Therefore, the conventional PBE0 functional is chosen for simplicity. The impact of density functional approximations are considered in detail below. Additionally, scalar-relativistic calculations[342] are carried out. We use the following nuclear g factors: –0.3653890 (^{95}Mo), 0.2355696 (^{183}W), 1.2632019 (^{43}Tc), 1.2878813 (^{187}Re), and 0.4399555 (^{189}Os).

Table 3.4: Considered basis sets and basis set combinations for the light (N, O, F, Cl) and heavy elements (Br, Mo, Tc, W, Re, Os). The suffix "-unc" denotes that the bases are used in the decontracted form. Note that the ccJ basis sets are only available up to Ne and thus combined with the cc bases. NBF is the total number of spherical AO basis functions. The even-tempered reference basis set uses 26085 basis functions for the molecular test set (average: 1534). "Avg." denotes the average number of basis functions for a molecule.

Bases	Light Elements	Ref.	Heavy Elements	Ref.	NBF	Avg.
1	IGLO-II-unc	[345]	Dyall-VDZ-unc	[346–349]	6421	378
2	IGLO-III-unc	[345]	Dyall-VTZ-unc	[346–349]	9176	540
3	pcJ-1-unc	[354]	Dyall-VDZ-unc	[346–349]	6895	406
4	pcJ-2-unc	[354]	Dyall-VTZ-unc	[346–349]	10 108	595
5	pcJ-3-unc	[354]	Dyall-VQZ-unc	[346–349]	12 614	742
6	cc-pVDZ-unc	[355, 356]	Dyall-VDZ-unc	[346–349]	6440	379
7	cc-pVTZ-unc	[355, 356]	Dyall-VTZ-unc	[346–349]	9425	554
8	cc-pVQZ-unc	[355, 356]	Dyall-VQZ-unc	[346–349]	11 634	554
9	ccJ-pVDZ-unc/cc-pVDZ-unc	[355–357]	Dyall-VDZ-unc	[346–349]	6740	396
10	ccJ-pVTZ-unc/cc-pVTZ-unc	[355–357]	Dyall-VTZ-unc	[346–349]	9614	565
11	ccJ-pVQZ-unc/cc-pVQZ-unc	[355–357]	Dyall-VQZ-unc	[346–349]	11 644	685
12	Sapporo-DZP-2012	[358]	Sapporo-DKH3-DZP-2012	[358, 359]	3369	198
13	Sapporo-TZP-2012	[358]	Sapporo-DKH3-TZP-2012	[358, 359]	6213	365
14	Sapporo-QZP-2012	[358]	Sapporo-DKH3-QZP-2012	[358, 359]	9804	577
15	Jorge-DZP-DKH	[360]	Jorge-DZP-DKH	[360–362]	3085	181
16	Jorge-TZP-DKH	[360]	Jorge-TZP-DKH	[360–362]	5038	296
17	x2c-SVPall-2c	[137]	x2c-SVPall-2c	[137]	3315	195
18	x2c-TZVPall-2c	[137]	x2c-TZVPall-2c	[137]	5095	300
19	x2c-QZVPall-2c	[363]	x2c-QZVPall-2c	[363]	8799	518
20	x2c-SVPall-2c-unc	[137]	x2c-SVPall-2c-unc	[137]	7614	448
21	x2c-TZVPall-2c-unc	[137]	x2c-TZVPall-2c-unc	[137]	9104	536
22	x2c-QZVPall-2c-unc	[363]	x2c-QZVPall-2c-unc	[363]	14 366	845
23	ANO-R-unc	[364]	ANO-R-unc	[364]	15 764	927
24	ANO-RCC-unc	[365]	ANO-RCC-unc	[365, 366]	15 757	927

Second, we complement the study presented in Ref. [280] at the 4c level with our own basis set study at the 2c level. The basis sets explored are given in Tab. 3.4. Note that out of those listed, only the IGLO and the Dyall basis sets overlap in Ref. [280]. We choose the large even-tempered (ET) basis set of Ref. [363] as a reference. This basis set employs 26085 basis functions (spherical AO representation) in total throughout the 17 molecules. The choice of such a large ET basis set in place of experimental findings allows us to consider the impact of the basis set without side effects. All basis sets except for the Dyall and the x2c-type bases are taken from the Basis Set Exchange Library.[140,367] Among the chosen segmented-contracted relativistic basis sets, only the Sapporo bases are optimized with the point charge model. Furthermore, the contractions of the Sapporo and Jorge basis are optimized with the third-order Douglas–Kroll–Hess[272–274] (DKH3) Hamiltonian. We note that while the ANO-R basis is optimized for X2C, we employ it in a decontracted form for consistency with the ANO-RCC basis, which is also commonly used in the decontracted form

(see for instance Refs. [19, 283, 306, 368, 369]). As the cc, ccJ, IGLO, and pcJ basis sets are optimized in non-relativistic calculations, they are employed in their decontracted form. Generally, relativistic all-electron Hamiltonians require re-optimized contraction coefficients even for the light elements.[137,246,363] The x2c-type basis sets are used in both their original segmented-contracted fashion and in a fully decontracted fashion. For the latter, we removed functions to avoid linear dependencies and also excluded (nearly) identical functions from the 2c extensions. We stress that this decontraction is only done to assess the flexibility of these bases, as decontracting segmented-contracted basis sets may easily lead to linear dependencies and convergence issues. Calculations are performed for the transition-metal complexes with the previous settings, i.e. the mSNSO-DLU-X2C Hamiltonian in a finite nucleus model is employed. The thresholds are the same as for the Hamiltonian study and again the PBE0 functional is considered. The mean absolute percent-wise deviation (MAPD) and its standard deviation (STD) are chosen as indicators for the quality of the basis set according to

$$\mathrm{MAPD} = \sum_{i=1}^{N=17} \frac{|A_{i,\mathrm{iso}}^{\mathrm{test}} - A_{i,\mathrm{iso}}^{\mathrm{ref}}|}{|A_{i,\mathrm{iso}}^{\mathrm{ref}}|} \tag{3.46}$$

where $A_{\mathrm{iso}}^{\mathrm{test}}$ and $A_{\mathrm{iso}}^{\mathrm{ref}}$ are the isotropic HFC constant for a given basis set and the reference.

Third, the performance of frequently used density functional approximations is studied for 12 of the 17 complexes considered previously. Here, we consider the S-VWN,[370–372] KT3,[373] BP86,[374,375] PBE,[350] TPSS,[211] revTPSS,[376,377] r^{2}SCAN,[378,379] BH&HLYP,[375,380,381] B3LYP,[380,382] PBE0,[350,351] B97,[383] B97-2,[384] TPSSh,[385] revTPSSh,[376,377] TPSS0,[385,386] CAM-B3LYP,[387] CAM-QPT-00,[388] CAM-QTP-02,[389] HSE06,[390–392] LC-ωPBE,[393] and ωB97X-D[394] functionals. Libxc[338–340] is used for the range-separated hybrid functionals, KT3, revTPSS(h), TPSS0, r^{2}SCAN, and B97 throughout this work. We also use the PBE0 functional including 40 % of HF exchange (PBE0-40HF) with XCFun.[341] A review of the construction of each functional is outside the scope of this work, and readers are encouraged to consult the above references for additional details on any DFA used in this study. The x2c-QVZPall-2c basis

set[363] is selected and COSMO[215,334] is applied using the default parameters[395] to compensate for the negative charge. This ensures negative eigenvalues for occupied molecular orbitals and spinors. Having assessed the error of the basis set and the Hamiltonian, the experimental findings[396–407] collected in Ref. [280] serve as reference.

In Sec. 3.3.6, the impact of the density functional approximation is also studied for a typical application with the mSNSO-DLU-X2C Hamiltonian. Here, the Pt complex $[Pt(C_6Cl_5)_4]^-$ is considered with the uncontracted Dyall-VTZ basis set[408] for Pt and the decontracted pcJ-2 bases for C and Cl,[354] as well as the segmented-contracted x2c-QZVPall-2c basis set for all atoms.[363] COSMO is again[215,334] applied with the default settings[395] to compensate the negative charge. The structure is taken from Ref. [280]. An SCF threshold of $10^{-8}\,E_h$ is applied and large grids are used for the numerical integration of the XC parts (grid 4a).[246,352,353] Here, the following functionals are chosen. KT3,[373] BP86,[374,375] PBE,[350] TPSS,[211] r^{2}SCAN,[378,379] BH&HLYP,[375,380,381] B3LYP,[380,382] PBE0,[350,351] PBE0-40HF,[280,350,351] B97,[383] TPSSh,[385] TPSS0,[385,386] CAM-B3LYP,[387] CAM-QPT-00,[388] CAM-QTP-02,[389] HSE06,[390–392] LC-ωPBE,[393] and ωB97X-D.[394] Libxc[338–340] is used for the range-separated hybrid functionals, TPSS0, B97, KT3, and r^{2}SCAN. Furthermore, calculations with the PBE0-40HF functional are carried out using XCFun.[341] The nuclear g factor is set to 1.2190420 (^{195}Pt). We note that our computational setting with the Dyall-VTZ/pcJ-2 basis leads to 3284 basis functions in the spherical AO representation, whereas the calculations in Ref. [129] employed only 2205 basis functions (Dyall-TZ/IGLO-III). Moreover, a significantly smaller grid was employed in this reference, see Refs. [246], [352], and [353] for the respective integration grids. The x2c-QZVPall-2c basis sets leads to 3003 contracted functions and 4720 primitive functions.

In Sec. 3.3.7, we apply the DLU-X2C method to study a series of Ln-based single molecule magnets reported in Ref. [14]. The structures given in Ref. [14] were used for all calculations, which were themselves optimized using DFT with the TPSS functional to a Cartesian gradient norm of 10^{-4} atomic units and confirmed to be minima via vibrational analysis.

Tailored integration grids (grid 4a) are used.[246] COSMO[215,334] was employed to model solvation effects using an epsilon value (ϵ_r) of 7.520, solvation radius of 1.30 Å, and refractive index of 1.4050 (tetrahydrofuran, THF). D3 dispersion corrections[248] were also used. SCF thresholds of $10^{-7}\,\mathrm{E_h}$ for the energy and 10^{-7} a.u. for the root mean square of the density matrix indicate the convergence. This methodology to characterize the ground-state electronic structure has been extensively used and validated in previous studies from our group on lanthanide and actinide complexes.[54,57,58,60,143,214] The 2c studies herein include the mSNSO approximation. Details regarding the basis sets and functionals explored for the DLU-X2C calculations, as well as comparisons with the computational methodology used to approximate the HFC in Ref. [14] are discussed in Sec. 3.3.7. The nuclear g factors are 0.7951560 (^{139}La) and 0.6379065 (^{175}Lu).

Finally, we apply the developed methodology to systems with more than one unpaired electron. In Sec. 3.3.8, we study the compound $[\mathrm{TbPc_2}]^-$, where Pc denotes bis(phthalocyaninato), with six unpaired electrons ($S = 3$) using the same computational settings as in Sec. 3.3.7. Note that fractional occupation numbers[409] (FON) are used to accelerate the SCF convergence with the r^{2}SCAN functional. We employ the same structure as in Ref. [260], which was itself determined in Ref. [410]. The nuclear g factor is 1.3427523 for ^{159}Tb.

3.3.5 Assessment of Accuracy

Comparison to Four-Component Results

The scalar-relativistic and the spin–orbit X2C Hamiltonians are compared to the parent four-component Dirac–Kohn–Sham (DKS) ansatz in Tab. 3.5 for 17 transition-metal compounds. Overall, the quasi-relativistic X2C and the DLU-X2C Hamiltonian sufficiently reproduce the DKS results. The DLU error is negligible and typically amounts to about 0.1 MHz. In comparison, the impact of spin–orbit coupling amounts to 10–200 MHz. As expected, spin–orbit

Table 3.5: Principal components of the hyperfine coupling constant in MHz. Non-collinear 4c results are taken from the Supporting Information of Ref. [280]. "PCC" denotes that the derivatives of $\boldsymbol{X}$ and $\boldsymbol{R}$ are neglected, whereas SR and SO refer to scalar-relativistic and spin–orbit calculations. Experimental results[396–407] were collected in Ref. [280].

Molecule	Hamiltonian	A_{iso}	$A_{\parallel}$	$A_{\perp}$	Molecule	Hamiltonian	A_{iso}	$A_{\parallel}$	$A_{\perp}$
$[\mathbf{MoNCl_4}]^{2-}$	SR X2C	162.0	227.6	129.1	$[\mathbf{TcNF_4}]^{-}$	SR X2C	−589.3	−884.9	−441.5
	SR DLU	162.1	227.6	129.1		SR DLU	−589.3	−884.9	−441.5
	SO X2C PCC	175.2	260.6	132.5		SO X2C PCC	−647.9	−1024.6	−459.6
	SO X2C	175.3	260.7	132.6		SO X2C	−648.5	−1025.3	−460.2
	SO DLU	175.3	260.7	132.6		SO DLU	−648.6	−1025.4	−460.1
	4c	176	262	133		4c	−650	−1031	−460
	Expt.	–	–	–		Expt.	−734	−1129	−537
$[\mathbf{MoOF_4}]^{-}$	SR X2C	139.3	216.1	100.8	$[\mathbf{TcNCl_4}]^{-}$	SR X2C	−463.9	−727.3	−332.2
	SR DLU	139.3	216.1	100.8		SR DLU	−464.0	−727.3	−332.3
	SO X2C PCC	157.4	251.1	110.6		SO X2C PCC	−498.1	−805.1	−344.6
	SO X2C	157.6	251.3	110.7		SO X2C	−498.6	−805.8	−345.1
	SO DLU	157.6	251.3	110.7		SO DLU	−498.6	−805.7	−345.0
	4c	158	253	111		4c	−500	−810	−345
	Expt.	–	268	–		Expt.	−561	−878	−402
$[\mathbf{MoOCl_4}]^{-}$	SR X2C	109.1	177.8	74.8	$[\mathbf{TcNBr_4}]^{-}$	SR X2C	−437.4	−696.7	−307.8
	SR DLU	109.1	177.8	74.8		SR DLU	−437.5	−696.7	−307.8
	SO X2C PCC	122.6	201.9	82.9		SO X2C PCC	−432.8	−668.8	−314.8
	SO X2C	122.7	202.1	83.0		SO X2C	−433.3	−669.5	−315.3
	SO DLU	122.7	202.1	83.0		SO DLU	−433.3	−669.5	−315.3
	4c	123	203	83		4c	−437	−676	−318
	Expt.	145	227	103		Expt.	−488	−743	−360
$[\mathbf{MoOF_5}]^{2-}$	SR X2C	142.2	217.7	104.4	$[\mathbf{ReNF_4}]^{-}$	SR X2C	−1482.2	−1967.0	−1239.7
	SR DLU	142.2	217.7	104.5		SR DLU	−1482.2	−1967.1	−1239.7
	SO X2C PCC	164.6	256.8	118.5		SO X2C PCC	−1793.8	−2756.3	−1312.5
	SO X2C	164.7	257.0	118.6		SO X2C	−1795.7	−2758.9	−1314.2
	SO DLU	164.7	257.0	118.6		SO DLU	−1795.7	−2758.9	−1314.2
	4c	166	259	119		4c	−1788	−2753	−1306
	Expt.	183	279	135		Expt.	−2117	−3079	−1637
$[\mathbf{MoOBr_5}]^{2-}$	SR X2C	103.8	169.8	70.8	$[\mathbf{ReNCl_4}]^{-}$	SR X2C	−1003.4	−1429.2	−790.5
	SR DLU	103.8	169.8	70.8		SR DLU	−1003.0	−1428.8	−790.1
	SO X2C PCC	112.8	176.2	81.1		SO X2C PCC	−1229.4	−1996.5	−845.8
	SO X2C	112.9	176.4	81.2		SO X2C	−1231.1	−1998.7	−847.2
	SO DLU	112.9	176.4	81.2		SO DLU	−1230.7	−1998.4	−846.9
	4c	114	178	82		4c	−1225	−1994	−841
	Expt.	128	184	99		Expt.	−1544	−2263	−1184
$[\mathbf{WOCl_4}]^{-}$	SR X2C	−142.4	−212.2	−107.5	$[\mathbf{ReNBr_4}]^{-}$	SR X2C	−854.1	−1268.3	−647.1
	SR DLU	−142.4	−212.2	−107.4		SR DLU	−853.9	−1268.1	−646.8
	SO X2C PCC	−193.2	−316.1	−131.8		SO X2C PCC	−1010.7	−1645.3	−693.4
	SO X2C	−193.5	−316.4	−132.0		SO X2C	−1012.3	−1647.3	−694.8
	SO DLU	−193.5	−316.4	−132.0		SO DLU	−1012.0	−1647.2	−694.5
	4c	−193	−316	−131		4c	−1009	−1646	−691
	Expt.	–	–	–		Expt.	−1340	−1994	−1013
$[\mathbf{WOF_5}]^{2-}$	SR X2C	−220.8	−298.7	−181.8	$[\mathbf{ReOBr_4}]$	SR X2C	−553.5	−959.4	−350.6
	SR DLU	−220.8	−298.7	−181.8		SR DLU	−553.6	−959.4	−350.6
	SO X2C PCC	−293.8	−439.3	−221.1		SO X2C PCC	−735.9	−1195.7	−505.9
	SO X2C	−294.1	−439.7	−221.3		SO X2C	−737.3	−1197.6	−507.1
	SO DLU	−294.1	−439.7	−221.3		SO DLU	−737.3	−1197.7	−507.1
	4c	−293	−420	−221		4c	−733	−1197	−501
	Expt.	−331	−496	−262		Expt.	–	–	–
$[\mathbf{WOBr_5}]^{2-}$	SR X2C	−116.6	−183.0	−83.4	$[\mathbf{ReOF_5}]^{-}$	SR X2C	−1162.3	−1651.0	−917.9
	SR DLU	−116.6	−183.0	−83.3		SR DLU	−1162.4	−1651.1	−918.1
	SO X2C PCC	−167.1	−278.7	−111.3		SO X2C PCC	−1604.4	−2469.0	−1172.1
	SO X2C	−167.3	−279.0	−111.5		SO X2C	−1606.2	−2471.4	−1173.6
	SO DLU	−167.3	−279.0	−111.5		SO DLU	−1606.3	−2471.6	−1173.7
	4c	−167	−279	−111		4c	−1600	−2466	−1166
	Expt.	–	–	–		Expt.	−1959	−2878	−1499
$[\mathbf{OsOF_5}]$	SR X2C	−370.9	−541.6	−285.6					
	SR DLU	−371.0	−541.6	−285.6					
	SO X2C PCC	−518.5	−811.2	−372.2					
	SO X2C	−519.2	−812.1	−372.8					
	SO DLU	−519.3	−812.1	−372.8					
	4c	−517	−811	−370					
	Expt.	−627	−935	−480					

effects are less pronounced for the $4d$ elements than for the $5d$ elements. The Fermi-contact term is the leading contribution for these molecules featuring a doublet ground-state configuration. The derivatives are of minor importance for the $4d$ elements (less than 1 MHz) but their impact rises for the $5d$ elements. For instance, the inclusion of the derivatives of $\boldsymbol{X}$ and $\boldsymbol{R}$ changes the HFC constant by about 2–3 MHz for the Re compounds. For this assessment, the derivatives of $\mathbf{X}$ and $\mathbf{R}$ were set to zero in the respective response equations. We note that neglecting these derivatives may result in error cancellation compared to the 4c results due to the picture-change effects of the two-electron integrals. From a formal point of view, a rigorous treatment of two-electron picture-change effects[411] together with the decoupling derivatives should result in an excellent agreement with the DKS approach. However, this also increases the computational demands for the 2c ansatz, as it requires modifications of the two-electron infrastructure. The mSNSO approximation leads to notable changes of the HFC constant and significantly improves the agreement with the 4c reference values. The maximum change amounts to about 70 MHz for $[ReOF_5]^-$. This is a relative change of 4%. The largest relative changes of about 5% are observed for the Mo complexes. The results indicate that the SNSO and mSNSO approximation lead to a consistent improvement of the results compared to the 4c reference. Moreover, we refer to the study in Ref. [129], where an atomic mean-field spin–orbit (AMFSO) approach was used. Therein, the deviations between 4c, AMFSO-X2C, SNSO-X2C, and mSNSO-X2C are also small. For the HFC in particular, the SNSO/mSNSO results are in excellent agreement with those of the AMFSO approach. Thus, the mSNSO approximation is sufficient for DFT approaches. Yet, more sophisticated treatments may be required for coupled-cluster or other post-Hartree–Fock methods.

Within the DLU scheme, the computational costs for the one-electron response and Sylvester equations to calculate the derivatives of $\mathbf{X}$ and $\mathbf{R}$ are drastically reduced. Therefore, they can be included with negligible computational overhead. The introduced error is negligible for the basis sets studied here. The DLU error is still small (typically 0.2–0.6 MHz) compared to the impact of the augmentation functions itself (2-30 MHz).

Assessment of Basis Sets

As the central idea of X2C is to decouple the positive and the negative energy subspace after the introduction of a basis set, a proper assessment of various relativistic basis sets is in order. Here, we consider fully decontracted and segmented-contracted basis sets of various cardinal numbers and assess their impact on isotropic hyperfine coupling constants for 16 of the 17 transition-metal complexes. $[WOF_5]^{2-}$ is neglected in the statistical evaluation due to convergence issues for the alignment of spin x and y with the ET basis. The MAPD and STD are shown in Fig. 3.3.

First, all decontracted basis sets possess small errors—typically in the range of 1–3% in MAPD. The ANO-R basis shows the smallest mean errors with 0.37% and a standard deviation of 0.24%. Very similar errors are found for the quadruple-ζ combinations of the correlation-consistent (cc, ccJ) and the Dyall basis sets. Here, the MAPDs amount to 0.49%

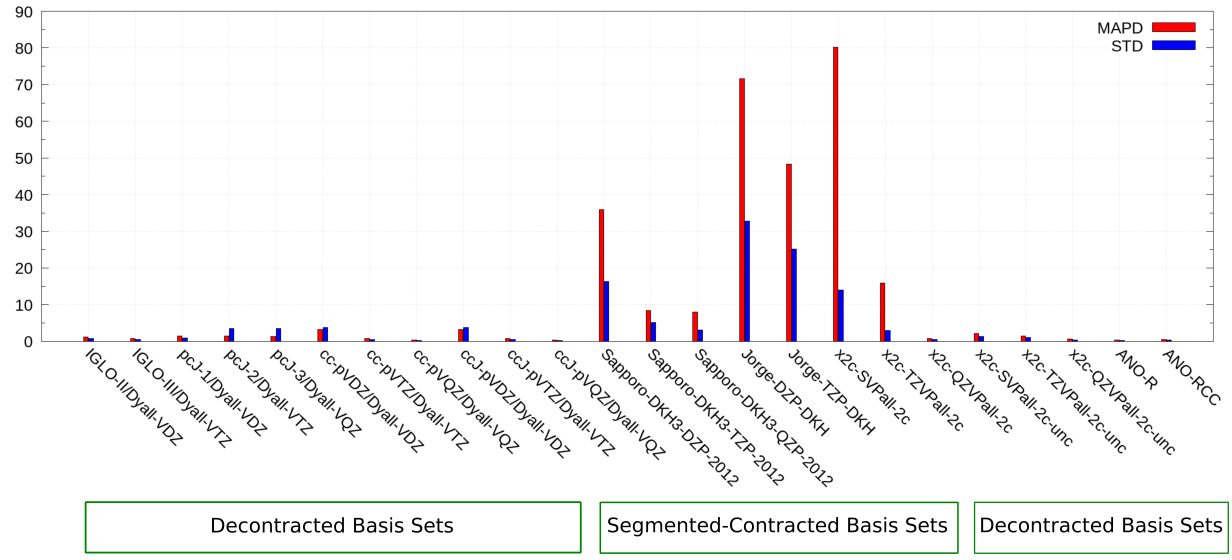

Figure 3.3: Assessment of various basis sets compared to an even-tempered reference for 16 of the 17 transition-metal complexes. $[WOF_5]^{2-}$ is neglected in the statistical evaluation due to convergence issues for the alignment of spin x and y with the ET basis. MAPD and STD denote the mean absolute percent-wise error and its standard deviation. For brevity, the suffix "unc" is omitted for the combinations of the Dyall basis and the ANO basis sets. See Tab. 3.4 for further details on the basis sets and their size.

for both combinations. However, this comes at the price of an increased dimension of the involved matrices. Even the comparably small IGLO-II/Dyall-VDZ combination features more basis functions than the segmented-contracted triple-ζ bases, see Tab. 3.4. As the different basis sets for the light atoms do not substantially affect the HFC constant of the heavy element, locally dense basis sets[322,412,413] may be used to reduce the computational demands, i.e. the large basis set is only used for the heavy element and a basis set of a decreased cardinal number is employed for the light element.

Second, the segmented-contracted double-ζ basis sets feature notably large errors. Here, the Sapporo-DKH3-DZP-2012 bases result in an MAPD of 35.93% and the Jorge-DKH-DZP or x2c-SVPall-2c bases result in MAPDs of 70.91% and 80.83%, respectively. These basis sets are thus clearly insufficient for accurate calculations of hyperfine coupling constants. Triple-ζ basis sets are a major improvement in this regard and the errors are reduced to 8–16% with the Sapporo and x2c-type bases. Notably, the Jorge-DKH-TZP basis still leads to a large MAPD of 48.56%. The quadruple-ζ Sapporo and x2c-type basis sets perform on par with the fully decontracted basis sets when comparing both the errors and number of functions. The x2c-QZVPall-2c and Sapporo-DKH3-QZP-2012 basis sets employ 8799 and 9804 functions for the 17 compounds. For the uncontracted Dyall basis sets, about 6500 (double-ζ), 9600 (triple-ζ), and 12000 (quadruple-ζ) functions are used throughout the molecular set. Decontracting the x2c-QZVPall-2c basis does not significantly alter the results, and consequently this segmented-contracted basis set is sufficiently flexible—in contrast to the double and triple-ζ basis sets. Decontracting the latter bases results in a major improvement and the MAPDs are in the same range as those of the uncontracted Dyall and ANO basis sets.

Overall, these findings confirm our previous studies for a smaller set of molecules and the scalar-relativistic approach.[342] Compared to other magnetic properties such as NMR shielding constants,[246,363] the good performance of the Sapporo basis sets is remarkable. This is further notable as these basis sets are optimized with the point charge model and fi-

nite nucleus size effects may be pronounced for the hyperfine coupling interaction of heavy elements.[18,279,414]

Assessment of Density Functional Approximations

Furthermore, we assessed the accuracy of a variety of pure, hybrid, and range-separated hybrid (RSH) density functional approximations in predicting the isotropic hyperfine coupling constants with the spin–orbit DLU-X2C Hamiltonian for a subset of 12 transition-metal complexes from the 4c study: $[MoOCl_4]^-$, $[MoOF_5]^{2-}$, $[MoOBr_5]^{2-}$, $[WOF_5]^{2-}$, $[TcNF_4]^-$, $[TcNCl_4]^-$, $[TcNBr_4]^-$, $[ReNF_4]^-$, $[ReNCl_4]^-$, $[ReNBr_4]^-$, $[ReOF_5]^-$, and $[OsOF_5]$. The resulting MAPDs and STDs when compared to experimental reference data are visualized in Fig. 3.4. Note that Harteee–Fock theory results in an MAPD of more than 100% and is clearly insufficient for these transition-metal complexes.

Unsurprisingly, pure density functionals without Hartree–Fock exchange performed the poor-

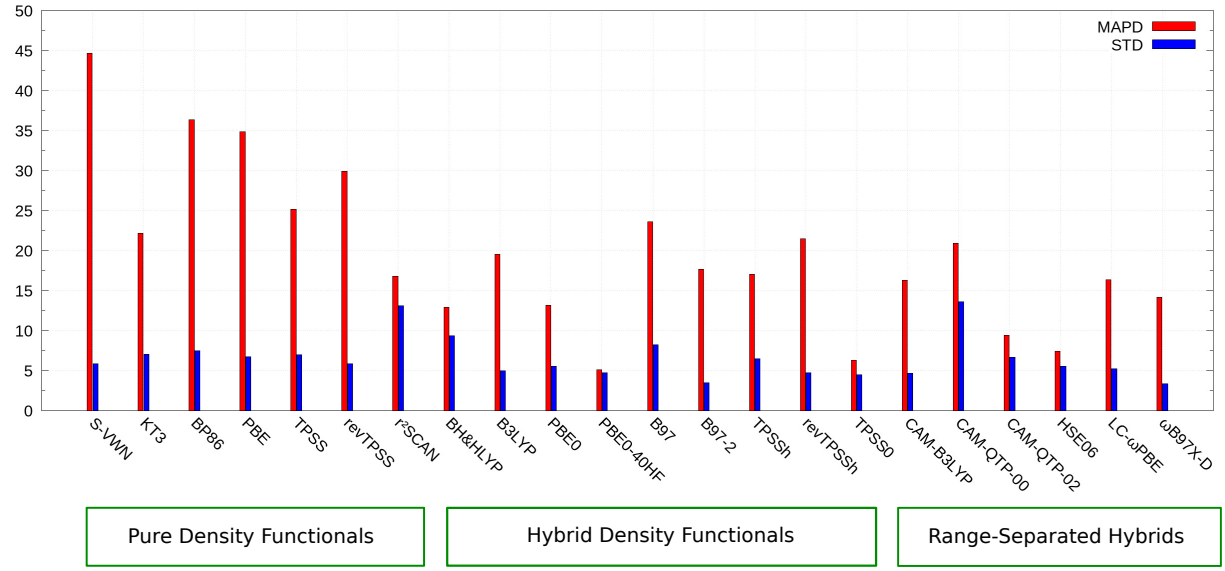

Figure 3.4: Assessment of various density functional approximations compared to the experimental findings for a subset of 12 transition-metal complexes. MAPD and STD denote the mean absolute percent-wise error and its standard deviation. Note that HF shows an MAPD and a STD of 122.10% and 55.23%, respectively. Therefore, the HF results are omitted.

est in the study, with MAPDs exceeding 20% for KT3, TPSS, PBE, BP86, and S-VWN. The r^{2}SCAN functional represents a notable exception to this with an MAPD of 16.76% and STD of 13.08%, outperforming some hybrid and RSH functionals such as B3LYP, B97, revTPSSh, and CAM-QTP-00. Despite being a hybrid, B3LYP performed rather poorly with an MAPD of 19.50%. The range-separated version CAM-B3LYP improves on this result marginally, but still falls in the latter half of functionals in ranking and is also the second worst RSH tested, with the first being CAM-QTP-00.

A clear trend that can be observed from the results is that functionals with HF exchange seemed to yield more accurate isotropic hyperfine coupling constants, which is evident in 9 of the top 10 functionals being (range-separated) hybrids. In particular, the modification of the PBE0 functional with 40% HF exchange produced the best MAPD and STD values by a considerable margin for this subset of transition metal complexes, with the next most accurate functionals being TPSS0, HSE06, and CAM-QTP-02. However, this large amount of HF exchange in PBE0-40HF may negatively affect other properties and PBE0 may be a more robust functional for general chemical properties. Interestingly, the use of a range separated over global hybrid scheme did not systematically improve the results, and the BH&HLYP and PBE0 functionals perform comparably well. These results agree with a recent functional study of magnetizabilities for 28 small molecules[415,416] and also other benchmark studies on magnetic properties[417–423] suggesting that inclusion of HF exchange is important for magnetic properties in general. These conclusions also hold for both spin–orbit DLU-X2C and previously reported ZORA results[17] for the hyperfine coupling constants of small mercury compounds.

3.3.6 Assessment of Efficiency and Further Studies

To test our implementation on a larger molecule, we study $[Pt(C_6Cl_5)_4]^-$ consisting of 45 atoms depicted in Fig. 3.5. The isotropic HFC constant and the principal components are listed in Tab. 3.6 at various levels of theory. Quasi-relativistic calculations are only performed for the hybrid functionals as the pure density functionals yield scalar-relativistic results with a comparably large deviation towards experimental findings. Note that we use the RI-J approximation in the 2c calculations to increase the efficiency of the approach. For the SCF procedure, the auxiliary basis set of the RI-J approximation needs to fit the electron density.[330,424,425] Consequently, the universal (uncontracted) x2c-type fitting bases[137,363] are a reasonable choice for the uncontracted Dyall-VTZ/pcJ-2 orbital bases. This differs significantly from the application of RI-J to post-Hartree–Fock or post-Kohn–Sham ansätze and response properties.[212,426–428] Here, the product of orbitals needs to be modeled by the auxiliary bases. Indeed, the scalar-relativistic calculations of the Dyall-VTZ/pcJ-2 basis confirmed that the RI-J approximation can be used with the universal x2c-type fitting basis sets. The errors from the RI-J approximation are smaller than those from neglecting the derivatives of $\mathbf{X}$ and $\mathbf{R}$ as well as the DLU error according to Sec. 3.3.5. The x2c-QZVPall-2c bases are combined with tailored auxiliary bases.[363]

Overall, the Dyall-VTZ/pcJ-2 and x2c-QZVPall-2c basis sets lead to similar results and a large amount of HF exchange is generally advantageous for accurate HFC constants. Spin–orbit effects are of great importance for the principal components of the HFC tensor, whereas the impact on the isotropic constant is comparably small and typically amounts to 50–100 MHz. The pure density functionals significantly underestimate the HFC constant with r^{2}SCAN again representing a notable exception. Yet, it is still outperformed by all hybrid functionals. B3LYP, PBE0, and TPSSh overestimate the HFC constant by 500–700 MHz. BH&HLYP and PBE0-40HF result in a good agreement with the experimental findings. These two functionals perform best among the global hybrids similar to Sec. 3.3.5. Also,

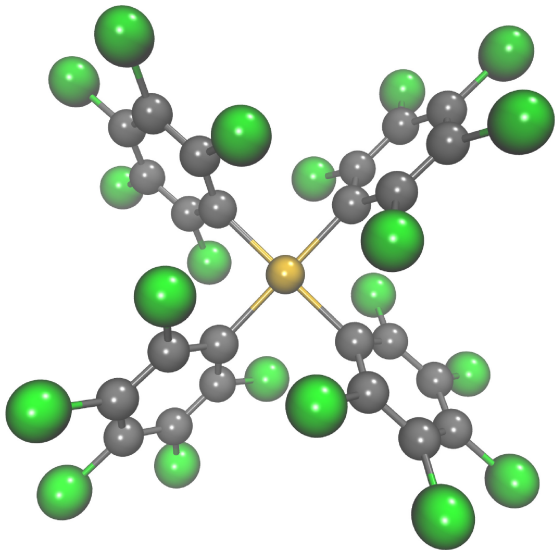

Figure 3.5: Molecular structure of $[Pt(C_6Cl_5)_4]^-$. Colors: Pt yellow, Cl green, C grey.

the range-separated functional LC-ωPBE leads to better results than the related PBE0 functional. In contrast, CAM-B3LYP does not substantially improve upon B3LYP. This confirms that range separation is not an *a priori* improvement, despite a comparably large amount of HF exchange being necessary. This suggests that more sophisticated functionals such as local hybrid functionals,[430] featuring a position-dependent admixture of HF exchange, may be useful for the HFC constant. A simple local mixing function based on the iso-orbital indicator[430] is generally not sufficient for the HFC of transition metals[431] and more elaborate approaches[417,432,433] may be helpful. A first ansatz with Johnson's local hybrid functional based on the correlation length[432] yields a scalar-relativistic HFC of 7165 MHz (Dyall-VTZ/pcJ-2 basis set, grid 3a). Note that we used the seminumerical exchange methodology for the evaluation of the respective XC terms[417] as outlined by Plessow and Weigend.[326] Similar to our recent benchmark studies of the NMR coupling constants,[417] ωB97X-D performs best for the full spin–orbit DLU-X2C, RI-J method in predicting the principal components of the hyperfine coupling constant.

We note that the 2c DLU-X2C/PBE0 calculation of one spin contribution to the HFC matrix of all atoms finished in 5.5 to 6 hours for the Dyall-VTZ/pcJ-2 basis set (79–85 SCF itera-

Table 3.6: Principal components of the hyperfine coupling constant and isotropic value in MHz for $[Pt(C_6Cl_5)_4]^-$. Scalar-relativistic (SR) calculations are carried out with the exact Coulomb integrals and the RI-J method. Two-component spin–orbit (SO) calculations only use the latter and the mSNSO approximation. Experimental (Expt.) results are taken from Ref. [429].

		Dyall-VTZ-unc/pcJ-2-unc				x2c-QZVPall-2c			
Functional	Hamiltonian	A_{iso}	A_{11}	A_{22}	A_{33}	A_{iso}	A_{11}	A_{22}	A_{33}
KT3	SR DLU	6106	5735	6255	6328	5951	5579	6089	6184
	SR DLU, RI-J	6107	5736	6255	6330	5945	5574	6083	6179
BP86	SR DLU	5317	4943	5432	5576	5193	4822	5298	5458
	SR DLU, RI-J	5316	4942	5431	5576	5192	4821	5298	5458
PBE	SR DLU	5582	5204	5715	5826	5441	5066	5564	5694
	SR DLU, RI-J	5579	5202	5712	5824	5439	5064	5561	5692
TPSS	SR DLU	6006	5626	6154	6237	5879	5500	6016	6120
	SR DLU, RI-J	6002	5622	6150	6234	5876	5497	6014	6118
r^{2}SCAN	SR DLU	8459	8238	8498	8641	8493	8277	8530	8673
	SR DLU, RI-J	8465	8245	8504	8648	8487	8269	8527	8666
BH&HLYP	SR DLU	7083	6890	7048	7311	7093	6900	7060	7320
	SR DLU, RI-J	7089	6896	7054	7317	7100	6907	7066	7326
	SO DLU, RI-J	7240	6327	7689	7705	7246	6335	7695	7707
B3LYP	SR DLU	8087	7787	8105	8367	8091	7790	8112	8369
	SR DLU, RI-J	8078	7775	8101	8357	8089	7787	8113	8367
	SO DLU, RI-J	7950	7131	8262	8456	7949	7134	8264	8450
PBE0	SR DLU	7893	7673	7851	8155	7901	7681	7860	8161
	SR DLU, RI-J	7888	7668	7846	8150	7906	7686	7866	8167
	SO DLU, RI-J	7871	7029	8257	8327	7871	7033	8259	8320
PBE0-40HF	SR DLU	7313	7129	7268	7542	7327	7143	7283	7554
	SR DLU, RI-J	7319	7136	7274	7548	7333	7150	7289	7560
	SO DLU, RI-J	7482	6590	7920	7935	7485	6595	7924	7935
TPSSh	SR DLU	8077	7819	8073	8340	8101	7844	8097	8360
	SR DLU, RI-J	8077	7817	8075	8339	8089	7826	8091	8346
	SO DLU, RI-J	8000	7283	8345	8373	8002	7291	8263	8452
TPSS0	SR DLU	7696	7493	7652	7942	7717	7515	7675	7961
	SR DLU, RI-J	7702	7500	7657	7948	7723	7522	7681	7967
	SO DLU, RI-J	7815	7018	8208	8218	7824	7029	8212	8231
CAM-B3LYP	SR DLU	7803	7546	7754	8109	7811	7555	7763	8115
	SR DLU, RI-J	7808	7552	7759	8114	7816	7560	7769	8121
	SO DLU, RI-J	7696	6800	8104	8184	7699	6802	8106	8189
CAM-QTP-00	SR DLU	6648	6465	6611	6868	6657	6475	6621	6876
	SR DLU, RI-J	6654	6471	6618	6874	6664	6482	6628	6883
	SO DLU, RI-J	6909	5951	7375	7400	6916	5960	7382	7406
CAM-QTP-02	SR DLU	7141	6905	7090	7429	7148	6912	7098	7435
	SR DLU, RI-J	7147	6912	7096	7435	7155	6919	7104	7441
	SO DLU, RI-J	7178	6219	7629	7685	7177	6222	7632	7677
HSE06	SR DLU	7749	7520	7715	8011	7757	7529	7726	8018
	SR DLU, RI-J	7752	7522	7720	8014	7762	7533	7731	8023
	SO DLU, RI-J	7720	6905	8089	8166	7722	6908	8089	8168
LC-ωPBE	SR DLU	7315	7099	7231	7615	7319	7103	7236	7618
	SR DLU, RI-J	7321	7105	7237	7621	7325	7109	7243	7624
	SO DLU, RI-J	7438	6548	7872	7894	7435	6546	7869	7889
ωB97X-D	SR DLU	7196	6930	7169	7488	7194	6927	7168	7485
	SR DLU, RI-J	7201	6935	7175	7494	7200	6933	7174	7491
	SO DLU, RI-J	7270	6421	7639	7749	7265	6419	7634	7742
Expt.		7322	6375	7735	7855	7322	6375	7735	7855

tions based on converged UKS orbitals) on 24 OpenMP threads of an Intel® Xeon® Gold 6212U CPU @ 2.40 GHz (code was compiled with Intel® Fortran Compiler 19.0.1.144). For

the x2c-QZVPall-2c bases, the calculations take 18.5 to 24.5 hours (70–103 SCF iterations). For comparison, the wall time with 12 OpenMP threads amounts to 26.5 to 41.9 hours for 64–106 SCF iterations. The calculation of the respective derivatives of the one-electron Hamiltonian for the HFC matrix of all atoms amounts to 15.4 minutes and 41.7 minutes for Dyall-VTZ/pcJ-2 and x2c-QZVPall-2c with the DLU scheme (24 threads). In comparison, the full X2C ansatz takes 630 minutes and 1851 minutes, respectively. Hence, the speed-up by the DLU scheme amounts to a factor of 41 and 44. Further speed-ups are possible by selecting the corresponding nuclei of interest similar to NMR coupling constants[290,322] and NMR chemical shifts.[422] This way the wall time for the DLU-X2C Hamiltonian derivatives is reduced to 0.3 (Dyall-VTZ/pcJ-2) and 0.9 minutes (x2c-QZVPall-2c); a speed-up by a factor of about 45–50 is observed, while the maximum errors for the principal components amount to only 2.0 MHz and 4.0 MHz, respectively. The errors for the isotropic HFC constant are 0.7 MHz and 0.4 MHz. Thus, the efficiency of our implementation is clearly demonstrated and the derivatives of the decoupling can routinely be included in DLU-X2C calculations. The computation time is clearly determined by the two-electron integrals in line with previous DLU studies.[130,133,288,290] Application of the MARI-J approximation[332] and the seminumerical exchange approximation[326,327] reduces the time for the two-electron integrals. However, it increases the number of SCF iterations for the Dyall-VTZ/pcJ-2 basis set from 79–85 to 82–130. The wall time amounts to 4.5–6.9 hours while changing the isotropic HFC constant by −5 MHz.

3.3.7 Application to Rare-Earth Single Molecule Magnets

Recently, the discovery of a series of La(II) and Lu(II)-based single molecule magnets: $[La(OAr^*)_3]^-$ **(1)**, $[Lu(NR_2)_3]^-$ **(2)**, and $[Lu(OAr^*)_3]^-$ **(3)** (OAr^* = 2,6-Ad_2-4-t-Bu-C_6H_2O, Ad = adamantyl, t-Bu= tert-butyl, R = $SiMe_3$ with Me = methyl) was reported.[14] The three molecules are depicted in Fig. 3.6. It was demonstrated in Section 3.2 through EPR

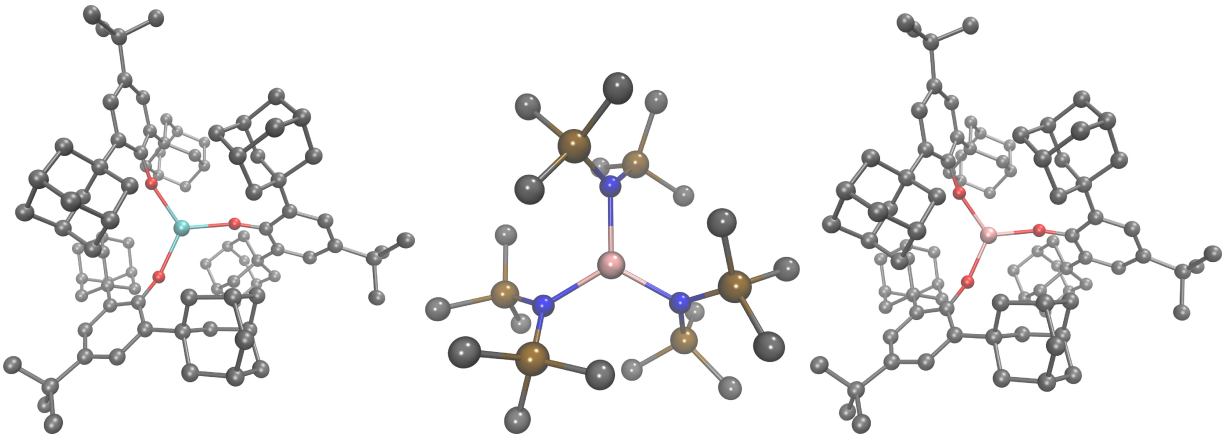

Figure 3.6: Molecular structures of $[La(OAr^*)_3]^-$ **(1)** (left), $[Lu(NR_2)_3]^-$ **(2)** (middle), and $[Lu(OAr^*)_3]^-$ **(3)** (right), OAr^* = 2,6-Ad_2-4-t-Bu-C_6H_2O, Ad = adamantyl, t-Bu= tert-butyl, R = $SiMe_3$ with Me = methyl. H atoms are omitted for clarity. Colors: La cyan, O red, C grey, Lu pink, N blue, Si brown.

and KS-DFT studies that variation of the *s*-orbital mixing present in the $6s/d$ SOMO of these complexes could be used to tune their magnetic structure, with $[Lu(OAr^*)_3]^-$ representing a desirable orbital configuration through its possession of a significant hyperfine clock transition of approximately 9 GHz and its enhanced magnetic relaxation times.

The scalar-relativistic DFT method used to approximate the hyperfine coupling matrix in this study qualitatively described the expected increase in isotropic hyperfine coupling constant with larger $6s$ character of the SOMO (arising from the Fermi-contact interaction). However, the values themselves possessed errors of roughly one order of magnitude when compared with experimental results, mostly attributed to the non-relativistic operator used to calculate the HFC matrix giving rise to a large picture-change error.[266] Herein, this method will be denoted SR-NR-DFT. While such a method proved useful when paired with experiment, improvements which can achieve quantitative accuracy are desired if *in silico* discovery of optimal SMMs is to be realized.

To assess the potential improvement obtained from the present method, we applied our DFT-based X2C approach to compute the hyperfine coupling matrix for **(1)**, **(2)**, and **(3)**, comparing with the SR-NR-DFT and experimentally determined EPR results. For direct

comparison, the same computational methodology[14] was used between the SR-NR-DFT and X2C calculations: The TPSS density functional[211] was used with all-electron NMR-tailored x2c-TZVPPall-s basis sets for the lanthanide atom (Ln) and x2c-SVPall-s basis sets for the ligand atoms.[246] In addition to the parent x2c-type basis sets, these feature additional tight p functions and minimal extension for the outer-core and inner valence region. The finite nucleus model and DLU were used for both scalar-relativistic (SR) and spin–orbit (SO) X2C calculations. These calculations were also repeated for the spin–orbit 2c extensions of the x2c-type basis sets[137] (x2c-TZVPPall-2c/Ln and x2c-SVPall-2c/H,C,N,O,Si). We also repeated the calculations using the r^{2}SCAN,[378,379] PBE0,[350,351] PBE0-40HF,[280,350,351] CAM-QTP-02,[389] HSE06,[390–392] and the ωB97X-D[394] functionals given the improvements we observed above with the r^{2}SCAN and hybrid functionals. Lastly, we performed calculations using the x2c-QZVPall-2c basis set for the Ln atoms[363] to assess the accuracy of the method. The results are given in Tab. 3.7.

Modest improvements are observed when going from the x2c-s to x2c-2c type basis sets on the Ln atom for the SO methods, and also when using a hybrid or RSH as opposed to a pure functional. Here, the triple-ζ basis sets are already sufficient for the SO calculations as the application of the x2c-QZVPall-2c basis alters the HFC constants by about 20–30 MHz. Larger changes of up to 150 MHz are found in the SR calculations. r^{2}SCAN again outperforms TPSS which is consistent with the findings of Sections 3.3.5 and 3.3.6. In some cases, the SR results for different basis set and functional configurations are closer to experiment than the SO results (e.g. x2c-TZVPPall-2c/PBE0-40HF), which is likely due to error cancellation. This can be posited from the inconsistent corrections in the SR results when going from pure to hybrid and RSH functionals, in contrast with a smoother convergence of the SO method. The PBE0-40HF and RSH functionals tested with x2c-TZVPPall-2c basis set perform similarly well when compared to experiment. The x2c-QZVPall-2c/ωB97X-D configuration yields accurate results for both the SO and SR methods in all three compounds. For SO in particular, deviations from experiment are lowered to tens of MHz or less. Overall,

Table 3.7: Hyperfine coupling constants calculated for the Ln(II)-based single molecule magnets $[La(OAr^*)_3]^-$ **(1)**, $[Lu(NR_2)_3]^-$ **(2)**, and $[Lu(OAr^*)_3]^-$ **(3)** at various levels of theory and compared with experimental results (Expt.).[14] See also Fig. 3.6. For brevity, only the basis set of the Ln atom is given here. The x2c-SVPall-s and x2c-SVPall-2c basis set is employed for the light elements. The SR-NR results are taken from Ref. [14]. All values are given in MHz.

Method	Hamiltonian	**(1)**	**(2)**	**(3)**
x2c-TZVPPall-s/TPSS	SR-NR	8274	17 040	23 950
	SR	1746	2259	3192
	SO	1716	2227	3139
x2c-TZVPPall-2c/TPSS	SR	1747	2258	3177
	SO	1726	2236	3151
x2c-QZVPall-2c/TPSS	SR	1746	2239	3168
	SO	1724	2212	3139
x2c-TZVPPall-2c/r^{2}SCAN	SR	1777	2372	3248
	SO	1749	2322	3202
x2c-QZVPall-2c/r^{2}SCAN	SR	1779	2375	3259
	SO	1750	2323	3211
x2c-TZVPPall-2c/PBE0	SR	1756	2270	3194
	SO	1804	2241	3241
x2c-QZVPall-2c/PBE0	SR	1839	2266	3266
	SO	1823	2235	3252
x2c-TZVPPall-2c/PBE0-40HF	SR	1843	2271	3300
	SO	1809	2243	3261
x2c-QZVPall-2c/PBE0-40HF	SR	1889	2355	3445
	SO	1837	2233	3277
x2c-TZVPPall-2c/CAM-QTP-02	SR	2080	2504	3499
	SO	2040	2464	3459
x2c-QZVPall-2c/CAM-QTP-02	SR	2100	2495	3499
	SO	2074	2463	3471
x2c-TZVPPall-2c/HSE06	SR	1824	2297	3291
	SO	1795	2262	3249
x2c-QZVPall-2c/HSE06	SR	1838	2283	3290
	SO	1817	2257	3260
x2c-TZVPPall-2c/ωB97X-D	SR	1901	2411	3501
	SO	1870	2378	3459
x2c-QZVPall-2c/ωB97X-D	SR	1929	2489	3655
	SO	1867	2359	3472
Expt.		1840 ± 25	2443 ± 50	3467 ± 50

the results demonstrate that the use of a relativistic hyperfine "contact" operator with finite nucleus corrects the majority of the picture-change error observed in SR-NR-DFT for these complexes.

Calculation of the spin–orbit DLU-X2C Hamiltonian derivatives for the x2c/TZVPPall-2c/TPSS calculations took roughly two minutes for **(1)** and **(3)** (ca. 2000 basis functions) and 16 seconds for **(2)** (ca. 800 basis functions) using 16 OpenMP threads of an Intel® Xeon® Gold 6148 CPU @ 2.40 GHz. In comparison, the derivatives took twenty minutes for **(1)** and **(3)** and two minutes for **(2)** without DLU. The differences in isotropic hyperfine coupling constants predicted with and without DLU constitute less than 0.1 % error introduced in all cases. On average, 10–20 SCF iterations were needed for the SO calculations based on converged UKS orbitals for x2c-TZVPPall-s/TPSS and x2c-TZVPPall-2c/TPSS, whereas approximately 40–60 SCF iterations were needed for x2c-TZVPPall-2c/PBE0 and x2c-QZVPall-2c/ωB97X-D.

3.3.8 Application to $[TbPc_2]^-$ with $S = 3$

So far, we have considered molecular systems with one unpaired electron, that is $S = 1/2$. However, the Kramers-unrestricted non-collinear method is straightforwardly applicable to systems with more than one unpaired electron.[271] To illustrate this feature of our implementation, we apply the mSNSO-DLU-X2C approach to $[TbPc_2]^-$, a single molecule magnet with six unpaired electrons. This system is notable for its large hyperfine coupling arising from strong magnetic anisotropy along the easy axis. Furthermore, its valence structure differs significantly from the Ln complexes studied in Sec. 3.3.7, where the spin density arises purely from the $4f$ shell as opposed to the $5d/6s$ orbital. The molecular structure is depicted in Fig. 3.7. Note that the electronic ground-state of $[TbPc_2]^-$ is well separated from the excited states.[260]

To study the HFC constant, we use the same methods as in the previous section. That is, the TPSS,[211] r^{2}SCAN,[378,379] PBE0,[350,351] PBE0-40HF,[280,350,351] CAM-QTP-02,[389] HSE06,[390–392] and the ωB97X-D[394] functionals are employed. The x2c-TZVPPall-2c basis set is used for Tb and the x2c-SVPall-2c basis set for all other atoms.[137] This basis set setup is motivated by the results observed in the last section. The isotropic hyperfine coupling constants calculated at the DFT level are given in Tab. 3.8.

Generally, the scalar-relativistic ansatz is not able to deliver accurate results, as it considers only the Fermi-contact and the spin-dipole contribution. For systems such as $[TbPc_2]^-$ with $S = 3$, the paramagnetic spin–orbit term is the leading contribution, and the Fermi contact term is minimal due to the primarily $4f$ valence structure.[260] Therefore, our SR results are almost universally off by a few hundred MHz, and the error is greater than that observed for the La and Lu complexes in Sec. 3.3.7. In comparison, the two-component calculations result in good agreement with the experimental findings due to inclusion of this spin–orbit term. Similar to the previous sections, PBE0-HF and ωB97X-D perform remarkably well. In contrast, CAM-QTP-02 and HSE06 lose some ground for $[TbPc_2]^-$. r^{2}SCAN is a notable exception for the scalar-relativistic results. This finding is likely caused by error cancellation as the PSO term and spin–orbit effects are pronounced for $[TbPc_2]^-$ in all calculations herein

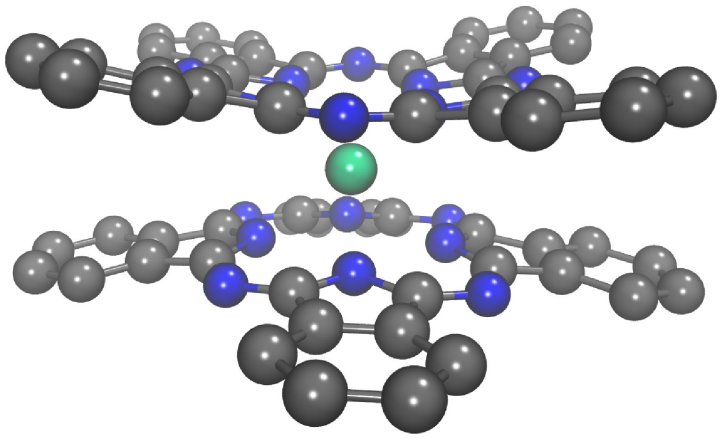

Figure 3.7: Molecular structure of $[TbPc_2]^-$. Pc denotes bis(phthalocyaninato). H atoms are omitted for clarity. Colors: Tb green, N blue, C grey.

Table 3.8: Isotropic hyperfine coupling constant for $[TbPc_2]^-$ with the scalar-relativistic (SR) and the spin–orbit (SO) DLU-X2C Hamiltonian. The latter uses the mSNSO approximation. For brevity, only the basis set of the Tb is given here. The x2c-SVPall-2c basis set is employed for the light elements. Experimental results (Expt.) are taken from Refs. [434] and [435], see footnotes. All values are given in MHz.

Functional	Basis Set	SR	SO
TPSS	x2c-TZVPPall-2c	189.2	352.4
r^2SCAN	x2c-TZVPPall-2c	519.0	613.3
PBE0	x2c-TZVPPall-2c	52.0	440.1
PBE0-40HF	x2c-TZVPPall-2c	26.4	510.5
CAM-QTP-02	x2c-TZVPPall-2c	−4.0	445.7
HSE06	x2c-TZVPPall-2c	55.0	442.7
ωB97X-D	x2c-TZVPPall-2c	135.9	488.0
Expt.		519[a]	
Expt.		556[a]	

[a] Result taken from Ref. [434]
[b] Result taken from Ref. [435]

and in the literature.[260]

The accuracy of our DFT-based X2C approach is on par with the multi-configurational ansatz by Wysocki and Park employing spin–orbit mean-field operators in scalar-relativistic low-order DKH.[260] They obtained a HFC constant of ca. 6000 MHz with an effective pseudospin Hamiltonian of $S = 1/2$ and consequently mapping this for $[TbPc_2]^-$ with $S = 3$ results in 500 MHz. This shows that a sophisticated treatment of relativistic effects can be combined with DFT for lanthanide molecules beyond Kramers doublets if the electronic ground state is sufficiently separated from the excited states.

3.3.9 Summary

An efficient implementation of the HFC matrix calculations in the quasi-relativistic (X2C) framework including the full spin–orbit X2C derivative and DLU has been reported. The method supports point and finite nucleus models for the scalar and vector potentials, is fully

integral direct, and all integrals and algebraic manipulations are parallelized using OpenMP. The hyperfine coupling matrix can be computed in a "black-box" fashion in the non-collinear approach through incorporation of post-processing scripts into the TURBOMOLE program suite.

Comparisons between the DKS level and the X2C/DLU-X2C ansatz including mSNSO were carried out for 17 transition-metal compounds. The X2C calculations reproduce the DKS results well in each case for lower formal cost, and is further accelerated by the DLU scheme, which was found to introduce errors of just ca. 0.1 MHz. Inclusion of the full X2C Hamiltonian derivative led to corrections in the range of 1–3 MHz in the HFC, which did not always bring the result closer to that of the DKS method. The worsening is likely due to the loss of error cancellation from neglecting the $\mathbf{X}$ and $\mathbf{R}$ derivatives, and may be amended through rigorous treatment of two-electron picture-change effects. When used with DLU, these derivatives do not contribute significantly to computational overhead, which is dominated by the two-electron integral calculations.

In addition, an extensive study of general parameters, such as relativistic basis set and density functional approximation was conducted. The segmented-contracted x2c-QZVPall-2c basis set was found to represent a balanced choice for both accuracy of hyperfine coupling constant and computational cost, performing similarly to its uncontracted version. Other segmented-contracted bases, such as the Sapporo and Jorge bases, expectedly performed better with increasing cardinal number, but were inferior to x2c-QZVPall-2c and all uncontracted basis sets studied. In line with prior observations, Hartree–Fock exchange was found to be critical for accurate calculations of hyperfine coupling constants for the 12 transition-metal complexes studied in the DFA analysis. With the exception of r^{2}SCAN, global hybrid and range-separated hybrid functionals performed better in general than pure functionals when compared with experiment. CAM-QTP-02 and ωB97X-D show the smallest deviations from the experimental findings among the range-separated hybrids. However, range-separated

hybrid functionals were not necessarily better than global hybrids, and common functionals such as PBE0 and TPSSh (ranked 6 and 10 out of the 22 studied) can be used without a significant compromise to accuracy.

mSNSO-DLU-X2C calculations were also performed on the Pt complex $[Pt(C_6Cl_5)_4]^-$, which echoed the necessity of including Hartree–Fock exchange in the density functional approximation used for accurate HFC matrix calculations. Furthermore, these calculations demonstrated the substantial speedup achieved by application of DLU on X2C Hamiltonian derivatives, reducing the computation time from 1851 minutes to 41.7 minutes for the Pt complex at the x2c-QZVPall-2c level (3003 contracted and 4720 primitive basis functions) using 24 threads on an Intel® Xeon® Gold 6212U CPU @ 2.40 GHz.

We then applied the method to compute the hyperfine coupling constants for a series of three recently discovered Ln(II) single molecule magnets $[La(OAr^*)_3]^-$, $[Lu(NR_2)_3]^-$, and $[Lu(OAr^*)_3]^-$ with magnetic structure conducive to facilitating clock transitions. The results dramatically correct previously obtained isotropic hyperfine coupling constants using scalar-relativistic density functional theory and a non-relativistic Fermi-contact expression, bringing the error down from thousands to tens of MHz when compared with experimental results. As demonstrated in this study, the non-relativistic HFC operator is insufficient for heavy atoms with valence orbitals of low angular momentum and large spin density near the nucleus. As this specific property is largely responsible for the desirable magnetic structure of this series, our results reaffirm the observation that efficient, "fully" relativistic or quasi-relativistic ansätze are necessary to accurately describe the magnetic structure of candidate molecular qubit systems. Notably, the segmented-contracted triple-ζ x2c-TZVPPall-2c basis sets can be used for the lanthanide atom without a significant compromise to accuracy. The PBE0-40HF, CAM-QTP-02, and ωB97X-D functionals also perform well for the three Ln(II) single molecule magnets. In contrast to the transition-metal complexes, the pure density functionals already yield very reasonable results for these molecules.

The general applicability of the Kramers-unrestricted non-collinear ansatz is finally demonstrated for $[TbPc_2]^-$ with six unpaired electrons. Here, the scalar-relativistic X2C Hamiltonian is clearly insufficient as the paramagnetic spin–orbit contribution is the leading term, and consequently a quasi-relativistic spin–orbit approach is needed for accurate results. The PBE0-40HF and ωB97X-D functionals lead to an isotropic hyperfine coupling constant of 508 MHz and 484 MHz, respectively. This is in remarkably good agreement with the experimentally obtained result of 519 MHz,[434] and our results are on par with existing multiconfigurational methods.[260]

The implementations of the HFC matrix and NMR shifts in the X2C framework can be used to calculate the EPR g-tensors; the specific methodology and working equations will be elaborated on in the following Section.

3.4 Quasi-Relativistic Calculation of EPR g-Tensors with Derivatives of the Decoupling Transformation, Gauge-Including Atomic Orbitals, and Magnetic Balance

3.4.1 Introduction

EPR spectroscopy is an essential experimental tool for the study of open-shell systems, especially those containing transition-metal and lanthanide elements. The EPR spectrum consists of two important parameters: (1) the g-tensor, used to indicate the shift relative to the free electron g-factor, and (2) the hyperfine coupling constant. To assist in the understanding and interpretation of the experimental findings, quantum chemical studies are often

employed to predict these quantities from first principles.[264,436–441] For example, predictions of EPR parameters from theory have helped to investigate the electronic origin of hyperfine clock transitions,[14] as well as validate trends in magnetic anisotropy orientations,[442] for distinct classes of lanthanide SMMs. These parameters can be compared to those extracted from experimental spectra, which is carried out through fitting the data to an effective spin Hamiltonian.[443]

From a theoretical point of view, the g-tensor is intrinsically relativistic, and the accurate description of spin–orbit coupling is thus extremely important for this property. Keystone methods used in relativistic quantum chemistry to study the g-tensor[102,103,265–267,269,270,282,444,445] include the zeroth-order regular approximation (ZORA),[275–277,292,446–448] the two-component (2c) Douglas–Kroll–Hess (DKH) ansatz[272–274] by Malkin *et al.*,[271] and the fully-relativistic four-component (4c) Dirac–Kohn–Sham theory by Komorovsky and co-workers.[280,293,449,450] The latter is undoubtedly the most accurate relativistic treatment. However, it also leads to considerable computational costs compared to the quasi-relativistic two-component ansätze. In addition to DFT, wavefunction-based approaches at the perturbation theory, coupled cluster, and configuration interaction level have also been reported.[451–453] Today, both ZORA and DKH, as well as other approximate quasi-relativistic Hamiltonians, are superseded by (one-electron) X2C theory[114–120] in many quantum chemistry program suites due to its formal advancements in implementing the relativistic decoupling transformation.[134,343,454–461] Furthermore, the application of analytical derivative theory[284,287] to X2C is straightforward compared to the more involved formulation in DKH.[462,463] Complete analytical derivatives of the X2C Hamiltonian are available for geometry derivatives,[127,133,283,285,311,464,465] electric properties,[128,286,466,467] and various magnetic properties.[15,288,290,294,306–308,342,468–470]

X2C has previously been applied to the study of EPR parameters by the groups of Autschbach[19,281] and Kaupp.[129] These studies interestingly neglect the derivatives of the relativistic decoupling transformation, claiming that such contributions are small. While we have re-

cently demonstrated that these additional derivative terms do not significantly impact the hyperfine coupling constants predicted with X2C theory,[15] the importance of these terms for obtaining accurate g-tensors is as of yet unexplored.

Moreover, Ref. [129] uses a restricted kinetic balance (RKB) condition[105] and a common gauge origin (CGO) to calculate the g-tensor. Autschbach noted that the RKB condition should be formally generalized to the restricted magnetic balance (RMB) condition[305] for EPR properties,[19,281] i.e. the vector potential needs to be included in the basis set expansion of the small component. However, the RKB condition is generally sufficient to recover the non-relativistic limit for first-order derivatives. The g-tensor is commonly obtained with spin–orbit perturbation theory in one-component approaches.[447,448,471–478] Here, the inclusion of the vector potential in the Pauli spin–orbit operator leads to the relativistic mass or Pauli kinetic energy correction and the diamagnetic or gauge correction.[447,471] Therefore, using RMB ensures that the two-component approach is directly comparable to the perturbative ansatz. Whereas the use of RMB leads to problematic integrals for the HFC constant and the related NMR coupling constants in X2C,[294] the integrals can be evaluated straightforwardly for magnetic field derivatives.[288,306–308] Thus, the RMB can be used for EPR g-tensors similar to NMR shieldings[288,306–308] and magnetic circular dichroism.[309]

A common gauge origin has been used in both X2C[129] and 4c[280,293,449,450] calculations of the g-tensor so far. Formally, the g-tensor depends on the chosen gauge origin in finite basis set calculations.[479] Consequently, the so-called gauge-including atomic orbitals[480,481] (GIAOs) should be employed to remove the gauge-origin dependence. This issue is of great importance for NMR shielding constants, and GIAOs are thus routinely included in their relativistic calculation.[288,306–308,482–490] In contrast to NMR shieldings, the g-tensor is a global property of the full molecule, and the gauge-origin dependence is less pronounced.[478,491,492] However, it was shown that a common gauge origin is insufficient for molecules featuring several separated spin centers or a non-local spin density distribution.[476] Therefore, GIAOs

are often employed in one-component calculations[447,448,471–478] and their use in relativistic two-component calculations is also desirable. For instance, a two-component gauge-origin invariant ZORA ansatz was implemented by Verma and Autschbach.[292]

In light of the above, our present work extends the existing X2C framework for the calculation of g-tensors in four distinct aspects. First, the derivatives of the unitary decoupling transformation are explicitly incorporated to evaluate the complete derivative of the X2C Hamiltonian with respect to the magnetic field. Second, we employ the RMB condition[305]. Third, we use GIAOs[480,481] for the basis set expansion. Fourth, the diagonal local approximation to the unitary decoupling transformation[132] (DLU) is introduced for g-tensors to accelerate solution of the one-electron X2C response equations for the decoupling derivatives, which is important for routine calculations of large molecules and metal clusters.[130,131,493–499]

In order to test this new X2C methodology, we perform extensive benchmarking of the relativistic Hamiltonian, basis set, and density functional approximation for a series of 17 transition-metal complexes. The impact of including the derivatives of the unitary decoupling transformation on the accuracy of the g-tensor is assessed through comparison to 4c results. The errors observed between the RKB-CGO, RMB-CGO, and RMB-GIAO formalisms are also compared to investigate the importance of the magnetic balance condition and GIAOs. This is further evaluated by investigating the gauge-dependence of $[(C_5Me_5)_2Y(\mu\text{-}S)_2Mo(\mu\text{-}S)_2Y(C_5Me_5)_2]^-$, which exhibits spin delocalization across the three metal atoms. These errors are discussed in the context of those arising from other approximations of the current X2C method, such as DLU. From these results, we identify a set of computational parameters that yield robust and efficient predictions of g-tensors, and apply them to the study of $[Pt(C_6Cl_5)_4]^-$ and a set of three Ln-based complexes. In doing so, we demonstrate the suitability of our method to characterizing systems of great interest to quantum information science and molecular magnetism.

3.4.2 Theory

Notation

We use the same notation as in our previous work on the HFC constant in Section 3.3. L and S refer to the large and small components, respectively. The subscripts $-$ and $+$ indicate the states of the negative- and positive-energy subspaces, respectively, which are commonly called positronic and electronic states. $\mathbb{M}$ denotes a matrix in the 4c space, while matrices in the space of spin-free one-component (1c) basis functions $\{\lambda_\mu\}$ are indicated as $\boldsymbol{M}$ and matrices in the 2c space ($\{\phi_\mu\} = \{\lambda_\mu\} \otimes \{\alpha, \beta\}$) are indicated as $\mathbf{M}$. Cartesian coordinates are denoted with the subscripts u, v while the superscript B indicates derivatives according to

$$\mathbf{h}_u^B = \left(\frac{\mathrm{d}\mathbf{h}}{\mathrm{d}B_u}\right)_{B_u=0} \tag{3.47}$$

We use Gaussian-based atomic units throughout this work.

Definition of the EPR g-Tensor

We use the approach of Malkin *et al.* for the relativistic g-tensor[271,449]

$$g_{uv} = \left.\frac{\mathrm{d}^2 E}{\mathrm{d}B_u \mathrm{d}S_v}\right|_{\vec{B}=0} = \frac{2c}{\langle \tilde{S}_v \rangle} \left.\frac{\mathrm{d}E(J_v, \vec{B})}{\mathrm{d}B_u}\right|_{\vec{B}=0} \tag{3.48}$$

with the external magnetic field $\vec{B}$ and the effective spin $\tilde{\vec{S}}$. The energy is calculated with the non-collinear approach,[500] where the magnetization vector $\vec{J}$ and the spin $\vec{S}$ are aligned along three orthogonal axes v.[501] The effective spin is determined by the configuration of the electronic ground state, and converged orbitals of a 1c calculation are needed to ensure a good starting point. The non-collinear formalism includes spin polarization and is straightforwardly applicable beyond Kramers doublets.[271] This approach differs from that of Verma

and Autschbach, who use a generalized collinear ansatz with a chosen spin quantization to calculate the EPR g-tensor[292] and the HFC tensor[17] in a ZORA framework.

X2C Hamiltonian in the Presence of a Magnetic Field

Magnetic perturbations are introduced into the Dirac equation with the principle of minimal coupling or minimal substitution.[295] The linear momentum operator $\hat{\vec{p}}$ is generalized to $\hat{\vec{\pi}}$ according to

$$\hat{\vec{p}} \longrightarrow \hat{\vec{\pi}} = \hat{\vec{p}} + \frac{1}{c}\hat{\vec{\mathcal{A}}} \tag{3.49}$$

where $\hat{\vec{\mathcal{A}}}$ denotes the vector potential. For g-tensors, the vector potential of a static and homogeneous external magnetic field reads

$$\vec{\mathcal{A}}_O(\vec{r}) = \frac{1}{2}\vec{B} \times \vec{r}_O \tag{3.50}$$

$$\vec{r}_O = \vec{r} - \vec{R}_O \tag{3.51}$$

$\vec{R}_O$ refers to the gauge origin, which bears no physical meaning and the obtained molecular properties should be gauge-origin independent. Therefore, field-dependent basis functions, the so-called gauge-including atomic orbitals or London orbitals, are introduced[480,481]

$$\lambda_\mu\left(\vec{B},\vec{r}\right) = \exp\left(-\mathrm{i}\Lambda_{\mu O}\right)\lambda_\mu\left(\vec{r}\right) \tag{3.52}$$

$$\Lambda_{\mu O}\left(\vec{B},\vec{r}\right) = \frac{1}{2c}(\vec{R}_{\mu O} \times \vec{r}) \cdot \vec{B} \tag{3.53}$$

Here, a (real) field-independent basis function λ_μ is augmented by a complex phase prefactor. We use the notation $\vec{R}_{\mu O} = \vec{R}_\mu - \vec{R}_O$, where $\vec{R}_\mu$ denotes the atom center of the respective basis function. Note that we use the Coulomb gauge in this work.

The basis set expansion of the respective one-electron Dirac–Hamilton operator using the

restricted magnetic balance condition reads[305]

$$\left|\psi_i^{\mathrm{L}}\right\rangle = \sum_{\mu} C_{\mu i}^{\mathrm{L}}\, e^{-\mathrm{i}\Lambda_{\mu O}} \left|\phi_\mu\right\rangle \tag{3.54}$$

$$\left|\psi_i^{\mathrm{S}}\right\rangle = \sum_{\mu} C_{\mu i}^{\mathrm{S}}\, e^{-\mathrm{i}\Lambda_{\mu O}} \frac{1}{2c}\vec{\sigma}\cdot\left(\hat{\vec{p}} + \frac{1}{c}\hat{\vec{\mathcal{A}}}_\mu\right)\left|\phi_\mu\right\rangle \tag{3.55}$$

where we used the identities of Ref. [305] to move the GIAO prefactor to the left of the generalized momentum in Eq. 3.55. Due to the use of GIAOs, the basis functions are already field-dependent. Therefore, the RMB can be introduced straightforwardly with no additional complexities. Matters are different for the hyperfine coupling constant, for which the dependence of basis functions on the vector potential solely arises through RMB.[19,281,470] Moreover, the g-tensor and HFC tensor can be used to compute the Fermi-contact and pseudo-contact contribution for pNMR shielding constants.[278,502,503]

The orbital contribution of pNMR or closed-shell NMR shielding constants are typically calculated within a magnetic balance based on the external magnetic field as RMB restores the bilinear terms in the vector potential.[288,306–308,342] Therefore, Eq. 3.55 ensures consistency of the NMR and EPR properties.

This basis set expansion results in the Dirac equation in a matrix representation according to[288,306–308]

$$\begin{pmatrix} \mathbf{V} & \mathbf{\Pi}^\dagger \\ \mathbf{\Pi} & (\frac{1}{4c^2}\mathbf{W} - \mathbf{T}) \end{pmatrix} \begin{pmatrix} \mathbf{C}_-^{\mathrm{L}} & \mathbf{C}_+^{\mathrm{L}} \\ \mathbf{C}_-^{\mathrm{S}} & \mathbf{C}_+^{\mathrm{S}} \end{pmatrix} = \begin{pmatrix} \mathbf{S} & \mathbf{0}_2 \\ \mathbf{0}_2 & \frac{1}{2c^2}\mathbf{T} \end{pmatrix} \begin{pmatrix} \mathbf{C}_-^{\mathrm{L}} & \mathbf{C}_+^{\mathrm{L}} \\ \mathbf{C}_-^{\mathrm{S}} & \mathbf{C}_+^{\mathrm{S}} \end{pmatrix} \begin{pmatrix} \boldsymbol{\epsilon}_- & \mathbf{0}_2 \\ \mathbf{0}_2 & \boldsymbol{\epsilon}_+ \end{pmatrix} \tag{3.56}$$

with the Dirac matrix $\mathbb{D}$ and the metric $\mathbb{M}$ on the left-hand and right-hand side. The overlap matrix $\mathbf{S}$ and the potential matrix $\mathbf{V}$ are well known from non-relativistic quantum

chemistry. These matrices are block-diagonal in the (2×2) superspace and are given by

$$\mathbf{S} = \begin{pmatrix} \boldsymbol{S} & 0 \\ 0 & \boldsymbol{S} \end{pmatrix}, \boldsymbol{S}_{\mu\nu} = \langle \lambda_\mu | e^{i\Lambda_{\mu\nu}} | \lambda_\nu \rangle \tag{3.57}$$

$$\mathbf{V} = \begin{pmatrix} \boldsymbol{V} & 0 \\ 0 & \boldsymbol{V} \end{pmatrix}, \boldsymbol{V}_{\mu\nu} = \langle \lambda_\mu | e^{i\Lambda_{\mu\nu}} \hat{V} | \lambda_\nu \rangle \tag{3.58}$$

with the electron-nuclei potential $\hat{V}$. All other matrices are not block-diagonal and read

$$\mathbf{\Pi}^\dagger_{\mu\nu} = \frac{1}{2} \langle \phi_\mu | e^{\mathrm{i}\Lambda_{\mu\nu}} \left[\vec{\sigma} \cdot (\hat{\vec{p}} + \frac{1}{c} \hat{\vec{\mathcal{A}}}_\nu)\right] \left[\vec{\sigma} \cdot (\hat{\vec{p}} + \frac{1}{c} \hat{\vec{\mathcal{A}}}_\nu)\right] | \phi_\nu \rangle \tag{3.59}$$

$$\mathbf{\Pi}_{\mu\nu} = \frac{1}{2} \langle \phi_\mu | e^{\mathrm{i}\Lambda_{\mu\nu}} \left[\vec{\sigma} \cdot (\hat{\vec{p}} + \frac{1}{c} \hat{\vec{\mathcal{A}}}_\nu)\right] \left[\vec{\sigma} \cdot (\hat{\vec{p}} + \frac{1}{c} \hat{\vec{\mathcal{A}}}_\nu)\right] | \phi_\nu \rangle \tag{3.60}$$

$$\mathbf{W}_{\mu\nu} = \langle \phi_\mu | e^{\mathrm{i}\Lambda_{\mu\nu}} \left[\vec{\sigma} \cdot (\hat{\vec{p}} + \frac{1}{c} \hat{\vec{\mathcal{A}}}_\nu)\right] \hat{V} \left[\vec{\sigma} \cdot (\hat{\vec{p}} + \frac{1}{c} \hat{\vec{\mathcal{A}}}_\nu)\right] | \phi_\nu \rangle \tag{3.61}$$

$$\mathbf{T}_{\mu\nu} = \frac{1}{2} \langle \phi_\mu | e^{\mathrm{i}\Lambda_{\mu\nu}} \left[\vec{\sigma} \cdot (\hat{\vec{p}} + \frac{1}{c} \hat{\vec{\mathcal{A}}}_\nu)\right] \left[\vec{\sigma} \cdot (\hat{\vec{p}} + \frac{1}{c} \hat{\vec{\mathcal{A}}}_\nu)\right] | \phi_\nu \rangle \tag{3.62}$$

where $\vec{\sigma}$ is a vector containing the Pauli spin matrices. Here, the generalized momentum matrix $\mathbf{\Pi}$ and the small-small block of the metric $\mathbf{T}$ are identical due to the magnetically balanced basis set expansion. In a restricted kinetic balanced basis,[105] these matrices differ as $\mathbf{T}$ becomes independent of the vector potential.

The unitary transformation of the Dirac Hamiltonian to obtain the X2C Hamiltonian[114–120] in the presence of a magnetic field is performed according to the procedure outlined in Chapter 1, Section 1.3.3. Note that all one-electron integrals explicitly depend on the external magnetic field due to the use of GIAOs. Moreover, $\mathbf{\Pi}$, $\mathbf{T}$, and $\mathbf{W}$ include a dependence on the magnetic field due to the restricted magnetic balance condition. The generalized momentum matrix $\mathbf{\Pi}$ is the only matrix where the dependence also arises due to the generalized momentum operator $\hat{\vec{\pi}}$ of the Dirac Hamilton operator.

Herein, we account for the missing two-electron picture-change correction with the modified

screened nuclear spin–orbit (mSNSO) ansatz,[125–128] and incorporate the DLU approximation as described in Section 1.3.3.

Gauge-Invariant Formalism for EPR g-Tensors

The energy derivatives are now formed in the same manner as done in non-relativistic quantum chemistry. Thus, no derivatives of the density matrix are required.[504,505] Carrying out the energy derivative for the g-tensor in Eq. 3.48 consequently leads to working equations similar to two-component geometry gradients[127,133,325]

$$\frac{\mathrm{d}E}{\mathrm{d}B_u} = \mathrm{tr}\left[\mathbf{P}\left(\vec{J}_v\right)\mathbf{h}_u^B\right] + \frac{1}{2}\ \mathrm{tr}\left[\mathbf{G}\left(\vec{J}_v\right)\mathbf{\Gamma}_u^B\right] + E_{\mathrm{XC},u}^B\left(\vec{J}_v\right) - \mathrm{tr}\left[\mathbf{Z}\left(\vec{J}_v\right)\ \mathbf{S}_u^B\right] \tag{3.63}$$

Here, $\mathbf{P}$ and $\mathbf{G}$ are the one and two-electron density matrix, while $\mathbf{Z}$ is the energy-weighted density matrix.[504,505] $\mathbf{h}$ and $\mathbf{\Gamma}$ are the one-electron Hamiltonian and the two-electron integrals in the atomic orbitals basis, respectively. E_{XC} is the exchange-correlation energy in DFT. The one-electron density matrix $\mathbf{P}$ reads

$$\mathbf{P} = \begin{pmatrix} \boldsymbol{P}^{\alpha\alpha} & \boldsymbol{P}^{\alpha\beta} \\ \boldsymbol{P}^{\beta\alpha} & \boldsymbol{P}^{\beta\beta} \end{pmatrix} \tag{3.64}$$

with the one-component matrices

$$\mathrm{Re}(\boldsymbol{P}_{\mu\nu}^{\sigma_1\sigma_2}) = \sum_i n_i \left[\mathrm{Re}(c_{\mu i}^{\sigma_1})\,\mathrm{Re}(c_{\nu i}^{\sigma_2}) + \mathrm{Im}(c_{\mu i}^{\sigma_1})\,\mathrm{Im}(c_{\nu i}^{\sigma_2})\right] \tag{3.65}$$

$$\mathrm{Im}(\boldsymbol{P}_{\mu\nu}^{\sigma_1\sigma_2}) = \sum_i n_i \left[-\mathrm{Re}(c_{\mu i}^{\sigma_1})\,\mathrm{Im}(c_{\nu i}^{\sigma_2}) + \mathrm{Im}(c_{\mu i}^{\sigma_1})\,\mathrm{Re}(c_{\nu i}^{\sigma_2})\right] \tag{3.66}$$

n_i is the occupation number of the corresponding two-component spinor and the superscript σ denotes the spin component ($\sigma = \alpha, \beta$). $c_{\mu i}$ are the spinor coefficients from an SCF procedure. The two-electron density matrix $\mathbf{G}$ is formed similarly.[325] Note that these matrices

are constructed from the spinors with $\vec{J}$ aligned along the v axis. As $\mathbf{S}_u^B$ is an antisymmetric and purely imaginary matrix, which is diagonal in the (2×2) superspace, we only need the respective $\alpha\alpha$ and $\beta\beta$ blocks of the energy-weighted density matrix, given by the spinor coefficients and energies, according to

$$\mathrm{Im}\left[\boldsymbol{Z}_{\mu\nu}^{\sigma\sigma}\right] = \sum_i n_i \left[-\mathrm{Re}(c_{\mu i}^{\sigma})\epsilon_i \,\mathrm{Im}(c_{\nu i}^{\sigma}) + \mathrm{Im}(c_{\mu i}^{\sigma})\epsilon_i \,\mathrm{Re}(c_{\nu i}^{\sigma})\right] \tag{3.67}$$

n_i is the occupation number. Therefore, the last term in Eq. 3.63 is simplified to

$$\mathrm{tr}\big(\mathbf{Z}\mathbf{S}_u^B\big) = -\,\mathrm{tr}\left(\mathrm{i}\left\{\mathrm{Im}\left[\boldsymbol{Z}^{\alpha\alpha}\right] + \mathrm{Im}\left[\boldsymbol{Z}^{\beta\beta}\right]\right\}\mathbf{S}_u^B\right) \tag{3.68}$$

The imaginary part of the energy-weighted density matrix is not needed for relativistic geometry gradients. However, it also arises for geometry gradients in finite magnetic fields.[506] An important point is that all terms in Eq. 3.63 except for the one with $\mathbf{h}_u^B$ arise solely due to the basis set expansion with GIAOs. Note that the computation of the two-electron integral derivatives is described in Refs. [422, 507, 508] and their generalization to a two-component framework is carried out as described in, e.g., Refs. [325] and [324]. Furthermore, the derivatives of the two-electron integrals in Eq. 3.63 are known from the right-hand side of the coupled-perturbed Hartree–Fock (CPHF) or Kohn–Sham (CPKS) equations for two-component NMR shielding tensors.[308,487,489,490,509] The crucial part for a relativistic treatment is the derivative of the one-electron Hamiltonian, which is also very similar to the perturbed density contribution or paramagnetic contribution to the NMR shielding tensor, which include the derivatives of the unitary transformation matrix.[288,306–308,510]

3.4.3 Implementation

The calculation of EPR g-tensors with a common gauge origin is implemented into the ridft module[130,133,137,324–327] of TURBOMOLE.[134,135,317,318] Here, the g-tensor is evaluated

after the SCF iterations. The gauge-invariant ansatz employing GIAOs is implemented into the mpshift module.[422,508,511–513] The spin-independent integral derivatives using GIAOs are taken from Ref. [288]. All new integrals are implemented using a combination of Gauss–Hermite and Gauss–Rys integration[319,320,514,515] as done previously for other magnetic[15,290,342] and electric properties.[289] The finite nucleus model is available throughout using the finite nucleus exponents of Ref. [247]. The (modified) screened-nuclear spin–orbit (SNSO, mSNSO) approximation is available for the spin-dependent integral (derivatives) of the relativistically modified potential $\mathbf{W}$.[125–128] X2C response and Sylvester matrix equations are solved by a generalization of the existing one-component routines[288] as done previously for the HFC constant[15] and NMR coupling constants.[290] As our previous works, the implementation is fully integral direct. We use $c = 137.0359990840\,\text{a.u.}$[323] for the speed of light in atomic units. Additional contributions from point charges or COSMO[215,334] arise due to the use of GIAOs and are treated without relativistic picture-change correction. Thus, we use the available non-relativistic integrals[422] for these terms.

The ridft module supports the (multipole-accelerated) resolution of the identity approximation (MARI-J, RI-J, and RI-K) throughout.[324,333] Additionally, the seminumerical exchange approximation is available.[326,327] The mpshift module only supports MARI-J and RI-J for integral derivatives.[422] Note that these do not require substantial changes for a two-component ansatz as the Coulomb term depends on the total density.[324] The analytical exchange integral derivatives with respect to the magnetic fields[508] are extended to a two-component framework as done previously for energies[324] and energy gradients.[325] Therefore, the integral routines are able to process the eight density matrices. For the contraction with the density matrix, we construct the symmetric and antisymmetric linear combinations.[325]

Density functional approximations are available up to the fourth rung of Jacob's ladder.[335–337] The kinetic energy density τ is generalized using the external magnetic field as suggested by Maximoff and Scuseria.[516] Interfaces to Libxc[338–340] and XCFun[341] are provided. For this

work, the existing one-component implementations[422,511,517] are extended like done previously for the SCF energy.[324]

All algebraic operations, transformations, and integral evaluations are parallelized using the OpenMP scheme[328,329] and we use the Intel® Math Kernel Library (Intel MKL) throughout this work. Preparation and post-processing scripts are available based on our previous endeavors for the hyperfine coupling matrix.[15] Three independent calculations based on converged unrestricted Kohn–Sham (UKS) or Hartree–Fock (UHF) orbitals are needed to obtain the complete EPR g-matrix. This matrix is then transformed into its principal axis system, where the g-matrix is diagonal, either through constructing the rank-2 tensor $\left(\boldsymbol{g}\boldsymbol{g}^{\mathrm{T}}\right)$ and subsequently diagonalizing, or by diagonalization of the symmetric part, which is given by $1/2\left(\boldsymbol{g}+\boldsymbol{g}^{\mathrm{T}}\right)$. We implemented both ansätze using Python scripts.

In the first 2c SCF iteration, the UKS/UHF density matrix is transformed to the complex 2c framework by requiring the wavefunction to be an eigenfunction of the spin operator $\hat{S}_v$ to prepare the orthogonal orientations of the magnetization vector. This turned out to be sufficient for all calculations herein, i.e. $\vec{J}$ and $\vec{S}$ were still aligned to the Cartesian axes after the SCF iterations converged. Alternatively, a weak finite magnetic field with different orientations could be used.[506]

3.4.4 Computational Details

We perform benchmark calculations to assess three essential parameters of a quantum chemical DFT calculation of the g-tensor—namely the Hamiltonian, the basis set, and the density functional approximation. This complements our previous work on the HFC constant.[15] First, we consider the 17 transition-metal complexes of Ref. [280], namely $[MoNCl_4]^{2-}$, $[MoOF_4]^{-}$, $[MoOCl_4]^{-}$, $[MoOF_5]^{2-}$, $[MoOBr_5]^{2-}$, $[WOCl_4]^{-}$, $[WOF_5]^{2-}$, $[WOBr_5]^{2-}$, $[TcNF_4]^{-}$, $[TcNCl_4]^{-}$, $[TcNBr_4]^{-}$, $[ReNF_4]^{-}$, $[ReNCl_4]^{-}$, $[ReNBr_4]^{-}$, $[ReOBr_4]$, $[ReOF_5]^{-}$, and $[OsOF_5]$,

and compare our X2C and DLU-X2C results to available 4c reference data. In line with that reference, we use the RKB condition for the basis set expansion and a common gauge origin placed at the heavy atom center. Decontracted IGLO-III bases are employed for the light elements, namely N, F, and Cl,[345] while the Dyall-VTZ basis set is used for Br[346,347] and the Dyall-TZ bases for Mo, Tc, W, Re, and Os.[347–349] The PBE0[350,351] functional is chosen with very large grids (grid 5a).[246,352,353] Furthermore, the mSNSO approximation is applied and an SCF convergence threshold of $10^{-9}\,\mathrm{E_h}$ is selected. There, we also discuss the impact of diffuse basis functions using the Sapporo-DKH3-QZP-2012-diffuse bases.[358,359] All two-component calculations are performed with converged UKS orbitals. In this work, "PCC" indicates that the derivatives of the decoupling and the renormalization matrices are neglected. Thus, the algorithm becomes similar to ordinary picture-change corrections of expectation values.[289] Like Ref. [280], we use the shift Δg in ppt (parts per thousand) relative to the g-factor of the free electron[323] ($g_e = 2.00231930436256$) as a metric for comparison. The impact of the balance condition and the gauge-invariant formalism is assessed for the same set of molecules using the described computational settings.

Second, the importance of the basis set is studied. To do so, the basis sets listed in Tab. 3.9 are considered. The x2c-SVPall-2c-s and x2c-TZVPall-2c-s bases are obtained by combining the extensions for NMR shieldings of Ref. [246] with the 2c extensions of Ref. [137]. Note that the comparably flat p and d functions of the NMR extensions were removed to avoid linear dependencies, as these functions were optimized to serve as a minimal version of the 2c extensions.[246] We measure the errors with respect to the large even-tempered basis set of Ref. [363]. Only the DLU-X2C Hamiltonian using the RMB-GIAO approach is discussed here, with the remaining methods discussed in the original reference.[518]

Third, we study common density functional approximations. As representatives for pure functionals, we choose S-VWN,[370–372] KT3,[373] BP86,[374,375] PBE,[350] TPSS,[211] revTPSS,[376,377] and r^{2}SCAN.[378,379] BH&HLYP,[375,380,381] B3LYP,[380,382,520] PBE0,[350,351] a modified version of

Table 3.9: Considered basis sets and basis set combinations for the light (N, O, F, Cl) and heavy elements (Br, Mo, Tc, W, Re, Os). The suffix "-unc" denotes that the bases are used in the decontracted form. NBF is the total number of spherical AO basis functions. The even-tempered reference basis set[246] uses an average of 1534 basis functions for the molecular test set. "Avg." denotes the average number of basis functions for a molecule.

Basis Set	Light Elements	Ref.	Heavy Elements	Ref.	Avg.
1	IGLO-II-unc	[345]	Dyall-VDZ-unc	[346–349]	378
2	IGLO-III-unc	[345]	Dyall-VTZ-unc	[346–349]	540
3	pcS-1-unc	[519]	Dyall-VDZ-unc	[346–349]	397
4	pcS-2-unc	[519]	Dyall-VTZ-unc	[346–349]	596
5	pcS-3-unc	[519]	Dyall-VQZ-unc	[346–349]	895
6	cc-pVDZ-unc	[355, 356]	Dyall-VDZ-unc	[346–349]	379
7	cc-pVTZ-unc	[355, 356]	Dyall-VTZ-unc	[346–349]	554
8	cc-pVQZ-unc	[355, 356]	Dyall-VQZ-unc	[346–349]	684
9	Sapporo-DZP-2012	[358]	Sapporo-DKH3-DZP-2012	[358, 359]	198
10	Sapporo-TZP-2012	[358]	Sapporo-DKH3-TZP-2012	[358, 359]	367
11	Sapporo-QZP-2012	[358]	Sapporo-DKH3-QZP-2012	[358, 359]	577
12	Jorge-DZP-DKH	[360]	Jorge-DZP-DKH	[360–362]	181
13	Jorge-TZP-DKH	[360]	Jorge-TZP-DKH	[360–362]	296
14	x2c-SVPall-2c	[137]	x2c-SVPall-2c	[137]	195
15	x2c-TZVPall-2c	[137]	x2c-TZVPall-2c	[137]	300
16	x2c-QZVPall-2c	[363]	x2c-QZVPall-2c	[363]	518
17	x2c-SVPall-2c-s	[137, 246]	x2c-SVPall-2c-s	[137, 246]	216
18	x2c-TZVPall-2c-s	[137, 246]	x2c-TZVPall-2c-s	[137, 246]	319
16	x2c-QZVPall-2c-s	[363]	x2c-QZVPall-2c-s	[363]	526
20	x2c-SVPall-2c-unc	[137]	x2c-SVPall-2c-unc	[137]	448
21	x2c-TZVPall-2c-unc	[137]	x2c-TZVPall-2c-unc	[137]	536
22	x2c-QZVPall-2c-unc	[363]	x2c-QZVPall-2c-unc	[363]	845
23	ANO-R-unc	[364]	ANO-R-unc	[364]	927
24	ANO-RCC-unc	[365]	ANO-RCC-unc	[365, 366]	927

PBE0 including 40% of Hartree–Fock (HF) exchange (PBE0-40HF),[280,350,351] B97,[383] B97-2,[384] TPSSh,[385] revTPSSh,[376,377] and TPSS0[385,386] are selected to cover frequently used global hybrid functionals. For common range-separated hybrids (RSHs), we employ the CAM-B3LYP,[387] CAM-QPT-00,[388] CAM-QTP-02,[389] HSE06,[390–392] LC-ωPBE,[393] and ωB97X-D[394] functionals. Libxc[338–340] is used for the range-separated hybrid functionals, KT3, revTPSS(h), TPSS0, r^{2}SCAN, and B97 throughout this work. We use XCFun[341] for PBE0-40HF. Additionally, Hartree–Fock calculations are performed. COSMO is employed with the default parameters to compensate the negative charge[215,334] and the x2c-QZVPall-2c basis set is cho-

sen for consistency with our previous studies on the HFC constant.[15] Errors are measured with respect to the experimental findings[396–407] collected in Ref. [280].

Fourth, we quantify the gauge-origin dependence of $[(C_5Me_5)_2Y(\mu\text{-}S)_2Mo(\mu\text{-}S)_2Y(C_5Me_5)_2]^-$ by comparing the g-tensors produced by the RKB-CGO method using Mo/Y as the common gauge origin and the RMB-GIAO method. The g-tensors were calculated using the mSNSO-DLU-X2C Hamiltonian, the x2c-TZVPPall-2c (Mo, Y) and x2c-SVPall-2c (H, C, S) basis set combination,[137] and the TPSSh[385] and ωB97X-D functionals.[394] Calculations were performed for the experimentally determined structure reported in Ref. [521]. We apply COSMO to treat the molecular environment in solution.[215,334] We use the parameters for tetrahydrofuran (THF), which are $\epsilon_r = 7.520$, a solvation radius of 1.30 Å, and a refractive index of 1.4050. The SCF procedure is considered converged with an energy threshold of $10^{-7}\,E_h$ and a criterion of 10^{-7} a.u. for the root mean square of the density matrix.

Fifth, we apply the mSNSO-DLU-X2C Hamiltonian and the three ansätze to the larger complex $[Pt(C_6Cl_5)_4]^-$. We chose the position of Pt as the common gauge origin for the RKB-CGO and RMB-CGO approaches. The structure is taken from Ref. [280] and we employ COSMO with the default parameters.[215,334] BH&HLYP,[375,380,381] B3LYP,[380,382,520] PBE0,[350,351] PBE0-40HF,[280,350,351] B97-2,[384] TPSSh,[385] TPSS0,[385,386] CAM-B3LYP,[387] CAM-QPT-00,[388] CAM-QTP-02,[389] HSE06,[390–392] LC-ωPBE,[393] and ωB97X-D[394] are considered. Fine grids (grid 4a) are used for the numerical integration of the XC parts.[246,352,353] The uncontracted Dyall-VTZ basis[522] is combined with the decontracted pcS-2 basis.[519] We use the universal (uncontracted) x2c-type fitting bases[137,363] for the RI-J approximation in the 2c calculations.[324] Furthermore, the x2c-QZVPall-2c basis[363] is applied together with the tailored auxiliary basis.[137,363] An SCF threshold of $10^{-8}\,E_h$ is selected. In total, the number of basis functions in the spherical atomic orbital representation amounts to 2668 (Dyall-VTZ-unc/pcS-2-unc) and 3003 (x2c-QZVPall-2c, 4720 primitive functions).

Lastly we study the three lanthanide complexes $[La(OAr^*)_3]^-$, $[Lu(NR_2)_3]^-$, and $[Lu(OAr^*)_3]^-$

(OAr* = 2,6-Ad_2-4-t-Bu-C_6H_2O, Ad = adamantyl, t-Bu= tert-butyl, R = $SiMe_3$ with Me = methyl) of Ref. [14] using the structures provided therein. The g-tensors are calculated with the x2c-SVPall-2c basis set for the light elements[137] and the x2c-TZVPPall-2c[137] basis set for La and Lu. The mSNSO-DLU-X2C Hamiltonian is applied and we employ the TPSS,[211] CAM-B3LYP,[387] LC-ωPBE,[393] and ωB97X-D[394] functionals with fine grids (grid 4a).[246,352,353] Additional calculations using the x2c-QZVPall-2c basis set[363] for Ln atoms and the r^{2}SCAN,[378,379] PBE0,[350,351] PBE0-40HF,[280,350,351] CAM-QTP-02,[389] and HSE06,[390–392] functionals are given in the original publication.[518] COSMO is applied using the same parameters as the study of $[(C_5Me_5)_2Y(\mu\text{-}S)_2Mo(\mu\text{-}S)_2Y(C_5Me_5)_2]^-$. The same convergence thresholds of $10^{-7}\,E_h$ for the energy and 10^{-7} a.u. for the root mean square of the density matrix are used. We employed a canonical orthogonalization with a threshold of 10^{-4} for the SCF procedure. The common gauge origin is placed at the La or Lu atom.

3.4.5 Assessment for Transition-Metal Complexes

Comparison to Four-Component Data and Hamiltonian Studies

Calculations of the g-tensor were performed using the X2C and DLU-X2C Hamiltonians for the 17 transition-metal complexes and the results are presented in Tab. 3.10 alongside those obtained from 4c Dirac–Kohn–Sham theory and experiment.

Both quasi-relativistic Hamiltonians accurately reproduce the 4c results, and the deviation of the isotropic g-shift towards the 4c results amounts to at most 4 ppt. Particularly, for the Mo and Tc complexes, the deviation is below 2 ppt and often even below 1 ppt. Similar trends are observed for the three principal components. Generally, the calculated g-tensors are also in good agreement with the experimental findings for the Mo, W, and Os complexes. Here, the deviation amounts to at most 10 ppt for $[MoOF_4]^-$ and 15 ppt for both $[WOBr_5]^{2-}$ and $[OsOF_5]$. Given the absolute value of the isotropic g-shift for these complexes the

Table 3.10: Principal components of the Δg-tensor in ppt. Non-collinear 4c results are taken from the Supporting Information of Ref. [280]. "PCC" denotes that the derivatives of **X** and **R** are neglected. Experimental (Expt.) results[396–407] were collected in Ref. [280]. All calculations utilize PBE0, a common gauge origin and the RKB condition. Results with the Sapporo-DKH3-QZP-2012-diffuse bases are listed in the original publication.[518]

Molecule	Hamiltonian	Δg_{iso}	$\Delta g_{\parallel}$	$\Delta g_{\perp}$	Molecule	Hamiltonian	Δg_{iso}	$\Delta g_{\parallel}$	$\Delta g_{\perp}$
$[\mathbf{MoNCl_4}]^{2-}$	X2C RKB PCC	−43.4	−88.9	−20.7	$[\mathbf{TcNF_4}]^{-}$	X2C RKB PCC	−41.5	−77.6	−23.4
	X2C RKB	−43.9	−89.5	−21.1		X2C RKB	−42.0	−78.3	−23.8
	DLU RKB PCC	−43.4	−88.9	−20.8		DLU RKB PCC	−41.5	−77.7	−23.4
	DLU RKB	−44.0	−89.5	−21.3		DLU RKB	−42.1	−78.4	−23.9
	4c RKB	−43	−90	−20		4c RKB	−41	−78	−23
	Expt.	−44	−96	−18		Expt.	−44	−107	−12
$[\mathbf{MoOF_4}]^{-}$	X2C RKB PCC	−75.9	−94.2	−66.8	$[\mathbf{TcNCl_4}]^{-}$	X2C RKB PCC	5.7	26.2	−4.6
	X2C RKB	−76.4	−94.8	−67.2		X2C RKB	5.2	25.5	−4.9
	DLU RKB PCC	−75.9	−94.1	−66.9		DLU RKB PCC	5.7	26.2	−4.5
	DLU RKB	−76.6	−94.9	−67.4		DLU RKB	5.2	25.6	−5.0
	4c RKB	−77	−96	−67		4c RKB	7	27	−3
	Expt.	−87	−108	−77		Expt.	0	6	−2
$[\mathbf{MoOCl_4}]^{-}$	X2C RKB PCC	−42.3	−16.9	−55.0	$[\mathbf{TcNBr_4}]^{-}$	X2C RKB PCC	79.6	178.4	30.1
	X2C RKB	−42.7	−17.5	−55.4		X2C RKB	79.0	177.7	29.7
	DLU RKB PCC	−42.4	−16.9	−55.1		DLU RKB PCC	79.6	178.5	30.2
	DLU RKB	−42.9	−17.6	−55.6		DLU RKB	78.9	177.6	29.5
	4c RKB	−42	−17	−55		4c RKB	81	180	31
	Expt.	−49	−37	−56		Expt.	69	145	32
$[\mathbf{MoOF_5}]^{2-}$	X2C RKB PCC	−104.5	−101.6	−105.9	$[\mathbf{ReNF_4}]^{-}$	X2C RKB PCC	−188.5	−329.0	−118.2
	X2C RKB	−104.9	−102.2	−106.3		X2C RKB	−189.2	−330.1	−118.8
	DLU RKB PCC	−104.5	−101.5	−105.9		DLU RKB PCC	−188.4	−328.8	−118.1
	DLU RKB	−105.1	−102.3	−106.5		DLU RKB	−189.4	−330.1	−119.0
	4c RKB	−106	−104	−108		4c RKB	−186	−326	−116
	Expt.	−104	−128	−91		Expt.	−206	−353	−132
$[\mathbf{MoOBr_5}]^{2-}$	X2C RKB PCC	−7.2	103.8	−62.7	$[\mathbf{ReNCl_4}]^{-}$	X2C RKB PCC	−75.2	−72.7	−76.4
	X2C RKB	−7.7	103.1	−63.1		X2C RKB	−76.0	−73.8	−77.0
	DLU RKB PCC	−7.4	103.7	−62.9		DLU RKB PCC	−75.1	−72.7	−76.3
	DLU RKB	−8.2	102.7	−63.7		DLU RKB	−75.9	−73.7	−77.0
	4c RKB	−7	104	−63		4c RKB	−74	−72	−74
	Expt.	−9	87	−57		Expt.	−78	−87	−73
$[\mathbf{WOCl_4}]^{-}$	X2C RKB PCC	−201.2	−180.8	−211.4	$[\mathbf{ReNBr_4}]^{-}$	X2C RKB PCC	10.1	109.3	−39.5
	X2C RKB	−201.9	−181.8	−212.0		X2C RKB	9.2	108.1	−40.2
	DLU RKB PCC	−201.1	−180.7	−211.3		DLU RKB PCC	10.2	109.3	−39.4
	DLU RKB	−201.9	−181.7	−211.9		DLU RKB	9.1	108.0	−40.4
	4c RKB	−198	−179	−208		4c RKB	11	109	−38
	Expt.	−229	−209	−239		Expt.	3	67	−29
$[\mathbf{WOF_5}]^{2-}$	X2C RKB PCC	−391.5	−455.8	−359.4	$[\mathbf{ReOBr_4}]$	X2C RKB PCC	−39.4	230.8	−174.5
	X2C RKB	−392.2	−456.9	−359.9		X2C RKB	−40.2	229.7	−175.2
	DLU RKB PCC	−391.4	−455.7	−359.3		DLU RKB PCC	−39.3	230.9	−174.4
	DLU RKB	−392.4	−457.0	−360.1		DLU RKB	−40.3	229.5	−175.3
	4c RKB	−388	−451	−356		4c RKB	−37	231	−172
	Expt.	−368	−443	−330		Expt.	−98	171	−232
$[\mathbf{WOBr_5}]^{2-}$	X2C RKB PCC	−190.3	−82.1	−244.5	$[\mathbf{ReOF_5}]^{-}$	X2C RKB PCC	−351.5	−317.8	−368.4
	X2C RKB	−191.1	−83.2	−245.1		X2C RKB	−352.3	−318.9	−369.0
	DLU RKB PCC	−190.3	−82.1	−244.4		DLU RKB PCC	−351.4	−317.6	−368.4
	DLU RKB	−191.5	−83.5	−245.4		DLU RKB	−352.4	−318.9	−369.2
	4c RKB	−187	−81	−240		4c RKB	−348	−314	−365
	Expt.	−172	−99	−206		Expt.	−269	−282	−262
$[\mathbf{OsOF_5}]$	X2C RKB PCC	−312.2	−182.7	−376.9					
	X2C RKB	−313.0	−183.8	−377.5					
	DLU RKB PCC	−312.1	−182.6	−376.9					
	DLU RKB	−313.1	−183.8	−377.7					
	4c RKB	−309	−180	−374					
	Expt.	−324	−197	−387					

Dyall-TZ/IGLO-III basis set and the PBE0 functional may already be considered sufficient. However, larger deviations are observed for the Re complexes with 60 ppt for $[ReOBr_4]$ and about 80 ppt for $[ReOF_5]^-$. These constitute errors of about 60% for $[ReOBr_4]$ and 30% for $[ReOF_5]^-$. The X2C g-tensors discussed here were obtained using the mSNSO method, which significantly improved their accuracy when compared to non-mSNSO calculations.

From these results, it is clear that the error introduced by the DLU scheme is negligible. The maximum error occurs at 0.4 ppt for the isotropic g-shift of $[WOBr_5]^{2-}$, compared to an absolute value of 190 ppt. The errors between the principal components are very similar. Thus, no error cancellation is observed and the DLU scheme appears to be a robust approximation. This is consistent with our previous findings for the HFC constant.[15]

The impact of the decoupling derivatives typically amounts to about 1 ppt for the heavier compounds. This verifies the assumptions of the previous X2C implementation for the EPR g-tensor reported in Ref. [129]. Notably, the error introduced by neglecting the decoupling derivatives is demonstrably larger than that introduced by DLU, and the derivatives can thus be routinely included in DLU-X2C calculations with almost no computational overhead when compared to a DLU-X2C energy calculation. For these complexes, the calculation of the g-tensor with the DLU-X2C Hamiltonian including derivatives takes only a few seconds. The computational costs are considered in detail in Sec. 3.4.5.

We proceed to study the impact of the balance condition, i.e. RKB-CGO, RMB-CGO, and RMB-GIAO, on the accuracy of the EPR g-tensor. The results are given in Tab. 3.11 for both X2C and DLU-X2C Hamiltonians. Overall, the impact of the RMB and the GIAOs on the g-tensor is small for these systems. The largest absolute deviations are found for the heavy W, Re, and Os compounds. There, deviations of about 2–3 ppt are observed. For $[ReNBr_4]^-$, this amounts to a relative change of about 17% for the isotropic g-shift, while it amounts to only 1% for $[ReOF_5]^-$. The modest impact of the RMB condition can be explained by the minor importance of the diamagnetic correction and the relativistic mass

Table 3.11: Comparison of two-component Hamiltonians (PBE0) for the principal components of the Δg-tensor in ppt. Experimental (Expt.) results[396–407] were collected in Ref. [280].

Molecule	Hamiltonian	Δg_{iso}	$\Delta g_{\parallel}$	$\Delta g_{\perp}$	Molecule	Hamiltonian	Δg_{iso}	$\Delta g_{\parallel}$	$\Delta g_{\perp}$
$[\mathbf{MoNCl_4}]^{2-}$	X2C RKB	−43.9	−89.5	−21.1	$[\mathbf{TcNF_4}]^{-}$	X2C RKB	−42.0	−78.3	−23.8
	X2C RMB	−43.2	−88.8	−20.4		X2C RMB	−41.2	−77.5	−23.1
	X2C GIAO	−42.4	−88.0	−19.7		X2C GIAO	−40.8	−76.6	−22.9
	DLU RKB	−44.0	−89.5	−21.3		DLU RKB	−42.1	−78.4	−23.9
	DLU RMB	−43.2	−88.8	−20.5		DLU RMB	−41.3	−77.6	−23.1
	DLU GIAO	−42.5	−88.0	−19.8		DLU GIAO	−40.9	−76.8	−22.9
	Expt.	−44	−96	−18		Expt.	−44	−107	−12
$[\mathbf{MoOF_4}]^{-}$	X2C RKB	−76.4	−94.8	−67.2	$[\mathbf{TcNCl_4}]^{-}$	X2C RKB	5.2	25.5	−4.9
	X2C RMB	−75.7	−94.0	−66.5		X2C RMB	5.9	26.3	−4.2
	X2C GIAO	−75.2	−93.3	−66.1		X2C GIAO	6.5	27.4	−3.9
	DLU RKB	−76.6	−94.9	−67.4		DLU RKB	5.2	25.6	−5.0
	DLU RMB	−75.7	−94.0	−66.6		DLU RMB	5.9	26.2	−4.2
	DLU GIAO	−75.2	−93.4	−66.2		DLU GIAO	6.5	27.4	−3.9
	Expt.	−87	−108	−77		Expt.	0	6	−2
$[\mathbf{MoOCl_4}]^{-}$	X2C RKB	−42.7	−17.5	−55.4	$[\mathbf{TcNBr_4}]^{-}$	X2C RKB	79.0	177.7	29.7
	X2C RMB	−42.0	−16.8	−54.7		X2C RMB	79.9	178.6	30.6
	X2C GIAO	−41.4	−15.9	−54.2		X2C GIAO	80.6	179.3	31.3
	DLU RKB	−42.9	−17.6	−55.6		DLU RKB	78.9	177.6	29.5
	DLU RMB	−42.1	−16.8	−54.8		DLU RMB	79.9	178.6	30.6
	DLU GIAO	−41.5	−15.9	−54.3		DLU GIAO	80.6	179.3	31.2
	Expt.	−49	−37	−56		Expt.	69	145	32
$[\mathbf{MoOF_5}]^{2-}$	X2C RKB	−104.9	−102.2	−106.3	$[\mathbf{ReNF_4}]^{-}$	X2C RKB	−189.2	−330.1	−118.8
	X2C RMB	−104.2	−101.4	−105.5		X2C RM	−188.7	−329.5	−118.3
	X2C GIAO	−103.4	−100.5	−104.9		X2C GIAO	−187.2	−326.5	−117.5
	DLU RKB	−105.1	−102.3	−106.5		DLU RKB	−189.4	−330.1	−119.0
	DLU RMB	−104.2	−101.4	−105.6		DLU RMB	−188.7	−329.5	−118.3
	DLU GIAO	−103.5	−100.6	−104.9		DLU GIAO	−187.2	−326.5	−117.5
	Expt.	−104	−128	−91		Expt.	−206	−353	−132
$[\mathbf{MoOBr_5}]^{2-}$	X2C RKB	−7.7	103.1	−63.1	$[\mathbf{ReNCl_4}]^{-}$	X2C RKB	−76.0	−73.8	−77.0
	X2C RMB	−6.7	104.1	−62.1		X2C RMB	−75.5	−73.3	−76.6
	X2C GIAO	−6.5	104.7	−62.1		X2C GIAO	−74.5	−72.2	−75.6
	DLU RKB	−8.2	102.7	−63.7		DLU RKB	−75.9	−73.7	−77.0
	DLU RMB	−7.0	104.0	−62.4		DLU RMB	−75.5	−73.4	−76.6
	DLU GIAO	−6.7	104.6	−62.4		DLU GIAO	−74.4	−72.2	−75.6
	Expt.	−9	87	−57		Expt.	−78	−87	−73
$[\mathbf{WOCl_4}]^{-}$	X2C RKB	−201.9	−181.8	−212.0	$[\mathbf{ReNBr_4}]^{-}$	X2C RKB	9.2	108.1	−40.2
	X2C RMB	−201.4	−181.3	−211.5		X2C RMB	9.8	108.7	−39.7
	X2C GIAO	−200.6	−180.4	−210.6		X2C GIAO	10.8	110.7	−39.1
	DLU RKB	−201.9	−181.7	−211.9		DLU RKB	9.1	108.0	−40.4
	DLU RMB	−201.4	−181.3	−211.5		DLU RMB	9.8	108.6	−39.6
	DLU GIAO	−200.5	−180.4	−210.6		DLU GIAO	10.8	110.7	−39.1
	Expt.	−229	−209	−239		Expt.	3	67	−29
$[\mathbf{WOF_5}]^{2-}$	X2C RKB	−392.2	−456.9	−359.9	$[\mathbf{ReOBr_4}]$	X2C RKB	−40.2	229.7	−175.2
	X2C RMB	−391.7	−456.3	−359.4		X2C RMB	−39.7	230.3	−174.6
	X2C GIAO	−389.2	−451.8	−358.0		X2C GIAO	−39.3	230.7	−174.2
	DLU RKB	−392.4	−457.0	−360.2		DLU RKB	−40.3	229.5	−175.3
	DLU RMB	−391.8	−456.4	−359.4		DLU RMB	−39.7	230.2	−174.6
	DLU GIAO	−389.3	−451.8	−358.0		DLU GIAO	−39.2	230.7	−174.2
	Expt.	−368	−443	−330		Expt.	−98	171	−232
$[\mathbf{WOBr_5}]^{2-}$	X2C RKB	−191.1	−83.2	−245.1	$[\mathbf{ReOF_5}]^{-}$	X2C RKB	−352.3	−318.9	−369.0
	X2C RMB	−190.5	−82.6	−244.5		X2C RMB	−351.7	−318.3	−368.5
	X2C GIAO	−190.1	−79.3	−245.5		X2C GIAO	−350.3	−315.1	−367.8
	DLU RKB	−191.5	−83.5	−245.4		DLU RKB	−352.4	−318.9	−369.2
	DLU RMB	−190.6	−82.7	−244.5		DLU RMB	−351.8	−318.3	−368.5
	DLU GIAO	−190.1	−79.3	−245.5		DLU GIAO	−350.3	−315.1	−367.8
	Expt.	−172	−99	−206		Expt.	−269	−282	−262
$[\mathbf{OsOF_5}]$	X2C RKB	−313.0	−183.8	−377.5					
	X2C RMB	−312.4	−183.3	−376.9					
	X2C GIAO	−311.8	−181.7	−376.8					
	DLU RKB	−313.1	−183.8	−377.7					
	DLU RMB	−312.4	−183.2	−376.9					
	DLU GIAO	−311.8	−181.7	−376.8					
	Expt.	−324	−197	−387					

correction terms in the spin–orbit perturbation ansatz,[471] as the additional derivatives of $\mathbf{W}_u^B$ due to RMB correspond to these two terms (cf. Eq. 7 in the Supporting Information of Ref. [518] and Eq. 17 in Ref. [447]). Additionally, the minor impact of the GIAOs for these systems can be rationalized by analyzing the individual terms for the EPR g-tensor in Eq. 3.63. The contribution of the one-electron potential and the two-electron integrals compensate each other to a large extent. The main advantage of GIAOs for these compounds is that the working equations become gauge-origin invariant. As expected, the DLU error is again negligible in all cases, and is lower than the impact of the balance condition. In Sec. 3.4.5, we explore a system which exhibits significant gauge-origin dependence, leading to a more pronounced GIAO impact.

To summarize, including the derivatives of the decoupling transformation and the restricted magnetic balance condition (with or without GIAOs) results in a minor but consistent improvement in g-tensor predictions for the majority of transition-metal complexes studied here. These corrections are larger in magnitude than the error imparted through the use of DLU. The formal improvements do not incur significant computational costs in excess of their counterparts (which use the kinetic balance and ignore these additional derivatives), and can thus be routinely included in the calculation of EPR g-tensors using X2C.

Basis Set Study

The results of the relativistic all-electron basis set study on the 17 aforementioned transition-metal complexes are summarized in Figure 3.8. For each basis set, the mean absolute percent-wise deviation (MAPD) and the corresponding standard deviation (STD) was computed over the sum of 15 compounds. Note that $[TcNCl_4]^-$ and $[WOF_5]^{2-}$ were neglected in the

statistical evaluation. The MAPD is calculated as follows:

$$\mathrm{MAPD} = \sum_{i=1}^{N=15} \frac{|\Delta g_{i,\mathrm{iso}}^{\mathrm{test}} - \Delta g_{i,\mathrm{iso}}^{\mathrm{ref}}|}{|\Delta g_{i,\mathrm{iso}}^{\mathrm{ref}}|} \tag{3.69}$$

where $\Delta g_{i,\mathrm{iso}}^{\mathrm{test}}$ and $\Delta g_{i,\mathrm{iso}}^{\mathrm{ref}}$ denote the isotropic g-shift for the test basis set and the reference basis set, respectively.

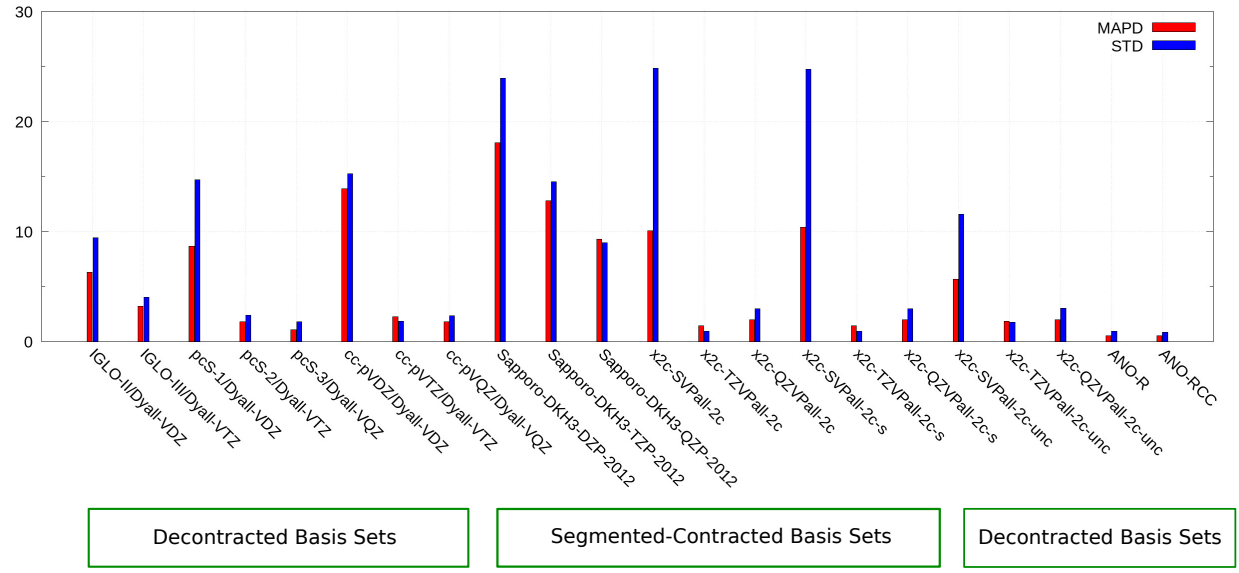

Figure 3.8: Assessment of various basis sets compared to an even-tempered reference for 15 of the 17 transition-metal complexes. $[TcNCl_4]^-$ is omitted due to a small absolute Δg shift (4 ppt) and $[WOF_5]^{2-}$ is neglected in the statistical evaluation due to convergence issues for the alignment of spin x and y with the ET basis. MAPD and STD denote the mean absolute percent-wise error and its standard deviation. For brevity, the suffix "unc" is omitted for the combinations of the Dyall basis and the ANO basis sets. See Tab. 3.9 for further details on the basis sets and their size. Note that we excluded the Jorge basis sets due to large errors of more than 90%.

From the figure, it is clear that the double-ζ bases for the heavy elements are generally insufficient. Conversely, the triple-ζ quality basis sets aside from the Sapporo-DKH3-TZP-2012 and IGLO-III configurations achieve accurate results when compared to the reference values, with MAPDs of less than 3% (x2c-TZVPall-2c: 1.46%, pcS-2/Dyall-VTZ: 1.82%, cc-pVTZ/Dyall-VTZ: 2.26%). In particular, going to the quadruple-ζ quality analog did not significantly change the MAPD and STD for all basis sets. This also holds true when

comparing the decontracted and contracted x2c-XZVPall-2c (X=T,Q) basis sets. The ANO-R and ANO-RCC basis sets achieve the lowest MAPD and STD of all configurations studied, at 0.52/0.94 and 0.53/0.87, respectively.

The Sapporo bases perform consistently worse than the others included in this study, which starkly contrasts with its strong performance for the HFC constant observed in our previous work for the same set of compounds.[15] Even the quadruple-ζ Sapporo basis sets yield an MAPD and STD of over 9.32%. Thus, the results are more similar to the NMR shielding studies, in which the x2c-type and Dyall bases outperformed the Sapporo bases.[246,363]

In summary, these results indicate that triple-ζ quality basis sets are sufficient for accurate calculations of the g-tensor when using the cc-pVTZ/Dyall-VTZ, x2c-TZVPall-2c, and x2c-TZVPall-2c-s basis sets for these species. In particular, quadruple-ζ or even decontracted basis sets are unnecessary if the x2c-TZVPall-2c basis set is used, which significantly reduces the total basis set dimension. Quadruple-ζ basis sets may be used for benchmark calculations.

Study of Density Functional Approximations

The impact of frequently used density functionals of various rungs of Jacob's ladder is shown in Fig. 3.9 for the set of 17 transition–metal complexes. Similar to other magnetic properties,[415–423,499] hybrid functionals usually lead to an improvement over pure density functionals. Yet, the errors of the hybrid functionals are systematically larger than those found previously for the HFC constant. Specifically, the errors for the g-tensor range from roughly 10% to 30%, whereas errors for the HFC constant span from 5% to less than 25%.[15] This increase in error is mainly caused by [$ReOBr_4$], as all functionals yield a Δg-shift of about -30 to -40 ppt compared to the experimental finding of -98 ppt (measured in H_2SO_4) for this compound. Setting the COSMO parameters for this solvent ($\epsilon_r = 21.9$ and refractive index 1.427) yields a Δg-shift of -37 ppt for ωB97X-D. Therefore, modeling the solvent

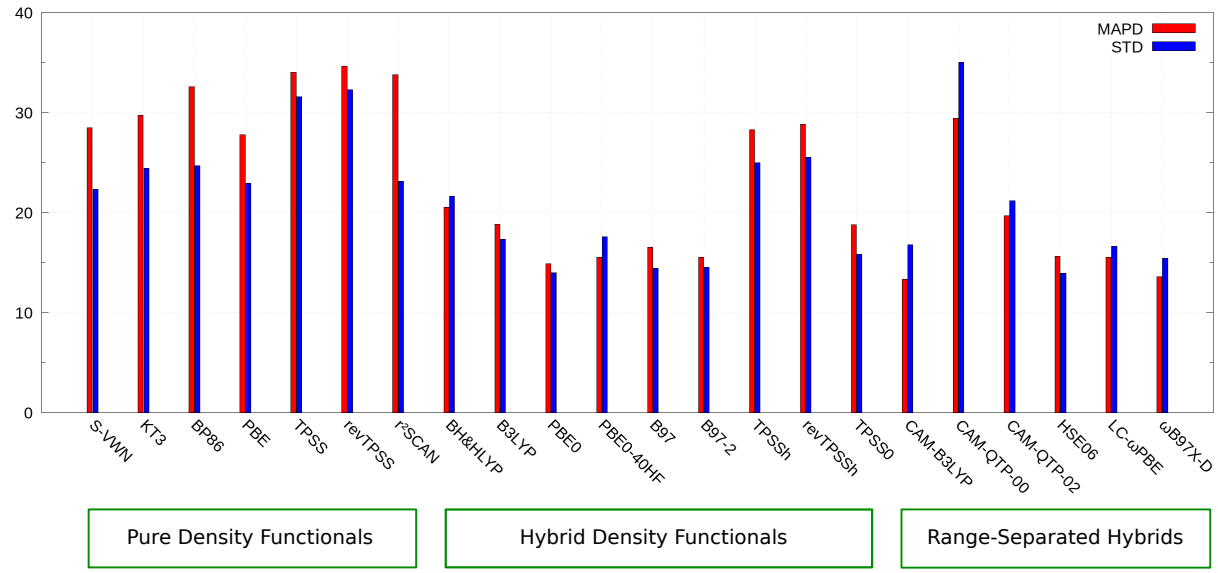

Figure 3.9: Assessment of density functional approximations compared to the experimental findings for 15 of the 17 transition-metal complexes. $[ReNBr_4]^-$ and $[TcNCl_4]^-$ are neglected in the statistical evaluation. MAPD and STD denote the mean absolute percent-wise error and its standard deviation.

with COSMO leads to a minor, ~ 1 ppt change in Δg-shift, and the discrepancy with the experimental result can likely be attributed to the DFT method error.

The errors of global hybrid functionals cover a range from 15% to 30%. The B97 family and PBE0 perform best within this class. Note that B97 and B3LYP performed poorly for the HFC constants. TPSSh and revTPSSh do not include a sufficient amount of HF exchange as shown by the reduced errors for TPSS0 with 25% of exchange instead of 10%. The performance of the latter is on par with B3LYP and BH&HLYP. Thus, considering the (generalized) kinetic energy density in the functional approximation does not generally reduce the errors for both pure density functionals and hybrid functionals.

Range-separation or the Coulomb-attenuating method do not achieve consistent improvements; whereas CAM-B3LYP reduced the errors compared to its parent B3LYP (13.35% vs. 18.81%), CAM-QTP-00 shows the largest errors among all hybrid functionals. CAM-B3LYP and ωB97X-D yield slightly smaller errors than PBE0 and are the top performs.

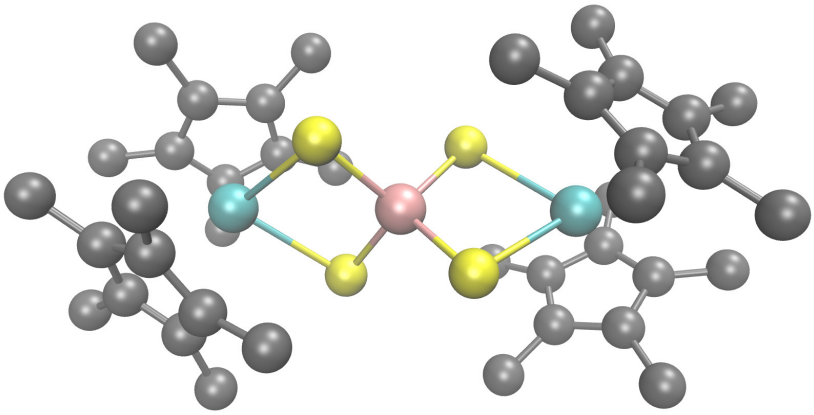

Figure 3.10: Molecular structure of $[(C_5Me_5)_2Y(\mu\text{-}S)_2Mo(\mu\text{-}S)_2Y(C_5Me_5)_2]^-$ from Ref. [521]. Color code: C, gray; S, yellow; Y, cyan; and Mo, pink. Hydrogen atoms are omitted.

Overall, ωB97X-D, CAM-B3LYP, PBE0, LC-ωPBE, B97-2, and HSE06 perform best with MAPDs of 13–15%. PBE0, ωB97X-D, and LC-ωPBE show very similar errors as for the HFC constant and are recommend for an error-balanced calculation of EPR spectra.

Gauge-Origin Dependence for Trimetallic Species

Recent investigations into the gauge-origin dependence of g-tensors and the associated error have demonstrated that it becomes non-negligible for large systems with more than one spin center, rivaling or exceeding the basis-set error in some cases.[476] In this section, we expound on these prior observations by comparing the g-tensors for $[(C_5Me_5)_2Y(\mu\text{-}S)_2Mo(\mu\text{-}S)_2Y(C_5Me_5)_2]^-$ calculated using a common gauge-origin method and our gauge-independent RMB-GIAO ansatz. This $S = 1/2$, MoS_4^{3-}-bridged diyttrium compound, depicted in Fig. 3.10, was experimentally shown to exhibit significant delocalization of the spin density from the Mo atom onto the Y atoms,[521] and it is thus expected to exhibit a more pronounced gauge-origin dependence. Herein, the CGO for the RKB-CGO method was chosen as the position of the Mo and Y atoms. Mo represents the area with the largest spin density and is approximately the "spin density center" as defined in Ref. [476]. The results with are given in Tab. 3.12.

Table 3.12: Principal components of the g-tensor and corresponding g-shift in ppt for $[(C_5Me_5)_2Y(\mu\text{-}S)_2Mo(\mu\text{-}S)_2Y(C_5Me_5)_2]^-$. RKB and RMB refer to restricted kinetic and magnetic balance, while CGO and GIAO denote a common gauge origin and gauge-including atomic orbitals, respectively. The atom specified after CGO denotes the coordinates of the chosen gauge origin. We use the mSNSO-DLU-X2C Hamiltonian with the x2c-TZVPPall-2c (Mo, Y) and x2c-SVPall-2c (H, C, S) basis set combinations. Additional data using the computationally optimized structure are given as Supporting Information of the original publication.[518] Experimental (Expt.) results are taken from Ref. [521].

		g-Tensor			g-Shift		
Functional	Hamiltonian	g_{11}	g_{22}	g_{33}	Δg_{11}	Δg_{22}	Δg_{33}
TPSSh	RKB CGO Mo	1.986	1.995	2.000	16.07	7.05	2.62
	RKB CGO Y1	1.986	1.993	2.001	16.15	9.14	0.90
	RKB CGO Y2	1.986	1.991	2.003	16.10	11.43	−1.08
	RMB GIAO	1.989	1.998	2.003	13.57	4.60	−0.20
ωB97X-D	RKB CGO Mo	1.980	1.984	1.989	22.03	18.72	13.61
	RKB CGO Y1	1.979	1.983	1.991	22.85	19.78	11.50
	RKB CGO Y2	1.978	1.982	1.993	24.06	20.50	9.22
	RMB GIAO	1.982	1.986	1.991	20.01	16.82	11.78
Expt.		1.972	1.980	1.988	30.32	22.32	14.32

Between the functionals studied here, the deviations of the g-tensor for the RKB CGO and RMB GIAO methods range from 2–7 ppt, which constitutes greater than 10% of all total g-shifts and their principal components. The largest changes of 50% and 25% are found for the g_{22} component with TPSSh and ωB97X-D, respectively. This is significantly larger than the gauge-origin dependence observed for the $[Pt(C_6Cl_5)_4]^-$ complex (explored in Sec. 3.4.5), which exhibits $\sim$ 1 ppt differences in absolute g-shifts that are, in and of themselves, 1–2 orders of magnitude larger than those observed for $[(C_5Me_5)_2Y(\mu\text{-}S)_2Mo(\mu\text{-}S)_2Y(C_5Me_5)_2]^-$. This reinforces prior observations that gauge-origin dependence becomes more pronounced for systems which exhibit appreciable spin-delocalization. The magnitude of the gauge error exceeds that observed from omitting the derivatives of the decoupling matrix and from the use of the DLU scheme in the previous transition-metal studies. These observations also hold for calculations on the computationally optimized structure.

The g-tensors with CGOs at the Mo and Y atoms may lie closer to experimental results

than those obtained from RMB-GIAO for the chosen functionals. This result may be attributed to DFT method error, or additionally to the manifestation of CGO as an unphysical "parameter" which can be varied to adjust g-tensor predictions. This can be observed by the variation in g-shifts with the choice of CGO between the Mo and Y atoms, which both improve and worsen them relative to the experimental values. Regardless, the g-tensors for both ansätze adequately match the experimental results, with deviations by at most 17 ppt.

In summary, the pronounced gauge-origin dependence observed for $[(C_5Me_5)_2Y(\mu\text{-}S)_2Mo(\mu\text{-}S)_2Y(C_5Me_5)_2]^-$ demonstrates that the choice of an intuitive common gauge origin (i.e. through the spin density center approach) may not be appropriate for such systems, motivating the use of GIAO-based methods.

Application to $[Pt(C_6Cl_5)_4]^-$

To further illustrate the accuracy of the method and to complement the previous DFT study in Sec. 3.4.5 for larger molecules, we apply the X2C and the DLU-X2C Hamiltonian to $[Pt(C_6Cl_5)_4]^-$, which is described by more than 2500 basis functions. The g-shifts are listed in Tab. 3.13. Generally, the uncontracted pcS-2/Dyall-VTZ and the segmented-contracted x2c-QZVPall-2c basis sets lead to very similar results between the RKB condition and the RMB condition using both the common gauge origin and RMB-GIAO ansatz. The largest change introduced by GIAOs is found for TPSSh and TPSS0 with 6 ppt.

Overall, the CAM-QTP functionals perform remarkably well for the isotropic shift and the three principal components. Note that the performance of CAM-QTP-00 is in stark contrast to the findings in Sec. 3.4.5 and the accuracy of CAM-QTP-00 thus depends significantly on the system under consideration.

Among the six top performers of the last section, PBE0, B97-2, and HSE06 perform poorly for $[Pt(C_6Cl_5)_4]^-$ with deviations of about 23–25% for the isotropic g-shift. ωB97X-D and

Table 3.13: Principal components of the g-shift for $[Pt(C_6Cl_5)_4]^-$ in ppt. RKB and RMB refer to restricted kinetic and magnetic balance, while CGO and GIAO denote a common gauge origin and gauge-including atomic orbitals, respectively. We use the mSNSO-DLU-X2C Hamiltonian. Experimental (Expt.) results are taken from Ref. [429].

		pcS-2-unc/Dyall-VTZ-unc				x2c-QZVPall-2c			
Functional	Hamiltonian	Δg_{iso}	Δg_{11}	Δg_{22}	Δg_{33}	Δg_{iso}	Δg_{11}	Δg_{22}	Δg_{33}
BH&HLYP	RKB CGO	553	−372	953	1078	549	−374	949	1072
	RMB CGO	554	−371	954	1079	550	−372	950	1072
	RMB GIAO	553	−371	953	1079	550	−372	950	1072
B3LYP	RKB CGO	425	−409	648	1002	420	−412	676	997
	RMB CGO	427	−408	685	1003	422	−410	678	998
	RMB GIAO	426	−408	683	1004	422	−410	678	998
PBE0	RKB CGO	462	−350	787	948	454	−354	779	938
	RMB CGO	463	−349	788	949	456	−352	780	939
	RMB GIAO	462	−349	787	949	456	−352	780	939
PBE0-40HF	RKB CGO	513	−337	888	988	510	−341	885	986
	RMB CGO	514	−337	890	989	511	−339	886	987
	RMB GIAO	513	−337	888	989	511	−339	886	987
B97-2	RKB CGO	460	−378	750	1008	455	−382	743	1006
	RMB CGO	461	−377	752	1009	457	−380	744	1007
	RMB GIAO	461	−377	750	1010	457	−380	745	1007
TPSSh	RKB CGO	326	−355	581	751	317	−359	576	734
	RMB CGO	327	−354	582	752	319	−357	578	736
	RMB GIAO	333	−351	588	762	325	−354	585	745
TPSS0	RKB CGO	435	−310	752	864	430	−313	747	856
	RMB CGO	436	−309	753	865	430	−313	747	856
	RMB GIAO	441	−307	759	873	437	−310	755	865
CAM-B3LYP	RKB CGO	535	−397	919	1083	534	−399	917	1084
	RMB CGO	536	−396	921	1084	535	−398	918	1085
	RMB GIAO	536	−396	919	1084	535	−398	918	1085
CAM-QTP-00	RKB CGO	601	−382	1034	1150	603	−384	1035	1158
	RMB CGO	602	−381	1036	1151	604	−382	1036	1158
	RMB GIAO	601	−381	1034	1150	604	−382	1036	1158
CAM-QTP-02	RKB CGO	614	−413	1057	1198	609	−416	1056	1186
	RMB CGO	615	−413	1058	1199	610	−415	1057	1187
	RMB GIAO	614	−413	1056	1198	610	−415	1057	1187
HSE06	RKB CGO	446	−364	759	943	443	−367	754	941
	RMB CGO	447	−363	760	945	444	−365	755	942
	RMB GIAO	447	−363	758	945	444	−365	755	943
LC-ωPBE	RKB CGO	534	−349	940	1011	531	−353	938	1008
	RMB CGO	535	−348	942	1012	532	−351	939	1008
	RMB GIAO	534	−348	940	1011	532	−351	939	1009
ωB97X-D	RKB CGO	529	−398	893	1093	528	−401	891	1094
	RMB CGO	530	−397	894	1094	529	−399	892	1095
	RMB GIAO	530	−397	893	1094	529	−399	892	1095
Expt.		594	−400	1005	1177	594	−400	1005	1177

CAM-B3LYP each reproduce one of the three components very well, but lose ground for the other components. Still, the error of the isotropic shifts amounts to only 11%. LC-ωPBE shows deviations of 7–13% for the principal components and the g-shift is essentially the same as that obtained with CAM-B3LYP and ωB97X-D.

In conclusion, we recommend CAM-B3LYP, LC-ωPBE, and ωB97X-D for g-tensor calculations of d elements, as these functionals yield reasonable results for the g-tensors of the 17 transition-metal complexes in Sec. 3.4.5 and $[Pt(C_6Cl_5)_4]^-$. LC-ωPBE and ωB97X-D appear to represent the best choices for calculating both the g-tensor and the HFC tensor.

Assessment of Efficiency for $[Pt(C_6Cl_5)_4]^-$

The computation times of an SCF and a g-tensor calculation for $[Pt(C_6Cl_5)_4]^-$ with the uncontracted pcS-2/Dyall-VTZ basis set (2668 basis functions) and the x2c-QZVPall-2c basis set (3003 contracted basis functions, 4720 primitive basis functions) are listed in Tab. 3.14. using 12 threads of an Intel® Xeon® Gold 6212U CPU @ 2.40 GHz.

The total time for an SCF calculation using the pcS-2/Dyall-VTZ basis set is 5.5–8 hours, while the RMB-GIAO approach for the g-tensor only takes 1 hour. The HF exchange (HF-K) integrals clearly dominate the computational costs for this approach. In contrast, the DLU one-electron part takes less time than the RI-J and the XC contributions while introducing an error of only 0.8 ppt. To compare, the RI-J error is 1.1 ppt. For pure density functionals and the RMB-GIAO approach, the computation time of the full X2C Hamiltonian is much larger than that of the respective RI-J integrals and the XC terms. Therefore, the one-electron X2C step will dominate the corresponding computational costs for pure density functionals.

The timings given herein are significantly faster than those obtained in Ref. [129] (24–48 hours with 8–12 cores of an Intel® Xeon® CPU X550 CPU @ 2.67 GHz), despite using a

Table 3.14: Computation time (in minutes) for various steps of an EPR g-tensor calculation with PBE0 using 12 threads of an Intel® Xeon® Gold 6212U CPU @ 2.40 GHz. The number of SCF iterations is given in parenthesis and 1e denotes the one-electron part.

		pcS-2-unc/Dyall-VTZ-unc		x2c-QZVPall-2c	
Ansatz	Part	X2C	DLU-X2C	X2C	DLU-X2C
SCF	Total	334.1–479.5 (69-109)		1593–2511 (64-106)	
RKB CGO	1e	9.5	0.3	64.8	1.0
RMB CGO	1e	9.5	0.4	69.7	1.5
RMB GIAO	1e	10.1	0.8	75.0	2.6
RMB GIAO	RI-J	1.2	1.2	2.5	2.5
RMB GIAO	HF-K	57.5	57.5	234.4	234.4
RMB GIAO	XC	2.0	2.0	7.1	7.1

significantly larger basis set (pcS-2/Dyall-VTZ with 2668 functions vs. IGLO-III/Dyall-TZ with 2205 functions), larger grids for the DFT part, and the RMB-GIAO ansatz including derivatives of the unitary transformation.

Matters are similar for the x2c-QZVPall-2c basis set. Here, the SCF procedure requires 26.5 to 41.9 hours for 64–106 iterations, see also Ref. [15], and the EPR g-tensor calculations amount to at most 4.2 hours. Again, the acceleration of the DLU scheme is significant as it leads to a speed-up by a factor of 29–61 for the one-electron part. The speed-up decreases from RKB-CGO to RMB-GIAO as more integral derivatives need to be evaluated and all blocks of the integrals are required for the interatomic off-diagonal corrections of DLU.

In conclusion, calculations of large molecules are possible with limited computational resources and the convergence of the SCF procedure is the time-determining part of the computational protocol. Therefore, the GIAO-RMB ansatz can be routinely used for large-scale calculations. With the DLU scheme, the one-electron parts is less demanding than the two-electron terms of pure density functionals.

3.4.6 Application to Lanthanide Molecules

We demonstrated in Section 3.3 that the one-electron X2C framework produces accurate hyperfine coupling constants for the three lanthanide complexes $[La(OAr^*)_3]^-$, $[Lu(NR_2)_3]^-$, and $[Lu(OAr^*)_3]^-$ of Ref. [14], which represent potential molecular qubit materials.[15] To further show that the spin Hamiltonian parameters for this class of important compounds can be accurately predicted by X2C, we proceed to calculate the g-tensors for these three lanthanide complexes using the RKB-CGO, RMB-CGO, and RMB-GIAO approaches and the CAM-B3LYP, LC-ωPBE, and ωB97X-D density functionals, which performed best in the benchmark studies of Sections 3.4.5 and 3.4.5. The TPSS functional was also included for consistency with the DFT study of these systems in the initial report.[14] Results obtained using the x2c-TZVPPall-2c/x2c-SVPall-2c basis set combination are provided in Table 3.15. Additional calculations, including those performed with the x2c-QZVPall-2c/x2c-SVPall-2c basis set, as well as with a selection of other functionals, are given in the supporting information of the original publication.[518] Calculations of the electric field gradient (EFG) and the nuclear quadrupole interaction (NQI) tensors with X2C are detailed in Appendix 3.5.

While in some cases the RMB GIAO ansatz yielded modest improvements to the predicted g-tensor components in $[La(OAr^*)_3]^-$, $[Lu(NR_2)_3]^-$, and $[Lu(OAr^*)_3]^-$, the overall differences between the three ansätze remained small. For the remainder of this section, we therefore compare RMB GIAO results with experimental results, and errors in g-tensor components are computed as shifts in ppt by: $\Delta g = (g - g_{expt}) \cdot 1000$.

Among the functionals studied, ωB97X-D produced the most accurate g-tensors when compared to experimental results, with errors less than 20 ppt between all three compounds. The largest errors were observed in $[Lu(NR_2)_3]^-$ for this functional, with each component of the g-tensor underestimating the experimental result. In comparison, the other RSH func-

Table 3.15: Principal components of the g-tensor for the three spin-$\frac{1}{2}$ La(II) and Lu(II) molecules $[La(OAr^*)_3]^-$, $[Lu(NR_2)_3]^-$, and $[Lu(OAr^*)_3]^-$ (OAr^* = 2,6-Ad_2-4-t-Bu-C_6H_2O, Ad = adamantyl, t-Bu= tert-butyl, R = $SiMe_3$ with Me = methyl).[14] RKB and RMB refer to restricted kinetic and magnetic balance, while CGO and GIAO denote a common gauge origin and gauge-including atomic orbitals, respectively. We use the mSNSO-DLU-X2C Hamiltonian. The x2c-TZVPPall-2c/x2c-SVPall-2c basis sets are employed. We refer to the Supporting Information of the original publication[518] for the results obtained using the x2c-QZVPall-2c/x2c-SVPall-2c basis sets. Experimental (Expt.) results are taken from Ref. [14]. The experimental uncertainties are 0.002.

		$[La(OAr^*)_3]^-$			$[Lu(NR_2)_3]^-$			$[Lu(OAr^*)_3]^-$		
Functional	Hamiltonian	g_{11}	g_{22}	g_{33}	g_{11}	g_{22}	g_{33}	g_{11}	g_{22}	g_{33}
TPSS	RKB CGO	1.897	1.897	1.998	1.885	1.885	1.995	1.907	1.907	1.995
	RMB CGO	1.897	1.897	1.998	1.886	1.886	1.996	1.909	1.909	1.998
	RMB GIAO	1.895	1.895	1.998	1.884	1.884	1.997	1.909	1.909	1.998
CAM-B3LYP	RKB CGO	1.928	1.928	1.998	1.874	1.874	1.996	1.916	1.920	1.997
	RMB CGO	1.930	1.930	2.000	1.875	1.876	1.998	1.918	1.922	1.999
	RMB GIAO	1.924	1.924	2.000	1.875	1.875	1.998	1.914	1.918	1.999
LC-ωPBE	RKB CGO	1.905	1.906	1.998	1.877	1.878	1.995	1.905	1.905	1.996
	RMB CGO	1.907	1.908	1.999	1.879	1.879	1.997	1.908	1.908	1.998
	RMB GIAO	1.905	1.907	1.999	1.879	1.879	1.997	1.908	1.909	1.998
ωB97X-D	RKB CGO	1.879	1.880	1.996	1.875	1.877	1.996	1.900	1.901	1.996
	RMB CGO	1.881	1.882	1.997	1.876	1.879	1.998	1.903	1.904	1.998
	RMB GIAO	1.879	1.881	1.997	1.876	1.878	1.998	1.902	1.903	1.998
Expt.		1.876	1.886	2.000	1.882	1.898	2.000	1.915	1.915	2.000

tionals CAM-B3LYP and LC-ωPBE struggle for both $[La(OAr^*)_3]^-$ and $[Lu(NR_2)_3]^-$, with errors reaching up to 48 ppt for the g_{11} component of $[La(OAr^*)_3]^-$. In such cases, the TPSS g-tensors were more accurate than those produced by these more advanced functionals, with errors not exceeding 19 ppt. The g-tensors produced by the four DFAs are accurate for $[Lu(OAr^*)_3]^-$, with errors under 15 ppt in each case.

Taken together, the RSH functionals do not yield a consistent improvement over pure density functionals for these systems. However, ωB97X-D continues to perform well between the above transition-metal complexes of the benchmark studies and the Ln complexes investigated here, suggesting that it is a robust option for calculating g-tensors for metal complexes. Overall, errors in the principal components of the g-tensor do not exceed 48 ppt for all functionals tested, indicating that g-tensors for the three Ln compounds can be accurately and

efficiently obtained using local exact two-component theory. These observations also hold for predictions of the g-tensor obtained using the x2c-QZVPall-2c/x2c-SVPall-2c basis sets, which is included in the Supporting Information of the original publication.[518] This confirms the findings of Sec. 3.4.5 and shows that triple-ζ basis sets are sufficient for the calculation of the g-tensor.

3.4.7 Summary

A gauge-origin invariant implementation of X2C theory for EPR g-tensors has been presented. This includes the complete derivative of the X2C Hamiltonian, which was not considered in prior implementations. Our method reinserts the previously omitted derivatives, resulting in a more rigorous formalism that can be used for routine relativistic g-tensor calculations.

Additionally, we employ GIAOs and the RMB condition for the basis set expansion, which allows the ansatz to accurately describe molecular systems with a spatially distributed spin density and ambiguous choice of common gauge origin. This is essential for the study of systems with strong magnetic exchange between metal atoms, which is a desirable property for enabling SMM behavior.

The working equations associated with these two advancements, which have been presented as part of this work, demonstrate that relativistic g-tensors can be obtained in a gauge-invariant formalism through re-purposing an existing two-component NMR shift implementation, which is already available in many relativistic codes.

To increase the computational efficiency of the method, we incorporated the DLU. In doing so, the relativistic one-electron part of the Hamiltonian becomes less demanding than the two-electron contributions of pure density functionals, and the costs associated with includ-

ing the full derivative of the X2C Hamiltonian and the gauge-invariant formalism become negligible.

The advancements described above for the relativistic g-tensor, as well as our prior work on hyperfine coupling constants, constitute a robust approach that can be readily applied to the prediction of EPR parameters for large transition metal and lanthanide-based complexes, which are of great magnetic interest for application as SMMs or molecular qubits. These calculations can be applied broadly to both the interpretation of existing EPR data, as well as the prediction of g-tensors for theoretical systems in search of optimal magnetic properties.

3.5 Electric Field Gradient and Nuclear Quadrupole Tensor in Exact Two-Component Theory

Theory

The nuclear quadrupole interaction (NQI) tensor $\overleftrightarrow{Q}$ is commonly used to supplement analysis of the hyperfine interaction, as demonstrated in the study of Ln(II) complexes discussed in Section 3.2.[14] The NQI tensor can be computed based on the electric field gradient (EFG), which is the second derivative of the potential. In this formalism, the NQI tensor at the position of the central lanthanide atom $\vec{R}_N$ reads

$$\overleftrightarrow{Q}(\vec{R}_N) = \frac{Q_c}{2I(I-1)}\overleftrightarrow{V}(\vec{R}_N) \tag{3.70}$$

where Q_c refers to the quadrupole constant and I refers to the nuclear spin of the studied isotope. The experimentally determined quadrupole moments of ^{139}La and ^{175}Lu are 0.20 b and 3.49 b, respectively.[249] The nuclear spins are 7/2 for both nuclei. The electric field gradient $\overleftrightarrow{V}$ consists of a nuclear contribution V_{pq}^{nuc} and an electronic contribution V_{pq}^{el}. In the

Born–Oppenheimer approximation, the nuclear contribution at the position of the nucleus N is directly obtained based on the quadrupole operator $\hat{Q}_{pq}$ according to

$$\begin{aligned} V_{pq}^{\mathrm{nuc}}(\vec{R}_N) &= \sum_{K \neq N} Z_K \; \hat{Q}_{pq}(\vec{R}_N, \vec{R}_K) \\ &= \sum_{K \neq N} Z_K \frac{3(R_{N,p} - R_{K,p})(R_{N,q} - R_{K,q}) - \delta_{pq}(\vec{R}_N - \vec{R}_K)^2}{|\vec{R}_N - \vec{R}_K|^5} \end{aligned} \tag{3.71}$$

Note that the point charge model is employed for the quadrupole operator. The electronic contribution depends on the electron density ρ or the density matrix $\mathbf{P}$ and follows as

$$V_{pq}^{\mathrm{el}}(\vec{R}_N) = -\int \rho(\vec{r}) \; \hat{Q}_{pq}(\vec{R}_N, \vec{r}) \; d^3r \tag{3.72}$$

In X2C, the evaluation of the electronic contribution requires a relativistic picture-change transformation.[523,524] The X2C Hamiltonian is obtained by the unitary transformation

$$\mathbb{U}^\dagger \mathbb{D} \mathbb{U} = \begin{pmatrix} \mathbf{h}^+ & \mathbf{0}_2 \\ \mathbf{0}_2 & \mathbf{h}^- \end{pmatrix} \qquad \text{with} \qquad \mathbb{U}^\dagger \mathbb{U} = \mathbb{U}\mathbb{U}^\dagger = \mathbb{I}_4 \tag{3.73}$$

and this transformation is also required for expectation values. Thus, the matrix representation of the quadrupole operator $\hat{Q}_{pq}$ is required in the four-component Dirac space. Note that $\hat{Q}_{pq}$ is an even operator.[269] Consequently, only the large-large (LL) and the small-small (SS) blocks will be non-zero. The unitary X2C transformation is then applied to transform the four-component representation to a two-component framework. In a restricted kinetically balanced basis set,[105] the matrix representation of the large-large block follows as

$$\left(\mathbf{Q}_{pq}^{\mathrm{LL}}\right)_{\mu\nu} = \begin{pmatrix} \left(\boldsymbol{Q}_{pq}\right)_{\mu\nu} & 0 \\ 0 & \left(\boldsymbol{Q}_{pq}\right)_{\mu\nu} \end{pmatrix} \quad \text{with} \quad \left(\boldsymbol{Q}_{pq}\right)_{\mu\nu} = \langle \lambda_\mu | \hat{Q}_{pq} | \lambda_\nu \rangle \tag{3.74}$$

Note that we dropped the superscript of the electronic contribution for simplicity. The small-

small block is of the same structure as the relativistically modified potential $\mathbf{W}$ and given by

$$\left(\mathbf{Q}_{pq}^{\mathrm{SS}}\right)_{\mu\nu} = \frac{1}{4c^2}\,\langle\phi_\mu|\left(\vec{\sigma}\cdot\hat{\vec{p}}\right)\hat{Q}_{pq}\left(\vec{\sigma}\cdot\hat{\vec{p}}\right)|\phi_\nu\rangle \tag{3.75}$$

Therefore, the general two-component matrix can be evaluated from four real matrices like $\mathbf{W}$ according to[524]

$$\left(\mathbf{Q}_{pq}^{\mathrm{SS}}\right)_{\mu\nu} = \begin{pmatrix} \boldsymbol{Q}_{pq}^{0} + \mathrm{i}\boldsymbol{Q}_{pq}^{z} & \boldsymbol{Q}_{pq}^{y} + \mathrm{i}\boldsymbol{Q}_{pq}^{x} \\ -\boldsymbol{Q}_{pq}^{y} + \mathrm{i}\boldsymbol{Q}_{pq}^{x} & \boldsymbol{Q}_{pq}^{0} - \mathrm{i}\boldsymbol{Q}_{pq}^{z} \end{pmatrix} \tag{3.76}$$

with the real one-component matrices

$$\left(\boldsymbol{Q}_{pq}^{0}\right)_{\mu\nu} = \langle\lambda_\mu|\hat{p}_x\hat{Q}_{pq}\hat{p}_x + \hat{p}_y\hat{Q}_{pq}\hat{p}_y + \hat{p}_z\hat{Q}_{pq}\hat{p}_z|\lambda_\nu\rangle \tag{3.77}$$

$$\left(\boldsymbol{Q}_{pq}^{x}\right)_{\mu\nu} = \langle\lambda_\mu|\hat{p}_y\hat{Q}_{pq}\hat{p}_z - \hat{p}_z\hat{Q}_{pq}\hat{p}_y|\lambda_\nu\rangle \tag{3.78}$$

$$\left(\boldsymbol{Q}_{pq}^{y}\right)_{\mu\nu} = \langle\lambda_\mu|\hat{p}_z\hat{Q}_{pq}\hat{p}_x - \hat{p}_x\hat{Q}_{pq}\hat{p}_z|\lambda_\nu\rangle \tag{3.79}$$

$$\left(\boldsymbol{Q}_{pq}^{z}\right)_{\mu\nu} = \langle\lambda_\mu|\hat{p}_x\hat{Q}_{pq}\hat{p}_y - \hat{p}_y\hat{Q}_{pq}\hat{p}_x|\lambda_\nu\rangle \tag{3.80}$$

The spin-free matrix $\boldsymbol{Q}_{pq}^{0}$ is symmetric, whereas the three spin-dependent matrices are anti-symmetric. Therefore, the picture-change correction (PCC) becomes

$$\mathbf{Q}_{pq}^{\mathrm{PCC}} = \begin{pmatrix} \mathbf{U}^{\mathrm{LL},\dagger} & \mathbf{U}^{\mathrm{SL},\dagger} \end{pmatrix} \mathbb{Q}_{pq} \begin{pmatrix} \mathbf{U}^{\mathrm{LL}} \\ \mathbf{U}^{\mathrm{SL}} \end{pmatrix} \tag{3.81}$$

After the picture-change transformation, we form the trace of $\mathbf{Q}_{pq}^{\mathrm{PCC}}$ and the two-component density matrix $\mathbf{P}$. Neglecting the spin-dependent contributions leads to a scalar-relativistic one-component approach. Note that we use the sign convention of Refs. [523] and [524]. Thus, the sign of $\overset{\leftrightarrow}{V}$ differs from Ref. [14]. The conversion factor assumes a nuclear spin of $I = 7/2$.

Herein, we implemented the picture-change correction for the EFG using the infrastructure developed in Refs. [289] and [510]. Thus, (local) X2C theory,[114–120] the arbitrary-

order DKH ansatz,[272–274,463,525] and the Barysz–Sadlej–Snijders Hamiltonian[111,526–528] are supported. The required integrals are evaluated with Gauss–Rys and Gauss–Hermite integration. The Gauss–Rys scheme[319,320,514,515] is used for the integration stemming from the Laplace-like transformation[529] and the Gauss–Hermite method is applied to the spatial integration. The SNSO approximation is available for the spin-dependent parts of the small-small block.[289] The EFG is transformed to its principal axis system by a straightforward diagonalization. In this principal axis system, the NQI tensor becomes

$$\overleftrightarrow{Q}(\mathrm{MHz}) = \begin{pmatrix} Q_{11} & 0 & 0 \\ 0 & Q_{22} & 0 \\ 0 & 0 & Q_{33} \end{pmatrix} = 5.5944 \cdot Q_c(\mathrm{b}) \cdot V_{zz}(\mathrm{a.u.}) \begin{pmatrix} -(1-\eta) & 0 & 0 \\ 0 & -(1-\eta) & 0 \\ 0 & 0 & 2 \end{pmatrix} \quad (3.82)$$

η is a dimensionless antisymmetry parameter.[14] The trace of the NQI tensor $\overleftrightarrow{Q}$ vanishes.

Results for Lanthanide Molecules

The electric field gradient and the nuclear quadrupole interaction tensors are calculated for $[La(OAr^*)_3]^-$, $[Lu(NR_2)_3]^-$, and $[Lu(OAr^*)_3]^-$. The same computational settings as for the hyperfine coupling tensor and the g-tensor are applied. Thus, the finite nucleus model is used for the self-consistent field procedure to avoid singularities and the point-charge model is used for the quadrupole operator $\hat{Q}_{pq}$ of the EFG. The principal components of the EFG tensors are given in Tab. 3.16. Using Eq. 3.82 the NQI tensor is calculated in the principal axis system. The results are listed in Tab. 3.17.

The scalar-relativistic (SR) results show that the picture-change correction is of great importance, as it changes both the EFG and the NQI by one order of magnitude over the SR-NR method. Moreover, the tensors show a pronounced dependence on the basis set and the density functional approximation. For the NQI of $[Lu(NR_2)_3]^-$ and $[Lu(OAr^*)_3]^-$, the scalar-

relativistic results with the picture-change correction span a range of about 20 MHz and 35 MHz. However, implementing the picture-change transformation considerably improves the prediction of the NQI over that obtained from the SR-NR method when compared to experimental findings, regardless of the basis set and functional used. The NQI of $[La(OAr^*)_3]^-$ remains close to the experimental result of zero, whereas the NQI of $[Lu(OAr^*)_3]^-$ is increased to be much closer to the experimental findings. Larger deviations are found for $[Lu(NR_2)_3]^-$. Here, the deviations towards the experimental result amount to about 20–30 MHz when considering the experimental uncertainties.

In comparison, the spin–orbit (SO) correction played a secondary role for both the EFG and NQI when compared to the picture-change correction. This resulted in a shift of the scalar-relativistic results of roughly 1–5 MHz for each configuration in either direction, with the exception being the x2c-TZVPPall-s/TPSS configuration for $[Lu(OAr^*)_3]^-$. This again shows that the x2c-TZVPPall-s is generally insufficient for two-component calculations. The large deviation of the results depending on basis set and density functional approximation is also observed for the spin–orbit method.

Our theoretical framework may be improved by the finite nucleus model for the quadrupole operator $\hat{Q}_{pq}$ in Eqs. 3.71 and 3.72 or by using very large fully decontracted basis sets as done in Refs. [523] and [524]. However, the latter seems to be impractical for large molecules such as the studied lanthanide compounds with 82–217 atoms.

Table 3.16: Principal components of the EFG in atomic units for the three spin-$\frac{1}{2}$ La(II) and Lu(II) molecules $[La(OAr^*)_3]^-$, $[Lu(NR_2)_3]^-$, and $[Lu(OAr^*)_3]^-$ (OAr^* = 2,6-Ad_2-4-t-Bu-C_6H_2O, Ad = adamantyl, t-Bu= tert-butyl, R = $SiMe_3$ with Me = methyl). Results are given in the principal axis system. The scalar-relativistic X2C ansatz combined with the non-relativistic EFG operator is taken from Ref. [14] and denoted SR-NR. Note that we changed the sign convention compared to that reference. The prefix x2c- of the basis set is omitted for brevity and only the basis set of the Ln atom is given here. Eigenvalues of the NQI tensor are given in ascending order.

		$[La(OAr^*)_3]^-$			$[Lu(NR_2)_3]^-$			$[Lu(OAr^*)_3]^-$		
Functional	Hamiltonian	V_{11}	V_{22}	V_{33}	V_{11}	V_{22}	V_{33}	V_{11}	V_{22}	V_{33}
TZVPPall-s/TPSS	SR-NR	−0.217	−0.173	0.389	−0.287	−0.285	0.573	−0.418	−0.397	0.814
	SR	−1.448	−1.395	2.843	−2.437	−2.413	4.850	−1.708	−1.686	3.394
	SO	−1.425	−1.371	2.796	−2.373	−2.350	4.723	−2.177	−2.148	4.325
TZVPPall-2c/TPSS	SR	−1.517	−1.460	2.977	−2.599	−2.574	5.173	−2.336	−2.304	4.640
	SO	−1.549	−1.491	3.039	−2.721	−2.696	5.417	−2.444	−2.411	4.855
QZVPall-2c/TPSS	SR	−1.535	−1.478	3.013	−2.659	−2.634	5.293	−2.345	−2.314	4.659
	SO	−1.546	−1.488	3.034	−2.705	−2.680	5.385	−2.373	−2.341	4.714
TZVPPall-2c/r^{2}SCAN	SR	−1.644	−1.582	3.226	−2.766	−2.742	5.508	−2.555	−2.522	5.077
	SO	−1.678	−1.615	3.293	−2.900	−2.874	5.775	−2.674	−2.640	5.314
QZVPall-2c/r^{2}SCAN	SR	−1.640	−1.579	3.219	−2.775	−2.785	5.560	−2.425	−2.492	4.917
	SO	−1.651	−1.589	3.241	−2.843	−2.818	5.661	−2.564	−2.532	5.097
TZVPPall-2c/PBE0	SR	−1.517	−1.460	2.978	−2.600	−2.575	5.175	−2.337	−2.306	4.643
	SO	−1.650	−1.589	3.239	−2.888	−2.862	5.750	−2.631	−2.597	5.228
QZVPall-2c/PBE0	SR	−1.619	−1.563	3.182	−2.815	−2.790	5.605	−2.514	−2.482	4.996
	SO	−1.631	−1.571	3.202	−2.860	−2.835	5.695	−2.550	−2.518	5.068
TZVPPall-2c/PBE0-40HF	SR	−1.825	−1.760	3.585	−2.824	−2.800	5.624	−2.621	−2.588	5.209
	SO	−1.801	−1.738	3.538	−2.943	−2.954	5.898	−2.743	−2.709	5.452
QZVPall-2c/PBE0-40HF	SR	−1.636	−1.584	3.219	−2.188	−2.793	5.611	−2.600	−2.568	5.168
	SO	−1.645	−1.596	3.241	−2.848	−2.823	5.672	−2.616	−2.584	5.200
TZVPPall-2c/CAM-QTP-02	SR	−2.041	−1.968	4.008	−3.107	−2.990	6.008	−2.623	−2.590	5.213
	SO	−2.012	−1.942	3.954	−3.157	−3.130	6.287	−2.743	−2.709	5.451
QZVPall-2c/CAM-QTP-02	SR	−1.908	−1.840	3.748	−3.083	−3.056	6.138	−2.856	−2.823	5.680
	SO	−1.886	−1.820	3.706	−2.991	−2.965	5.956	−2.698	−2.665	5.364
TZVPPall-2c/HSE06	SR	−1.731	−1.668	3.398	−2.769	−2.745	5.514	−2.527	−2.495	5.022
	SO	−1.710	−1.647	3.357	−2.903	−2.877	5.779	−2.644	−2.610	5.254
QZVPall-2c/HSE06	SR	−1.629	−1.570	3.199	−2.847	−2.821	5.668	−2.762	−2.730	5.493
	SO	−1.613	−1.554	3.167	−2.767	−2.743	5.510	−2.606	−2.574	5.180
TZVPPall-2c/CAM-B3LYP	SR	−1.900	−1.832	3.732	−2.918	−2.892	5.810	−2.662	−2.628	5.291
	SO	−1.878	−1.810	3.688	−3.055	−3.028	6.083	−2.662	−2.628	5.291
QZVPall-2c/CAM-B3LYP	SR	−1.783	−1.719	3.502	−2.980	−2.954	5.934	−2.884	−2.850	5.734
	SO	−1.767	−1.703	3.470	−2.899	−2.873	5.772	−2.732	−2.698	5.431
TZVPPall-2c/LC-ωPBE	SR	−1.821	−1.759	3.581	−2.850	−2.824	5.674	−2.617	−2.584	5.201
	SO	−1.861	−1.798	3.659	−2.987	−2.960	5.947	−2.738	−2.703	5.441
QZVPall-2c/LC-ωPBE	SR	−1.741	−1.690	3.431	−2.844	−2.819	5.663	−2.604	−2.571	5.175
	SO	−1.760	−1.699	3.449	−2.874	−2.960	5.947	−2.738	−2.703	5.441
TZVPPall-2c/ωB97X-D	SR	−1.895	−1.825	3.720	−2.849	−2.827	5.675	−2.626	−2.593	5.219
	SO	−1.869	−1.803	3.672	−2.987	−2.964	5.951	−2.745	−2.711	5.457
QZVPall-2c/ωB97X-D	SR	−1.711	−1.651	3.362	−2.848	−2.825	5.672	−2.608	−2.575	5.183
	SO	−1.714	−1.663	3.377	−2.874	−2.852	5.726	−2.619	−2.585	5.204

Table 3.17: Principal components of the NQI in MHz for the three spin-$\frac{1}{2}$ La(II) and Lu(II) molecules $[La(OAr^*)_3]^-$, $[Lu(NR_2)_3]^-$, and $[Lu(OAr^*)_3]^-$ (OAr^* = 2,6-Ad_2-4-t-Bu-C_6H_2O, Ad = adamantyl, t-Bu= tert-butyl, R = $SiMe_3$ with Me = methyl). Results are given in the principal axis system. The scalar-relativistic X2C ansatz combined with the non-relativistic EFG operator is taken from Ref. [14] and denoted SR-NR. Note that we changed the sign convention compared to that reference. The prefix x2c- of the basis set is omitted for brevity and only the basis set of the Ln atom is given here. Eigenvalues of the NQI tensor are given in ascending order.

		$[La(OAr^*)_3]^-$			$[Lu(NR_2)_3]^-$			$[Lu(OAr^*)_3]^-$		
Functional	Hamiltonian	Q_{11}	Q_{22}	Q_{33}	Q_{11}	Q_{22}	Q_{33}	Q_{11}	Q_{22}	Q_{33}
TZVPPall-s/TPSS	SR-NR	−0.243	−0.194	0.436	−5.60	−5.57	11.2	−8.17	−7.76	15.9
	SR	−1.620	−1.561	3.181	−47.45	−46.98	94.42	−33.25	−32.82	66.08
	SO	−1.594	−1.534	3.129	−46.20	−45.75	91.95	−42.38	−41.81	84.20
TZVPPall-2c/TPSS	SR	−1.697	−1.634	3.331	−50.60	−50.11	100.7	−45.48	−44.86	90.33
	SO	−1.733	−1.668	3.401	−52.98	−52.48	105.5	−47.58	−46.93	94.51
QZVPall-2c/TPSS	SR	−1.717	−1.654	3.371	−51.77	−51.28	103.1	−45.65	−45.05	90.70
	SO	−1.730	−1.665	3.394	−52.66	−52.17	104.8	−46.20	−45.58	91.77
TZVPPall-2c/r^{2}SCAN	SR	−1.839	−1.770	3.610	−53.85	−53.38	107.2	−49.74	−49.10	98.84
	SO	−1.877	−1.807	3.684	−56.46	−55.96	112.4	−52.06	−51.40	103.5
QZVPall-2c/r^{2}SCAN	SR	−1.835	−1.767	3.602	−54.03	−54.22	108.3	−47.21	−48.52	95.73
	SO	−1.848	−1.778	3.626	−55.35	−54.86	110.2	−49.92	−49.30	99.22
TZVPPall-2c/PBE0	SR	−1.697	−1.634	3.332	−50.62	−50.13	100.8	−45.50	−44.89	90.39
	SO	−1.846	−1.778	3.624	−56.23	−55.72	112.0	−51.22	−50.57	101.8
QZVPall-2c/PBE0	SR	−1.811	−1.749	3.560	−54.80	−54.32	109.1	−48.94	−48.32	97.27
	SO	−1.825	−1.758	3.583	−55.68	−55.19	110.9	−49.65	−49.02	98.66
TZVPPall-2c/PBE0-40HF	SR	−2.042	−1.969	4.011	−54.98	−54.51	109.5	−51.03	−50.39	101.4
	SO	−2.015	−1.944	3.959	−57.30	−57.52	114.8	−53.40	−52.74	106.1
QZVPall-2c/PBE0-40HF	SR	−1.830	−1.772	3.602	−42.60	−54.38	109.2	−50.62	−50.00	100.6
	SO	−1.840	−1.785	3.626	−55.45	−54.96	110.4	−50.94	−50.30	101.2
TZVPPall-2c/CAM-QTP-02	SR	−2.284	−2.202	4.484	−60.49	−58.21	117.0	−51.07	−50.42	101.5
	SO	−2.251	−2.173	4.425	−61.47	−60.93	122.4	−53.40	−52.73	106.1
QZVPall-2c/CAM-QTP-02	SR	−2.135	−2.059	4.194	−60.02	−59.50	119.5	−55.60	−54.96	110.6
	SO	−2.110	−2.036	4.146	−58.23	−57.72	116.0	−52.53	−51.89	104.4
TZVPPall-2c/HSE06	SR	−1.937	−1.866	3.802	−53.91	−53.44	107.4	−49.20	−48.57	97.77
	SO	−1.913	−1.843	3.756	−56.51	−56.00	112.5	−51.48	−50.82	102.3
QZVPall-2c/HSE06	SR	−1.823	−1.757	3.579	−55.43	−54.92	110.4	−53.77	−53.15	106.9
	SO	−1.805	−1.738	3.543	−53.87	−53.39	107.3	−50.74	−50.11	100.9
TZVPPall-2c/CAM-B3LYP	SR	−2.126	−2.050	4.176	−56.81	−56.30	113.1	−51.83	−51.17	103.0
	SO	−2.101	−2.025	4.126	−59.49	−58.95	118.4	−51.83	−51.17	103.0
QZVPall-2c/CAM-B3LYP	SR	−1.995	−1.923	3.919	−58.02	−57.50	115.5	−56.15	−55.49	111.6
	SO	−1.977	−1.906	3.883	−56.44	−55.94	112.4	−53.20	−52.53	105.7
TZVPPall-2c/LC-ωPBE	SR	−2.038	−1.968	4.006	−55.49	−54.98	110.5	−50.95	−50.95	101.3
	SO	−2.082	−2.011	4.094	−58.15	−57.62	115.8	−53.31	−52.63	105.9
QZVPall-2c/LC-ωPBE	SR	−1.948	−1.891	3.838	−55.37	−54.87	110.2	−50.70	−50.06	100.8
	SO	−1.958	−1.901	3.859	−55.95	−55.44	111.4	−50.94	−50.28	101.2
TZVPPall-2c/ωB97X-D	SR	−2.120	−2.042	4.162	−55.47	−55.04	110.5	−51.12	−50.48	101.6
	SO	−2.091	−2.018	4.109	−55.96	−55.52	111.5	−53.45	−52.79	106.2
QZVPall-2c/ωB97X-D	SR	−1.914	−1.847	3.762	−55.45	−55.00	110.4	−50.77	−50.13	100.9
	SO	−1.918	−1.860	3.778	−55.96	−55.52	111.5	−50.98	−50.33	101.3
Expt.				0			60 ± 20			100 ± 20

Chapter 4

Bread, Butter, and Gravy:

Perspective and Conclusions

This material is based on work supported by the National Science Foundation under grant nos. CHE-1800431, CHE-2102568, and DGE-1839285.

In this thesis, recent examples which highlight the development and application of computational methods for the study of f-element complexes were provided. The case was made for a generally useful electronic structure methodology based on scalar-relativistic ECPs, DFAs of at least GGA-quality, and metal atom basis sets at the triple-ζ level, which was shown in Section 2.2 to provide physically-motivated explanations for the existence of the first linear metallocene species observed for Tb and Dy. The computational approach established in these initial studies was subsequently utilized to assess the synthetic feasibility of theoretical actinide-based metallocene species in Section 2.3, guiding synthetic efforts towards the isolation of the first biscyclopentadienyl uranium compound. Aside from contributing directly to the discovery of such "next-generation" metallocenes,[218] Chapter 2 more importantly exemplifies the necessity of employing computational approaches in the interrogation of new f-element chemistry. Whereas the biscyclooctatetraenyl "uranocene" system $U(COT)_2$ was one of the first organoactinide complexes to be synthesized,[157] it took the intervention of *in-silico* studies before this second milestone could be reached.

Where a computational model reliant on effective core potentials proved insufficient due to the lack of explicit core electrons, such as for the characterization of f-element magnetic molecules reported in Section 3.2, a scalar-relativistic all-electron DFT approach was proposed. This method explained trends in hyperfine coupling and quadrupole coupling constants observed in experimental EPR measurements for a series of La and Lu-based qubit candidates. The predicted s-orbital character arising from the SOMO was found to serve as a useful descriptor for the chemical design of molecular spin qubits with large hyperfine interactions and associated clock transitions. Such initial calculations were subsequently refined in follow up work detailed in Sections 3.3, 3.4, and 3.5 through implementation of new, relativistic magnetic property operators within quasirelativistic exact two-component theory, producing results that dramatically improved errors by an order of magnitude for the Ln systems described in Section 3.2. Extensive benchmark calculations were performed to assess the accuracy of these predictions across a variety of tested basis sets, density func-

tionals, and relativistic Hamiltonians, culminating in a set of recommended parameters for general application to metal complexes. Given the accuracy of these newly realized tools, the toolbox of routine computational methods for the f-elements has been expanded to the realm of efficient magnetic property predictions.

Despite the merits of current techniques demonstrated above, numerous challenges for electronic structure methods applied to f-element molecules remain, hindering their general relevance and scope. The systems studied throughout this work are representative of limiting cases with respect to their complexity, due to the fact that they mostly constitute monometallic species. Of course, larger compounds with greater than one Ln or An atom exhibit significantly more complex electronic structure, which in turn places increased demands on the quantum chemistry treatment for its required accuracy and computational efficiency.

Moving forward, methods which can rigorously describe systems with multiple open f valence shells will be of tremendous value to aid in the design of magnetic materials and extended systems, an area of potential growth and investment from commercial and industrial interests. Of course, this indicates a need for unilateral expansion across the three primary sectors mentioned throughout this work: More accurate treatment of (A) correlation and (B) relativistic effects, and (C) improvement of computational efficiency.

Computational methods must also grow in tandem with the field of Ln/An chemistry, and foster a mutually beneficial relationship which pushes the boundaries of both the accuracy of their *in-silico* description as well as the experimentally accessible chemical space of compounds with new ligands, oxidation states, and coordination environments. Several steps towards this end have already been described in this work, especially regarding the improvement of EPR parameters predicted *in-silico* to reinforce and guide experimental data. This marriage of theoretical and synthetic efforts may in turn enable the rational design of molecules and materials that can subsequently be applied to solve problems in

magnetism,[20–22] small molecule activation,[36,166,530] and nuclear fuel and waste processing,[63].

It remains to be seen if such broad advances will be possible working within any one quantum chemistry method. Much of the above efforts were put forward with the goal to improve density functional approximations with respect to sectors (A) and (B) while leveraging its established formal advantage in (C). However, it is apparent that these characteristics are inherently coupled, and more rigorous physical descriptions are often associated with deleterious effects on computational cost, as highlighted in Chapters 2 and 3 of this work.

Regardless, the author is confident that computational efforts will continue to be useful insofar as they can be developed and applied to accomplish well-defined scientific goals, and it is clear that there will be no shortage of interesting problems in the burgeoning field of f-element chemistry moving forward.

References

(1) Dolg, M. In *Computational Methods in Lanthanide and Actinide Chemistry*; John Wiley & Sons, Ltd: 2015; Chapter 16, pp 425–450.

(2) Kerridge, A. In *Computational Methods in Lanthanide and Actinide Chemistry*; John Wiley & Sons, Ltd: 2015; Chapter 5, pp 121–146.

(3) Saue, T.; Visscher, L. In *Computational Methods in Lanthanide and Actinide Chemistry*; John Wiley & Sons, Ltd: 2015; Chapter 3, pp 55–87.

(4) Pyykkö, P. *Chem. Rev.* **1988**, *88*, 563–594.

(5) Jenkins, T. F.; Woen, D. H.; Mohanam, L. N.; Ziller, J. W.; Furche, F.; Evans, W. J. *Organometallics* **2018**, *37*, 3863–3873.

(6) Evans, W. J. *Organometallics* **2016**, *35*, 3088–3100.

(7) Aravena, D.; Atanasov, M.; Neese, F. *Inorg. Chem.* **2016**, *55*, 4457–4469.

(8) Karlström, G.; Lindh, R.; Malmqvist, P.-Å.; Roos, B. O.; Ryde, U.; Veryazov, V.; Widmark, P.-O.; Cossi, M.; Schimmelpfennig, B.; Neogrady, P., et al. *Comput. Mater. Sci.* **2003**, *28*, 222–239.

(9) Aquilante, F.; De Vico, L.; Ferré, N.; Ghigo, G.; Malmqvist, P.-å.; Neogrády, P.; Pedersen, T. B.; Pitoňák, M.; Reiher, M.; Roos, B. O., et al. *J. Comput. Chem.* **2010**, *31*, 224–247.

(10) Boggio-Pasqua, M.; Groenhof, G. *Comput. Theor. Chem.* **2014**, *1040–1041*, 6–13.

(11) Levine, D. S.; Hait, D.; Tubman, N. M.; Lehtola, S.; Whaley, K. B.; Head-Gordon, M. *J. Chem Theory Comput.* **2020**, *16*, 2340–2354.

(12) Pople, J. A. *Rev. Mod. Phys.* **1999**, *71*, 1267.

(13) Hermosilla, L.; Calle, P.; García de la Vega, J. M.; Sieiro, C. *J. Phys. Chem. A* **2005**, *109*, 1114–1124.

(14) Kundu, K.; White, J. R. K.; Moehring, S. A.; Yu, J. M.; Ziller, J. W.; Furche, F.; Evans, W. J.; Hill, S. *Nat. Chem.* **2021**, *14*, 392–397.

(15) Franzke, Y. J.; Yu, J. M. *J. Chem. Theory Comput.* **2022**, *18*, 323–343.

(16) Smith, R. L.; Wysocki, A. L.; Park, K. *Phys. Chem. Chem. Phys.* **2020**, *22*, 21793–21800.

(17) Verma, P.; Autschbach, J. *J. Chem. Theory Comput.* **2013**, *9*, 1932–1948.

(18) Malkin, E.; Malkin, I.; Malkina, O. L.; Malkin, V. G.; Kaupp, M. *Phys. Chem. Chem. Phys.* **2006**, *8*, 4079–4085.

(19) Autschbach, J. *J. Chem. Theory Comput.* **2017**, *13*, 710–718.

(20) Woodruff, D. N.; Winpenny, R. E. P.; Layfield, R. *Chem. Rev.* **2013**, *113*, 5110–5148.

(21) Meihaus, K. R.; Long, J. R. *Dalton Trans.* **2014**, *44*, 2517–2528.

(22) Guo, F.-S.; Day, B. M.; Chen, Y.-C.; Tong, M.-L.; Mansikkamäki, A.; Layfield, R. A. *Science* **2018**, *362*, 1400–1403.

(23) Jensen, W. B. *J. Chem. Ed.* **1982**, *59*, 634.

(24) Lavelle, L. *J. Chem. Ed.* **2008**, *85*, 1482.

(25) Jensen, W. B. *J. Chem. Ed.* **2009**, *86*, 1186.

(26) Lavelle, L. *J. Chem. Ed.* **2009**, *86*, 1187.

(27) Evans, W. J. *Inorg. Chem.* **2007**, *46*, 3435–3449.

(28) Pyykkö, P. *Chem. Rev.* **2012**, *112*, 371–384.

(29) Kramida, A.; Ralchenko, Y.; Reader, J.; and NIST ASD Team, NIST Atomic Spectra Database (ver. 5.9), [Online]. Available: `https://physics.nist.gov/asd` [2022, July 2]. National Institute of Standards and Technology, Gaithersburg, MD. 2021.

(30) Dyall, K. G.; Grant, I. P.; Johnson, C. T.; Parpia, F. A.; Plummer, E. P. *Comp. Phys. Comm.* **1989**, *55*, 425–456.

(31) Cotton, S., *Lanthanide and Actinide Chemistry*; John Wiley & Sons: 2013.

(32) Choppin, G. R. *J. Alloys Compd.* **2002**, *344*, 55–59.

(33) Pimentel, G. C.; Spratley, R. D., *Understanding Chemistry*; Holden-Day: San Francisco, CA; p 862: 1971.

(34) Tsoureas, N.; Maron, L.; Kilpatrick, A. F. R.; Layfield, R. A.; Cloke, F. G. N. *J. Am. Chem. Soc.* **2019**, *142*, 89–92.

(35) Fox, A. R.; Bart, S. C.; Meyer, K.; Cummins, C. C. *Nature* **2008**, *455*, 341.

(36) Evans, W. J.; Fang, M.; Zucchi, G.; Furche, F.; Ziller, J. W.; Hoekstra, R. M.; Zink, J. I. *J. Am. Chem. Soc.* **2009**, *131*, 11195–11202.

(37) Kolarik, Z. *Chem. Rev.* **2008**, *108*, 4208–4252.

(38) Panak, P. J.; Geist, A. *Chem. Rev.* **2013**, *113*, 1199–1236.

(39) Kaltsoyannis, N. *Inorg. Chem.* **2012**, *52*, 3407–3413.

(40) Layfield, R. A.; Murugesu, M., *Lanthanides and Actinides in Molecular Magnetism*; Wiley-VCH: 2015.

(41) Meyer, G. *Chem. Rev.* **1988**, *88*, 93–107.

(42) Wedal, J. C.; Evans, W. J. *J. Am. Chem. Soc.* **2021**, *143*, 18354–18367.

(43) Evans, W. J. *J. Alloys Compd.* **2009**, *488*, 493–510.

(44) Moeller, T. *J. Chem. Ed.* **1970**, *47*, 417.

(45) Bochkarev, M. N.; Fedushkin, I. L.; Fagin, A. A.; Petrovskaya, T. V.; Ziller, J. W.; Broomhall-Dillard, R. N. R.; Evans, W. J. *Angew. Chem., Int. Ed. Engl.* **1997**, *36*, 133–135.

(46) Evans, W. J.; Allen, N. T.; Ziller, J. W. *J. Am. Chem. Soc.* **2000**, *122*, 11749–11750.

(47) Bochkarev, M. N.; Fedushkin, I. L.; Dechert, S.; Fagin, A. A.; Schumann, H. *Angew. Chem., Int. Ed.* **2001**, *40*, 3176–3178.

(48) Bochkarev, M. N.; Fagin, A. A. *Chem. - Eur. J.* **1999**, *5*, 2990–2992.

(49) Cassani, M. C.; Lappert, M. F.; Laschi, F. *Chem. Commun.* **1997**, 1563–1564.

(50) Ryan, A. J.; Evans, W. J. In *The Periodic Table I: Historical Development and Essential Features*; Springer International Publishing: 2019; Chapter 6.

(51) Woen, D. H.; Chen, G. P.; Ziller, J. W.; Boyle, T. J.; Furche, F.; Evans, W. J. *Angew. Chem., Int. Ed.* **2017**, *56*, 2050–2053.

(52) MacDonald, M. R.; Ziller, J. W.; Evans, W. J. *J. Am. Chem. Soc.* **2011**, *133*, 15914–15917.

(53) MacDonald, M. R.; Bates, J. E.; Fieser, M. E.; Ziller, J. W.; Furche, F.; Evans, W. J. *J. Am. Chem. Soc.* **2012**, *134*, 8420–8423.

(54) MacDonald, M. R.; Bates, J. E.; Ziller, J. W.; Furche, F.; Evans, W. J. *J. Am. Chem. Soc.* **2013**, *135*, 9857–9868.

(55) Langeslay, R. R.; Fieser, M. E.; Ziller, J. W.; Furche, F.; Evans, W. J. *Chem. Sci.* **2015**, *6*, 517–521.

(56) MacDonald, M. R.; Fieser, M. E.; Bates, J. E.; Ziller, J. W.; Furche, F.; Evans, W. J. *J. Am. Chem. Soc.* **2013**, *135*, 13310–13313.

(57) Windorff, C. J.; Chen, G. P.; Cross, J. N.; Evans, W. J.; Furche, F.; Gaunt, A. J.; Janicke, M. T.; Kozimor, S. A.; Scott, B. L. *J. Am. Chem. Soc.* **2017**, *139*, 3970–3973.

(58) Ryan, A. J.; Darago, L. E.; Balasubramani, S. G.; Chen, G. P.; Ziller, J. W.; Furche, F.; Long, J. R.; Evans, W. J. *Chem. - Eur. J.* **2018**, *24*, 7702–7709.

(59) Wedal, J. C.; Furche, F.; Evans, W. J. *Inorg. Chem.* **2021**, *60*, 16316–16325.

(60) Gould, C. A.; McClain, K. R.; Yu, J. M.; Groshens, T. J.; Furche, F.; Harvey, B. G.; Long, J. R. *J. Am. Chem. Soc.* **2019**, *141*, 12967–12973.

(61) Dumas, M. T.; Chen, G. P.; Hu, J. Y.; Nascimento, M. A.; Rawson, J. M.; Ziller, J. W.; Furche, F.; Evans, W. J. *J. Organomet. Chem.* **2017**, *849-850*, 38–47.

(62) Ryan, A. J.; Balasubramani, S. G.; Ziller, J. W.; Furche, F.; Evans, W. J. *J. Am. Chem. Soc.* **2020**, *142*, 9302–9313.

(63) Lumetta, G. J.; Nash, K. L.; Clark, S. B.; Friese, J. I., *Separations for the nuclear fuel cycle in the 21st century*; American Chemical Society: Washington, DC, 2006.

(64) Bursten, B. E.; Fang, A. *Inorg. Chim. Acta* **1985**, *110*, 153–160.

(65) Strittmatter, R. J.; Bursten, B. E. *J. Am. Chem. Soc.* **1991**, *113*, 552–559.

(66) Bursten, B. E.; Rhodes, L. F.; Strittmatter, R. J. *J. Am. Chem. Soc.* **1989**, *111*, 2756–2758.

(67) Bursten, B. E.; Rhodes, L. F.; Strittmatter, R. J. *J. Am. Chem. Soc.* **1989**, *111*, 2758–2766.

(68) Bursten, B. E.; Rhodes, L. F.; Strittmatter, R. J. *J. Less-Common Met.* **1989**, *149*, 207–211.

(69) Zhang, Q.; Hu, S.-X.; Qu, H.; Su, J.; Wang, G.; Lu, J.-B.; Chen, M.; Zhou, M.; Li, J. *Angew. Chem., Int. Ed.* **2016**, *55*, 6896–6900.

(70) Kaltsoyannis, N. *Chem. - Eur. J.* **2018**, *24*, 2815–2825.

(71) Su, J.; Windorff, C. J.; Batista, E. R.; Evans, W. J.; Gaunt, A. J.; Janicke, M. T.; Kozimor, S. A.; Scott, B. L.; Woen, D. H.; Yang, P. *J. Am. Chem. Soc.* **2018**, *140*, 7425–7428.

(72) *Computational Methods in Lanthanide and Actinide Chemistry*; Dolg, M., Ed.; John Wiley & Sons, Ltd: 2015.

(73) Engel, E.; Dreizler, R. M., *Density Functional Theory: An Advanced Course*, 1st ed.; Springer Berlin, Heidelberg: Heidelberg, Germany, 2011.

(74) Parr, R. G.; Weitao, Y., *Density-functional theory of atoms and molecules*, 1st ed.; Oxford University Press, New York, Oxford: 1989, pp 142–200.

(75) Hohenberg, P.; Kohn, W. *Phys. Rev.* **1964**, *136*, B864–B871.

(76) Thomas, L. H. *Math. Proc. Camb. Philos. Soc.* **1927**, *23*, 542–548.

(77) Kohn, W.; Sham, L. J. *Phys. Rev.* **1965**, *140*, A1133–A1138.

(78) Schwerdtfeger, P. *Chem. Phys. Chem* **2011**, *12*, 3143–3155.

(79) Von Barth, U.; Gelatt, C. D. *Phys. Rev. B.* **1980**, *21*, 2222.

(80) Dolg, M. In *Relativistic Electronic Structure Theory*, Schwerdtfeger, P., Ed.; Theoretical and Computational Chemistry, Vol. 11; Elsevier: 2002; Chapter 14, pp 793–862.

(81) Cao, X.; Dolg, M. *Coord. Chem. Rev.* **2006**, *250*, 900–910.

(82) Dolg, M. In *Handbook of Relativistic Quantum Chemistry*, Liu, W., Ed.; Springer: Berlin, Heidelberg, 2017; Chapter 14, pp 449–478.

(83) Dolg, M.; Stoll, H.; Preuss, H. *J. Chem. Phys.* **1989**, *90*, 1730–1734.

(84) Phillips, J. C.; Kleinman, L. *Phy. Rev.* **1959**, *116*, 287.

(85) Phillips, J. C. *Phys. Rev.* **1958**, *112*, 685.

(86) Pitzer, R. M.; Winter, N. W. *J. Phys. Chem.* **1988**, *92*, 3061–3063.

(87) Dolg, M.; Stoll, H.; Savin, A.; Preuss, H. *Theor. Chim. Acta* **1989**, *75*, 173–194.

(88) Stoll, H.; Fuentealba, P.; Dolg, M.; Flad, J.; Szentpály, L. V.; Preuss, H. *J. Chem. Phys.* **1983**, *79*, 5532–5542.

(89) Cao, X.; Dolg, M. *J. Chem. Phys.* **2001**, *115*, 7348–7355.

(90) Cao, X.; Dolg, M. *J. Mol. Struct.: THEOCHEM* **2002**, *581*, 139–147.

(91) Dolg, M.; Stoll, H.; Preuss, H. *J. Chem. Phys.* **1989**, *90*, 1730–1734.

(92) Dolg, M.; Stoll, H.; Preuss, H. *Theor. Chim. Acta* **1993**, *85*, 441–450.

(93) Küchle, W.; Dolg, M.; Stoll, H.; Preuss, H. *J. Chem. Phys.* **1994**, *100*, 7535–7542.

(94) Cao, X.; Dolg, M.; Stoll, H. *J. Chem. Phys.* **2003**, *118*, 487–496.

(95) Moritz, A.; Dolg, M. *Chem. Phys.* **2007**, *337*, 48–54.

(96) Dolg, M.; Cao, X. *J. Phys. Chem. A* **2009**, *113*, 12573–12581.

(97) Cao, X.; Dolg, M. *J. Mol. Struct.: THEOCHEM* **2004**, *673*, 203–209.

(98) Hülsen, M.; Weigand, A.; Dolg, M. *Theo. Chem. Acc.* **2009**, *122*, 23–29.

(99) Energy-consistent Pseudopotentials of the Stuttgart/Cologne Group, url = `http://www.tc.uni-koeln.de/PP/clickpse.en.html`, note = Accessed: 2022-06-03.

(100) Leininger, T.; Nicklass, A.; Küchle, W.; Stoll, H.; Dolg, M.; Bergner, A. *Chem. Phys. Lett.* **1996**, *255*, 274–280.

(101) Rinehart, J. D.; Long, J. R. *Chem. Sci.* **2011**, *2*, 2078–2085.

(102) Pyykkö, P. *Annu. Rev. Phys. Chem.* **2012**, *63*, 45.

(103) Saue, T. *ChemPhysChem* **2011**, *12*, 3077–3094.

(104) Lipparini, F.; Gauss, J. *J. Chem. Theory Comput.* **2016**, *12*, 4284–4295.

(105) Stanton, R. E.; Havriliak, S. *J. Chem. Phys.* **1984**, *81*, 1910–1918.

(106) Aucar, G. A.; Saue, T.; Visscher, L.; Jensen, H. J. A. *J. Chem. Phys.* **1999**, *110*, 6208–6218.

(107) Kutzelnigg, W. *Phys. Rev. A* **2003**, *67*, 032109.

(108) Saue, T.; Fægri, K.; Helgaker, T.; Gropen, O. *Mol. Phys.* **1997**, *91*, 937–950.

(109) Belpassi, L.; Storchi, L.; Quiney, H. M.; Tarantelli, F. *Phys. Chem. Chem. Phys.* **2011**, *13*, 12368–12394.

(110) Peng, D.; Reiher, M. *Theor. Chem. Acc.* **2012**, *131*, 1081.

(111) Barysz, M.; Sadlej, A. J. *J. Mol. Struct.: THEOCHEM* **2001**, *573*, 181–200.

(112) Foldy, L. L.; Wouthuysen, S. A. *Phys. Rev.* **1950**, *78*, 29–36.

(113) Heully, J.-L.; Lindgren, I.; Lindroth, E.; Lundqvist, S.; Mårtensson-Pendrill, A.-M. *J. Phys. B: At. Mol. Phys.* **1986**, *19*, 2799–2815.

(114) Kutzelnigg, W.; Liu, W. *J. Chem. Phys.* **2005**, *123*, 241102.

(115) Liu, W.; Kutzelnigg, W. *J. Chem. Phys.* **2007**, *126*, 114107.

(116) Liu, W.; Peng, D. *J. Chem. Phys.* **2006**, *125*, 044102.

(117) Liu, W.; Peng, D. *J. Chem. Phys.* **2006**, *125*, 149901.

(118) Iliaš, M.; Saue, T. *J. Chem. Phys.* **2007**, *126*, 064102.

(119) Liu, W.; Peng, D. *J. Chem. Phys.* **2009**, *131*, 031104.

(120) Peng, D.; Liu, W.; Xiao, Y.; Cheng, L. *J. Chem. Phys.* **2007**, *127*, 104106.

(121) Dyall, K. G. *J. Chem. Phys.* **1997**, *106*, 9618–9626.

(122) Dyall, K. G. *J. Chem. Phys.* **1998**, *109*, 4201–4208.

(123) Dyall, K. G.; Enevoldsen, T. *J. Chem. Phys.* **1999**, *111*, 10000–10007.

(124) Dyall, K. G. *J. Chem. Phys.* **2001**, *115*, 9136–9143.

(125) Boettger, J. C. *Phys. Rev. B* **2000**, *62*, 7809–7815.

(126) Filatov, M.; Zou, W.; Cremer, D. *J. Chem. Phys.* **2013**, *139*, 014106.

(127) Zou, W.; Filatov, M.; Cremer, D. *J. Chem. Phys.* **2015**, *142*, 214106.

(128) Yoshizawa, T.; Zou, W.; Cremer, D. *J. Chem. Phys.* **2016**, *145*, 184104.

(129) Wodyński, A.; Kaupp, M. *J. Phys. Chem. A* **2019**, *123*, 5660–5672.

(130) Peng, D.; Middendorf, N.; Weigend, F.; Reiher, M. *J. Chem. Phys.* **2013**, *138*, 184105.

(131) Zhang, T.; Kasper, J. M.; Li, X. In *Annual Reports in Computational Chemistry*, Dixon, D. A., Ed.; Elsevier: Amsterdam, The Netherlands, 2020; Chapter 2, pp 17–37.

(132) Peng, D.; Reiher, M. *J. Chem. Phys.* **2012**, *136*, 244108.

(133) Franzke, Y. J.; Middendorf, N.; Weigend, F. *J. Chem. Phys.* **2018**, *148*, 104410.

(134) Balasubramani, S. G. et al. *J. Chem. Phys.* **2020**, *152*, 184107.

(135) Furche, F.; Ahlrichs, R.; Hättig, C.; Klopper, W.; Sierka, M.; Weigend, F. *Wiley Interdiscip. Rev.: Comput. Mol. Sci.* **2014**, *4*, 91–100.

(136) Davidson, E. R.; Feller, D. *Chem. Rev.* **1986**, *86*, 681–696.

(137) Pollak, P.; Weigend, F. *J. Chem. Theory Comput.* **2017**, *13*, 3696–3705.

(138) Gulde, R.; Pollak, P.; Weigend, F. *J. Chem. Theory Comput.* **2012**, *8*, 4062–4068.

(139) Weigend, F.; Ahlrichs, R. *Phys. Chem. Chem. Phys.* **2005**, *7*, 3297–3305.

(140) Basis Set Exchange Library ver2, BSE Library v0.8.12, `https://www.basissetexchange.org/` (retrieved March 5, 2020).

(141) Perdew, J. P.; Schmidt, K. In *AIP Conference Proceedings*, 2001; Vol. 577, pp 1–20.

(142) Rappoport, D.; Crawford, N. R. M.; Furche, F.; Burke, K. In *Encyclopedia of Inorganic and Bioinorganic Chemistry*; John Wiley & Sons, Ltd: 2011.

(143) Fieser, M. E.; MacDonald, M. R.; Krull, B. T.; Bates, J. E.; Ziller, J. W.; Furche, F.; Evans, W. J. *J. Am. Chem. Soc.* **2014**, *137*, 369–382.

(144) Siladke, N. A.; Meihaus, K. R.; Ziller, J. W.; Fang, M.; Furche, F.; Long, J. R.; Evans, W. J. *J. Am. Chem. Soc.* **2011**, *134*, 1243–1249.

(145) Laurent, A. D.; Jacquemin, D. *Int. J. Quantum Chem.* **2013**, *113*, 2019–2039.

(146) Wilkinson, G.; Rosenblum, M.; Whiting, M.; Woodward, R. *J. Am. Chem. Soc.* **1952**, *74*, 2125–2126.

(147) Moffitt, W. *J. Am. Chem. Soc.* **1954**, *76*, 3386–3392.

(148) Kauffman, G. B. *J. Chem. Educ.* **1983**, *60*, 185.

(149) Elschenbroich, C., *Organometallics*; John Wiley & Sons: 2016.

(150) Rajanbabu, T.; Nugent, W. A.; Taber, D. F.; Fagan, P. J. *J. Am. Chem. Soc.* **1988**, *110*, 7128–7135.

(151) Kaminsky, W. *J. Polym. Sci., Part A: Polym. Chem.* **2004**, *42*, 3911–3921.

(152) Resconi, L.; Cavallo, L.; Fait, A.; Piemontesi, F. *Chem. Rev.* **2000**, *100*, 1253–1346.

(153) Brintzinger, H. H.; Fischer, D.; Mülhaupt, R.; Rieger, B.; Waymouth, R. M. *Angew. Chem., Int. Ed. Engl.* **1995**, *34*, 1143–1170.

(154) Chirik, P. J. *Dalton Trans.* **2007**, *1*, 16–25.

(155) Neidig, M. L.; Clark, D. L.; Martin, R. L. *Coord. Chem. Rev.* **2013**, *257*, 394–406.

(156) Fischer, R. D. *Theor. Chim. Acta* **1963**, *1*, 418–431.

(157) Streitwieser, A.; Muller-Westerhoff, U.; Sonnichsen, G.; Mares, F.; Morrell, D.; Hodgson, K. O.; Harmon, C. *J. Am. Chem. Soc.* **1973**, *95*, 8644–8649.

(158) Chang, A. H.; Pitzer, R. M. *J. Am. Chem. Soc.* **1989**, *111*, 2500–2507.

(159) Seyferth, D. *Organometallics* **2004**, *23*, 3562–3583.

(160) Parry, J. S.; Cloke, F. G. N.; Coles, S. J.; Hursthouse, M. B. *J. Am. Chem. Soc.* **1999**, *121*, 6867–6871.

(161) Maynadié, J.; Berthet, J.-C.; Thuéry, P.; Ephritikhine, M. *J. Am. Chem. Soc.* **2006**, *128*, 1082–1083.

(162) Langeslay, R. R.; Windorff, C. J.; Dumas, M. T.; Ziller, J. W.; Evans, W. J. *Organometallics* **2018**, *37*, 454–458.

(163) Layfield, R.; Guo, F.-S.; Mansikkamäki, A.; Tong, M.-L.; Chen, Y.-C. *Angew. Chem.* **2019**, *58*, 10163–10167.

(164) Ephritikhine, M. *Organometallics* **2013**, *32*, 2464–2488.

(165) Bursten, B. E.; Strittmatter, R. J. *Angew. Chem., Int. Ed. Engl.* **1991**, *30*, 1069–1085.

(166) Liddle, S. T. *Angew. Chem., Int. Ed.* **2015**, *54*, 8604–8641.

(167) Chilton, N. F.; Collison, D.; McInnes, E. J. L.; Winpenny, R. E. P.; Soncini, A. *Nat. Commun.* **2013**, *4*, 2551.

(168) Sievers, J. Z. *Z. Phys. B: Condens. Matter Quanta* **1982**, *45*, 289–296.

(169) Ungur, L.; Chibotaru, L. F. *Phys. Chem. Chem. Phys.* **2011**, *13*, 20086.

(170) Chilton, N. F.; Goodwin, C. A. P.; Mills, D. P.; Winpenny, R. E. P. *Chem. Commun.* **2015**, *51*, 101.

(171) Day, B. M.; Guo, F.-S.; Layfield, R. A. *Acc. Chem. Res.* **2018**, *51*, 1880–1889.

(172) Habib, F.; Brunet, G.; Vieru, V.; Korobkov, I.; Chibotaru, L. F.; Murugesu, M. *J. Am. Chem. Soc.* **2013**, *135*, 13242–13245.

(173) Liu, J.-L.; Chen, Y.-C.; Tong, M.-L. *Chem. Soc. Rev.* **2018**, *47*, 2431–2453.

(174) Chen, Y.-C.; Liu, J.-L.; Ungur, L.; Liu, J.; Li, Q.-W.; Wang, L.-F.; Ni, Z.-P.; Chibotaru, L. F.; Chen, X.-M.; Tong, M.-L. *J. Am. Chem. Soc.* **2016**, *138*, 2829–2837.

(175) Gupta, S. K.; Rajeshkumar, T.; Rajaraman, G.; Murugavel, R. *Chem. Sci* **2016**, *7*, 5181–5191.

(176) Gregson, M.; Chilton, N. F.; Arciu, A.-M.; Tuna, F.; Crowe, I. F.; Lewis, W.; Blake, A. J.; Collison, D.; McInnes, E. J. L.; Winpenny, R. E. P.; Liddle, S. T. *Chem. Sci.* **2016**, *7*, 155–165.

(177) Liu, J.; Chen, Y.-C.; Liu, J.-L.; Vieru, V.; Ungur, L.; Jia, J.-H.; Chibotaru, L. F.; Lan, Y.; Wernsdorfer, W.; Gao, S.; Chen, X.-M.; Tong, M.-L. *J. Am. Chem. Soc.* **2016**, *138*, 5441–5450.

(178) Ding, Y.-S.; Chilton, N. F.; Winpenny, R. E. P.; Zheng, Y.-Z. *Angew. Chem., Int. Ed.* **2016**, *55*, 16071–16074.

(179) Meihaus, K. R.; Long, J. R. *J. Am. Chem. Soc.* **2013**, *135*, 17952–17957.

(180) Ungur, L.; Le Roy, J. J.; Korobkov, I.; Murugesu, M.; Chibotaru, L. F. *Angew. Chem., Int. Ed.* **2014**, *53*, 4413–4417.

(181) Sørensen, M. A. et al. *Nat. Commun.* **2018**, *9*, 1292–1301.

(182) Fieser, M. E.; Palumbo, C. T.; La Pierre, H. S.; Halter, D. P.; Voora, V. K.; Ziller, J. W.; Furche, F.; Meyer, K.; Evans, W. J. *Chem. Sci.* **2017**, *8*, 7424–7433.

(183) Huh, D. H.; Darago, L. E.; Ziller, J. W.; Evans, W. J. *Inorg. Chem.* **2018**, *57*, 2096–2102.

(184) Meihaus, K. R.; Fieser, M. E.; Corbey, J. R.; Evans, W. J.; Long, J. R. *J. Am. Chem. Soc.* **2015**, *137*, 9855–9860.

(185) Goodwin, C. A. P.; Ortu, F.; Reta, D.; Chilton, N. F.; Mills, D. P. *Nature* **2017**, *548*, 439–445.

(186) Guo, F.-S.; Day, B. M.; Chen, Y.-C.; Tong, M.-L.; Mansikkamäki, A.; Layfield, R. A. *Angew Chem., Int. Ed.* **2017**, *56*, 11445–11449.

(187) McClain, K. R.; Gould, C. A.; Chakarawet, K.; Teat, S. J.; Groshens, T. J.; Long, J. R.; Harvey, B. G. *Chem. Sci.* **2018**, *9*, 8492–8503.

(188) Sitzmann, H.; Dezember, T.; Schmitt, O.; Weber, F.; Wolmershäuser, G.; Ruck, M. *Z. Anorg. Allg. Chem.* **2000**, *626*, 2241–2244.

(189) Evans, W. J.; Hughes, L. A.; Hanusa, T. P. *J. Am. Chem. Soc.* **1984**, *106*, 4270–4272.

(190) Visseaux, M.; Barbier-Baudry, D.; Blacque, O.; Hafid, A.; Richard, P.; Weber, F. *New J. Chem* **2000**, *24*, 939–942.

(191) Weber, F.; Sitzmann, H.; Schultz, M.; Sofield, C. D.; Andersen, R. A. *Organometallics* **2002**, *21*, 3139–3146.

(192) Evans, W. J.; Perotti, J. M.; Brady, J. C.; Ziller, J. W. *J. Am. Chem. Soc.* **2003**, *125*, 5204–5212.

(193) Nocton, G.; Ricard, L. *Dalton Trans.* **2014**, *43*, 4380–4387.

(194) Kilpatrick, A. F. R.; Cloke, F. G. N. *Dalton Trans.* **2017**, *46*, 5587–5597.

(195) Palumbo, C. T.; Ziller, J. W.; Evans, W. J. *Organomet. Chem.* **2018**, *867*, 142–148.

(196) Ruspic, C.; Moss, J. R.; Schuürmann, M.; Harder, S. *Angew. Chem., Int. Ed.* **2008**, *47*, 2121–2126.

(197) Van Velzen, N. J. C.; Harder, S. *Organometallics* **2018**, *37*, 2263–2271.

(198) Kaupp, M.; Schleyer, P. v. R.; Dolg, M.; Stoll, H. *J. Am. Chem. Soc.* **1992**, *114*, 8202–8208.

(199) Staroverov, V. N.; Scuseria, G. E.; Tao, J.; Perdew, J. P. *J. Chem. Phys.* **2003**, *119*, 12129–12137.

(200) Neese, F.; Olbrich, G. *Chem. Phys. Lett.* **2002**, *362*, 170–178.

(201) Grimme, S.; Antony, J.; Ehrlich, S.; Krieg, H. *J. Chem. Phys.* **2010**, *132*, 154104.

(202) Deglmann, P.; Furche, F. *J. Chem. Phys.* **2002**, *117*, 9535–9538.

(203) Furche, F.; Ahlrichs, R. *J. Chem. Phys.* **2002**, *117*, 7433–7447.

(204) Baurenschmitt, R.; Ahlrichs, R. *Chem. Phys. Lett.* **1996**, *256*, 454–464.

(205) Bates, J. E.; Furche, F. *J. Chem. Phys.* **2012**, *137*, 164105.

(206) Humphrey, W.; Dalke, A.; Schulten, K. *J. Mol. Graph.* **1996**, *14*, 33–38.

(207) Fronzoni, G.; Colavita, P.; Stener, M.; De Alti, G.; Decleva, P. *J. Chem. Phys.* **2001**, *105*, 9800–9812.

(208) Bean, D. E.; Folwer, P. W.; Morris, M. J. *J. Organomet. Chem.* **2011**, *696*, 2093–2100.

(209) Reed, A. E.; Weinstock, R. B.; Weinhold, F. *J. Chem. Phys.* **1985**, *83*, 735–746.

(210) Ishimura, K.; Hada, M.; Nakatsuji, H. *J. Chem. Phys.* **2002**, *117*, 6533.

(211) Tao, J.; Perdew, J. P.; Staroverov, V. N.; Scuseria, G. E. *Phys. Rev. Lett.* **2003**, *91*, 146401.

(212) Weigend, F.; Köhn, A.; Hättig, C. *J. Chem. Phys.* **2002**, *116*, 3175–3183.

(213) Deglmann, P.; Furche, F.; Ahlrichs, R. *Chem. Phys. Lett.* **2002**, *362*, 511–518.

(214) Yu, J. M.; Furche, F. *Inorg. Chem.* **2019**, *58*, 16004–16010.

(215) Klamt, A.; Schüürmann, G. *J. Chem. Soc., Perkin Trans. 2* **1993**, 799–805.

(216) *CRC Handbook of Chemistry and Physics*, 81st ed.; Lide, D. R., Ed.; CRC Press: Boca Ratón, USA, 2008.

(217) Fricke, B.; Greiner, W.; Waber, J. *Theor. Chim. Acta* **1971**, *21*, 235–260.

(218) Guo, F.-S.; Tsoureas, N.; Huang, G.-Z.; Tong, M.-L.; Mansikkamäki, A.; Layfield, R. A. *Angew. Chem., Int. Ed.* **2020**, *59*, 2299–2303.

(219) Arute, F. et al. *Nature* **2019**, *574*, 505–510.

(220) Devoret, M. H.; Schoelkopf, R. J. *Science* **2013**, *339*, 1169–1174.

(221) Wright, K. et al. *Nat. Commum.* **2019**, *10*, 1–6.

(222) Carolan, J. et al. *Science* **2015**, *349*, 711–716.

(223) Sarma, S. D.; Freedman, M.; Nayak, C. *Npj Quantum Inf.* **2015**, *1*, 1–13.

(224) Loss, D.; DiVincenzo, D. P. *Phys. Rev. A* **1998**, *57*, 120.

(225) Kane, B. E. *Nature* **1998**, *393*, 133–137.

(226) Yang, K.; Paul, W.; Phark, S.-H.; Willke, P.; Bae, Y.; Choi, T.; Esat, T.; Ardavan, A.; Heinrich, A. J.; Lutz, C. P. *Science* **2019**, *366*, 509–512.

(227) Thiele, S.; Balestro, F.; Ballou, R.; Klyatskaya, S.; Ruben, M.; Wernsdorfer, W. *Science* **2014**, *344*, 1135–1138.

(228) Gaita-Ariño, A.; Luis, F.; Hill, S.; Coronado, E. *Nat. Chem.* **2019**, *11*, 301–309.

(229) Zadrozny, J. M.; Gallagher, A. T.; Harris, T. D.; Freedman, D. E. *J. Am. Chem. Soc.* **2017**, *139*, 7089–7094.

(230) Schweiger, A.; Jeschke, G., *Principles of Pulse Electron Paramagnetic Resonance*; Oxford University Press on Demand: 2001.

(231) Nguyen, T. N.; Wernsdorfer, W.; Shiddiq, M.; Abboud, K. A.; Hill, S.; Christou, G. *Chem. Sci.* **2016**, *7*, 1156–1173.

(232) Zadrozny, J. M.; Niklas, J.; Poluektov, O. G.; Freedman, D. E. *ACS Cent. Sci.* **2015**, *1*, 488–492.

(233) Shiddiq, M.; Komijani, D.; Duan, Y.; Gaita-Ariño, A.; Coronado, E.; Hill, S. *Nature* **2016**, *531*, 348–351.

(234) Giménez-Santamarina, S.; Cardona-Serra, S.; Clemente-Juan, J. M.; Gaita-Arino, A.; Coronado, E. *Chem. Sci.* **2020**, *11*, 10718–10728.

(235) Ghosh, S.; Datta, S.; Friend, L.; Cardona-Serra, S.; Gaita-Ariño, A.; Coronado, E.; Hill, S. *Dalton Trans.* **2012**, *41*, 13697–13704.

(236) Miao, K. C.; Blanton, J. P.; Anderson, C. P.; Bourassa, A.; Crook, A. L.; Wolfowicz, G.; Abe, H.; Ohshima, T.; Awschalom, D. D. *Science* **2020**, *369*, 1493–1497.

(237) Hitchcock, P. B.; Lappert, M. F.; Maron, L.; Protchenko, A. V. *Angew. Chem., Int. Ed.* **2008**, *47*, 1488–1491.

(238) Ryan, A. J.; Ziller, J. W.; Evans, W. J. *Chem. Sci.* **2020**, *11*, 2006–2014.

(239) Moehring, S. A.; Miehlich, M.; Hoerger, C. J.; Meyer, K.; Ziller, J. W.; Evans, W. J. *Inorg. Chem.* **2020**, *59*, 3207–3214.

(240) Woen, D. H.; Evans, W. J. In *Handbook on the Physics and Chemistry of Rare Earths*; Elsevier: 2016; Vol. 50, pp 337–394.

(241) Ariciu, A.-M.; Woen, D. H.; Huh, D. N.; Nodaraki, L. E.; Kostopoulos, A. K.; Goodwin, C. A.; Chilton, N. F.; McInnes, E. J.; Winpenny, R. E.; Evans, W. J., et al. *Nat. Commun.* **2019**, *10*, 1–8.

(242) Shiddiq, M.; Komijani, D.; Duan, Y.; Gaita-Ariño; Coronado, E.; Hill, S. *Nature* **2016**, *531*, 348–351.

(243) Wolfowicz, G.; Tyryshkin, A. M.; George, R. E.; Riemann, H.; Abrosimov, N. V.; Becker, P.; Pohl, H.-J.; Thewalt, M. L. W.; Lyon, S. A.; Morton, J. J. L. *Nat. Nanotechnol.* **2013**, *8*, 561–564.

(244) Stoll, S.; Schweiger, A. *J. Magn. Reson.* **2006**, *178*, 42–55.

(245) Stoll, S.; Goldfarb, D. *eMagRes* **2018**, 95–114.

(246) Franzke, Y. J.; Treß, R.; Pazdera, T. M.; Weigend, F. *Phys. Chem. Chem. Phys.* **2019**, *21*, 16658–16664.

(247) Visscher, L.; Dyall, K. G. *At. Data Nucl. Data Tables* **1997**, *67*, 207–224.

(248) Grimme, S.; Antony, J.; Ehrlich, S.; Krieg, H. *J. Chem. Phys.* **2010**, *132*, 154104.

(249) Stone, N. *At. Data Nucl. Data Table* **2016**, *111-112*, 1–28.

(250) Autschbach, J.; Ziegler, T. *J. Chem. Phys.* **2000**, *113*, 936–947.

(251) Haiduke, R. L. A.; da Silva, A. B. F.; Visscher, L. *Chem. Phys. Rev.* **2007**, *445*, 95–98.

(252) Van Lenthe, E.; Baerends, E. J. *J. Chem. Phys.* **2000**, *112*, 8279–8292.

(253) Schwerdtfeger, P.; Pernpointner, M.; Laerdahl, J. K. *J. Chem. Phys.* **1999**, *111*, 3357–3364.

(254) Srebro, M.; Autschbach, J. *J. Phys. Chem. Lett.* **2012**, *3*, 576–581.

(255) Stone, N. *At. Data Nucl. Data Tables* **2005**, *90*, 75–176.

(256) Hanson, R. M. *J. Appl. Crystallogr.* **2010**, *43*, 1250–1260.

(257) Wolfowicz, G.; Tyryshkin, A. M.; George, R. E.; Riemann, H.; Abrosimov, N. V.; Becker, P.; Pohl, H.-J.; Thewalt, M. L. W.; Lyon, S. A.; Morton, J. L. *Nat. Nanotechnol.* **2013**, *8*, 561–564.

(258) Zadrozny, J. M.; Niklas, J.; Poluektov, O. G.; Freedman, D. E. *ACS. Cent. Sci.* **2015**, *1*, 488–492.

(259) Lan, T. N.; Kurashige, Y.; Yanai, T. *J. Chem. Theory Comput.* **2014**, *10*, 1953–1967.

(260) Wysocki, A. L.; Park, K. *Inorg. Chem.* **2020**, *59*, 2771–2780.

(261) Datta, D.; Gauss, J. *J. Chem. Theory Conput.* **2019**, *15*, 1572–1592.

(262) Kossmann, S.; Neese, F. *J. Phys. Chem. A* **2010**, *114*, 11768–11781.

(263) Sharkas, K.; Pritchard, B.; Autschbach, J. *J. Chem. Theory Comput.* **2015**, *11*, 538–549.

(264) *Calculation of NMR and EPR Parameters. Theory and Applications*; Kaupp, M., Bühl, M., Malkin, V. G., Eds.; Wiley-VCH: Weinheim, Germany, 2004.

(265) Autschbach, J. In *Relativistic Methods for Chemists*, Barysz, M., Ishikawa, Y., Eds.; Springer Netherlands: Dordrecht, 2010, pp 521–598.

(266) Autschbach, J. *J. Chem. Phys.* **2012**, *136*, 150902.

(267) Autschbach, J. *Philos. Trans. R. Soc., A* **2014**, *372*, 20120489.

(268) Dyall, K. G.; Fægri Jr., K., *Introduction to Relativistic Quantum Chemistry*; Oxford University Press: New York, 2007.

(269) Reiher, M.; Wolf., A., *Relativistic Quantum Chemistry – The Fundamental Theory of Molecular Science*, 2nd ed.; Wiley-VCH: Weinheim, Germany, 2015.

(270) *Handbook of Relativistic Quantum Chemistry*; Liu, W., Ed.; Springer: Berlin, Heidelberg, 2017.

(271) Malkin, I.; Malkina, O. L.; Malkin, V. G.; Kaupp, M. *J. Chem. Phys.* **2005**, *123*, 244103.

(272) Douglas, M.; Kroll, N. M. *Ann. Phys. (NY)* **1974**, *82*, 89–155.

(273) Hess, B. A. *Phys. Rev. A* **1986**, *33*, 3742–3748.

(274) Jansen, G.; Hess, B. A. *Phys. Rev. A* **1989**, *39*, 6016–6017.

(275) Chang, C.; Pelissier, M.; Durand, P. *Phys. Scr.* **1986**, *34*, 394–404.

(276) Van Lenthe, E.; Baerends, E. J.; Snijders, J. G. *J. Chem. Phys.* **1993**, *99*, 4597–4610.

(277) Van Lenthe, E.; Baerends, E. J.; Snijders, J. G. *J. Chem. Phys.* **1994**, *101*, 9783–9792.

(278) Autschbach, J.; Patchkovskii, S.; Pritchard, B. *J. Chem. Theory Comput.* **2011**, *7*, 2175–2188.

(279) Malkin, E.; Repiský, M.; Komorovský, S.; Mach, P.; Malkina, O. L.; Malkin, V. G. *J. Chem. Phys.* **2011**, *134*, 044111.

(280) Gohr, S.; Hrobárik, P.; Repiský, M.; Komorovský, S.; Ruud, K.; Kaupp, M. *J. Phys. Chem. A* **2015**, *119*, 12892–12905.

(281) Feng, R.; Duignan, T. J.; Autschbach, J. *J. Chem. Theory Comput.* **2021**, *17*, 255–268.

(282) Liu, W. *Mol. Phys.* **2010**, *108*, 1679–1706.

(283) Cheng, L.; Gauss, J. *J. Chem. Phys.* **2011**, *135*, 084114.

(284) Cheng, L.; Stopkowicz, S.; Gauss, J. *Int. J. Quantum Chem.* **2014**, *114*, 1108–1127.

(285) Zou, W.; Filatov, M.; Cremer, D. *J. Chem. Phys.* **2011**, *134*, 244117.

(286) Filatov, M.; Zou, W.; Cremer, D. *J. Phys. Chem. A* **2012**, *116*, 3481–3486.

(287) Cremer, D.; Zou, W.; Filatov, M. *Wiley Interdiscip. Rev.: Comput. Mol. Sci.* **2014**, *4*, 436–467.

(288) Franzke, Y. J.; Weigend, F. *J. Chem. Theory Comput.* **2019**, *15*, 1028–1043.

(289) Kehry, M.; Franzke, Y. J.; Holzer, C.; Klopper, W. *Mol. Phys.* **2020**, *118*, e1755064.

(290) Franzke, Y. J.; Mack, F.; Weigend, F. *J. Chem. Theory Comput.* **2021**, *17*, 3974–3994.

(291) Schmitt, S.; Jost, P.; van Wüllen, C. *J. Chem. Phys.* **2011**, *134*, 194113.

(292) Verma, P.; Autschbach, J. *J. Chem. Theory Comput.* **2013**, *9*, 1052–1067.

(293) Remigio, R. D.; Repisky, M.; Komorovsky, S.; Hrobarik, P.; Frediani, L.; Ruud, K. *Mol. Phys.* **2017**, *115*, 214–227.

(294) Yoshizawa, T. *Chem. Phys.* **2019**, *518*, 112–122.

(295) Gell-Mann, M. *Nuovo Cim.* **1956**, *4*, 848–866.

(296) Bohr, A.; Weisskopf, V. F. *Phys. Rev.* **1950**, *77*, 94–98.

(297) Hennum, A. C.; Klopper, W.; Helgaker, T. *J. Chem. Phys.* **2001**, *115*, 7356–7363.

(298) Visser, O.; Aerts, P.; Hegarty, D.; Nieuwpoort, W. *Chem. Phys. Lett.* **1987**, *134*, 34–38.

(299) Ishikawa, Y.; Baretty, R.; Binning, R. *Chem. Phys. Lett.* **1985**, *121*, 130–133.

(300) Repiský, M.; Komorovský, S.; Malkina, O. L.; Malkin, V. G. *Chem. Phys.* **2009**, *356*, 236–242.

(301) Enevoldsen, T.; Visscher, L.; Saue, T.; Jensen, H. J. A.; Oddershede, J. *J. Chem. Phys.* **2000**, *112*, 3493–3498.

(302) Visscher, L.; Enevoldsen, T.; Saue, T.; Jensen, H. J. A.; Oddershede, J. *J. Comput. Chem.* **1999**, *20*, 1262–1273.

(303) Gomez, S. S.; Romero, R. H.; Aucar, G. A. *J. Chem. Phys.* **2002**, *117*, 7942–7946.

(304) Giménez, C. A.; Maldonado, A. F.; Aucar, G. A. *Theor. Chem. Acc.* **2016**, *135*, 201.

(305) Komorovský, S.; Repiský, M.; Malkina, O. L.; Malkin, V. G.; Malkin Ondík, I.; Kaupp, M. *J. Chem. Phys.* **2008**, *128*, 104101.

(306) Cheng, L.; Gauss, J.; Stanton, J. F. *J. Chem. Phys.* **2013**, *139*, 054105.

(307) Yoshizawa, T.; Zou, W.; Cremer, D. *J. Chem. Phys.* **2017**, *146*, 134109.

(308) Yoshizawa, T.; Hada, M. *J. Chem. Phys.* **2017**, *147*, 154104.

(309) Sun, S.; Li, X. *J. Chem. Theory Comput.* **2020**, *16*, 4533–4542.

(310) Van Wüllen, C.; Michauk, C. *J. Chem. Phys.* **2005**, *123*, 204113.

(311) Zou, W.; Filatov, M.; Cremer, D. *J. Chem. Theory Comput.* **2012**, *8*, 2617–2629.

(312) Kutzelnigg, W. *Theor. Chim. Acta* **1988**, *73*, 173–200.

(313) Stevens, R. M.; Pitzer, R. M.; Lipscomb, W. N. *J. Chem. Phys.* **1963**, *38*, 550–560.

(314) O'Shea, S. F.; Santry, D. P. *Theor. Chim. Acta* **1975**, *37*, 1–16.

(315) Lawson, C. L.; Hanson, R. J.; Kincaid, D. R.; Krogh, F. T. *ACM Trans. Math. Softw.* **1979**, *5*, 308–323.

(316) Blackford, L. S.; Demmel, J.; Dongarra, J.; Duff, I.; Hammarling, S.; Henry, G.; Heroux, M.; Kaufman, L.; Lumsdaine, A.; Petitet, A.; Pozo, R.; Remington, K.; Whaley, R. C. *ACM Trans. Math. Softw.* **2002**, *28*, 135–151.

(317) Ahlrichs, R.; Bär, M.; Häser, M.; Horn, H.; Kölmel, C. *Chem. Phys. Lett.* **1989**, *162*, 165–169.

(318) Developers' version of TURBOMOLE V7.5.1 2021, a development of University of Karlsruhe and Forschungszentrum Karlsruhe GmbH, 1989-2007, TURBOMOLE GmbH, since 2007; available from `https://www.turbomole.org` (retrieved August 28, 2021).

(319) Dupuis, M.; Rys, J.; King, H. F. *J. Chem. Phys.* **1976**, *65*, 111–116.

(320) Rys, J.; Dupuis, M.; King, H. F. *J. Comput. Chem.* **1983**, *4*, 154–157.

(321) *CRC Handbook of Chemistry and Physics*, 78th ed.; Lide, D. R., Ed.; CRC Press: Boca Ratón, USA, 1997.

(322) Mack, F.; Schattenberg, C. J.; Kaupp, M.; Weigend, F. *J. Phys. Chem. A* **2020**, *124*, 8529–8539.

(323) CODATA internationally recommened 2018 values of the fundamental physical constans, `https://physics.nist.gov/cuu/Constants/index.html` (retrieved December 28, 2020).

(324) Armbruster, M. K.; Weigend, F.; van Wüllen, C.; Klopper, W. *Phys. Chem. Chem. Phys.* **2008**, *10*, 1748–1756.

(325) Baldes, A.; Weigend, F. *Mol. Phys.* **2013**, *111*, 2617–2624.

(326) Plessow, P.; Weigend, F. *J. Comput. Chem.* **2012**, *33*, 810–816.

(327) Holzer, C. *J. Chem. Phys.* **2020**, *153*, 184115.

(328) OpenMP Architecture Review Boards OpenMP API shared-memory parallel programming, `https://www.openmp.org` (retrieved September 26, 2021).

(329) Holzer, C.; Franzke, Y. J., OpenMP version of ridft, rdgrad, and egrad with contributions to mpshift, dscf, and grad; improved OpenMP version of aoforce and escf, released with TURBOMOLE V7.4 and further improved in TURBOMOLE V7.5.

(330) Eichkorn, K.; Treutler, O.; Öhm, H.; Häser, M.; Ahlrichs, R. *Chem. Phys. Lett.* **1995**, *242*, 283–290.

(331) Weigend, F.; Kattannek, M.; Ahlrichs, R. *J. Chem. Phys.* **2009**, *130*, 164106.

(332) Sierka, M.; Hogekamp, A.; Ahlrichs, R. *J. Chem. Phys.* **2003**, *118*, 9136–9148.

(333) Weigend, F. *Phys. Chem. Chem. Phys.* **2002**, *4*, 4285–4291.

(334) Schäfer, A.; Klamt, A.; Sattel, D.; Lohrenz, J. C. W.; Eckert, F. *Phys. Chem. Chem. Phys.* **2000**, *2*, 2187–2193.

(335) Perdew, J. P.; Schmidt, K. *AIP Conf. Proc.* **2001**, *577*, 1–20.

(336) Becke, A. D. *J. Chem. Phys.* **2014**, *140*, 18A301.

(337) Mardirossian, N.; Head-Gordon, M. *Mol. Phys.* **2017**, *115*, 2315–2372.

(338) Marques, M. A. L.; Oliveira, M. J. T.; Burnus, T. *Comput. Phys. Commun.* **2012**, *183*, 2272–2281.

(339) Lehtola, S.; Steigemann, C.; Oliveira, M. J. T.; Marques, M. A. L. *SoftwareX* **2018**, *7*, 1–5.

(340) Libxc, 5.1.4, available from `https://www.tddft.org/programs/libxc/` (retrieved July 30, 2021).

(341) Ekström, U.; Visscher, L.; Bast, R.; Thorvaldsen, A. J.; Ruud, K. *J. Chem. Theory Comput.* **2010**, *6*, 1971–1980.

(342) Gillhuber, S.; Franzke, Y. J.; Weigend, F. *J. Phys. Chem. A* **2021**, *125*, 9707–9723.

(343) Repiský, M.; Komorovský, S.; Kadek, M.; Konecny, L.; Ekström, U.; Malkin, E.; Kaupp, M.; Ruud, K.; Malkina, O. L.; Malkin, V. G. *J. Chem. Phys.* **2020**, *152*, 184101.

(344) Tutorial for EPR A tensors with the ReSpect program suite, `http://www.respectprogram.org/tutorials-hfcc.html` (retrieved August 17, 2021).

(345) Kutzelnigg, W.; Fleischer, U.; Schindler, M. In *Deuterium and Shift Calculation*; Springer: Berlin, Heidelberg, Germany, 1991, pp 165–262.

(346) Dyall, K. G. *Theor. Chem. Acc.* **2006**, *115*, 441–447.

(347) Basis sets available from the Dirac program web site, `http://dirac.chem.sdu.dk` (retrieved March 26, 2020).

(348) Dyall, K. G. *Theor. Chem. Acc.* **2007**, *117*, 483–489.

(349) Gomes, A. S. P.; Dyall, K. G.; Visscher, L. *Theor. Chem. Acc.* **2010**, *127*, 369–381.

(350) Perdew, J. P.; Burke, K.; Ernzerhof, M. *Phys. Rev. Lett.* **1996**, *77*, 3865–3868.

(351) Adamo, C.; Barone, V. *J. Chem. Phys.* **1999**, *110*, 6158–6170.

(352) Treutler, O.; Ahlrichs, R. *J. Chem. Phys.* **1995**, *102*, 346–354.

(353) Treutler, O. Entwicklung und Anwendung von Dichtefunktionalmethoden, Ph.D. Thesis, Germany: University of Karlsruhe (TH), 1995.

(354) Jensen, F. *J. Chem. Theory Comput.* **2006**, *2*, 1360–1369.

(355) Dunning, T. H. *J. Chem. Phys.* **1989**, *90*, 1007–1023.

(356) Woon, D. E.; Dunning, T. H. *J. Chem. Phys.* **1993**, *98*, 1358–1371.

(357) Benedikt, U.; Auer, A. A.; Jensen, F. *J. Chem. Phys.* **2008**, *129*, 064111.

(358) Noro, T.; Sekiya, M.; Koga, T. *Theor. Chem. Acc.* **2012**, *131*, 1124.

(359) Noro, T.; Sekiya, M.; Koga, T. *Theor. Chem. Acc.* **2013**, *132*, 1363.

(360) Jorge, F. E.; Canal Neto, A.; Camiletti, G. G.; Machado, S. F. *J. Chem. Phys.* **2009**, *130*, 064108.

(361) Campos, C. T.; Jorge, F. E. *Mol. Phys.* **2013**, *111*, 167–173.

(362) Martins, L.; Jorge, F.; Machado, S. *Mol. Phys.* **2015**, *113*, 3578–3586.

(363) Franzke, Y. J.; Spiske, L.; Pollak, P.; Weigend, F. *J. Chem. Theory Comput.* **2020**, *16*, 5658–5674.

(364) Zobel, J. P.; Widmark, P.-O.; Veryazov, V. *J. Chem. Theory Comput.* **2020**, *16*, 278–294.

(365) Roos, B. O.; Lindh, R.; Malmqvist, P.-Å.; Veryazov, V.; Widmark, P.-O. *J. Phys. Chem. A* **2004**, *108*, 2851–2858.

(366) Roos, B. O.; Lindh, R.; Malmqvist, P.-Å.; Veryazov, V.; Widmark, P.-O. *J. Phys. Chem. A* **2005**, *109*, 6575–6579.

(367) Pritchard, B. P.; Altarawy, D.; Didier, B.; Gibson, T. D.; Windus, T. L. *J. Chem. Inf. Model.* **2019**, *59*, 4814–4820.

(368) Cheng, L.; Gauss, J. *J. Chem. Phys.* **2011**, *135*, 244104.

(369) Cheng, L.; Gauss, J.; Stanton, J. F. *J. Chem. Phys.* **2015**, *142*, 224309.

(370) Dirac, P. A. M. *Proc. Roy. Soc. Lond. A* **1929**, *123*, 714–733.

(371) Slater, J. C. *Phys. Rev.* **1951**, *81*, 385–390.

(372) Vosko, S. H.; Wilk, L.; Nusair, M. *Can. J. Phys.* **1980**, *58*, 1200–1211.

(373) Keal, T. W.; Tozer, D. J. *J. Chem. Phys.* **2004**, *121*, 5654–5660.

(374) Perdew, J. P. *Phys. Rev. B* **1986**, *33*, 8822–8824.

(375) Becke, A. D. *Phys. Rev. A* **1988**, *38*, 3098–3100.

(376) Perdew, J. P.; Ruzsinszky, A.; Csonka, G. I.; Constantin, L. A.; Sun, J. *Phys. Rev. Lett.* **2009**, *103*, 026403.

(377) Perdew, J. P.; Ruzsinszky, A.; Csonka, G. I.; Constantin, L. A.; Sun, J. *Phys. Rev. Lett.* **2011**, *106*, 179902.

(378) Furness, J. W.; Kaplan, A. D.; Ning, J.; Perdew, J. P.; Sun, J. *J. Phys. Chem. Lett.* **2020**, *11*, 8208–8215.

(379) Furness, J. W.; Kaplan, A. D.; Ning, J.; Perdew, J. P.; Sun, J. *J. Phys. Chem. Lett.* **2020**, *11*, 9248–9248.

(380) Lee, C.; Yang, W.; Parr, R. G. *Phys. Rev. B* **1988**, *37*, 785–789.

(381) Becke, A. D. *J. Chem. Phys.* **1993**, *98*, 1372–1377.

(382) Becke, A. D. *J. Chem. Phys.* **1993**, *98*, 5648–5652.

(383) Becke, A. D. *J. Chem. Phys.* **1997**, *107*, 8554–8560.

(384) Wilson, P. J.; Bradley, T. J.; Tozer, D. J. *J. Chem. Phys.* **2001**, *115*, 9233–9242.

(385) Staroverov, V. N.; Scuseria, G. E.; Tao, J.; Perdew, J. P. *J. Chem. Phys.* **2003**, *119*, 12129–12137.

(386) Grimme, S. *J. Phys. Chem. A* **2005**, *109*, 3067–3077.

(387) Yanai, T.; Tew, D. P.; Handy, N. C. *Chem. Phys. Lett.* **2004**, *393*, 51–57.

(388) Jin, Y.; Bartlett, R. J. *J. Chem. Phys.* **2016**, *145*, 034107.

(389) Haiduke, R. L. A.; Bartlett, R. J. *J. Chem. Phys.* **2018**, *149*, 131101.

(390) Heyd, J.; Scuseria, G. E.; Ernzerhof, M. *J. Chem. Phys.* **2003**, *118*, 8207–8215.

(391) Heyd, J.; Scuseria, G. E.; Ernzerhof, M. *J. Chem. Phys.* **2006**, *124*, 219906.

(392) Krukau, A. V.; Vydrov, O. A.; Izmaylov, A. F.; Scuseria, G. E. *J. Chem. Phys.* **2006**, *125*, 224106.

(393) Vydrov, O. A.; Scuseria, G. E. *J. Chem. Phys.* **2006**, *125*, 234109.

(394) Chai, J.-D.; Head-Gordon, M. *Phys. Chem. Chem. Phys.* **2008**, *10*, 6615–6620.

(395) Manual of TURBOMOLE V7.5.1 2021, a development of University of Karlsruhe and Forschungszentrum Karlsruhe GmbH, 1989-2007, TURBOMOLE GmbH, since 2007; available from `https://www.turbomole.org/turbomole/turbomole-documentation/` (retrieved August 28, 2021).

(396) Schmitte, J.; Friebel, C.; Weller, F.; Dehnicke, K. *Z. Anorg. Allg. Chem.* **1982**, *495*, 148–156.

(397) Sunil, K. K.; Rogers, M. T. *Inorg. Chem.* **1981**, *20*, 3283–3287.

(398) Manoharan, P. T.; Rogers, M. T. *J. Chem. Phys.* **1968**, *49*, 5510–5519.

(399) Van Kemenade, J. T. C. Ligand Hyperfine Interactions in Oxyhalides of Pentavalent Chromium, Molybdenum and Tungsten, Ph.D. Thesis, The Netherlands: Technical University Delft, 1970.

(400) Baldas, J.; Boas, J. F.; Bonnyman, J. *Aus. J. Chem.* **1989**, *42*, 639–648.

(401) Baldas, J.; Boas, J. F.; Bonnyman, J.; Williams, G. A. *J. Chem. Soc., Dalton Trans.* **1984**, 2395–2400.

(402) Kersting, M.; Friebel, C.; Dehnicke, K.; Krestel, M.; Allmann, R. *Z. Anorg. Allg. Chem.* **1988**, *563*, 70–78.

(403) Voigt, A.; Abram, U.; Kirmse, R. *Inorg. Chem. Commun.* **1998**, *1*, 141–142.

(404) Voigt, A.; Abram, U.; Böttcher, R.; Richter, U.; Reinhold, J.; Kirmse, R. *Chem. Phys.* **2000**, *253*, 171–181.

(405) Abram, U.; Braun, M.; Abram, S.; Kirmse, R.; Voigt, A. *J. Chem. Soc., Dalton Trans.* **1998**, 231–238.

(406) Borisova, L. V.; Ermakov, A. N.; Plastinina, Y. I.; Prasolova, O. D.; Marov, I. N. *Analyst* **1982**, *107*, 500–504.

(407) Holloway, J. H.; Hope, E. G.; Raynor, J. B.; Townson, P. T. *J. Chem. Soc., Dalton Trans.* **1992**, 1131–1134.

(408) Dyall, K. G.; Gomes, A. S. P. *Theor. Chem. Acc.* **2009**, *125*, 97–100.

(409) Nava, P.; Sierka, M.; Ahlrichs, R. *Phys. Chem. Chem. Phys.* **2003**, *5*, 3372–3381.

(410) Branzoli, F.; Carretta, P.; Filibian, M.; Zoppellaro, G.; Graf, M. J.; Galan-Mascaros, J. R.; Fuhr, O.; Brink, S.; Ruben, M. *J. Am. Chem. Soc.* **2009**, *131*, 4387–4396.

(411) Sikkema, J.; Visscher, L.; Saue, T.; Iliaš, M. *J. Chem. Phys.* **2009**, *131*, 124116.

(412) Chesnut, D. B.; Moore, K. D. *J. Comput. Chem.* **1989**, *10*, 648–659.

(413) Chesnut, D.; Rusiloski, B.; Moore, K.; Egolf, D. *J. Comput. Chem.* **1993**, *14*, 1364–1375.

(414) Autschbach, J. *ChemPhysChem* **2009**, *10*, 2274–2283.

(415) Lehtola, S.; Dimitrova, M.; Fliegl, H.; Sundholm, D. *J. Chem. Theory Comput.* **2021**, *17*, 1457–1468.

(416) Lehtola, S.; Dimitrova, M.; Fliegl, H.; Sundholm, D. *J. Chem. Theory Comput.* **2021**, *17*, 4629–4631.

(417) Holzer, C.; Franzke, Y. J.; Kehry, M. *J. Chem. Theory Comput.* **2021**, *17*, 2928–2947.

(418) Teale, A. M.; Lutnæs, O. B.; Helgaker, T.; Tozer, D. J.; Gauss, J. *J. Chem. Phys.* **2013**, *138*, 024111.

(419) Hedegård, E. D.; Kongsted, J.; Sauer, S. P. A. *J. Chem. Theory Comput.* **2013**, *9*, 2380–2388.

(420) Flaig, D.; Maurer, M.; Hanni, M.; Braunger, K.; Kick, L.; Thubauville, M.; Ochsenfeld, C. *J. Chem. Theory Comput.* **2014**, *10*, 572–578.

(421) Stoychev, G. L.; Auer, A. A.; Izsák, R.; Neese, F. *J. Chem. Theory Comput.* **2018**, *14*, 619–637.

(422) Reiter, K.; Mack, F.; Weigend, F. *J. Chem.Theory Comput.* **2018**, *14*, 191–197.

(423) Lutnæs, O. B.; Teale, A. M.; Helgaker, T.; Tozer, D. J.; Ruud, K.; Gauss, J. *J. Chem. Phys.* **2009**, *131*, 144104.

(424) Eichkorn, K.; Weigend, F.; Treutler, O.; Ahlrichs, R. *Theor. Chem. Acc.* **1997**, *97*, 119–124.

(425) Weigend, F. *Phys. Chem. Chem. Phys.* **2006**, *8*, 1057–1065.

(426) Weigend, F.; Häser, M.; Patzelt, H.; Ahlrichs, R. *Chem. Phys. Lett.* **1998**, *294*, 143–152.

(427) Hättig, C. *Phys. Chem. Chem. Phys.* **2005**, *7*, 59–66.

(428) Eshuis, H.; Yarkony, J.; Furche, F. *J. Chem. Phys.* **2010**, *132*, 234114.

(429) Alonso, P.; Alcalá, R.; Usón, R.; Forniés, J. *J. Phys. Chem. Solids* **1991**, *52*, 975–978.

(430) Jaramillo, J.; Scuseria, G. E.; Ernzerhof, M. *J. Chem. Phys.* **2003**, *118*, 1068–1073.

(431) Wodyński, A.; Kaupp, M. *J. Chem. Theory Comput.* **2020**, *16*, 314–325.

(432) Johnson, E. R. *J. Chem. Phys.* **2014**, *141*, 124120.

(433) Perdew, J. P.; Staroverov, V. N.; Tao, J.; Scuseria, G. E. *Phys. Rev. A* **2008**, *78*, 052513.

(434) Ishikawa, N.; Sugita, M.; Wernsdorfer, W. *Angew. Chem., Int. Ed.* **2005**, *44*, 2931–2935.

(435) Taran, G.; Bonet, E.; Wernsdorfer, W. *J. Appl. Phys.* **2019**, *125*, 142903.

(436) Neese, F. In *eMagRes*; American Cancer Society: 2017, pp 1–22.

(437) McWeeny, R. *J. Chem. Phys.* **1965**, *42*, 1717–1725.

(438) McWeeny, R., *Spins in Quantum Chemistry*; Academic Press: New York, USA, 1970.

(439) Harriman, J. E., *Theoretical Foundations of Electron Spin Resonance*; Physical Chemistry: A Series of Monographs, Vol. 37; Academic Press: New York, USA, 1978.

(440) McWeeny, R., *Methods of Molecular Quantum Mechanics*, 2nd ed.; Academic Press, London: 1989.

(441) *EPR Spectroscopy: Fundamentals and Methods*; Goldfarb, D., Stoll, S., Eds.; John Wiley & Sons: Chichester, United Kingdom, 2018.

(442) Briganti, M.; Lucaccini, E.; Chelazzi, L.; Ciattini, S.; Sorace, L.; Sessoli, R.; Totti, F.; Perfetti, M. *J. Am. Chem. Soc.* **2021**, *143*, 8108–815.

(443) *Calculation of NMR and EPR Parameters: Theory and Applications*; Kaupp, M., Bühl, M., Malkin, V. G., Eds.; Wiley-VCH: Weinheim, Germany, 2004.

(444) Dyall, K. G.; Fægri Jr., K., *Introduction to Relativistic Quantum Chemistry*; Oxford University Press: New York, USA, 2007.

(445) Liu, W. *J. Chem. Phys.* **2020**, *152*, 180901.

(446) Van Lenthe, E.; Wormer, P. E. S.; van der Avoird, A. *J. Chem. Phys.* **1997**, *107*, 2488–2498.

(447) Autschbach, J.; Pritchard, B. *Theor. Chem. Acc.* **2011**, *129*, 453–466.

(448) Aquino, F.; Govind, N.; Autschbach, J. *J. Chem. Theory Comput.* **2011**, *7*, 3278–3292.

(449) Repiský, M.; Komorovský, S.; Malkin, E.; Malkina, O. L.; Malkin, V. G. *Chem. Phys. Lett.* **2010**, *488*, 94–97.

(450) Cherry, P. J.; Komorovsky, S.; Malkin, V. G.; Malkina, O. L. *Mol. Phys.* **2017**, *115*, 75–89.

(451) Vad, M. S.; Pedersen, M. N.; Nørager, A.; Jensen, H. J. A. *J. Chem. Phys.* **2013**, *138*, 214106.

(452) Hélène, B. *ChemPhysChem* **2006**, *7*, 1575–1589.

(453) Lan, T. N.; Chalupský, J.; Yanai, T. *Mol. Phys.* **2015**, *113*, 1750–1767.

(454) Zhang, Y. et al. *J. Chem. Phys.* **2020**, *152*, 064113.

(455) Saue, T. et al. *J. Chem. Phys.* **2020**, *152*, 204104.

(456) Williams-Young, D. B.; Petrone, A.; Sun, S.; Stetina, T. F.; Lestrange, P.; Hoyer, C. E.; Nascimento, D. R.; Koulias, L.; Wildman, A.; Kasper, J.; Goings, J. J.; Ding, F.; DePrince III, A. E.; Valeev, E. F.; Li, X. *Wiley Interdiscip. Rev.: Comput. Mol. Sci.* **2020**, *10*, e1436.

(457) Werner, H.-J. et al. *J. Chem. Phys.* **2020**, *152*, 144107.

(458) Aquilante, F. et al. *J. Comput. Chem.* **2016**, *37*, 506–.541.

(459) Matthews, D. A.; Cheng, L.; Harding, M. E.; Lipparini, F.; Stopkowicz, S.; Jagau, T.-C.; Szalay, P. G.; Gauss, J.; Stanton, J. F. *J. Chem. Phys.* **2020**, *152*, 214108.

(460) Smith, D. G. A. et al. *J. Chem. Phys.* **2020**, *152*, 184108.

(461) Aprà, E. et al. *J. Chem. Phys.* **2020**, *152*, 184102.

(462) Nakajima, T.; Hirao, K. *Chem. Rev.* **2012**, *112*, 385–402.

(463) Reiher, M. *Wiley Interdiscip. Rev.: Comput. Mol. Sci.* **2012**, *2*, 139–149.

(464) Cheng, L.; Gauss, J. *J. Chem. Phys.* **2011**, *135*, 244104.

(465) Zou, W.; Guo, G.; Suo, B.; Liu, W. *J. Chem. Theory Comput.* **2020**, *16*, 1541–1554.

(466) Yoshizawa, T.; Filatov, M.; Cremer, D.; Zou, W. *Mol. Phys.* **2019**, *117*, 1164–1171.

(467) Zhu, H.; Gao, C.; Filatov, M.; Zou, W. *Phys. Chem. Chem. Phys.* **2020**, *22*, 26776–26786.

(468) Sun, Q.; Liu, W.; Xiao, Y.; Cheng, L. *J. Chem. Phys.* **2009**, *131*, 081101.

(469) Sun, Q.; Xiao, Y.; Liu, W. *J. Chem. Phys.* **2012**, *137*, 174105.

(470) Filatov, M.; Zou, W.; Cremer, D. *J. Phys. Chem. A* **2012**, *116*, 3481–3486.

(471) Schreckenbach, G.; Ziegler, T. *J. Phys. Chem. A* **1997**, *101*, 3388–3399.

(472) Schreckenbach, G.; Ziegler, T. *Theor. Chem. Acc.* **1998**, *99*, 71–82.

(473) Patchkovskii, S.; Ziegler, T. *J. Chem. Phys.* **1999**, *111*, 5730–5740.

(474) Patchkovskii, S.; Ziegler, T. *J. Am. Chem. Soc.* **2000**, *122*, 3506–3516.

(475) Patchkovskii, S.; Strong, R. T.; Pickard, C. J.; Un, S. *J. Chem. Phys.* **2005**, *122*, 214101.

(476) Glasbrenner, M.; Vogler, S.; Ochsenfeld, C. *J. Chem. Phys.* **2018**, *148*, 214101.

(477) Glasbrenner, M.; Vogler, S.; Ochsenfeld, C. *J. Chem. Phys.* **2019**, *150*, 024104.

(478) Tran, V. A.; Neese, F. *J. Chem. Phys.* **2020**, *153*, 054105.

(479) Kutzelnigg, W. *J. Mol. Struct.: THEOCHEM* **1989**, *202*, 11–61.

(480) London, F. *J. Phys. Radium* **1937**, *8*, 397–409.

(481) Ditchfield, R. *Mol. Phys.* **1974**, *27*, 789–807.

(482) Iliaš, M.; Saue, T.; Enevoldsen, T.; Jensen, H. J. A. *J. Chem. Phys.* **2009**, *131*, 124119.

(483) Komorovský, S.; Repiský, M.; Malkina, O. L.; Malkin, V. G. *J. Chem. Phys.* **2010**, *132*, 154101.

(484) Olejniczak, M.; Bast, R.; Saue, T.; Pecul, M. *J. Chem. Phys.* **2012**, *136*, 014108.

(485) Olejniczak, M.; Bast, R.; Saue, T.; Pecul, M. *J. Chem. Phys.* **2012**, *136*, 239902.

(486) Fukuda, R.; Hada, M.; Nakatsuji, H. *J. Chem. Phys.* **2003**, *118*, 1027–1035.

(487) Yoshizawa, T.; Hada, M. *Chem. Phys. Lett.* **2015**, *618*, 132–141.

(488) Hayami, M.; Seino, J.; Nakai, H. *J. Chem. Phys.* **2018**, *148*, 114109.

(489) Wolff, S. K.; Ziegler, T.; van Lenthe, E.; Baerends, E. J. *J. Chem. Phys.* **1999**, *110*, 7689–7698.

(490) Autschbach, J. *Mol. Phys.* **2013**, *111*, 2544–2554.

(491) Neese, F.; Solomon, E. I. *Inorg. Chem.* **1998**, *37*, 6568–6582.

(492) Gauss, J.; Kállay, M.; Neese, F. *J. Phys. Chem. A* **2009**, *113*, 11541–11549.

(493) Seino, J.; Nakai, H. *J. Chem. Phys.* **2012**, *136*, 244102.

(494) Seino, J.; Nakai, H. *J. Chem. Phys.* **2012**, *137*, 144101.

(495) Lichtenberger, N.; Franzke, Y. J.; Massa, W.; Weigend, F.; Dehnen, S. *Chem. - Eur. J.* **2018**, *24*, 12022–12030.

(496) Balmer, M.; Franzke, Y. J.; Weigend, F.; von Hänisch, C. *Chem. - Eur. J.* **2020**, *26*, 192–197.

(497) Eulenstein, A. R.; Franzke, Y. J.; Bügel, P.; Massa, W.; Weigend, F.; Dehnen, S. *Nat. Commun.* **2020**, *11*, 5122.

(498) Eulenstein, A. R.; Franzke, Y. J.; Lichtenberger, N.; Wilson, R. J.; Deubner, H. L.; Kraus, F.; Weigend, F.; Dehnen, S. *Nat. Chem.* **2021**, *13*, 149–155.

(499) Franzke, Y. J.; Holzer, C.; Mack, F. *J. Chem. Theory Comput.* **2022**, *18*, 1030–1045.

(500) Van Wüllen, C. *J. Comput. Chem.* **2002**, *23*, 779–785.

(501) ReSpect homepage and manual for EPR g-tensors, `http://respectprogram.org/epr-gt.html` (retrieved March 11, 2022).

(502) Komorovský, S.; Repiský, M.; Ruud, K.; Malkina, O. L.; Malkin, V. G. *J. Phys. Chem. A* **2013**, *117*, 14209–14219.

(503) Moon, S.; Patchkovskii, S. In *Calculation of NMR and EPR Parameters*, Kaupp, M., Bühl, M., Malkin, V. G., Eds.; Wiley-VCH: Weinheim, Germany, 2004; Chapter 20, pp 325–338.

(504) Pulay, P. *Mol. Phys.* **1969**, *17*, 197–204.

(505) Rice, J.; Amos, R. *Chem. Phys. Lett.* **1985**, *122*, 585–590.

(506) Pausch, A.; Klopper, W. *Mol. Phys.* **2020**, *118*, e1736675.

(507) Wolinski, K.; Hinton, J. F.; Pulay, P. *J. Am. Chem. Soc.* **1990**, *112*, 8251–8260.

(508) Häser, M.; Ahlrichs, R.; Baron, H. P.; Weis, P.; Horn, H. *Theor. Chim. Acta* **1992**, *83*, 455–470.

(509) Krykunov, M.; Ziegler, T.; van Lenthe, E. *J. Phys. Chem. A* **2009**, *113*, 11495–11500.

(510) Franzke, Y. J. Calculation of NMR Parameters in a Modern Relativistic Density Functional Framework: Theory, Implementation, and Application, Dissertation, Germany: Karlsruhe Institute of Technology (KIT), 2021.

(511) Huniar, U. Berechnung der chemischen Verschiebung der NMR mit Methoden der Dichtefunktionaltheorie (DFT), Diploma Thesis, Germany: University of Karlsruhe (TH), 1999.

(512) Kollwitz, M.; Gauss, J. *Chem. Phys. Lett.* **1996**, *260*, 639–646.

(513) Kollwitz, M.; Häser, M.; Gauss, J. *J. Chem. Phys.* **1998**, *108*, 8295–8301.

(514) Dupuis, M.; Marquez, A. *J. Chem. Phys.* **2001**, *114*, 2067–2078.

(515) Gautschi, W. *ACM Trans. Math. Softw.* **1994**, *20*, 21–62.

(516) Maximoff, S. N.; Scuseria, G. E. *Chem. Phys. Lett.* **2004**, *390*, 408–412.

(517) Reiter, K. Weiterentwicklung und Anwendung von quantenchemischen Methoden zur Berechnung von Molekülen im Magnetfeld, Dissertation, Germany: Karlsruhe Institute of Technology (KIT), 2018.

(518) Franzke, Y. J.; Yu, J. M. *J. Chem. Theory Comput.* **2022**, *18*, 2246–2266.

(519) Jensen, F. *J. Chem. Theory Comput.* **2008**, *4*, 719–727.

(520) Stephens, P. J.; Devlin, F. J.; Chabalowski, C. F.; Frisch, M. J. *J. Phys. Chem.* **1994**, *98*, 11623–11627.

(521) Darago, L. E.; Boshart, M. D.; Nguyen, B. D.; Perlt, E.; Ziller, J. W.; Lukens, W. W.; Furche, F.; Evans, W. J.; Long, J. R. *J. Am. Chem. Soc.* **2021**, *143*, 8465–8475.

(522) Dyall, K. G. *Theor. Chem. Acc.* **2011**, *129*, 603–613.

(523) Mastalerz, R.; Barone, G.; Lindh, R.; Reiher, M. *J. Chem. Phys.* **2007**, *127*, 074105.

(524) Autschbach, J.; Peng, D.; Reiher, M. *J. Chem. Theory Comput.* **2012**, *8*, 4239–4248.

(525) Reiher, M. *Theor. Chem. Acc.* **2006**, *116*, 241–252.

(526) Barysz, M.; Sadlej, A. J.; Snijders, J. G. *Int. J. Quantum Chem.* **1997**, *65*, 225–239.

(527) Barysz, M.; Sadlej, A. J. *J. Chem. Phys.* **2002**, *116*, 2696–2704.

(528) Kedziera, D.; Barysz, M. *Chem. Phys. Lett.* **2007**, *446*, 176–181.

(529) Bronshtein, I. N.; Semendyayev, K. A.; Musiol, G.; Mühlig, H., *Handbook of Mathematics*, 6th ed.; Springer: Berlin, Heidelberg, Germany, 2015.

(530) Fox, A. R.; Bart, S. C.; Meyer, K.; Cummins, C. C. *Nature* **2008**, *455*, 341.

(531) Hennum, A. C.; Klopper, W.; Helgaker, T. *J. Chem. Phys.* **2001**, *115*, 7356–7363.

(532) Landau, L. D.; Lifshitz, E. M., *Course of theoretical physics*, 4. rev. Engl. ed.; Pergamon Press, Oxford: 1998; Vol. 2: The classical theory of fields.

Appendix A

Nuclear Current Density and Vector Potential

The form of the vector potential that appears in the generalized momentum operator expressions of the hyperfine coupling constant and g-tensor of Chapter 3 can vary depending on whether a point-nucleus or finite-nucleus model is employed. The information presented in this section was first explored by Bohr and Weisskopf[296] and reformulated by Hennum, Klopper, and Helgaker.[531] The basic results are presented below. For ease of presentation, vectors are denoted by an arrow ($\vec{v}$) and tensors are denoted by bold capital letters ($\mathbf{M}$) from this point forward. An atomic system with the nucleus placed at the origin is considered.

A model for the nuclear current density can be derived as:

$$\vec{j}_{ext}(\vec{r}) = \rho(\vec{r}) \left(\vec{r} \times (\vec{m} \cdot (\mathbf{Q} - \mathbf{M})^{-1}) \right), \tag{A.1}$$

where $\rho(\vec{r})$ is the chosen nuclear charge density model, $\vec{m}$ is the magnetic dipole moment,

and matrices $\mathbf{Q}$ and $\mathbf{M}$ will be defined below. This model can be obtained from taking the general quantum mechanical expression for the current density, $\vec{j}(\vec{r}) = \rho(\vec{r})\hat{\vec{\nabla}}\psi(\vec{r})$, and inserting an ansatz to the velocity distribution $\hat{\vec{\nabla}}\psi$ into the expression for the magnetic dipole moment, given as

$$\vec{m} = \frac{1}{2}\int d\vec{r}\,\rho(\vec{r})\left(\vec{r}\times\hat{\vec{\nabla}}\psi\right). \tag{A.2}$$

We know that the expression $\hat{\vec{\nabla}}\psi$ should take the form of some $\vec{r}\times\vec{g}$, where $\vec{r}$ is the position vector and $\vec{g}$ is an unknown vector expression, since $\hat{\vec{\nabla}}\psi$ is orthogonal to $\hat{\vec{\nabla}}\rho(\vec{r})$. Thus, we now attempt to find an expression for $\vec{g}$. We insert this ansatz into Eq. A.2

$$m_x = \int d\vec{r}\,\rho(\vec{r})\left(xyg_y + xzg_z - g_x y^2 - g_x z^2\right) \tag{A.3}$$

$$m_y = \int d\vec{r}\,\rho(\vec{r})\left(yxg_x + yzg_z - g_y x^2 - g_y z^2\right) \tag{A.4}$$

$$m_z = \int d\vec{r}\,\rho(\vec{r})\left(xzg_x + zyg_y - g_z x^2 - g_z y^2\right) \tag{A.5}$$

where the components (m_x, m_y, m_z) correspond to those of the magnetic dipole moment. These expressions can be written in terms of the traceless quadrupole moment tensor

$$Q_{ij} = \int \left(3x_i x_j - r^2\delta_{ij}\right)\rho(\vec{r})d\vec{r}. \tag{A.6}$$

Writing out the expression

$$\mathbf{Q}\cdot\vec{g}=\begin{pmatrix}\int\left(2x^2g_x-y^2g_x-z^2g_x+3xyg_y+3xzg_z\right)\rho(\vec{r})d\vec{r}\\ \int\left(2y^2g_y-x^2g_y-z^2g_y+3xyg_x+3yzg_z\right)\rho(\vec{r})d\vec{r}\\ \int\left(2z^2g_z-x^2g_z-y^2g_z+3xzg_x+3xzg_x\right)\rho(\vec{r})d\vec{r}\end{pmatrix} \tag{A.7}$$

we can compare with our expression for the magnetic dipole moment in Eqs. A.3 to A.5 in order to obtain

$$\vec{g}=\vec{m}\cdot(\mathbf{Q}-\mathbf{M})^{-1} \tag{A.8}$$

where

$$\mathbf{M}=\begin{pmatrix}\frac{2}{3}\int(x^2+y^2+z^2)\rho(\vec{r})d\vec{r} & 0 & 0\\ 0 & \frac{2}{3}\int(x^2+y^2+z^2)\rho(\vec{r})d\vec{r} & 0\\ 0 & 0 & \frac{2}{3}\int(x^2+y^2+z^2)\rho(\vec{r})d\vec{r}\end{pmatrix}. \tag{A.9}$$

With our expression for $\vec{g}$, our nuclear current density model finally becomes:

$$\vec{j}_{ext}(\vec{r})=\rho(\vec{r})\left(\vec{r}\times(\vec{m}\cdot(\mathbf{Q}-\mathbf{M})^{-1})\right) \tag{A.10}$$

The corresponding vector potential can be written as:

$$\hat{\vec{A}}(\vec{r})=\int d\vec{r}\,'\,\frac{\vec{j}_{ext}(\vec{r}\,')}{|\vec{r}-\vec{r}\,'|}, \tag{A.11}$$

and it can subsequently be evaluated for different choices of the charge density $\rho(\vec{r})$. For one

that is spherically symmetric, as is the case for a Gaussian, the quadrupole moment is zero ($\mathbf{Q} = 0$). Furthermore, for the choice[247]

$$\rho(\vec{r}) = G_\eta(\vec{r}) = \left(\frac{\eta}{\pi}\right)^{3/2} e^{-\eta r^2}, \tag{A.12}$$

the vector potential can be subsequently evaluated as:

$$\begin{aligned} \hat{\vec{A}}(\vec{r}) &= -\vec{m} \cdot (\mathbf{Q} - \mathbf{M})^{-1} \times \int d\vec{r}\,' \, \frac{G_\eta(\vec{r}\,')\vec{r}\,'}{|\vec{r} - \vec{r}\,'|} \\ &= -\frac{1}{3}\vec{m} \times \hat{\vec{\nabla}} \int d\vec{r}\,' \, \frac{G_\eta(\vec{r}\,')}{|\vec{r} - \vec{r}\,'|} \end{aligned} \tag{A.13}$$

where the integrals in $\mathbf{M}$ have been explicitly evaluated. This result is equivalent (up to a constant) to Eqs. (38) and (39) of Ref [531]. For the limit of a point charge, $\rho(\vec{r})$ can be taken as $\delta(\vec{r} - \vec{r}\,')$.[298,299] The vector potential in the point-charge model reads[532]

$$\hat{\vec{A}}(\vec{r}) = \frac{\vec{m} \times \vec{r}}{r^3}. \tag{A.14}$$

For a molecular system, this results in

$$\hat{\vec{A}}(\vec{r}) = \sum_N \hat{\vec{A}}_N(\vec{r}) = \sum_N \frac{\vec{m} \times \vec{r}_N}{r_N^3} \qquad \text{with} \quad \vec{r}_N = \vec{r} - \vec{R}_N \tag{A.15}$$

where $\vec{R}_N$ denotes the position of nucleus N.